

**PHOTOTHERMAL DETERMINATION
OF TISSUE OPTICAL COEFFICIENTS USING
AN OPTICAL FIBRE SENSOR**

Jan Laufer, Dipl.-Ing.

*Thesis submitted for the Degree of
Doctor of Philosophy (Ph.D.)
of the University of London*



Department of Medical Physics and Bioengineering
University College London

November 2000

ProQuest Number: U642579

All rights reserved

INFORMATION TO ALL USERS

The quality of this reproduction is dependent upon the quality of the copy submitted.

In the unlikely event that the author did not send a complete manuscript and there are missing pages, these will be noted. Also, if material had to be removed, a note will indicate the deletion.



ProQuest U642579

Published by ProQuest LLC(2015). Copyright of the Dissertation is held by the Author.

All rights reserved.

This work is protected against unauthorized copying under Title 17, United States Code.
Microform Edition © ProQuest LLC.

ProQuest LLC
789 East Eisenhower Parkway
P.O. Box 1346
Ann Arbor, MI 48106-1346

ABSTRACT

This thesis is concerned with the development of an optical fibre sensor for the photothermal determination of the optical coefficients of tissue. The detection of differences in tissue optical properties might be used for the diagnosis of cancers and other tissue pathologies.

The sensor consists of a thin transparent polymer film mounted at the distal end of an optical fibre. The film acts as a Fabry-Perot interferometer. The absorption of short, low energy laser pulses transmitted through the film and into the tissue generates thermal as well as acoustic transients, which propagate into the film and modulate its thickness. The changes in the optical thickness of the film are detected interferometrically. The temporal and amplitude characteristics of the detected photoacoustic and photothermal signals are determined by the optical, acoustic, thermal and spatial properties of the tissue. The interpretation of photothermal signals may allow the diagnosis of tissue pathologies.

Photothermal signals detected using the optical fibre sensor were used in conjunction with a numerical model and model-based parameter estimation to determine the optical properties of tissue phantoms. The optical fibre sensor was found to be applicable to the determination of optical coefficients from the photothermal signal provided the thermal coefficients of the target were known with high certainty. The analysis of the parameter sensitivity revealed that the optical fibre sensor in its present configuration is more sensitive to the thermal coefficients than the optical coefficients of the target. Pulsed photothermal radiometry was found to have higher sensitivity to the optical coefficients than has the optical fibre sensor in its present form. However, modifications to the configuration of the sensor can produce a performance matching that of pulsed photothermal radiometry.

TABLE OF CONTENTS

ABSTRACT	2
TABLE OF FIGURES.....	9
LIST OF TABLES.....	16
ACKNOWLEDGEMENTS	18
1 INTRODUCTION	19
1.1 Background to this work	19
1.2 Origins of the optical properties of tissue.....	22
1.2.1 Terminology in tissue optics	22
<i>1.2.1.1 Absorption</i>	<i>22</i>
<i>1.2.1.2 Scattering.....</i>	<i>23</i>
<i>1.2.1.3 Scattering by spherical particles</i>	<i>27</i>
1.2.2 Absorption of light in tissue.....	28
1.2.3 Scattering of light in tissue.....	31
1.3 Models of light transport in tissue	32
1.3.1 Stochastic models.....	33
<i>1.3.1.1 The Monte Carlo technique</i>	<i>33</i>
<i>1.3.1.2 Random walk theory.....</i>	<i>34</i>
1.3.2 Deterministic models: the radiative transport equation	35
1.3.3 Solution methods for the radiative transport equation	36
<i>1.3.3.1 The diffusion approximation of the radiative transport</i> <i>equation.....</i>	<i>36</i>
<i>1.3.3.2 Numerical solutions to the radiative transport equation</i>	<i>37</i>

1.4 Measurement of the optical properties of tissue.....	38
1.4.1 Low coherence reflectometry.....	38
1.4.2 Coherent backscatter	39
1.4.3 Time-resolved spectroscopy.....	40
1.4.4 Frequency-domain spectroscopy.....	42
1.4.5 Spatially resolved reflectance spectroscopy.....	43
1.4.6 The inverse Monte Carlo method.....	45
1.4.7 Section summary.....	46
1.5 Optical properties of tissues in the near-infrared spectrum	46
1.6 Summary	50
2 HEAT TRANSPORT IN TISSUE.....	51
2.1 Overview of heat transfer in tissue	51
2.1.1 Radiation	53
2.1.2 Convection	54
2.1.3 Conduction.....	55
2.2 Analytical solutions to the heat diffusion equation	56
2.2.1 The Green's function	56
2.3 Numerical solutions to the heat diffusion equation	58
2.3.1 The finite difference method.....	59
2.3.2 The finite element method	59
2.4 Measurement of the thermal properties of tissue.....	60
2.5 The thermal properties of tissue	61
2.5.1 Effect of perfusion on the thermal properties of tissue.....	68
2.6 Effect of temperature on the optical and thermal tissue properties	69
3 REVIEW OF PHOTOTHERMAL SPECTROSCOPY	71
3.1 Instrumentation and detection techniques.....	71
3.1.1 Sources	71
3.1.2 Pyroelectric detection.....	72
3.1.3 Radiometric detection	74

3.1.4 Piezoelectric detection	75
3.1.5 Fluorescence.....	76
3.1.6 Interferometric techniques	76
3.1.7 Optical beam deflection	77
3.1.8 Photothermal displacement.....	78
3.1.9 Modulated optical reflectance.....	79
3.2 Photothermal spectroscopy on tissue.....	79
3.2.1 Choice of excitation wavelength.....	82
3.3 Photoacoustic spectroscopy	83
3.4 Summary	85

4 DETERMINATION OF OPTICAL COEFFICIENTS USING PULSED PHOTOTHERMAL RADIOMETRY	88
4.1 Introduction	88
4.2 Pulsed Photothermal Radiometry – Theory	89
4.2.1 Non-scattering homogeneous absorber.....	91
4.2.2 Homogenous scattering and absorbing media	92
4.3 Pulsed Photothermal Radiometry - Measurement and analysis.....	95
4.3.1 Set-up and methods	95
4.3.2 Performance of the photoconductive infrared detector.....	97
4.3.2.1 <i>Linearity</i>	97
4.3.2.2 <i>Sensitivity</i>	99
4.3.2.3 <i>Noise</i>	100
4.3.2.4 <i>Response time</i>	100
4.3.2.5 <i>Specificity</i>	101
4.3.3 Non-scattering absorbers	101
4.3.4 Absorbing and scattering medium.....	104

4.4 Confidence limits on the determined optical coefficients	107
4.5 Discussion	109
4.6 Conclusions	112

5 THE PHOTOACOUSTIC-PHOTOTHERMAL OPTICAL FIBRE

SENSOR – THEORY	115
5.1 Principles of operation	115
5.2 Low finesse Fabry-Perot interferometer output.....	117
5.2.1 Phase sensitivity and dc level.....	119
5.2.2 Effect of reflection coefficients on signal intensity modulation	121
5.2.3 Phase sensitivity of different materials for the sensing film.....	125
5.2.4 Illumination of the sensing film using an optical fibre	126
5.2.4.1 <i>Effect of a tilt angle between fibre and interferometer.....</i>	<i>131</i>
5.2.4.2 <i>Effect of a wedge.....</i>	<i>133</i>
5.3 Interaction of thermal and acoustic transients with the sensor	135
5.3.1 Acoustically induced phase modulation	135
5.3.2 Thermally induced phase modulation	137
5.4 Thermal Sensitivity	138
5.5 Noise analysis	141
5.5.1 Photodiode noise	142
5.5.2 Amplifier noise	143
5.5.3 Laser noise	148
5.5.3.1 <i>Intensity noise.....</i>	<i>148</i>
5.5.3.2 <i>Phase noise.....</i>	<i>148</i>
5.5.4 Overall system noise	149
5.6 Thermal detection limit.....	150
5.7 Discussion	151

6 A NUMERICAL MODEL OF THE OPTICAL FIBRE SENSOR.....	155
6.1 A Finite Element model of the optical fibre sensor	156
6.1.1 The finite element model for the interpretation of measurements on non-scattering liquid absorbers.....	159
6.1.2 Hybrid Monte Carlo/Finite Element model for measurements on turbid media.....	167
6.2 Model-based parameter estimation	170
6.2.1 Model in matrix terms.....	172
6.2.2 Linear maximum a posteriori estimation (MAP).....	172
6.2.2.1 Assumptions.....	172
6.2.2.2 Estimation involving subjective information	173
6.2.3 Implementation of the minimisation algorithm	176
6.3 Sensitivity of the photothermal signal to changes in the model parameters.....	178
6.4 Chapter summary.....	181
7 THE PHOTOTHERMAL OPTICAL FIBRE SENSOR – EXPERIMENTAL	183
7.1 Performance of the optical fibre sensor.....	185
7.1.1 Linearity	185
7.1.2 Sensitivity.....	185
7.1.3 Noise	185
7.1.4 Response time	186
7.1.5 Specificity	189
7.2 Detection of photothermal signals in tissue phantoms.....	190
7.2.1 Materials and methods	190
7.2.1.1 Dye adsorption to the sensing film.....	191
7.2.2 Measurements on tissue phantoms.....	196
7.3 Determination of optical parameters using model-based parameter estimation.....	197
7.3.1 Measurements on pure absorbers.....	198

7.3.1.1	<i>Normalised signals</i>	199
7.3.1.2	<i>Two-parameter fit</i>	201
7.3.1.3	<i>Two parameter fit with large initial uncertainties</i>	204
7.3.2	Estimation of the absorption and reduced scattering coefficient of turbid gels	206
7.4	Summary	210
8	COMPARISON OF THE OPTICAL FIBRE SENSOR WITH OTHER PHOTOTHERMAL TECHNIQUES	212
8.1	Performance of the optical fibre sensor as a thermal detector	212
8.1.1	Thermal detection limit	212
8.1.2	Rise time and bandwidth	214
8.2	Fibre-optic photothermal radiometry	215
8.3	Accuracy of optical coefficients determined using photothermal techniques	218
8.3.1	Confidence limits of the determined optical coefficients	219
8.3.2	Comparison of the parameter sensitivities	221
8.3.2.1	<i>Pulsed photothermal radiometry</i>	222
8.3.2.2	<i>The optical fibre sensor</i>	224
8.4	Summary	233
	CONCLUDING REMARKS AND OUTLOOK	235
	APPENDIX A: DERIVATION OF THE HEAT DIFFUSION EQUATION	240
	APPENDIX B: SINGLE FILM INTERFERENCE	245
	PUBLICATIONS ARISING FROM THIS WORK	248
	REFERENCES	249

TABLE OF FIGURES

Figure 1.1 <i>The co-ordinate system for scattering theory.</i>	23
Figure 1.2 <i>Absorption spectrum of water in the visible and infrared wavelength region.</i>	28
Figure 1.3 <i>The absorption spectra for HbO₂ and Hb in the near-infrared wavelength region.</i>	29
Figure 1.4 <i>Typical absorption spectrum of lipids in the near-infrared wavelength region.</i>	30
Figure 1.5 <i>Absorption spectra of reduced and oxidised cytochrome c oxidase.</i>	31
Figure 1.6 <i>Illustration of the contributions to the energy radiance $L(\Omega)$ in an infinitesimally small tissue volume.</i>	35
Figure 1.7 <i>Schematic of a possible set-up for the detection of coherent backscatter. The two photon paths follow the same series of scattering events between the scattering centres i and j in reverse order. The phase difference between the photons, $\Delta\phi$, at the detector is proportional to the path length difference for the two routes.</i>	39
Figure 1.8 <i>Relationship between time-resolved and frequency-domain techniques. Photon propagation through tissue results in a temporal broadening of the pulse (time domain) or, in the frequency-domain, phase delay and a reduction in amplitude. Modulation and phase are related to time-resolved measurements through the Fourier transform.</i>	42
Figure 1.9 <i>Spectra of the absorption and reduced scattering coefficient of tumour and normal tissue of the human kidney ($N = 4$).</i>	48
Figure 1.10 <i>Spectra of the absorption and reduced scattering coefficient of tumour and normal tissue of the human liver ($N = 4$).</i>	48
Figure 1.11 <i>Spectra of the absorption and reduced scattering coefficient of tumour and normal tissue of the human breast ($N = 4$).</i>	49

Figure 1.12 Spectra of the absorption and reduced scattering coefficient of human dermis and subdermis ($N = 4$). (The feature at 815 nm is an artefact caused by a faulty CCD pixel.).....	49
Figure 2.1 Diagram illustrating the heat transport in tissue. Heat is generated in dV , transported in volume V by conduction and convection, stored in V and exchanged over area A	52
Figure 2.2 Emission spectrum of a perfect black-body at different temperatures.	53
Figure 2.3 Variation of the specific heat capacity for bovine and porcine fat with temperature in vitro.	66
Figure 3.1 Diagram of a typical experimental configuration of a pyroelectric detector.	73
Figure 3.2 Piezoelectric detection.....	75
Figure 3.3 Diagram of optical beam deflection technique.	78
Figure 3.4 Attenuation spectrum of a typical silver halide optical fibre (data taken from Oxford Electronics Ltd., Oxford, U.K.).	81
Figure 3.5 Typical photoacoustic signals generated in ink at various concentrations (a). Graph (b) illustrates how the absorption coefficient can be determined from the shape of the photoacoustic signal by fitting an exponential function between A and B	83
Figure 4.1 Theoretical PPTR responses showing the effect of scattering on the decay of the signal.	94
Figure 4.2 Theoretical fluence profiles for different reduced scattering coefficients obtained using equation (4.10)......	94
Figure 4.3 Experimental set-up for measurements using pulsed photothermal radiometry.	96
Figure 4.4 Experimental set-up for measuring the linearity of the radiometric detector using a black-body.....	98
Figure 4.5 Output of the HgCdTe detector with increasing temperature together with the linear regression in comparison to the radiant excitance of a blackbody.	99
Figure 4.6 Typical PPTR signal detected on a purely absorbing gel together with the best fit to the data.	103

Figure 4.7 Theoretical radiometric photothermal signals calculated using two different sets of μ_a , μ_s' , and K .	105
Figure 4.8 PPTR response of a turbid gel together with the best fit. The optical coefficients of the gel were $\mu_a = 2.70 \text{ mm}^{-1}$ and $\mu_s' = 2.80 \text{ mm}^{-1}$. The optical coefficients obtained from the non-linear curve fit were $\mu_a = 2.84 \text{ mm}^{-1}$ and $\mu_s' = 2.54 \text{ mm}^{-1}$.	105
Figure 4.9 Residuals contour plot for a non-scattering, absorbing gel.	108
Figure 4.10 Subsurface fluence profiles in turbid gels computed using the Monte Carlo method and the diffusion approximation. Good agreement between the diffusion approximation and the Monte Carlo method can be noted for μ_s' smaller than μ_a (a), while an increase in μ_s' produces marked differences in the fluence profiles.	110
Figure 4.11 Normalised theoretical PPTR plots obtained using two sets of different optical coefficients.	111
Figure 5.1 Schematic diagram of the photoacoustic-photothermal optical fibre sensor.	115
Figure 5.2 Intensity output of a low finesse Fabry-Perot interferometer as a function of phase bias ϕ . The diagram illustrates the working point of the interferometer – the phase bias has to be set to quadrature to produce the most linear relationship between phase shift and intensity.	116
Figure 5.3 Polymer sensing film acting as a low finesse interferometer.	118
Figure 5.4 Maximum permissible phase shift of the Fabry-Perot interferometer while maintaining linearity.	120
Figure 5.5 Normalised phase sensitivity $dI/I/d\phi$ for different reflection coefficients r_1 and r_2 ($I = 1 \text{ mW}$).	122
Figure 5.6 Fringe visibility M for different reflection coefficients r_1 and r_2 .	123
Figure 5.7 Phase sensitivities of different film materials in contact with water (¹ Polyvinylidene flouride, ² low density polyethylene, ³ polyethylene terephthalate, ⁴ polyethersulfone).	125
Figure 5.8 Diagram of a Fabry-Perot interferometer illuminated by the divergent beam from an optical fibre.	127

Figure 5.9	<i>Effect of beam divergence on fringe visibility of a low finesse Fabry-Perot interferometer for different cavity thicknesses ($z_0 = 0$, $n_1 = n_2 = 1.44$, $n = 1.64$). ...</i>	130
Figure 5.10	<i>Illumination of the Fabry-Perot interferometer by an optical fibre positioned at an angle. The ellipse centred at O' represents the area of the interferometer exposed to the incident light.</i>	131
Figure 5.11	<i>Effect of phase dispersion on fringe visibility for different ratios of tilt angle and beam divergence.</i>	132
Figure 5.12	<i>Illumination of a wedged interferometer cavity by an optical fibre.</i>	133
Figure 5.13	<i>Effect of different wedge angles on fringe visibility.</i>	134
Figure 5.14	<i>Temperature profile in the target and the sensing film along the central axis of the optical fibre sensor at different steps in time.</i>	137
Figure 5.15	<i>Noise model of a photodiode – current amplifier combination.</i>	144
Figure 5.16	<i>Contributions of the individual noise sources to the system noise voltage v_{on} appearing at the amplifier output (v_{op} – photodiode noise, v_{ov} – amplifier input noise voltage, v_{of} – Johnson noise current, v_{oi} - amplifier input noise current).</i>	146
Figure 6.1	<i>Diagram showing the interpretation of the experimental geometry of the optical fibre sensor in the 2D finite element model.</i>	157
Figure 6.2	<i>Illumination geometry of the optical fibre sensor.</i>	159
Figure 6.3	<i>Intensity distribution of light exiting a 400 μm multimode fibre at a distance of 10 mm from the fibre tip. The error bars represent the standard deviation of eight measurements.</i>	160
Figure 6.4	<i>Theoretical photothermal signals calculated for different μ_a and a film thickness of 12 μm using the finite element model of the optical fibre sensor. The inset shows the rise in amplitude of the photothermal signal with increasing absorption coefficient.</i>	165
Figure 6.5	<i>Computed temperature profiles across the target absorber and water-backed polymer sensing film at different times. The absorption coefficient of the target was 3.0 mm^{-1} and the absorption coefficient of the polymer film was 0.25 mm^{-1}. The excitation light is assumed to be incident from the right hand side.</i>	166

Figure 6.6 Theoretical plots of photothermal responses calculated for different reduced scattering coefficients using the finite element model. The absorption coefficient was held constant.....	169
Figure 6.7 Qualitative graph of the probability density function $f(Y \beta)$ which has a maximum where the difference between the experimental observations and model predictions is equal to zero. Through maximisation of $f(Y \beta)$, values for β can be obtained, which might have led to measurement Y	174
Figure 6.8 Implementation of the predictor-corrector method in which an average parameter derivative obtained from two subsequent estimations is used to predict the final parameter.	177
Figure 6.9 Sensitivities of all parameters included in MBPE calculated using typical uncertainties for measurements made on tissue.	180
Figure 7.1 Experimental set-up of the optical fibre sensor.....	183
Figure 7.2 Experimental set-up for measuring the thermal response time of the optical fibre sensor.	187
Figure 7.3 Normalised sensor response to a step change in temperature together with the theoretical response calculated using the FEM of the optical fibre sensor for a PET film of 50 μm and 12 μm thickness.	188
Figure 7.4 Adsorption of dye molecules onto the surface of the polymer film due to electrostatic and van der Waals' forces.	191
Figure 7.5 Photothermal signal detected in distilled water before and after exposure of the sensing film to an absorbing dye. The FEM of the sensor was used to simulate the effect of a 200 nm dye layer on the surface of the PET film.	193
Figure 7.6 Normalised photothermal signals detected using the optical fibre sensor in quasi non-scattering gels with absorption coefficients ranging from 0.53 to 3.14 mm^{-1}	198
Figure 7.7 Normalised photothermal signals together with the theoretical signals calculated using the estimated absorption coefficients shown in Table 7.1.....	200
Figure 7.8 Comparison of the theoretical signal calculated from the estimated set of parameters from Table 7.2 and the experimental data for a 'true' $\mu_a = 3.14 \text{ mm}^{-1}$. The parameters were obtained using small initial uncertainties in the thermal	

<i>parameters. The error bars represent the standard deviation of 10 measurements.</i>	<i>201</i>
<i>Figure 7.9 Enlarged section of the signal shown in Figure 7.8 illustrating the error in the FEM due to the estimated uncertainties in the model parameters. Note that the uncertainty of the FEM falls within the standard deviation of the measurement.</i>	<i>203</i>
<i>Figure 7.10 Comparison of the FEM data obtained using the set of parameters in Table 7.4 and experimental data. The parameters were obtained by assuming large initial uncertainties in the thermal parameters, which produced large final uncertainties and an unsatisfactory agreement with the data.</i>	<i>206</i>
<i>Figure 7.11 Photothermal signals detected in turbid gels. The absorption coefficient was the same in all samples, while the reduced scattering coefficient ranged from 0.2 to 2.2 mm⁻¹. The increase in the scattering coefficient does not produce a significant change in the shape of the photothermal signal.</i>	<i>207</i>
<i>Figure 8.1 Contour plot of the residuals calculated from a photothermal signal ($\mu_a = 2.05 \text{ mm}^{-1}$) and the numerical model of the optical fibre sensor. The asterisk represents the minimum residual and the grey area the uncertainty in the estimated μ_a calculated using MBPE. The innermost contour line represents the confidence limit obtained from the noise of the signal.</i>	<i>220</i>
<i>Figure 8.2 Normalised parameter sensitivities for a photothermal signal observed using PPTR in turbid media calculated using typical uncertainties in the properties of tissue in vivo.</i>	<i>223</i>
<i>Figure 8.3 Normalised parameter sensitivities calculated using typical uncertainties in the properties of tissue in vivo for the case of a highly absorbing target ($\mu_a = 2.0 \text{ mm}^{-1} \pm 0.2 \text{ mm}^{-1}$).</i>	<i>225</i>
<i>Figure 8.4 Normalised parameter sensitivities calculated using measured uncertainties in the optical coefficients of tumour and normal tissue at 1064 nm ($\mu_a = 0.03 \text{ mm}^{-1} \pm 0.02 \text{ mm}^{-1}$). Only the thermal conductivity shows a reduced sensitivity compared to a highly absorbing target (Figure 8.3).</i>	<i>226</i>
<i>Figure 8.5 Normalised parameter sensitivities of normalised theoretical photothermal signals for PPTR and the optical fibre sensor to the optical coefficients.</i>	<i>228</i>

Figure 8.6 *Normalised parameter sensitivities of normalised theoretical photothermal signals to the thermal coefficients.*229

Figure 8.7 *Sensitivity ratio of the thermal coefficients to the absorption coefficient of photothermal signals detected using the sensor and PPTR. The sensitivity ratio was calculated from the normalised parameter sensitivities of normalised signals.*.....230

Figure 8.8 *Normalised parameter sensitivities of normalised signals for various configurations of the optical fibre sensor. An optical fibre sensor detecting one-dimensional heat flow using a very thin (2 μm) sensing film bounded by an insulator is most sensitive to the absorption coefficient and matches the sensitivity of PPTR.*231

LIST OF TABLES

Table 2.1 <i>Thermal conductivity and diffusivity together with the temperature coefficients of different types human tissue measured in vitro.</i>	62
Table 2.2 <i>Thermal conductivity of various human normal tissues and tumours measured in vitro. (Source: Bowman 1981)</i>	64
Table 2.3 <i>Specific heat capacities of various types of human and animal tissues.</i>	65
Table 2.4 <i>Densities of various types of human tissue (data taken from Woodard et al).</i>	67
Table 4.1 <i>Comparison of the ‘true’ absorption coefficient to μ_a (\pm SD) determined from photothermal measurements. The standard deviations were calculated using the fitted absorption coefficients obtained from four measurements.</i>	103
Table 4.2 <i>Comparison of the ‘known’ absorption and reduced scattering coefficients of the turbid gels with those determined from PPTR signals. The standard deviation was calculated from the variation in the coefficients determined from 4 individual measurements.</i>	106
Table 5.1 <i>Temperature sensitivities of different materials for $\lambda=800$ nm, $l=50$ μm (¹Polymethylmethacrylate, ²polyethylene terephthalate, ³low density polyethylene, ⁴polyvinylidene flouride, ⁵polyethersulfone).</i>	139
Table 5.2 <i>Thermal detection limits of various materials calculated for a film thickness of 50 μm and a bandwidth of 10 kHz. (¹Polymethylmethacrylate, ²polyethylene terephthalate, ³low density polyethylene, ⁴polyvinylidene flouride, ⁵polyethersulfone)</i>	151
Table 6.1 <i>Standard deviations applied to the calculation of the parameter sensitivities.</i>	179
Table 7.1 <i>Absorption coefficients estimated from normalised signals using small uncertainties in the thermal coefficients.</i>	199
Table 7.2 <i>Initial and estimated parameters and uncertainties obtained from a photothermal measurement on a tissue phantom with a ‘true’ $\mu_a = 3.14$ mm⁻¹. The initial uncertainties in the thermal coefficients were small, which produced an estimated μ_a close to the true value.</i>	202

Table 7.3 Absorption coefficients obtained from photothermal measurements on quasi non-scattering gels using a two parameter fit and small initial uncertainties.	203
Table 7.4 Initial and estimated parameters and uncertainties obtained from a photothermal measurement ($\mu_a = 3.14 \text{ mm}^{-1}$). The initial uncertainties in the thermal coefficients were comparable to those of tissue. Note the strong deviation of all parameters from the true values and the smaller reduction in the final uncertainties.	205
Table 7.6 Results obtained from experimental data using MBPE for a non-scattering gel with absorption coefficient $\mu_a = 2.05 \text{ mm}^{-1}$	208
Table 7.7 Results obtained from experimental data using MBPE for a turbid gel with 'known' optical coefficients $\mu_a = 2.05 \text{ mm}^{-1}$ and $\mu_s' = 1.22 \text{ mm}^{-1}$	209
Table 7.8 Results obtained from experimental data using MBPE for a turbid gel with 'known' optical coefficients $\mu_a = 2.05 \text{ mm}^{-1}$ and $\mu_s' = 2.20 \text{ mm}^{-1}$	209

ACKNOWLEDGEMENTS

I would not have been able to complete the work that is described in this thesis without the support and help of others. The work had many moments where I found it difficult to carry on but fortunately I could always rely on the help of my colleagues and friends. First and foremost I would like to thank my supervisor Tim Mills for his support throughout my Ph.D. and especially for his encouragement at the times when the work was hard going. His creativity provided many ideas for working around problems and his sense of humour certainly helped me to keep things in perspective.

Paul Beard is perhaps the person I am most indebted to. No matter how busy he might have been at the time, I was always able to approach Paul with even the most banal problems and found in him an attentive listener. At the early stages of this project, Paul gave me valuable advice on how to approach a Ph.D., which changed my attitude towards it and turned what seemed to me a mountain of tedious work into something that was interesting and also enjoyable. Paul also read my thesis with great attention to detail, which I am very grateful for.

I would also like to thank Dave Delpy, Mark Cope, Matthias Kohl, Jem Hebden, Martin Schweiger and everyone from this department who has helped me in the past. Outside of this department, Perry Xiao and many others at Southbank University as well as Mike Bluck from the Computational Mechanics department at Imperial College have given help with heat transport problems and contributed in a significant way.

My most personal thanks go to Tanya, my parents and the rest of my family and my friends for their support. I would also like to acknowledge the Engineering and Physical Sciences Research Council which provided the funding for this work.

1 INTRODUCTION

1.1 Background to this work

The idea for the development of a photoacoustic-photothermal optical fibre sensor arose from complications in the treatment of atherosclerosis using laser angioplasty. Atherosclerosis is an excessive thickening of the artery wall by fibro-lipid and calcified plaques, which become raised and may eventually occlude the vessel. During laser angioplasty, an optical fibre is inserted into an artery, for example the femoral artery, and advanced to the blocked region of the blood vessel where the ablative action of laser energy removes the occlusion. One of the potential risks of the treatment is the accidental perforation of the vessel wall. Knowledge of the composition and the thickness of the vessel wall in front of the optical fibre would improve the chances of a successful treatment. This led to the development of guided laser angioplasty for which various guidance techniques have been suggested, some of which have been used clinically, such as angiography, which relies on X-ray imaging. Photoacoustic spectroscopy was first suggested by Mills¹ in 1988 as a tool for the detection of atheromatous plaque. Laser pulses of a few nanoseconds in duration generate acoustic transients, which, if detected, could provide information on the optical, acoustic and spatial properties of the tissue. The information on the properties of the tissue can be obtained by examining the amplitude and temporal characteristics of the detected thermoelastic waves. Spatial properties of the tissue may be gleaned from measurements of the time of arrival of thermoelastic waves that are reflected at interfaces in the tissue where there are changes in acoustic impedance.

The absorption of a laser pulse in the tissue produces thermal and acoustic transients. If there is no significant relaxation of temperature within the duration of a laser pulse, the spatial distribution of temperature immediately after the absorption of a laser pulse depends on the optical and thermal coefficients of the tissue. The rate of subsequent diffusion of heat is directly linked to the initial temperature distribution and hence optical and thermal coefficients. By monitoring the cooling of the heated area, information on the optical and thermal properties of the tissue can be obtained.

Mills proposed the use of a thin transparent film mounted in front of the distal end of an optical fibre as a means of detecting photoacoustic and photothermal signals. The transparent film would allow the transmission of low energy excitation pulses but it would also act as a low finesse Fabry-Perot interferometer with which acoustic and thermal transients could be detected. After the analysis of the photoacoustic and photothermal signals determined the type of tissue, high energy therapeutic laser light could also be transmitted without causing damage to the film. The size of the proposed optical fibre sensor would enable it to be introduced into a blood vessel but it could also be used within the biopsy channel of an endoscope, which would make *in vivo* photoacoustic and photothermal measurements of remote organs possible. It could also be used for interstitial measurements by inserting the optical fibre sensor through a large diameter needle. The non-destructive determination of tissue optical properties makes the optical fibre sensor an interesting device for the diagnosis of cancers. Cancers of the intestinal tract, for example, are diagnosed by taking needle biopsies, whereby a small sample of tissue is removed. This destructive technique has been suspected of inducing secondary metastases^{2,3,4,5}. The non-destructive contact measurement using the optical fibre sensor would present a very useful and much less harmful alternative to needle biopsies.

This thesis describes the development of an optical fibre sensor for the photothermal determination of optical coefficients of tissue. After an introduction to tissue optics and photothermal techniques, the performance of the optical fibre sensor as a Fabry-Perot interferometer will be discussed. The determination of optical coefficients from measurements on turbid gels using pulsed photothermal radiometry, which is an established and well-documented photothermal technique of determining the optical and thermal properties of materials, is described in chapter 4. Chapter 5 is concerned with the theoretical and practical aspects of the optical fibre sensor acting as a Fabry-Perot interferometer. In chapter 6, the numerical model of the optical fibre sensor, which was required for the calculation of three-dimensional heat conduction in the tissue and sensor, is introduced. Model-based parameter estimation, the statistical procedure employed for obtaining the optical coefficients from photothermal signals, is discussed. The experimental aspects of the optical fibre sensor and the manufacture of turbid tissue phantoms are examined in chapter 7. The validation of the numerical model is described and the

determination of optical coefficients from photothermal measurements on turbid tissue phantoms and the accuracy with which they can be obtained are discussed. The performance of the optical fibre sensor is compared to those of other photothermal detectors in chapter 8. The accuracy with which optical coefficients can be obtained using pulsed photothermal radiometry and the optical fibre sensor is also analysed. The conclusions are presented in the final chapter of this thesis and an outlook on future work is also provided.

1.2 Origins of the optical properties of tissue

In tissue optics, the term ‘optical properties’ refers to the two possible interactions of light with tissue - absorption and scattering. This section introduces the conventions used in this thesis to describe the optical properties of tissue. The relationship between the structure and composition of tissue and its optical properties is also discussed. The wavelength of light that can be used for the excitation and detection of photothermal signals ranges from the visible to the infrared. The optical properties of tissue will therefore be discussed for those wavelengths.

1.2.1 Terminology in tissue optics

In this section the terminology of tissue optical properties is discussed and the conventions that are used in this thesis are set out.

1.2.1.1 Absorption

Absorption of an electromagnetic wave is present when there is no emission of a secondary wave from the illuminated object. The degree of absorption is dependent upon the atoms or groups of atoms within molecules that are known as chromophores. The incident optical energy is converted to other forms of energy, mainly thermal energy but also acoustic energy provided impulse or high frequency heating has been produced. The absorption of optical energy can also produce changes in the chemical structure of the target medium, which may also contribute to a reduction in the amount of energy that is converted to heat,

If the medium is a non-scattering absorber of homogeneous absorbing properties, then the light attenuation can be described using the Lambert-Bouguer law:

$$I_t = I_0 \exp(-\mu_a z) \quad (1.1)$$

where μ_a is the absorption coefficient, z is the depth into the medium, I_t is the transmitted intensity and I_0 is the incident intensity. The absorbance, A , or optical density, OD , is the logarithmic ratio of the incident and transmitted intensity:

$$A = OD = \log_{10} \frac{I_0}{I_t} \quad (1.2)$$

1.2.1.2 Scattering

When electromagnetic waves penetrate an object, oscillatory motions of electrons and nuclei are induced. The oscillations cause a re-radiation of electromagnetic waves. If there is no change in the energy balance of the incident wave and the re-radiated wave, the light is scattered elastically. Inelastic scattering is present when an energy difference between the primary and secondary wave exists, which can be observed in the case of Raman and Brillouin scattering. Only elastic scattering will be considered in discussions on optical scattering in this thesis.

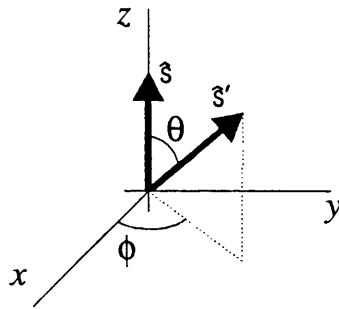


Figure 1.1 *The co-ordinate system for scattering theory.*

When a parallel beam of light is scattered or absorbed by particles, an effect on the intensity in the 'shadow' of the particle compared to the unobstructed intensity can be observed. A particle can be characterised by its effect on the magnitude, which can be defined using the total or extinction cross-section σ_t . Consider the case where photons,

propagating on a path \hat{s} , are scattered into direction \hat{s}' as shown in Figure 1.1. The directions \hat{s}' into which photons could be scattered do not occur with equal probability but depend on the type of particle that causes the scattering as well as the overall structure of the scattering medium, i.e. lattice spacing etc. The probability function describing the angle between the two paths is given by the differential scattering cross-section

$$\left(\frac{d\sigma(\hat{s}, \hat{s}')}{d\hat{s}} \right) = r^2 \frac{I_s(\hat{s}')}{I_{in}(\hat{s})} \quad (1.3)$$

where σ is the scattering cross section, $d\hat{s} = \sin \theta d\theta d\phi$, I_s is the scattered intensity, I_{in} is the incident intensity and r is the distance from the scattering centre to the point of observation. The integral of this expression over all angles is called the total scattering cross-section, which represents a measure of the ability of a particle to scatter light:

$$\sigma_s = \int_{4\pi} \frac{d\sigma}{d\hat{s}} d\hat{s} \quad (1.4)$$

The differential cross-section term $d\sigma/d\hat{s}$ may be replaced by the term $\sigma_s f(\hat{s}, \hat{s}')$, where $f(\hat{s}, \hat{s}')$ is the normalised likelihood for photons to be scattered from an initial direction \hat{s} into direction \hat{s}' . The normalised function f is referred to as single scattering phase function. If all scattering particles are identical in their contribution and are evenly distributed in the medium with a density ρ then the scattering coefficient is

$$\mu_s = \rho \sigma_s \quad (1.5)$$

The scattering coefficient is a measure of the likelihood that a photon will be scattered as it travels through a scattering medium. The scattering coefficient is typically expressed in units of mm^{-1} . The probability that a photon propagating in a scattering medium with scattering coefficient μ_s is not scattered over a distance d is equal to $\exp(-\mu_s d)$. The total scattering coefficient for a medium made that contains a variety of different scatterers is

$$\mu_s = \sum_i \rho_i \sigma_{si} \quad (1.6)$$

while the equivalent for the phase function produces the average single scattering phase function:

$$f_{mean}(\hat{s}', \hat{s}) = \frac{\sum_i \rho_i(r, t) \sigma_{si}(\lambda) f(\hat{s}, \hat{s}')}{\sum_i \rho_i(r, t) \sigma_{si}(\lambda)} \quad (1.7)$$

where λ is the wavelength of the incident light. If the scattering particles have a spherical geometry, then the phase function becomes $f(\lambda, r, t, (\hat{s}, \hat{s}')) = f(\lambda, r, t, \nu)$, where $\nu = \hat{s} \cdot \hat{s}' = \cos \theta$ is the cosine of the angle between the incident and scattered light. Hence the scattering phase function is independent of the axial angle ϕ . The case of spherical symmetry allows the scattering phase function to be described by the mean cosine of the scattering angle, g , which is also called the anisotropy factor:

$$g = 2\pi \int_{-1}^1 \nu f(\nu) d\nu \quad \nu = \cos \theta \quad (1.8)$$

For $g = 0$, the scattering of light is isotropic, while scattering for $g \rightarrow 1$ becomes more forward peaked and for $g \rightarrow -1$ becomes backward peaked. An approximation to the scattering phase function is the Henyey-Greenstein⁶ phase function given as:

$$f_{HG}(\nu) = \frac{1}{4\pi} \frac{1 - g^2}{(1 + g^2 - 2g\nu)^{3/2}} \quad (1.9)$$

g can be used to obtain the reduced scattering coefficient, μ_s' , which is an expression of the distance over which a multiple of anisotropic ($g \neq 0$) scattering events has the equivalent effect as a single isotropic event

$$\mu_s' = \mu_s(1 - g) \quad (1.10)$$

The total attenuation coefficient μ_t is given as:

$$\mu_t = \mu_s + \mu_a \quad (1.11)$$

The combination of the reduced scattering coefficient and the absorption coefficient gives the transport coefficient, μ_t' :

$$\mu_t' = \mu_s' + \mu_a \quad (1.12)$$

The transport coefficient should not be confused with the effective attenuation coefficient, μ_{eff} , and its inverse, the effective penetration depth, δ , which can only be applied to diffuse light. The expression for μ_{eff} and δ has been derived from the diffusion approximation of the radiative transport equation and is shown as:

$$\delta = \frac{1}{\mu_{\text{eff}}} = \frac{1}{\sqrt{3\mu_a(\mu_a + \mu_s')}} \quad (1.13)$$

The ratio of the scattering coefficient to the extinction coefficient is termed the albedo, a :

$$a = \frac{\mu_s}{\mu_s + \mu_a} = \frac{\mu_s}{\mu_t} \quad (1.14)$$

The reduced albedo is given as:

$$a' = \frac{\mu_s'}{\mu_s' + \mu_a} = \frac{\mu_s'}{\mu_t'} \quad (1.15)$$

The inverses of some of the optical coefficients listed above are defined as the photon mean free paths:

The absorption mean free path:

$$l_a = \frac{1}{\mu_a} \quad (1.16)$$

The scattering mean free path:

$$l_s = \frac{1}{\mu_s} \quad (1.17)$$

The reduced scattering mean free path:

$$l_s' = \frac{1}{\mu_s'} \quad (1.18)$$

The extinction mean free path:

$$l_t = \frac{1}{\mu_t} \quad (1.19)$$

The transport mean free path:

$$l_t' = \frac{1}{\mu_t}, \quad (1.20)$$

1.2.1.3 Scattering by spherical particles

Mie scattering theory, named after Gustav Mie who solved the theoretical problem of scattering of light by particles such as spheres and cylinders⁷, can be applied to calculate the wavelength-dependent scattering coefficient of optical phantoms provided the size distribution per volume and the refractive index are known. A number of expressions derived from Mie theory do exist for limited geometries. For the derivation of Mie theory, the reader may be referred to the literature (Bohren and Huffmann, 1983)⁸.

Mie theory is very useful for the accurate calculation of the scattering coefficient of tissue phantoms. Such phantoms were used in studies discussed in this thesis for the determination of optical coefficients from photothermal signals. The signals were generated in aqueous gels, which contained a molecular absorber and polystyrene microspheres as scattering particles. The refractive index and the size distribution of the spheres were given by the manufacturer. Mie theory was used to obtain a reliable estimate of the scattering coefficient of the gels. Mie theory requires that optical scattering is due to single particles. This needs to be borne in mind when tissue phantoms are made. High concentrations of scattering particles can cause clustering and Mie theory would no longer be valid.

Gustav Mie's theory can be used to describe the scattering of a plane electromagnetic wave by a spherical particle. The theory is accurate for the entire spectrum of electromagnetic waves. Here, the solution is given for only the scattering cross section, but a similar expression can be obtained for the extinction cross section:

$$\sigma_s = \frac{2\pi}{k^2} \sum_{n=1}^{\infty} (2n+1) (|a_n|^2 + |b_n|^2) \quad (1.21)$$

where the expressions a_n and b_n contain modified Bessel functions and take into account the relative refractive index, the size of the scattering particle and the wavelength. Computer

programs for the calculation of the extinction cross section are available, one of them is listed in Bohren and Huffman⁸.

1.2.2 Absorption of light in tissue

The main absorbers in tissue are water, protein, lipids and haemoglobin. Proteins strongly absorb in the ultraviolet wavelength range, while water is dominating in the infrared. The absorption of water in the visible and infrared is illustrated in Figure 1.2.

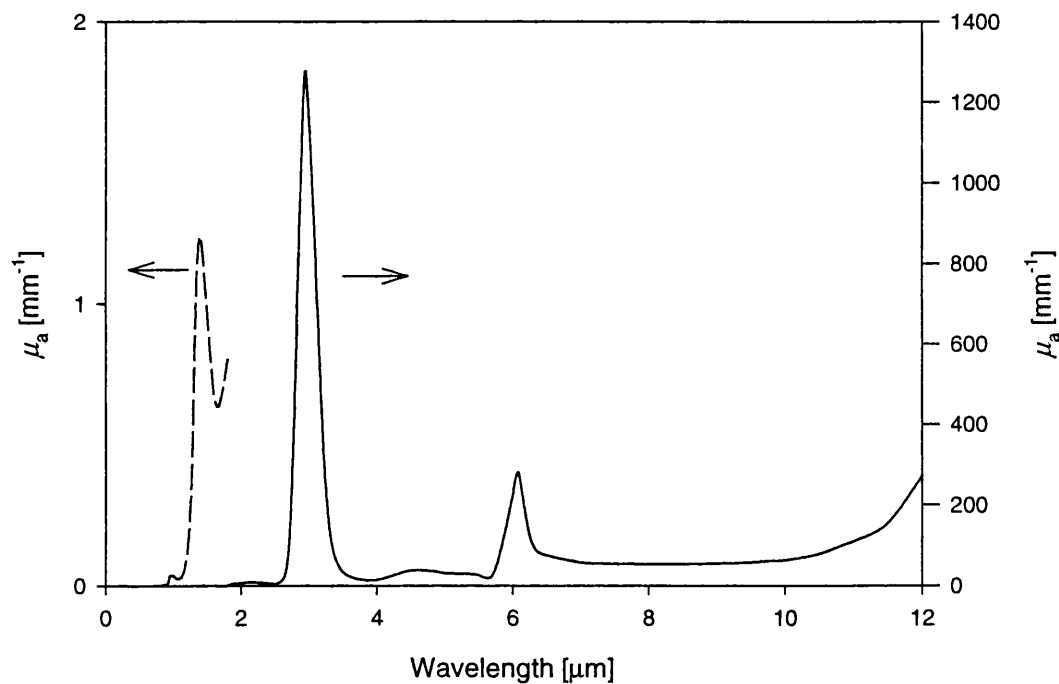


Figure 1.2 Absorption spectrum of water in the visible and infrared wavelength region.

Between these two highly absorbing regions are wavelengths, which penetrate tissue very deeply. This region is sometimes termed the “therapeutic window” due to the large penetration depths of light in the visible and near-infrared wavelength range. Within this window, tissue chromophores such as oxy- and deoxyhaemoglobin, cytochrome and

melanin have an influence on the penetration depth. Blood, for example, will affect the absorption of light depending on its oxygenation and the vascularisation of the tissue. Figure 1.3 depicts the absorption spectra of oxy- and deoxyhaemoglobin. The higher the blood content per unit volume of tissue, the higher the absorption. Note the increased absorption by HbO₂ for wavelengths larger than 850 nm. This feature is very likely to affect *in vivo* measurements using the optical fibre sensor. If the excitation wavelength is chosen to be in the near-infrared, such as that of an Nd:YAG laser (1064 nm), then the absorption of the excitation pulse, and hence signal shape, will depend on the HbO₂ concentration in the tissue.

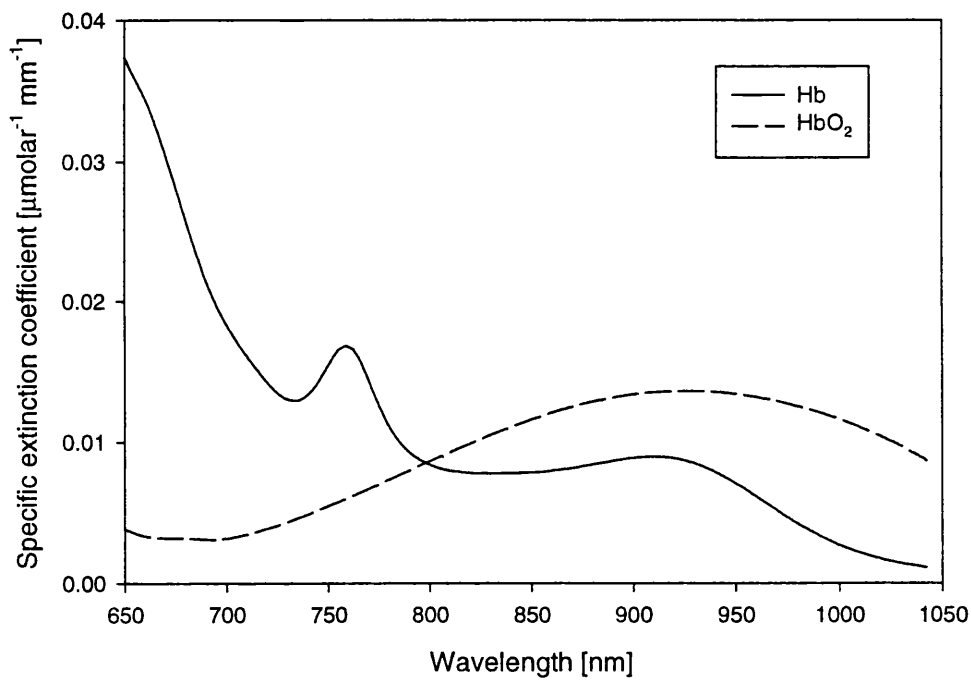


Figure 1.3 The absorption spectra for HbO₂ and Hb in the near-infrared wavelength region.

Lipids also contribute to absorption and can be of relatively high concentration in certain tissue types, such as the subdermis and subcutaneous breast tissue. A typical absorption spectrum of lipids is shown in Figure 1.4. Lipids produce marked absorption

peaks at 930 nm and 1050 nm - the latter would again affect the absorption of the excitation laser pulse at 1064 nm.

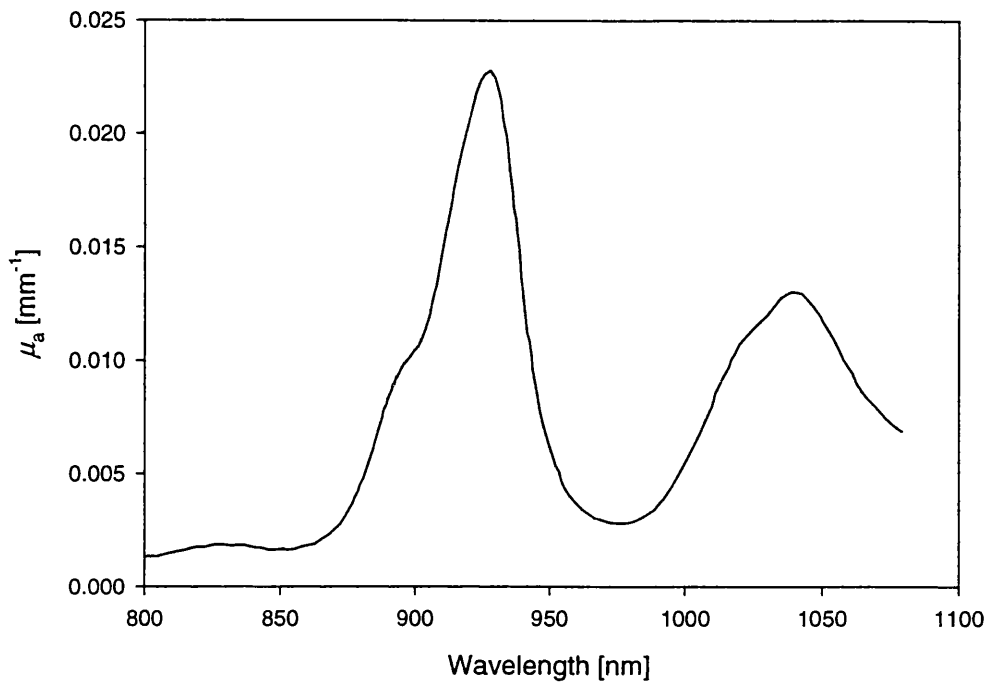


Figure 1.4 Typical absorption spectrum of lipids in the near-infrared wavelength region.

Proteins also exhibit absorption features in the near-infrared wavelength region. Cytochrome c oxidase, for example, is found in the mitochondrial membrane and plays an important role in the oxygen consumption of cells by donating electrons. This protein molecule contains redox active groups, which change their state (i.e. accepting or donating electrons) during the electron transport. The two states of the cytochrome c oxidase produce characteristic absorption features as shown in Figure 1.5. These features are used in near-infrared spectroscopy to obtain information about oxygen availability in the cells and cell metabolism⁹.

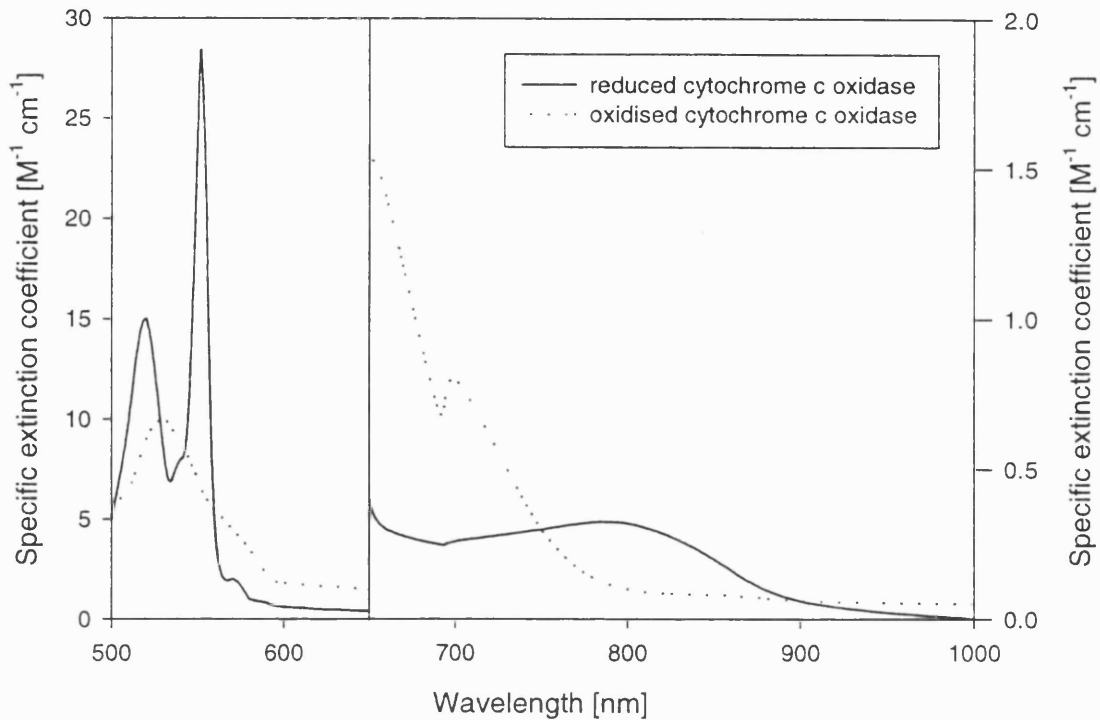


Figure 1.5 Absorption spectra of reduced and oxidised cytochrome c oxidase.

1.2.3 Scattering of light in tissue

Optical scattering in biological tissue is caused by cell components of different molecular composition compared to that of the surrounding medium. The differences in the chemical composition result in fluctuations in density and hence refractive index, which give rise to scattering of light. Soft tissue is dominated by water (70 - 80%), but also contains lipids and proteins, which are embedded in membranes. Lipids and proteins also form the main constituents of vacuoles, cell nuclei and collagen fibres. The refractive index of water-dominated cytoplasm and lipids is, for example, 1.35^{10} and 1.47^{11} respectively. A refractive index mismatch of that magnitude produces a relative refractive index of 1.09. A protein-dominated structure, such as collagen, has a refractive index of approximately 1.47. The refractive index of collagen fibre bundles in tissue, however, is lower at 1.38 since the fibre bundles contain water¹². The refractive index mismatch is therefore 1.022, which is

lower than that produced by lipids. The magnitude of scattering is therefore dependent upon the materials that produce the change in refractive index.

A description of optical scattering on a molecular level would be unnecessarily complex. Instead, scattering in tissue is assumed to originate from spherical particles such as mitochondria, vacuoles and nuclei. The membranes of these cellular structures produce differences in the refractive index compared to the surrounding medium, which gives rise to optical scattering. Cylindrical structures such as collagen fibre bundles also contribute to scattering. If the dimensions of the scattering particles are smaller than the wavelength of the incident light, isotropic or Rayleigh scattering can be observed. Rayleigh scattering is the re-emission of an electromagnetic wave from an object smaller than the wavelength of the incident light, such as gas molecules in the earth's atmosphere, for example. Scattering by larger particles such as small droplets of water observed in clouds or mitochondria in biological cells, are not characterised by Rayleigh scattering. The larger the scattering particles, the more important are the effects of constructive and destructive interference between the emitted waves. A more complicated angular distribution of scattering is the result.

1.3 Models of light transport in tissue

Various analytical and numerical methods have been developed to describe the transport of light in tissue. Such models are important in the development of therapeutic techniques and in the quantitative analysis of diagnostic measurements. The distribution of the incident radiation is important in, for example, photodynamic therapy of cancers where the biological effect is directly linked to the local light fluence. In photothermal applications, the spatial light distribution is needed to calculate the temperature distribution and hence heat source in the target.

The general problem addressed by models of light transport can be described as the irradiance of an arbitrarily shaped object, the optical properties of which may be a function of position and time, by internal and external sources of light. A complete solution describes the time dependence of the electromagnetic field at any point. Three basic

requirements for solving this problem have been outlined by Patterson *et al*¹³. The requirements are:

- (i) a mathematical description of the interaction of optical radiation with tissue;
- (ii) information about the optical properties of the irradiated tissue (usually provided by experiment) and;
- (iii) workable solutions of the mathematical equations to provide sufficiently accurate calculations under circumstances of biomedical interest.

The requirements will be used in the following section to examine a small number of different models of light transport, which have been usefully applied to tissue optics.

1.3.1 Stochastic models

Stochastic methods model photon interactions either explicitly, such as the Monte Carlo method, or implicitly, by deriving the probability density functions for photon transitions, such as the random walk theory. Both methods will be outlined in the following sections.

1.3.1.1 The Monte Carlo technique

The Monte Carlo (MC) technique is a stochastic method to describe single scattering events in scattering media. The propagation of a photon through a medium in which optical scattering and absorption are present is determined by two parameters: the mean free path until an event of absorption or scattering occurs and the scattering phase function. At boundaries, a photon may be reflected or transmitted. The path of a photon is obtained by using probability densities for the incremental steps between photon - tissue interactions, for the angle of deflection in the event of scattering and for the transmittance at boundaries of different refractive index. The MC technique describes the propagation of photons very accurately. It is, however, a statistical method, which may require large computing power

depending on the model. The number of photons needed for a particular simulation depends on the problem that is investigated. To acquire the reflectance from the surface of an object with specified optical coefficients, a few thousand photons will yield a useful answer. For the mapping of fluence profiles in turbid objects, which are required, for example, to describe the laser-induced temperature rise in tissue, tens of thousands of photons are required to provide an answer of adequate accuracy. This reflects the statistical nature of MC calculations, which are rigorous, but may need a large number of computations to achieve a satisfactory result. Nevertheless, MC models are powerful and flexible in, for example, modelling of the light distribution in tissue with layered optical properties.

In most MC simulations, photons are regarded as neutral particles. Photons are not treated as a wave phenomenon. Features such as phase and polarisation are ignored. The simplifications serve to calculate the radiant energy transport in turbid media. MC techniques can, however, handle phase and polarisation but these options are not considered in this description. A full discussion of the MC model, which was employed in this work, is given by Wang *et al*¹⁴.

1.3.1.2 Random walk theory

Random walk theory is a statistical method, which describes photon migration along the elements of a discrete lattice. Although this method employs simple geometries such as cubes and therefore restricts the directions in which photons could travel, descriptions of light transport have been achieved using a relatively simple mathematical analysis¹⁵. In the case of a homogenous space in which the motion of photons has equal probability in all lattice directions, random walk theory can be considered to be a finite difference approximation of the diffusion equation, which is discussed in section 1.3.3.1. Random walk theory has been applied to obtain expressions for the time-dependent transmittance through homogenous scattering slabs and have been shown to be in general agreement with Monte Carlo simulations and results generated using diffusion theory¹⁶.

1.3.2 Deterministic models: the radiative transport equation

The limitations of Mie theory have been indicated in the preceding section. Multiple scattering of electromagnetic waves, which is present in tissue, can not be addressed satisfactorily using Mie theory. Solutions to Maxwell's equations have been found¹⁷, but are of enormous complexity and are only applicable to very simple, limited geometries. To obtain such solutions, previous knowledge of the variations in optical density of the object is also required. Descriptions of such detail are impossible to acquire for tissue.

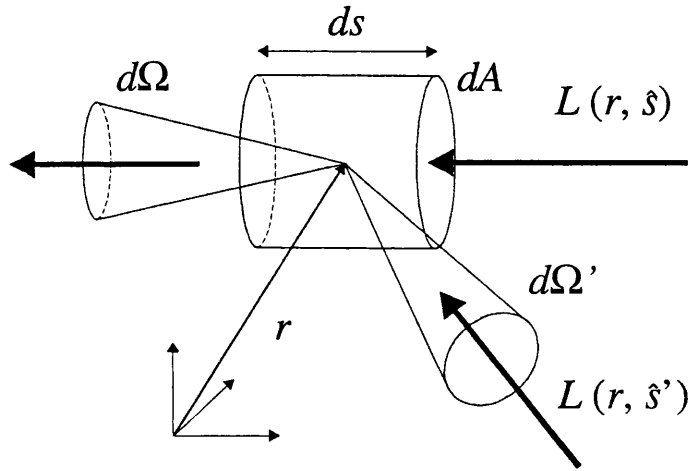


Figure 1.6 Illustration of the contributions to the energy radiance $L(\Omega)$ in an infinitesimally small tissue volume.

A more amenable description of light transport is the radiative transport equation. An incident energy radiance, $L(r, \hat{s})$, is attenuated by the total attenuation coefficient, μ_t , over the infinitesimal length ds :

$$dL(r, \hat{s}) = -\mu_t L(r, \hat{s}) ds \quad (1.22)$$

Incorporating the source term $S(r, \hat{s})$, and the contribution of light scattered from all directions \hat{s}' onto \hat{s} according to the spatial phase function one arrives at the equation of radiative transfer, which describes the balance of radiance in an arbitrary volume of tissue.

The equation of radiative transfer can be given as

$$dL(r, \hat{s}) = -\mu_t(r) L(r, \hat{s}) ds + \int_{4\pi} d\mu_s(r, \hat{s}' \rightarrow \hat{s}) L(r, \hat{s}') d\Omega' ds + S(r, \hat{s}) ds \quad (1.23)$$

where the left hand side represents the net change in radiance due to energy flow, the first term on the right hand side reflects the energy lost due to absorption and scattering, the integral incorporates the contribution of radiance due to scattering coming from other directions and $S(r, \hat{s})$ is the source term.

In radiative transport theory, the wave nature of light can be ignored. Instead propagation of light is expressed as the flow of energy through a medium. Some mathematically 'exact' solutions have been obtained in the sense that the radiance can be expressed in mathematical terms, such as one-dimensional solutions for planetary atmospheres. The evaluation of such terms, however, typically involves numerical methods, which are no more accurate than the approximate analytical solutions. In the next section, the diffusion approximation as one example of approximate solutions of the radiative transport equation, which is widely used in tissue optics, is discussed.

1.3.3 Solution methods for the radiative transport equation

1.3.3.1 The diffusion approximation of the radiative transport equation

The derivation of the diffusion approximation for an infinite homogeneous slab, which is irradiated at normal incidence is given in published articles^{13,18} and will not be outlined here. In these articles, it has been shown that the expressions for irradiance and the scattering phase function can be expanded using polynomials. If the expansion is terminated after the first term, the so-called P1 diffusion approximation is obtained:

$$D\nabla^2\psi(r) - \mu_a\psi(r) + s(r) = 0 \quad (1.24)$$

where D is the diffusion coefficient according to

$$D = \frac{1}{3(\mu_a + \mu_s(1 - g))} \quad (1.25)$$

and ψ is the radiant energy fluence rate. The diffusion approximation represents a reduction of the equation of radiative transfer to a differential equation, which can be solved analytically for simple geometries. A solution to the diffusion equation was used in photothermal studies presented in this thesis to calculate the fluence distribution in turbid tissue phantoms. It is important to note that the diffusion approximation is only valid for materials where the effect of absorption is very much less than that of scattering and in regions far away from boundaries and sources¹⁹.

1.3.3.2 Numerical solutions to the radiative transport equation

Numerical models for the solution of the radiative transport equation and the diffusion approximation have become important alternatives to analytic models. The methods of finite differences²⁰ and finite elements^{21,22}, for example, have been employed to model photon transport in tissue by using the diffusion approximation as the underlying model for the light transport. Using finite elements enables the definition of complicated geometries and complex distributions of optical properties, sources and detectors, which would be very difficult if not impossible to achieve with analytic methods. Such flexibility is compromised by the time needed for the calculations and the substantial computation hardware involved. The rapid progress in computer technology of recent years, however, has reduced these disadvantages and the finite element method has become an established technique to describe light transport in complex tissues.

1.4 Measurement of the optical properties of tissue

The aim of the work presented in this thesis is the development of an optical fibre sensor for the *in vivo* determination of tissue optical properties from photothermal measurements. While a large number of techniques are capable of measuring optical properties of excised tissue *in vitro*, it is the determination of optical coefficients found in the living human being that are very important in the planning of treatments or the diagnosis of diseases such as cancer. *In vitro* data on the optical properties of tissue is valuable but may vary significantly from *in vivo* values. The optical fibre sensor would have the advantage that *in vivo* measurements on tissues could be performed deep inside the body. Such locations are difficult to reach with most other optical techniques while the optical fibre sensor could be used interstitially or during endoscopy. The prospect of simultaneous detection of photoacoustic and photothermal signals, both of which may yield information about the subsurface distribution of optical properties, would further add to the diagnostic value of the technique. In this section, existing methods for the measurement of the optical coefficients of tissue will be reviewed and their ability to obtain optical properties of tissue *in vivo* is discussed.

1.4.1 Low coherence reflectometry

Low coherence reflectometry has been employed to measure the optical properties of tissue²³ and has also been used for imaging of the coronary arterial wall²⁴. The basic physical principle of low coherence reflectometry relies on the detection of the interference of the illuminating low-coherence light with light scattered from an object within the tissue. The reflections are due to differences in the refractive index across the tissue, which are detected by matching the path length in a Michelson interferometer to the path length taken by the light reflected from an object in the tissue. The path length is typically varied by moving the mirror of the reference arm of the Michelson interferometer. The change in the reflected optical power due to single back-scattering with increasing depth is measured and the optical coefficients are determined from the data using a first-order scattering theory

that relates the back-scattered power to the transport coefficient and the scattering coefficient of turbid media.

1.4.2 Coherent backscatter

The method of coherent backscatter can be applied to measure *in vivo* optical coefficients of tissue. The following discussion on the potential of this technique is based on studies by Eddowes *et al*^{25,26}.

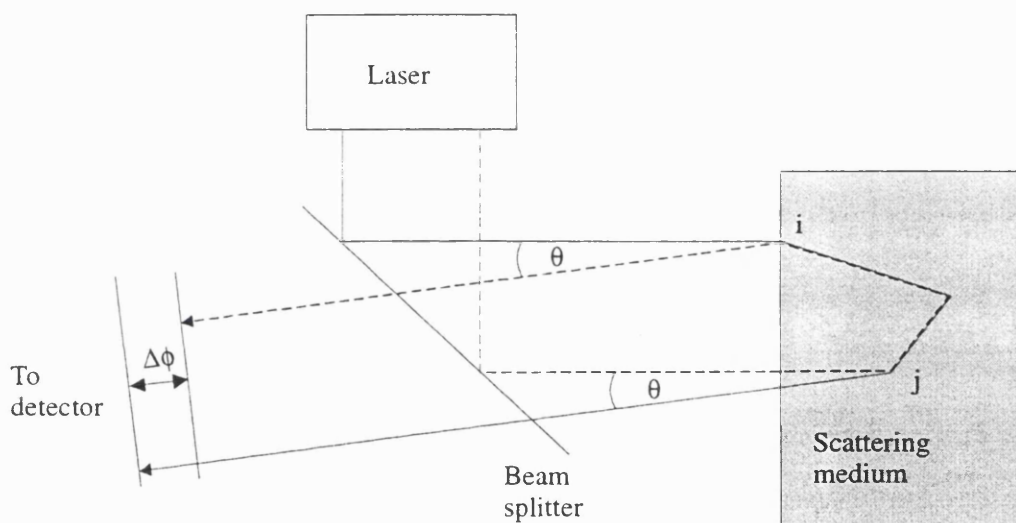


Figure 1.7 Schematic of a possible set-up for the detection of coherent backscatter. The two photon paths follow the same series of scattering events between the scattering centres *i* and *j* in reverse order. The phase difference between the photons, $\Delta\phi$, at the detector is proportional to the path length difference for the two routes.

Coherent backscatter relies on the detection of photons, which enter the tissue at different positions but are scattered such that they follow the same series of scattering events between two scattering centres in reverse order, as shown in Figure 1.7. On emerging, their paths are parallel. Using so-called angular-resolved backscattering, the scattered photons exit the tissue at an angle to the axis of the incident light until a lens,

placed at a focal length of a detector, brings them together at a point. The technique of coherent backscatter also requires the incident and backscattered light to have the same state of polarisation. The position of that point depends on the angle at which the light emerged from the tissue. The phase difference between the photons at the detector is proportional to the difference in path length for the two routes. The path length difference is dependent upon the angle between incident and backscattered photons and the relative position of the scattering centres, but not the actual path between them. The angular distribution of backscattered intensity can be related to the optical coefficients of the tissue such that the full-width-half-maximum is proportional to the reduced scattering coefficient whilst an increase in the absorption coefficient produces a rounding of the peak and a slight increase in the full-width-half-maximum.

It has been shown that it is possible to extract absorption and scattering coefficients from *in vivo* measurements on human tissue. The determined values compared well with published data.

Although coherent backscatter is able to determine optical coefficients of tissue, it has the disadvantage that it can not be used endoscopically. It has also been suggested that there are upper and lower limits to the value of the absorption coefficient that can be determined using this technique. The maximum μ_a that can be obtained is determined by factors, which are specific to the set-up, such as noise levels etc. The lower limit of the detectable absorption coefficient is related to the set-up as well as the target. The absorption coefficient is determined by the rounding of the cusp of the peak within an angular range, which is dependent on the transport length of the sample. Unless the angular range of the rounding is larger than the angular resolution of the instrument, the absorption can not be measured accurately.

1.4.3 Time-resolved spectroscopy

Time-resolved spectroscopy uses the temporal spread of photons which can be observed when a very short (typically a few picoseconds) laser pulse is transmitted through a scattering medium. The path lengths of individual photons cause their delayed arrival at the

detector as illustrated in Figure 1.8. The temporal distribution of photons is known as a temporal point spread function (TPSF). Optical coefficients of tissue can be determined by fitting an analytic theory to the measured TPSF²⁷.

Time-resolved spectroscopy could be applied to measure *in vivo* tissue optical properties inside the human body during, for example, endoscopy. The set-up would consist of two optical fibres, which would be held at a fixed distance from each other. A picosecond laser pulse would be launched into one fibre, while the scattered diffuse reflectance would be detected at the end of the other fibre using a fast detector. The restriction of this method is the validity of the diffusion approximation of the radiative transfer equation. In practice, this means that the tissue has to be sufficiently thick and that the fibres are a number of optical diffusion lengths apart. It has been shown that the temporal spread of the source pulse is very small for small fibre separations and that the detected signal is therefore very close to the system response, leading to large errors in the determined optical coefficients²⁸. Small source and detector spacing would also require the detection hardware to have a high temporal resolution.

1.4.4 Frequency-domain spectroscopy

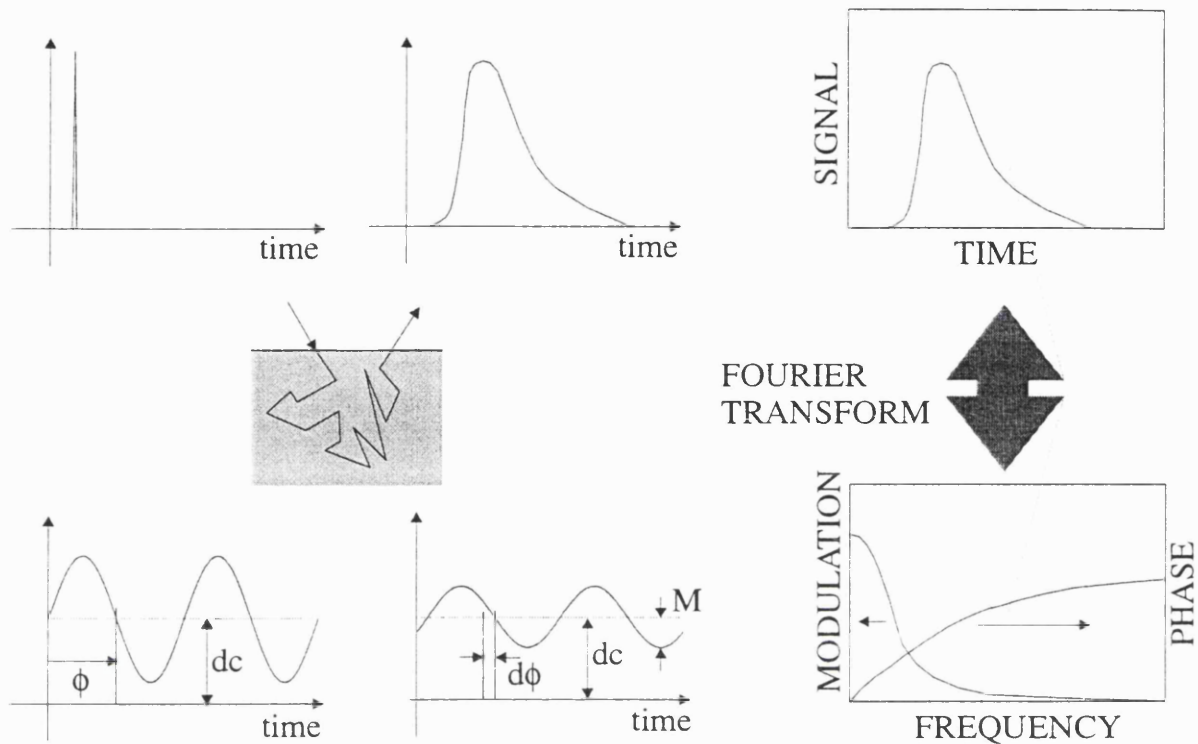


Figure 1.8 Relationship between time-resolved and frequency-domain techniques. Photon propagation through tissue results in a temporal broadening of the pulse (time domain) or, in the frequency-domain, phase delay and a reduction in amplitude. Modulation and phase are related to time-resolved measurements through the Fourier transform.

The previous section dealt with the propagation of an infinitesimally narrow light pulse in turbid media where it undergoes temporal broadening due to the many different paths on which photons travel through the tissue. In frequency-domain spectroscopy, a sinusoidally modulated light source is employed. The intensity captured by the detector after the light has propagated through the tissue will also be sinusoidal in time, but the oscillation will be reduced in amplitude and will be delayed in time as illustrated in Figure 1.8. The measured quantities are the phase angle between source and transmitted signal and the amplitude compared to the dc level, also called modulation. Phase and modulation can be detected at

all frequencies. The time domain signal is related to modulation and phase by the Fourier transform. Frequency sweeping would generate the Fourier transform of the time-domain signal. Frequency-domain spectroscopy has a number of advantages²⁹, such as intrinsically narrow bandwidth and noise resistance and, at least for low frequency measurements, less expensive hardware compared to time-resolved techniques etc. Frequency-domain spectroscopy has been successfully applied in studies on turbid media, where analytical solutions to the standard diffusion equation were used to obtain accurate absorption and reduced scattering coefficients in the near-infrared spectrum^{30,31,32}. Frequency-domain methods have also been employed to measure the optical properties of tumours and normal tissue *in vivo*³³. Interestingly, the authors decided to extract physiological parameters from the optical measurements, rather than to publish a library of optical coefficients since it is unclear whether cataloguing of optical coefficients will be sufficient to identify malignancies. The extracted physiological quantities were haemoglobin (Hb) concentrations (oxy- and deoxyhaemoglobin, total), blood volume fraction, oxygen saturation of Hb and water concentration. The results showed distinctive differences in the Hb and water concentrations between the normal and tumour locations.

Frequency-domain techniques are suitable for the measurement of tissue optical properties *in vivo* and could be used during endoscopy. The typical source detector spacing is of the order of 1 cm to allow for the use of the diffusion approximation. A possible experimental configuration would be to feed both source and detector fibres through the biopsy channel and to use a mechanical device at the tip, which would separate the fibres by a known distance.

1.4.5 Spatially resolved reflectance spectroscopy

Spatially resolved reflectance spectroscopy has been successfully used for the measurement of optical properties of tissue *in vivo*^{34,35,36}. The optical probe typically consists of one or more source fibres and a number of detector fibres. The optimal distance between the source and detector fibres has been investigated by a number of authors^{37,38}. It has been shown that the measurement of predominately forward-oriented photon fluxes or backward-

oriented photon fluxes is determined by the separation of source and detector fibre. At the optimal separation distance, small changes in the scattering coefficient have a minimal effect on the fluence. For tissue in the near-infrared wavelength range, the optimal distance is of the order of 5 mm. Bevilacqua *et al* used a spatially resolved reflectance probe with multiple detector fibres, which were positioned at distances from 0.3 – 1.4 mm from the source³⁹. This configuration allowed the group to differentiate a small volume of heterogeneous tissue rather than obtaining average optical quantities from a large volume. Near-infrared light, typically provided by diode lasers, is coupled into the source fibres and the diffusely reflected light collected by the detector fibres illuminates photodiodes or a CCD. Monte Carlo simulations can be used to determine absorption and scattering coefficients from measurements of the diffuse reflectance. The system developed by Bevilacqua *et al* was used to measure the optical properties of the human brain during surgery, showing distinct differences in the optical coefficients of human skull, white matter, scar tissue, optic nerve and tumours.

Bays *et al*³⁷ reported spatially resolved reflectance measurements made *in vivo* during endoscopy. The probe consisted of two sideways looking fibres. The source fibre was fixed while the detector fibre was moved parallel to the axis of the source fibre. The tip of the fibre was attached to an optical prism, which was placed behind a pinhole mask. The distance between the pinholes provided an accurate way of controlling the separation between source and detector. The optical parameters obtained from measurements in the oesophagus show a large variation. The effective attenuation coefficient showed a standard deviation of 40% around the mean and the reduced scattering coefficient had a standard deviation of 32%. The authors explained the errors with the real variance in the optical coefficients and inhomogeneities in oesophageal tissue.

1.4.6 The inverse Monte Carlo method

The so-called inverse Monte Carlo method is a convenient and flexible method to determine the optical coefficients of tissue *in vitro* from measurements of their transmittance and reflectance. This technique has been applied by the author for different studies to obtain the absorption and scattering coefficients of various types of tissue in the near-infrared wavelength range. Optical spectra of different tissues will be presented in section 1.5. The tissue types included human dermis and subdermis⁴⁰, myometrium and fibroid of the human womb⁴¹ and different types of cancers together with the surrounding normal tissue⁴². The inverse MC method has also been applied to measure the temperature dependence of optical coefficients of human dermis and subdermis in the physiological range⁴³.

The tissue samples can be illuminated by a single-wavelength or, for spectroscopic measurements, a broadband light source. Broadband illumination and detection using spectroscopy has the advantage of detecting spectral features of the optical coefficients. The reflected and transmitted intensities are detected using an integrating sphere, which is connected to a detector. A MC model for an identical geometry as that of the tissue sample calculates the reflected and transmitted intensities for a particular pair of μ_a and μ_s . The measured transmittance and reflectance are then converted to values of absorption and scattering using a look-up table. A more detailed description of the inverse MC method employed for measurements presented in this thesis can be found in a publication by Simpson *et al*⁴⁰. The inverse MC method used by Simpson *et al* provides optical coefficients with an accuracy of $\pm 20\%$ compared to values obtained using time-resolved spectroscopy. The method has also been applied *in vivo* in studies using spatially resolved reflectance spectroscopy.

1.4.7 Section summary

Some of the described techniques have been used to measure the optical properties of human tissue *in vivo*. Adequate measurements have been performed using, for example spatially resolved reflectance spectroscopy on areas, which are not easily accessible, such as the oesophagus. The performance of the optical fibre sensor in obtaining optical coefficients will be compared to these techniques. Most of these discussed methods, however, only collect information on optical parameters. The optical fibre sensor has the potential to be used to determine not only optical coefficients, but also acoustic, thermal and spatial properties of tissue. Its design would also allow measurements to be made on any organ that can be accessed endoscopically or, in some cases, percutaneously.

1.5 Optical properties of tissues in the near-infrared spectrum

The near-infrared wavelength range of light is of high interest in tissue optics because light can penetrate deeply into the tissue. Regions with abnormal optical properties, which may be an indication of pathological conditions, could be detected. The discussion of the optical coefficients of tissue is therefore restricted to the near-infrared wavelength spectrum.

The author measured the optical properties of cancers and the normal surrounding tissue of the human breast, kidney and liver *ex vivo* between 600 and 1064 nm using the inverse MC method. A total of eight samples were obtained and measured from each patient. Four of those samples were taken from the tumour and another four samples were taken from the normal surrounding tissue. The absorption and scattering spectra are shown in Figure 1.9, Figure 1.10 and Figure 1.11. The reduced scattering coefficients of all tissues decreased with increasing wavelength. Cancers produced generally larger values of reduced scattering coefficient compared to the normal surrounding tissue. The absorption coefficient is also lower in tumour tissue compared to the normal surrounding tissue. The absorption spectra show features of absorption by deoxyhaemoglobin (765 nm) and water (965 nm). The increase in absorption coefficient with decreasing wavelength can also be attributed to deoxyhaemoglobin.

The optical properties of human dermis and subdermis were also measured. The absorption spectrum of subdermis, which is dominated by fat cells, shows contributions from lipids (925 nm) as well as deoxyhaemoglobin and water. The spectra of the optical coefficients of dermis and subdermis are shown in Figure 1.12.

The difference in the reduced scattering coefficient of cancers compared to normal surrounding tissue agrees with other studies⁴⁴ in that the difference is marked when the data of a single subject is analysed. Troy *et al*⁴⁵ have shown that there is no significant difference in the optical coefficients of tumours and normal tissue of the human breast due to patient intervariability when data from a number of subjects is combined. The results of the measurements on cancers presented in this thesis are nevertheless encouraging for the development of the optical fibre sensor for the detection of cancer. Using the inverse MC method, it has been shown that differences in the optical coefficients of tumours and normal tissue can be detected *in vitro*.

The optical properties of tissue are very different when measured *in vivo* due to the presence of oxygenated haemoglobin, higher blood content and hydration. Studies in which the optical coefficients of normal and malignant tissue have been measured *in vivo* present very different results. Fishkin *et al* made frequency-domain photon migration measurements on the abdominal tumour of one patient and report that the absorption coefficient is very much larger in the malignant tissue compared to normal tissue while the difference in the scattering coefficient between the two tissue types is not very large. The authors explained these findings with the progressed stage of the tumour in which the necrotic zone possesses a reduced number of cells and increased water content. This could diminish the density of the scatterers. Fishkin *et al*³³ suggest that tumours of an earlier stage may show more distinct differences in the scattering coefficient. The difference in absorption coefficient is to be explained with the presence of oxygenated haemoglobin, which, as shown in section 1.2.2, can affect the absorption of wavelengths larger than 900 nm.

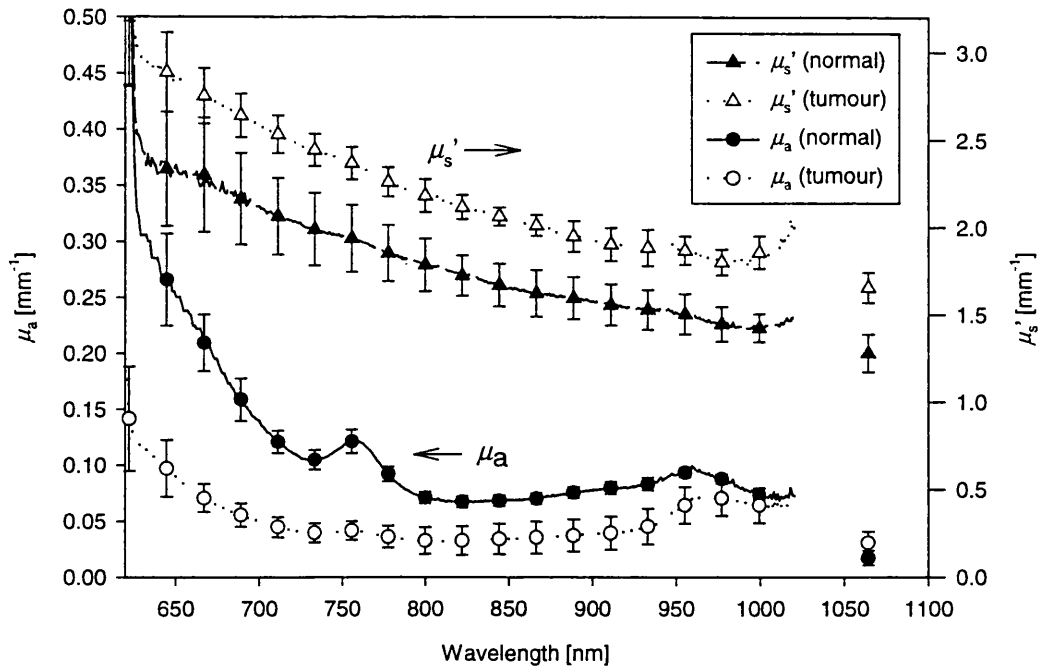


Figure 1.9 Spectra of the absorption and reduced scattering coefficient of tumour and normal tissue of the human kidney ($N = 4$).

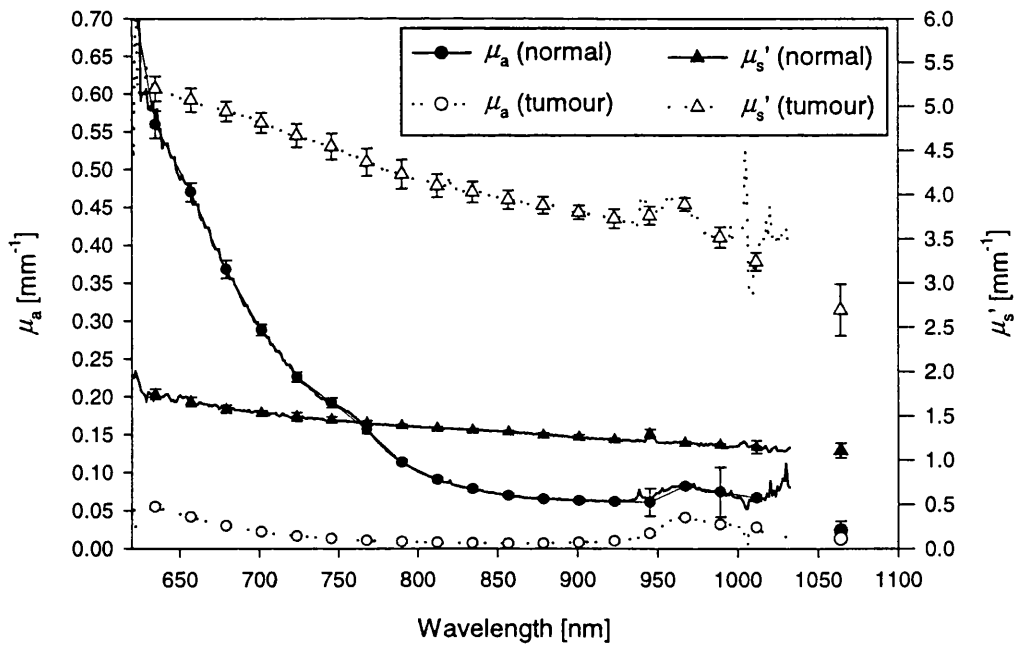


Figure 1.10 Spectra of the absorption and reduced scattering coefficient of tumour and normal tissue of the human liver ($N = 4$).

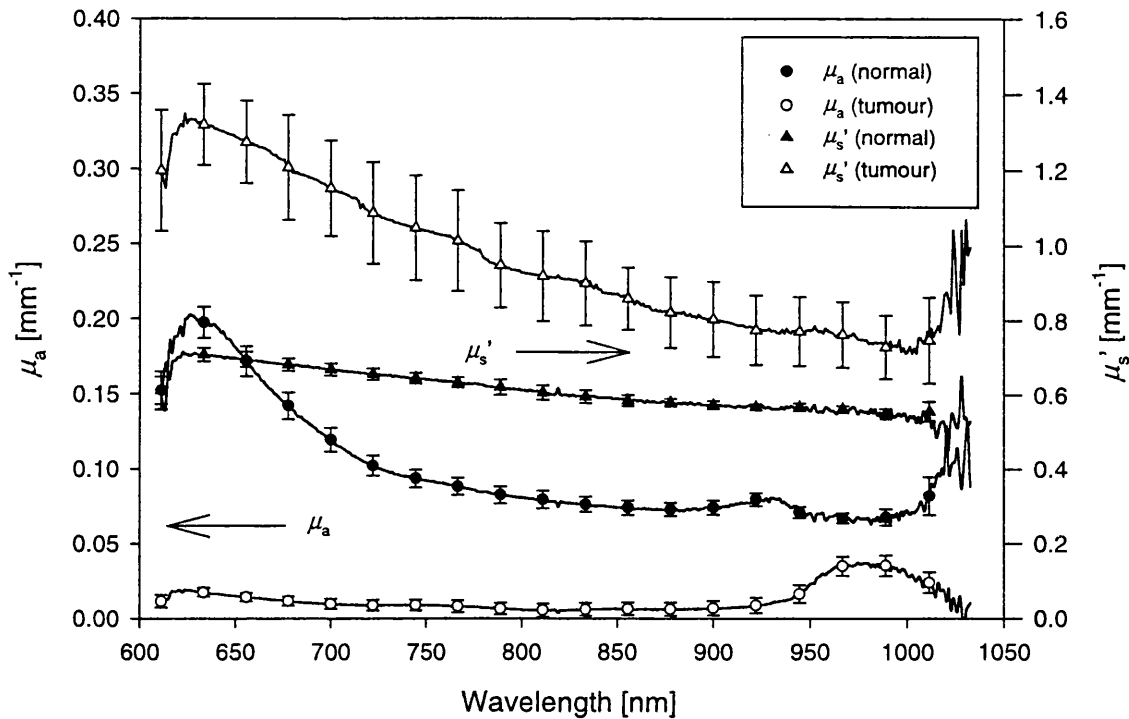


Figure 1.11 Spectra of the absorption and reduced scattering coefficient of tumour and normal tissue of the human breast ($N = 4$).

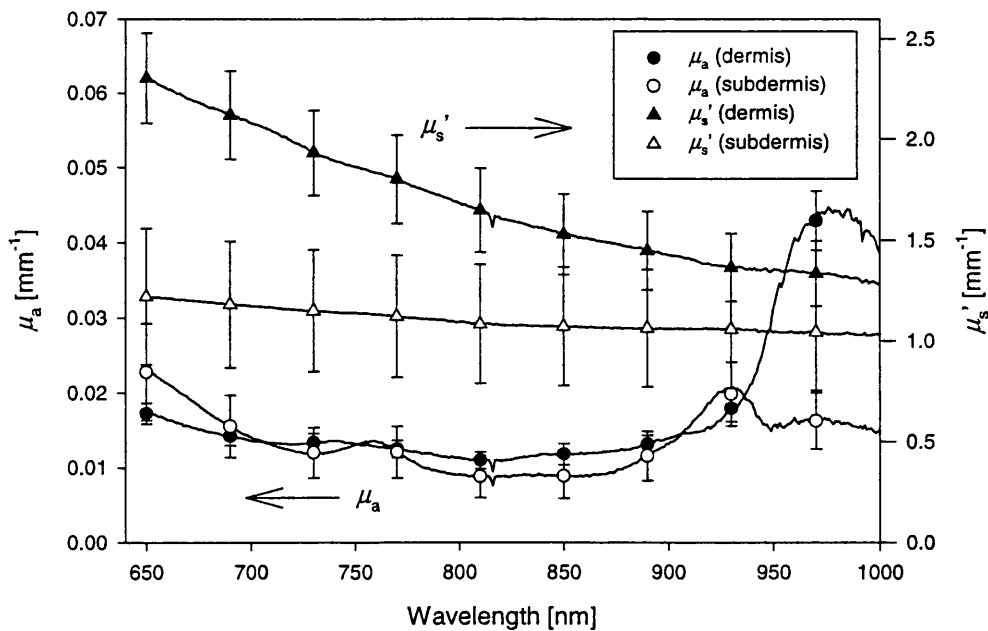


Figure 1.12 Spectra of the absorption and reduced scattering coefficient of human dermis and subdermis ($N = 4$). (The feature at 815 nm is an artefact caused by a faulty CCD pixel.)

The optical fibre sensor may prove to be sufficiently sensitive to detect similar differences in tissue *in vivo*, which could lead to complementary methods of cancer detection. While the differences in the optical coefficients measured *in vitro* are encouraging, it has to be borne in mind that the *in vivo* optical coefficients of tissue may be different to the *in vitro* values presented here.

1.6 Summary

The purpose of the work described in this thesis is the development of an optical fibre sensor for the endoscopic and minimally invasive detection of cancers. The detection of photothermally determined differences in the optical coefficients of normal and tumour tissue was envisaged to be the means of diagnosing cancer. The analysis of photothermal signals required the description of heat transport in tissue, which is outlined in the next chapter. A review of existing photothermal techniques is given in chapter 3. A summary of the first chapters is given at the end of chapter 3.

2 HEAT TRANSPORT IN TISSUE

In this thesis, the use of the optical fibre sensor for the determination of optical coefficients of tissue from photothermal signals is discussed. The detection of time-dependent diffusion of temperature fields into the sensor and the tissue is used to determine the optical coefficients of the tissue. Laser-tissue interaction and heat conduction in tissue is therefore a fundamental part of the background of this thesis. In this section, an overview of heat transfer in tissue will be given. The relevance of the individual types of heat transfer to the work presented in this thesis will be discussed and mathematical models of heat transfer will be reviewed:

2.1 Overview of heat transfer in tissue

In living tissue, heat is constantly produced through metabolism. Heat is also being transferred to other locations within the body or to adjacent media. If the heat that is gained by an organism is equal to the heat that is 'lost', the organism is said to be in heat balance. This can be expressed by applying the principle of conservation of energy to a volume of tissue:

$$\dot{Q}_{\text{gain}} = \dot{Q}_{\text{storage}} + \dot{Q}_{\text{loss}} + W \quad (2.1)$$

where the terms express, from left to right, the rates of heat gained due to, for example, laser energy deposition, heat stored in the tissue, heat loss to adjacent tissues or media through conduction and convection and the rate of work performed by the tissue. The different forms of heat transport in tissue are illustrated in Figure 2.1, which was reproduced from Welch *et al*⁴⁶. The rates of work and heat produced by the metabolism are usually negligible in studies involving laser irradiation.

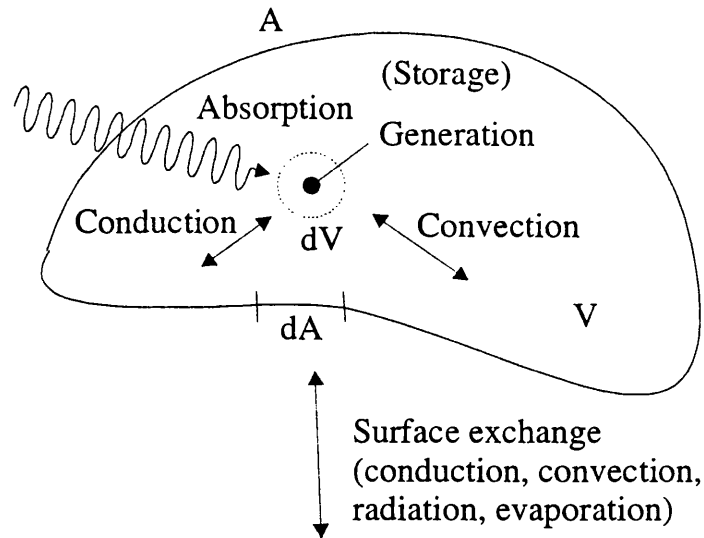


Figure 2.1 Diagram illustrating the heat transport in tissue. Heat is generated in dV , transported in volume V by conduction and convection, stored in V and exchanged over area A .

The transport of heat is present in tissue whenever a temperature difference exists. The transfer of thermal energy is governed by the laws of thermodynamics. The first law, which is an application of the law of conservation of energy, states that if heat, as a form of energy, is supplied to a physical system, its internal energy is increased and mechanical work is performed. The amount of heat lost by regions of a closed system is equal to the amount of heat gained by other regions. The second law of thermodynamics addresses the direction of heat transfer. Heat will always flow from regions of higher temperature towards regions of lower temperature, in order to produce a temperature equilibrium. There are three types of heat transfer: radiation, conduction and convection. The concepts and the underlying theories are outlined in the following sections.

2.1.1 Radiation

Radiation is the non-contact transfer of energy by an electromagnetic wave. The wavelength of the thermal radiation ranges from 0.1 to 20 μm . Emission of energy is accompanied by the loss of internal energy from the emitting body. Thermal emissions are due to, for example, lattice vibrations as opposed to electronic transitions.

Thermal emission of electromagnetic waves can be described using the model of an ideal black-body. A black-body emits the maximum amount of energy for a given temperature. Its emissive power is given by Planck's equation, which expresses the emissive power at temperature T and wavelength λ :

$$W_b(\lambda, T) = \frac{K \lambda^{-5}}{\exp\left(\frac{hc}{\lambda kT}\right) - 1} \quad (2.2)$$

The constant K is equal to $2\pi h c^2$ and k ($= 1.380622 \cdot 10^{-23} \text{ J K}^{-1}$) and h ($= 6.626 \cdot 10^{-34} \text{ J s}$) are the Boltzmann and Planck constants, respectively.

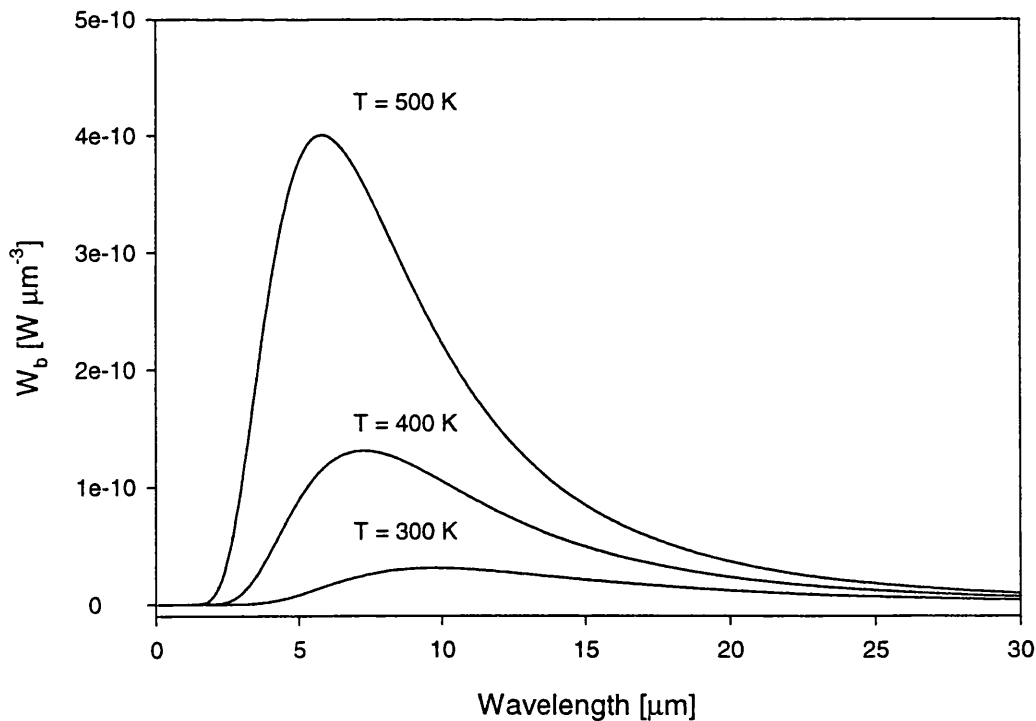


Figure 2.2 Emission spectrum of a perfect black-body at different temperatures.

Figure 2.2 illustrates the effect of temperature on the emission spectrum of a perfect black-body. The emission maximum shifts to shorter wavelengths as the temperature increases. The total emitted energy is the integral of $W_b(\lambda, T)$ over λ and is known as the Stefan-Boltzmann law

$$E_b = \int_0^{\infty} W_b(\lambda, T) d\lambda = \sigma T^4 \quad (2.3)$$

where $\sigma (= 5.67 \cdot 10^{-8} \text{ W m}^{-2} \text{ K}^{-4})$ is the Stefan constant.

Most emitters are not ideal black-bodies and therefore possess less emissivity. Their total emitted power is a fraction of the radiation produced by a perfect emitter. The thermal emissivity is a function of surface roughness, surface temperature, and surface material. Such emitters are termed grey body, which refers to an imperfect emitter, the emissivity of which is independent of wavelength λ . The total power emitted by a grey body is given as

$$E(T) = \varepsilon \sigma T^4 \quad (2.4)$$

where $\varepsilon \leq 1$ is the emissivity. The surface of the human body has an emissivity of about 0.97.

In the work described in this thesis, the detection of infrared radiation is used in pulsed photothermal radiometry to determine optical coefficients from measurements on turbid gels, which is described in chapter 4.

2.1.2 Convection

Convection is the transfer of heat due to movement of fluid. Convection is the most important heat transfer mechanism in fluids. The movement is caused by differences in density due to spatial variations in temperature. This process is termed free convection. Forced convection refers to the movement of liquid by external force, which typically produces a far greater rate of heat transfer than free convection. Heat transport through convection may affect photothermal measurements made using the optical fibre sensor

when the tissue is highly perfused by blood. The deposited heat would disperse more quickly due to convection.

2.1.3 Conduction

Conduction is the governing process of heat transfer between tissue and the optical fibre sensor. The sensor is assumed to be in perfect thermal contact with the tissue and that heat loss due to radiation is negligible. Heat conduction is the transfer of thermal energy due to a temperature gradient for which direct physical contact between the objects is required. The transfer of thermal energy occurs at atomic and molecular level. In solids, heat is transferred through lattice vibrations and movement of free electrons. In stationary liquids, random motions of molecules cause collisions to transfer heat from regions of high temperature to regions of low temperature.

The Fourier law describes the transfer of heat through conduction. It states that the amount of energy Q conducted through a medium is equivalent to

$$Q = -kA(T_2 - T_1) \Delta t / \Delta L \quad (2.5)$$

where k is the thermal conductivity of the material, A is the area perpendicular to the direction of heat conduction, and T_1 and T_2 refer to the temperature difference. The time difference Δt is the time during which heat conduction occurs and ΔL is the distance over which heat is conducted.

Heat flow is defined as the rate at which thermal energy is conducted per unit area A and unit time t as given by

$$f_c = \frac{Q}{A \Delta t} = - \frac{k(T_2 - T_1)}{\Delta L} \quad (2.6)$$

where f_c is the heat flow vector. For infinitesimally small L , the differential form of the Fourier law of conduction is obtained, which is the governing equation for heat conduction in stationary media:

$$f_c = -k \nabla T \quad (2.7)$$

where ∇T is the spatial temperature gradient.

2.2 Analytical solutions to the heat diffusion equation

Mathematical solutions of the heat conduction equation, which can be derived from Fourier's law (see also Appendix A) are discussed in this section. The equation of heat conduction is:

$$\frac{\partial T}{\partial t} = \alpha \left(\frac{\partial^2 T}{\partial x^2} + \frac{\partial^2 T}{\partial y^2} + \frac{\partial^2 T}{\partial z^2} \right) \quad (2.8)$$

where α is the thermal diffusivity. The thermal diffusivity α is defined as

$$\alpha = \frac{k}{\rho c} \quad (2.9)$$

where k is the thermal conductivity, ρ is the density and c is the specific heat capacity. The equation of heat conduction describes the time-dependent change in temperature due to heat flow across the boundaries of an infinitesimal volume with thermal property α . Analytical solutions of the heat conduction equation have been obtained for various geometries and boundary conditions. Specific solutions have been applied to analyse photothermal signals detected using pulsed photothermal radiometry, which is discussed in chapter 4.

2.2.1 The Green's function

Green's functions are useful in the solution of partial differential equations and represent the response of a system to a unit impulse. They are used for the derivation of the analytic expressions describing the radiometric signal detected using pulsed photothermal radiometry. This section is taken from Carslaw and Jaeger⁴⁷ and reproduced here for completeness. According to Carslaw and Jaeger, the Green's function in the context of heat conduction is described "*as the temperature at $r(x, y, z)$ at the time t due to an instantaneous point source of strength unity generated at the point $r'(x', y', z')$ at the time t' the solid being initially at zero temperature, and the surface being kept at zero temperature*". The Green's function satisfies the heat conduction equation

$$\frac{\partial T}{\partial t} = \alpha \nabla^2 T(r, t) \quad (2.10)$$

where $T(r, t)$ is the temperature rise at the time t and position $r(x, y, z)$ in an infinite medium due to the initial temperature $f(r)$ inside the material. ∇ is the gradient symbol. The temperature rise at point r and time t is the integral of a Green's function according to:

$$T(r, t) = \int_{-\infty}^{+\infty} \int_{-\infty}^{+\infty} \int_{-\infty}^{+\infty} g(r, t, r', t'=0) f(r) dx' dy' dz' \quad (2.11)$$

The function $g(r, t, r', t')$ is called Green's function. Considering three-dimensional flow of heat in an infinite and isotropic medium, the Green's function g is, according to Carslaw and Jaeger, given by

$$g(r, t, r', t') = \frac{1}{8 [\pi \alpha (t-t')]^{3/2}} \exp\left(-\frac{|r-r'|^2}{4\alpha(t-t')}\right) \quad (2.12)$$

Equation (2.11) describes the temperature rise at time t and position r in an infinite medium with an initial temperature distribution $f(r)$ which is obtained from a distribution of instantaneous temperature sources at time $t' = 0$ over its volume. Equation (2.11) can be regarded as the temperature rise in an infinite medium due to a point source of heat generated at $t = t'$ and r' . The temperature generated by an amount of energy Q at time $t' = 0$ and point $r' = 0$ is given by

$$T(r, t) = \frac{Q}{\rho c} \frac{1}{8 [\pi \alpha t]^{3/2}} \exp\left(-\frac{|r|^2}{4\alpha t}\right) \quad (2.13)$$

This general treatment can be extended to describe laser irradiation of semi-infinite media with an infinitely wide beam, which simplifies the description of the conduction of heat to one spatial dimension. An application to such a problem is presented in chapter 4 in which pulsed photothermal radiometry is applied to determine optical coefficients from turbid gels. Analytical solutions to the heat conduction equation can also be obtained to describe the spatial and temporal temperature distributions in, for example, discrete absorbers, such as melanin particles, or homogeneously absorbing layers due to the absorption of laser light. Solutions to such problems are helpful in the prediction of treatments of, for example,

port-wine stains using lasers. More details about analytical solutions of the heat conduction equation are given elsewhere^{48,47}.

An analytic expression for the conduction of heat in an optically transparent film on an absorbing substrate was obtained by de Jesus *et al*⁴⁹. The expression was used by the author for the interpretation of photothermal signals detected in a thin polymer film on non-scattering liquids using bulk interferometry. The theory was found to be in good agreement with the experimental observations and was very encouraging for the subsequent work on the optical fibre sensor. However, analytic solutions to the heat conduction equation are typically reduced to one spatial dimension and the experimental methods take account of this by employing a large area of photothermal excitation compared to the area of detection. The optical fibre sensor is characterised by small areas of excitation and detection and the theoretical model of the optical fibre sensor was therefore required to model radial heat flow as well as to be amenable to the modelling of the inhomogeneous thermal and optical properties of tissue. It was found that these issues could only be addressed with numerical models, which provided sufficiently accurate and flexible methods for the calculation of photothermal signals detected using the sensor.

2.3 Numerical solutions to the heat diffusion equation

Analytical solutions to the heat conduction equation are typically obtained for infinite or semi-infinite media with isotropic thermal properties. Problems in obtaining analytical solutions appear when the medium has time-dependent thermal and optical properties, requires the use of mixed boundary conditions or is simply of a complex geometry. Another limitation may be the unavailability of a suitable Green's function. Such problems can usually not be solved analytically and require the use of numerical techniques. The methods of finite differences and finite elements will be introduced in the following sections. The method of finite elements will be used extensively for the interpretation of photothermal signals detected using the optical fibre sensor.

2.3.1 The finite difference method

The concept of the finite difference method is the substitution of the derivatives by differences. This transforms the differential equation into a set of algebraic equations, which can be solved by taking the initial and boundary conditions into consideration. The temperature can therefore be calculated for each position in the discrete grid.

The finite difference method is useful for problems where temperature-dependent thermal coefficients, time-dependent surface temperatures, arbitrary heat sources, and layered geometries have to be modelled. The finite difference method, however, is not as advantageous as the finite element method, which is discussed in the next section. Complicated geometries, general boundary conditions and variable or non-linear material properties can be handled much easier using finite elements⁵⁰.

2.3.2 The finite element method

The method of finite elements is an established technique for solving partial differential equations numerically. It has been widely used in problems of steady-state and time-dependent heat conduction as well as in mechanical problems. A full discussion of the theoretical background of finite elements would go beyond the scope of this thesis. There are many references on the subject of finite elements^{51,52}, which discuss the principles of this method in detail. In this section, only a general overview of the method will be given.

The finite element method can be applied to the modelling of heat transport in media such as tissue, which could possess non-constant properties of tissue and spatially and temporally varying perfusion rates due to varying vascularisation. Initial or prescribed temperatures, heat fluxes and convective heat transfer can be assigned to individual nodes. Another advantage of the finite element method is its ability to compute complex geometries.

The finite element method has been used to describe the heat transport in the optical fibre sensor and the adjacent tissue. The computed temperature profiles were used to calculate the photothermal signal detected by the sensor, which depended upon the

geometry of the sensor and the optical and thermal coefficients that were assumed for tissue or the tissue phantom. The finite element method was the most convenient way of computing the heat transfer between the tissue and the optical fibre sensor. The more complex thermal geometry of the sensor compared to semi-infinite media combined with the principal aim of computing photothermal signals generated in heterogeneous tissue can only be addressed by numerical methods. The finite element method was also convenient for incorporating initial temperature distributions, generated using numerical models of light transport in tissue, such as Monte Carlo models. The finite element model of the optical fibre sensor is described in chapter 6.

2.4 Measurement of the thermal properties of tissue

For the work presented in this thesis, the thermal properties of tissue were considered to be similar to those of water and that temperature dependence of thermal parameters was also assumed to be negligible. Such assumptions are probably valid for studies on materials of well-known thermal coefficients, which are carried out in the laboratory environment. However, if the optical fibre sensor is used for *in vivo* measurements then the thermal properties of tissue can no longer be considered constant or similar to water. Some types of tissue, for example breast and subcutaneous tissue, have a high lipid content which may alter the thermal properties. It has also been shown that the temperature of *in vivo* tissue also affects the thermal conductivity due to changes in the perfusion rate.

Two different techniques of measuring thermal properties of tissue are discussed in this section. There is a large number of reviews of techniques for measuring thermal properties. Valvano has written an excellent review in *Optical-thermal response of laser-irradiated tissue*⁵³, in which various techniques for measuring thermal properties of tissue are outlined. Another source of information on the thermal properties of tissue is a review by Duck¹⁰.

The transport of heat in tissue is determined by a number of processes, such as conduction, convection, radiation, metabolism and evaporation. Most techniques for the measurement of thermal conductivity and diffusivity employ thermal probes, which use the

thermistor bead as a heat source and as a temperature sensor. For all of these techniques, heat is introduced into the tissue in which it dissipates by either conduction or, as in the case of living tissue, by conduction and convection due to blood perfusion.

For the constant temperature heating technique, a variable voltage is applied to a thermistor in order to keep its temperature at a predefined value for a duration of typically tens of seconds. The applied power varies during the measurement in order to maintain a constant temperature. By fitting a linear regression through the time-dependent response of the ratio of power and temperature, the values for thermal conductivity and diffusivity can be determined.

The sinusoidal heating method, proposed by Valvano⁵⁴, has the advantage to measure the intrinsic thermal properties of tissue in the presence of perfusion. The measurements require two separate thermistors. A computer-controlled instrument applies a combination of steady-state and sinusoidal electrical power to one of the thermistors. The instrument also measures the temperature of the heated thermistor. The other thermistor is placed far away from the heated region and is used to measure the baseline temperature. By fitting an analytic theory to the sinusoidal temperature response, values for the thermal conductivity and diffusivity can be obtained.

2.5 The thermal properties of tissue

Measurements on excised tissue have shown that tissue thermal properties can be approximated with those of water^{55,54}. Animal and human tissues were measured at temperatures ranging from 3 – 45 °C. Values for the thermal conductivity, k , and diffusivity, α , and their temperature dependence were obtained. The average thermal properties of all types of tissue (animal and human) measured by Valvano *et al* were found to be:

$$\begin{aligned}k &= 4.574 + 0.01403 T && [\text{mW cm}^{-1} \text{ }^\circ\text{C}^{-1}] \\ \alpha &= 0.1284 + 0.0053 T && [\text{mm}^2 \text{ s}^{-1}]\end{aligned}$$

The average thermal conductivity of tissue was obtained from extensive studies on different tissue types *in vitro*. The thermal conductivities of different types of tissue is listed in Table 2.1 below and reflects the effects of the varying tissue composition.

<i>Tissue</i>	k_0 [mW cm ⁻¹ K ⁻¹]	k_1 [mW cm ⁻¹ K ⁻²]	α_0 [cm ² s ⁻¹]	α_1 [cm ² s ⁻¹ K ⁻¹]
Adenocarcinoma (breast)	4.194	0.03911	0.001617	-0.000049
Colon cancer	5.450	-	0.001349	-
Fat of spleen	3.431	-0.00254	0.001321	-0.000002
Liver	4.692	0.01161	0.001279	0.000036
Lung	3.080	0.02395	0.001071	0.000082
Lung	4.071	0.01176	0.001192	0.000031
Myocardium	4.925	0.01195	0.001289	0.000050
Pancreas	4.365	0.02844	0.001391	0.000084

Table 2.1 Thermal conductivity and diffusivity together with the temperature coefficients of different types human tissue measured *in vitro*.

Some tissue constituents such as lipids, proteins or water may be dominating the thermal properties depending on the tissue type. The temperature dependent thermal coefficients can be obtained from equations (2.14) and (2.15) using the values given in Table 2.1:

$$k = k_0 + k_1 T \quad (2.14)$$

$$\alpha = \alpha_0 + \alpha_1 T \quad (2.15)$$

The thermal properties of tissue are determined by the relative concentration of the cell constituents. An empirical relationship⁵⁶ between thermal conductivity and mass fraction of water, lipids and protein has been published as

$$k [\text{mW cm}^{-1} \text{ } ^\circ\text{C}^{-1}] = \rho \sum_n \frac{k_n m_n}{\rho_n} = \rho (6.28 m_{\text{Water}} + 1.17 m_{\text{Protein}} + 2.31 m_{\text{Fat}}) \quad (2.16)$$

where ρ is the density. Similar expressions have been found for specific heat capacity and density:

$$c [\text{J g}^{-1} \text{ } ^\circ\text{C}^{-1}] = \sum_n c_n m_n = 4.2 m_{\text{Water}} + 1.09 m_{\text{Protein}} + 2.3 m_{\text{Fat}} \quad (2.17)$$

and

$$\rho [\text{g cm}^{-3}] = \frac{1}{\sum_n \frac{m_n}{\rho_n}} = \frac{1}{m_{\text{Water}} + 0.649 m_{\text{Protein}} + 1.227 m_{\text{Fat}}} \quad (2.18)$$

The thermal coefficients of cancers and of normal surrounding tissue are of great interest to the future application of the optical fibre sensor to the detection of cancers. Cancers may be characterised not only by their optical properties, but also by differences in the thermal coefficients. The thermal coefficients for a number of different cancers and their normal surrounding tissue are listed in Table 2.2. The coefficients were obtained by Bowman⁵⁷ in an extensive study on different tumour types. It was found that all tumours, except particular carcinomas of the breast and the liver, had a greater thermal conductivity than the normal tissue.

<i>Tissue</i>	k_0 [mW cm ⁻¹ K ⁻¹]
Breast	
Atrophic normal tissue	4.99 ± 0.04
Scirrhous carcinoma	3.97 ± 0.04
Mucinous (colloid) carcinoma	5.27 ± 0.41
Colon	
Normal	5.56 ± 0.09
Metastatic colon carcinoma	5.56 ± 0.12
Liver	
Normal	5.72 ± 0.09
Metastatic colon carcinoma	5.20 ± 0.08
Normal	5.08 ± 0.11
Metastatic pancreatic carcinoma	5.62 ± 0.21
Lung	
Normal	5.18 ± 0.21
Squamous cell carcinoma	6.66 ± 0.18
Pancreas	
Normal	3.45 ± 0.05
Metastatic carcinoma	4.78 ± 0.39
Normal	4.68 ± 0.06
Metastatic gastric carcinoma	4.92 ± 0.54

Table 2.2 Thermal conductivity of various human normal tissues and tumours measured in vitro. (Source: Bowman 1981⁵⁷)

The specific heat capacity is dependent upon the composition of the tissue as illustrated by equation (2.17). The values for the specific heat of various tissue types presented in Table 2.3 below have been taken from Duck⁵⁸.

<i>Tissue</i>	<i>c</i> [J g ⁻¹ K ⁻¹]
Brain (white matter, human)	3.84
Brain (grey matter, human)	3.60
Fat (canine)	2.30 – 2.68
Kidney (human)	3.89
Kidney (human)	3.60
Liver (human)	3.60
Muscle	3.72

Table 2.3 *Specific heat capacities of various types of human and animal tissues.*

The data in Table 2.3 illustrates that the specific heat can vary between different tissue types, depending on the tissue composition. The greatest difference in specific heat can be expected between tissues with high and low fat content, which can be found in close proximity in the human breast. The variation in the thermal properties may affect the performance of photothermal methods used for the characterisation of breast tumours. The standard deviation for the displayed values is $\pm 16\%$. The specific heat capacity of fat as one of the main tissue components is also strongly dependent on temperature and on fatty acid composition. An approximate empirical expression⁵⁹ is used to calculate the temperature dependence of the specific heat capacity of bovine and porcine fats, which is illustrated in Figure 2.3 below.

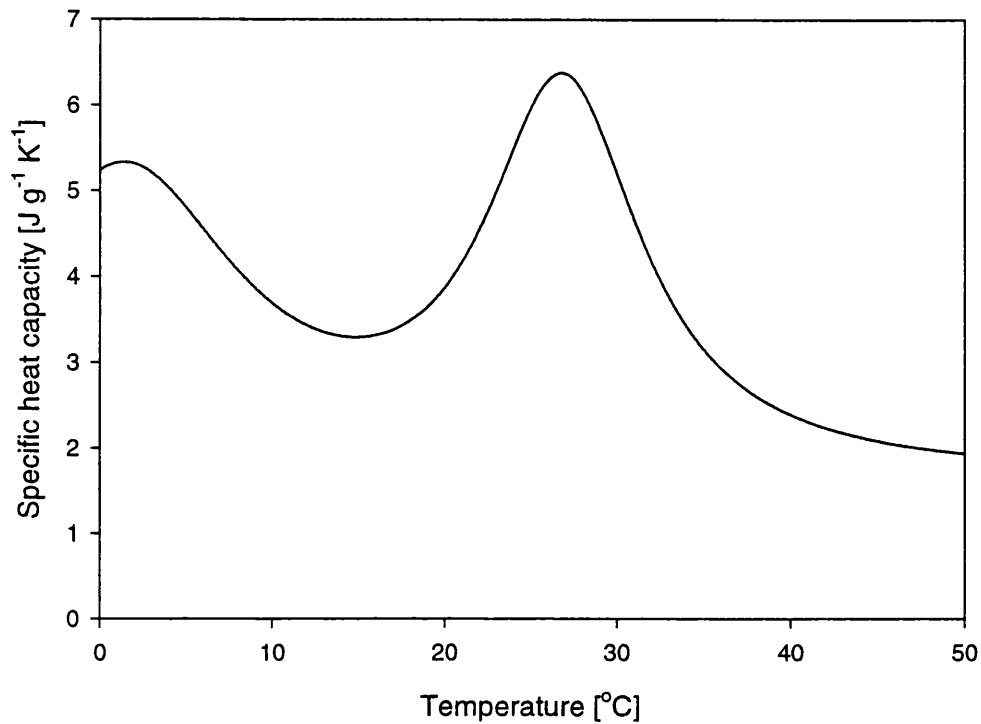


Figure 2.3 Variation of the specific heat capacity for bovine and porcine fat with temperature *in vitro*.

Similar data for lipid derived from human tissue does not appear to be available. Figure 2.3 nevertheless indicates that the specific heat capacity may vary significantly in tissues with high lipid content, such as breast tissue, which may complicate the diagnosis of breast cancer using the optical fibre sensor.

The density of different types of tissue can be calculated using equation (2.18) provided the mass percentage of the water, lipid and protein components are known. The densities of various types of tissue have been measured by Woodard *et al*⁶⁰ and are listed in Table 2.4.

<i>Tissue</i>	ρ [g mm ⁻³]
Adipose tissue 1	0.97 · 10 ⁻³
Adipose tissue 2	0.95 · 10 ⁻³
Adipose tissue 3	0.93 · 10 ⁻³
Adrenal gland	1.03 · 10 ⁻³
Aorta	1.05 · 10 ⁻³
Connective tissue	1.12 · 10 ⁻³
GI tract – wall of small intestine	1.05 · 10 ⁻³
Kidney	1.05 · 10 ⁻³
Mammary gland	1.05 · 10 ⁻³
Muscle – skeletal 1	1.07 · 10 ⁻³
Muscle – skeletal 2	1.05 · 10 ⁻³
Muscle – skeletal 2	0.99 · 10 ⁻³
Ovary	1.02 · 10 ⁻³
Pancreas	0.99 · 10 ⁻³
Skin	1.05 · 10 ⁻³

Table 2.4 *Densities of various types of human tissue (data taken from Woodard et al⁶¹).*

The density of the different types of tissue was found to vary within $\pm 5.0\%$. The standard deviation in the density was due to the variation in the composition of tissue.

Knowledge of the thermal properties of living tissue is especially important since the optical coefficients of tissue will be determined from the shape of the photothermal sensor signal. Variations in the thermal properties of tissue alter the time course of photothermal signals. A discrepancy between the thermal coefficients used in a theoretical model describing the photothermal signals and the ‘real’ values present in the tissue would consequently lead to errors in the determined optical coefficients. Photothermal

investigations of tissue optical properties using the sensor would therefore need an additional measurement of the thermal properties of tissue.

The temperature rise in the target due to the absorption of a laser pulse is dependent upon the value of specific heat capacity and density. The value of those parameters in tissue is dependent upon its composition and physiological state and may therefore introduce errors in the determined optical coefficients. The thermal coefficients will affect the amplitude and the time course of the photothermal signal. The variation in the values of thermal conductivity, specific heat and density between different types of soft tissue is relatively small, provided the tissue composition is dominated by water. If the composition of tissue is dominated by fat, the thermal constants show markedly different values. This presents a problem for the proposed use of the optical fibre sensor, since a diagnosis of, for example, cancer will rely on separate point measurements on different sites in order to compare the photothermal responses of normal and cancerous tissue. In order to obtain the optical coefficients of tissue, the thermal coefficient need to be known. Deviations in the thermal properties of the measured tissues would produce errors in the optical coefficients determined from the photothermal signal.

The thermal properties of tissues are determined by a combination of factors such as tissue composition as well as physiological factors like perfusion. The effect of physiological factors on the thermal properties of tissue is examined in the following section.

2.5.1 Effect of perfusion on the thermal properties of tissue

Valvano *et al* showed the effects of perfusion on the thermal coefficients by using an isolated rat liver⁶², which was perfused with a buffer solution at a known rate. The results show an increase in the values for thermal conductivity and diffusivity with rising perfusion. Jain *et al*⁶³ have investigated the effect of blood flow on heat transfer in a mammary carcinoma *in vivo*. A comparison of the thermal conductivity measured in four tumours with and without blood flow produced an increase ranging from 14 to 132%. Such changes may significantly affect photothermal signals detected using the optical fibre

sensor. An increased thermal diffusivity will result in a faster decay of the signal. The magnitude of the change in decay will also depend on the rate of perfusion in the tissue.

The temperature of living tissue has also been reported to affect the thermal coefficients⁶⁴. Warming of tissue results in an increase in perfusion in order to diffuse excessive heat. An increase in tissue temperature can increase thermal conductivity to up to six times the normal value. Gullino *et al*⁶⁵ investigated temperature gradients and local perfusion in mammary carcinoma *in vivo*. The authors found that convective heat transfer in tumours due to blood flow is inefficient compared to normal tissue and that the transport of heat in tumours is largely conductive. It was also found, however, that blood perfusion varies greatly within the tumour. Some regions were found to possess almost zero blood flow while other regions in the same tumour produced blood flow nearly three times the average perfusion rate. Perfusion of tumours by blood was found to be low in general, which also helped to maintain relatively large temperature gradients. The temperature dependence of blood flow in tumours and normal tissue has also been addressed by Dudar *et al*⁶⁶ who found that normal tissue has a much greater capacity of varying blood perfusion compared to tumours. Normal tissue was able to increase its flow capacity up to six times when heated by a few degrees compared to its typical values. Tumours on the other hand showed less flexibility and could only double their maximum flow capacity when exposed to higher temperatures.

2.6 Effect of temperature on the optical and thermal tissue properties

The temperature rises generated by the absorption of low energy laser pulses used in the optical fibre sensor are of the order of a few degrees. The effects of excessive heat producing irreversible changes to tissue, such as coagulation, will therefore not be discussed.

Temperature variations affect, for example, the thermal properties of tissue constituents such as water. Using an average value for the temperature-dependent thermal conductivity of tissue, which was determined by Valvano, of $k = 4.574 + 0.014 T$, a change in temperature of 5 °C will produce a 1.5 % change in thermal conductivity. Temperature

also has an effect on the refractive index of tissue constituents, which in turn will produce changes in the optical coefficients. Assuming again a temperature increase of 5 °C, the refractive index of water⁶⁷, for example, is reduced by 0.03 %. The change in μ_s' in a turbid tissue phantom for such a change in n has been estimated using Mie theory. Assuming a constant refractive index of the scattering particles, the increase in μ_s' is approximated as 0.072%.

Changes in the optical coefficients of human dermis and subdermis have been measured by the author for temperatures within in the physiological range⁴³. Dermis produced a positive temperature coefficient for the reduced scattering coefficient of $4.7 \cdot 10^{-3} \pm 0.5 \cdot 10^{-3} \text{ } ^\circ\text{C}^{-1}$ while subdermis produced a negative temperature coefficient of $-1.4 \cdot 10^{-3} \pm 0.3 \cdot 10^{-3} \text{ } ^\circ\text{C}^{-1}$. No significant changes were detected for the absorption coefficient. Results from other studies⁶⁸ noted changes in the scattering coefficient of muscle tissue of $1\text{-}2\% \text{ } ^\circ\text{C}^{-1}$ for a temperature change from 30 to 40 °C. Troy *et al* detected temperature dependent changes in the scattering coefficient of canine prostate of $23 \cdot 10^{-3} \text{ } ^\circ\text{C}^{-1}$.

The change in the optical coefficients of tissue is small and the temperature dependence has therefore not been taken into account in the finite element model of the optical fibre sensor discussed in chapter 6. The temperature increase caused by the absorption of the excitation laser pulse is small and its effect on the thermal and optical properties of tissue phantoms and tissue *in vitro* can be neglected. The same assumption, however, does not apply to measurements on tissue *in vivo* where optical and thermal parameters can vary with changing temperature, as discussed in section 2.5.1.

In the next chapter, current photothermal techniques are reviewed. At the end of chapter 3, the first three chapters will be summarised and the purpose of the work described in this thesis will be outlined.

3 REVIEW OF PHOTOTHERMAL SPECTROSCOPY

Photothermal spectroscopy is widely used in material science due to its ability of non-destructive and non-contact characterisation of material properties. Photothermal spectroscopy has been applied to detect the excitation spectra of various materials, to determine the thermal diffusivity of thin films^{69,70}, the determination of absolute absorption coefficients of materials at the excitation wavelength^{71,72}, and depth profiling of layered media⁷³. Photothermal techniques have also been used for airborne monitoring of oil spills⁷⁴, where the oil-water medium is illuminated by a laser pulse. The temperature rise in the different materials is detected over different spectral bands, from which the thickness of the oil layer is determined. Other applications of photothermal techniques include the detection of microcracks in aircraft structures and the measurement of thermal resistance at contact interfaces⁷⁵. There are of course many other applications, most of which have been reviewed by Almond and Patel⁷⁶. Photothermal spectroscopy has also been extensively studied for biomedical applications, which are reviewed in section 3.2 later on.

3.1 Instrumentation and detection techniques

3.1.1 Sources

The optical sources for the generation of photothermal responses can be classified into high power broad spectral sources and lasers. Some of the most commonly used broad spectrum sources include the Xenon lamp, the globar and the Nernst glower. The globar source is an electrically heated rod of silicon carbide, while the Nernst glower is equipped with a tube of oxide of a mixture of zirconia, yttria and thoria.

Lasers are perhaps the most widely used sources of optical excitation, since they provide well-defined region of localised heating, which is important for photothermal investigations. There are many different laser sources available, which provide a variety of excitation wavelengths that can be used for spectroscopic purposes. Recent advances in

laser technology also produced continuously tuneable lasers, which have sufficient power to be used for photothermal excitation.

The output of the optical sources is often modulated depending on the application. Periodic or transient modulation can be achieved using devices such as mechanical choppers, acousto-optic and electro-optic modulators, by techniques such as beam deflection or by modulation of the electric drive current of the source. For the work presented in this thesis, a pulsed laser was used as a source of optical excitation.

3.1.2 Pyroelectric detection

Pyroelectric transducers have been widely used to monitor thermal transients⁷⁷ and have also been applied to the measurement of the thermal diffusivity of air^{78,79} and the detection of gases⁸⁰. A pyroelectric material has a low crystalline symmetry to produce a permanent electric dipole moment, which gives rise to an internal electric field along a particular axis⁸¹. Conducting electrodes can be applied to the material and charge is stored in these electrodes. A change in temperature will produce a change in the lattice spacing of the material, and hence the electric field. The resulting change in the charge in the electrodes can be detected as a current. Only certain materials possess pyroelectric qualities due to their unique crystallographic structure. In a typical photo-pyroelectric set-up, the pyroelectric film has a metallic coating on both surfaces and is in contact with the sample as shown in Figure 3.1 below. Continuous-wave or pulsed optical excitation is incident on the sample. The generated heat is conducted through the sample and detected by the pyroelectric material. The analysis of such measurements typically requires the solution of the heat conduction equation for a system containing an air layer, the sample, the coupling medium, the detector and the backing material. A typical material used to make pyroelectric detectors is polyvinylidene fluoride (PVDF). A principle advantage of pyroelectric transducers is their flat frequency response over a reasonably large bandwidth. Pyroelectric detectors are fast sensors, which can have response times of a few nanoseconds⁸² to mechanical stresses. In this case, however, the detectors should be referred to as piezoelectric transducers.

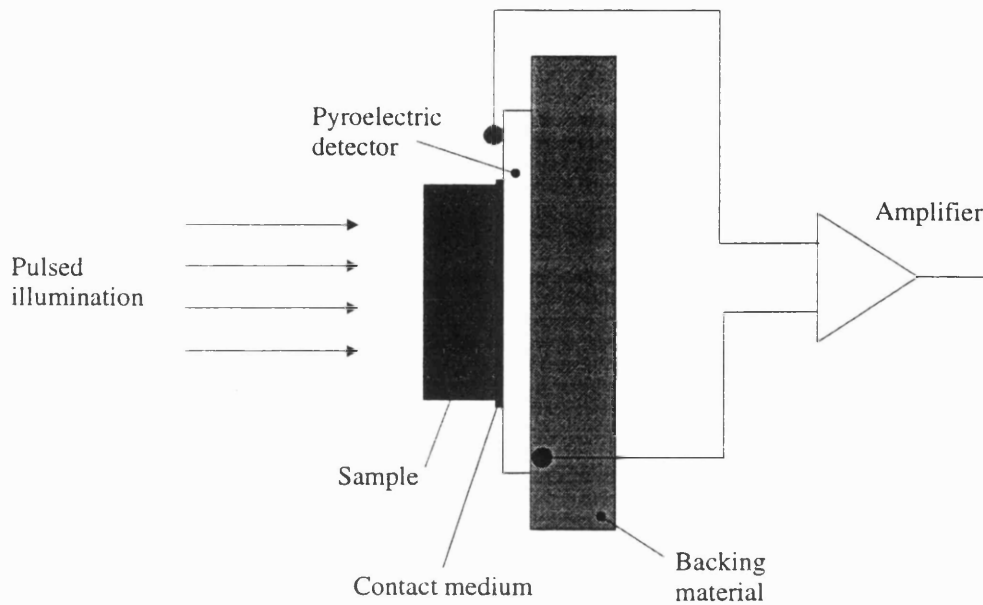


Figure 3.1 *Diagram of a typical experimental configuration of a pyroelectric detector.*

The wide bandwidth makes pyroelectric detectors suitable for simultaneous photoacoustic and photothermal measurements. The response times that can be expected for photothermal measurements, however, are much longer since they are determined by thermal diffusion. The frequencies used for photothermal measurements with pyroelectric transducers are typically between 0.1 to 3000 Hz, which is comparable to the bandwidth of the optical fibre sensor. Pyroelectric detectors can therefore be regarded as alternatives for monitoring acoustic and thermal waves at the distal end of an optical fibre. The potential disadvantages are the need of wiring which would have to run along the fibre as well as the deposition of metallic layers on both sides of the pyroelectric material, which would prohibit the transmission of the excitation laser pulses.

Using the optical fibre sensor in its proposed configuration, in which a transparent polymer film is acting as a Fabry-Perot interferometer, allows for the coaxial excitation and detection of photothermal and photoacoustic signals. Pyroelectric detectors may be an alternative to the interferometric technique used in the optical fibre sensor since they do allow for simultaneous photoacoustic and photothermal measurements.

3.1.3 Radiometric detection

Photothermal radiometry relies on the detection of infrared radiation from the surface of an object. The time course of the radiation emitted from the object depends on the optical and thermal properties of its material. The intensity of the emitted infrared radiation depends on the temperature at the surface of the object. In photothermal spectroscopy, this temperature is locally modulated using optical excitation, which can be pulsed or sinusoidal. The detection of infrared emission from the surface of the affected area can yield information on the optical, thermal, and spatial properties of the object. The measurement geometry can be of the backward emission type, where photothermal excitation and detection occur on the same side of the object, or the forward emission type, which can be applied on thin slabs of material where excitation and detection of the infrared response occur on opposite sides of the object.

Detectors used for radiometry include pyroelectric and photonic detectors. Pyroelectric detectors are only useful if strong signals are measured. In such a detector, a thermally isolated, thin membrane of pyroelectric material with thin layers of metal electrodes deposited on both sides is used as the sensing element. The pyroelectric film is darkened on the side of the incident radiation in order to enhance the absorption of infrared light over a broad spectral range. The absorption of light in the coating and subsequent conduction of heat produces a temperature rise in the pyroelectric material, which is detected as a change in voltage. Photonic detectors, which are typically made of semiconductor materials, are more sensitive and offer a broader bandwidth than pyroelectric detectors. Commonly used materials include InSb (Indium-Antimony), which provides a detection range of 2-5.5 μm , and $\text{CdHg}_x\text{Te}_{1-x}$ (Mercury-Cadmium-Telluride), which has a wider spectral sensitivity ranging from 2 to 12 μm depending on the relative quantities of Hg and Te. The absorption of incident infrared radiation generates free electrons in the semiconductor material. Photonic detectors require cooling to reduce the current produced by thermal emissions of the semiconductor itself. This can be achieved using liquid nitrogen. Photonic detectors offer greater sensitivity and bandwidth (1-2 MHz) compared with pyroelectric detectors, which have bandwidth of a few kHz. A HgCdTe detector is used for pulsed photothermal radiometry discussed in chapter 4. Pulsed

photothermal radiometry is applied to the determination of optical coefficients from photothermal signals, which were detected in turbid tissue phantoms.

Photothermal radiometry has the interesting potential that both the wavelength of excitation and the wavelength of detection can be varied, which may yield very specific responses from tissue. Due to recent advances in laser technology, the excitation wavelength can be tuned continuously over a very large range. The detection wavelength is typically varied using interference filters in front of the detector. This technique was first suggested by Kanstad and Nordal⁸³.

3.1.4 Piezoelectric detection

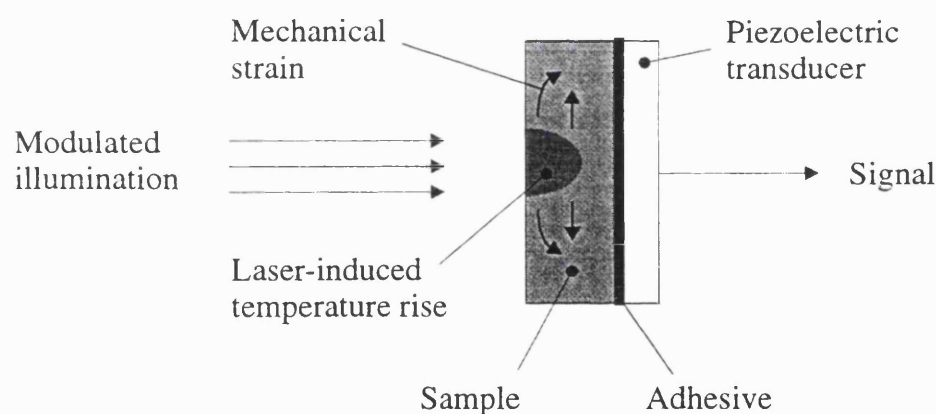


Figure 3.2 *Piezoelectric detection*

A piezoelectric transducer is used to detect the photothermally induced strain in the target material as shown in Figure 3.2. The transducer has to be attached to the target in order to be able to detect the mechanical strains. The strain in the sample, which is transmitted to the transducer, gives rise to a voltage. The required mechanical coupling of the transducer is the major limitation of the technique. It does, however, have the advantage of allowing measurements to be made at high frequencies (> 1 MHz)⁷⁶.

3.1.5 Fluorescence

Fluorescence of a ruby crystal has been used to measure the thermal properties of materials at high pressures⁸⁴. A small ruby sphere and a thin aluminium foil were placed at a measured separation inside a NaCl crystal. The foil was heated by a laser pulse, while the ruby crystal was illuminated using a continuous-wave laser in order to produce fluorescence. The heat produced in the film diffused through the ruby sphere and shifted the wavelengths of the fluorescence peaks, which was used to measure the temperature in the sphere. The thermal properties of NaCl were deduced from the time-course of the temperature change. The temperatures produced in the ruby ranged between 5 to 25 K above ambient temperatures. A similar device could perhaps be employed as a temperature transducer in an optical fibre sensor.

3.1.6 Interferometric techniques

The interferometric techniques discussed in this section refer to the interference of optical radiation as opposed to the interference of thermal waves, which has recently been used to increase the sensitivity of pyroelectric transducers⁷⁹. The phenomenon of interference of light reflected from the faces of thin transparent films and the effect of acoustically or thermally induced changes in the optical thickness of the film on the reflected intensity has been exploited for the detection of acoustic and thermal transients generated in the substrate material⁸⁵.

The change in the interference pattern formed by the reflections of a probe beam from a transparent plate sample following the absorption of pulsed optical excitation has been used as a photothermal interferometric detection technique for the characterisation of materials⁸⁶. The technique requires the sample under study to have very good surface quality and should ideally possess parallel boundaries, which presents a substantial limitation. The technique has the advantage that samples with thicknesses ranging from several micrometers to several centimeters can be investigated.

Interferometric detection of thermal changes in the optical thickness of thin dielectric films deposited on an optical fibre has been used to make fibre-optic thermal transducers, which have been applied to *in vitro* temperature measurements in the vitreous of the eye during laser irradiation⁸⁷. The concept of ultrasound sensing using thin polymer films⁸⁸ and its applicability to the detection of abnormalities in biological tissue has been explored. Interferometric temperature sensing using thin films and its implementation in the optical fibre sensor are described in more detail in chapter 5.

Other interferometric temperature sensors make use of the temperature dependence of high-birefringence fibres⁸⁹. A section of a birefringent fibre is the sensitive element, which is positioned between two spiral polarisation couplers. White light is launched into the first coupler which divides the light between the two polarisation modes, while the second coupler combines the modes again, which produces interference. A temperature change in the fibre produces a change in the optical path difference between the polarisation modes due to the temperature dependence of the birefringence and the length of the fibre. Interferometric techniques are also employed for the detection of optical beam deflection and for the measurement of the thermal displacement of the surface of a sample following pulsed heating. These techniques are reviewed in section 3.1.7 and 3.1.8, in which the technique of photothermal displacement is discussed.

3.1.7 Optical beam deflection

The spatial variation in the refractive index of a sample or a medium adjacent to a sample due to a temperature variation is used to deflect a laser beam as shown in Figure 3.3. If the deflection is monitored, the transient temperature in the sample can be recorded. The magnitude of deflection is dependent upon the material through which the probe beam is guided. Air produces a very low degree of deflection, while carbontetrachloride produces the highest deflection. A temperature sensitivity of 10^{-7} K can be achieved. Interferometric techniques have also been applied to the detection of optical beam deflection⁹⁰. The main drawback of such techniques is the non-linearity of the detected signal with regard to the excitation.

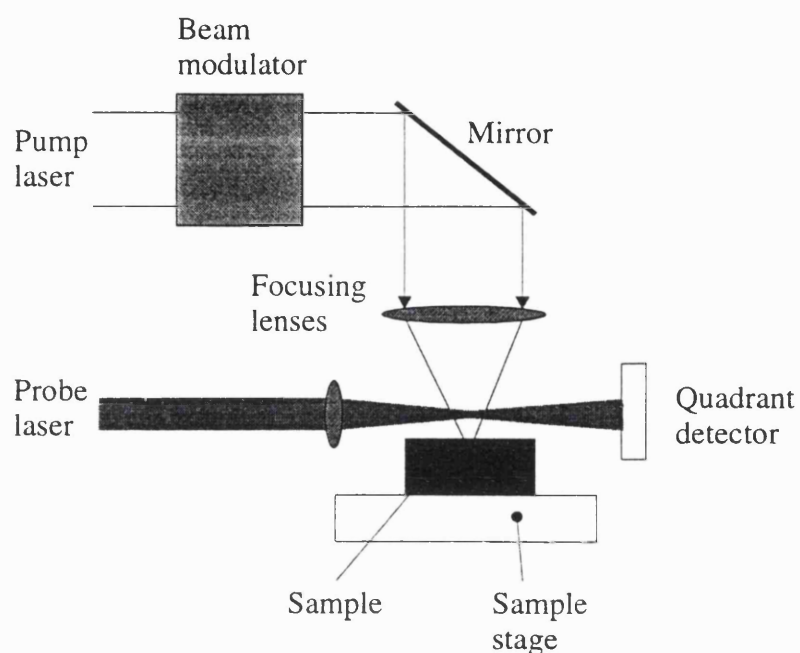


Figure 3.3 *Diagram of optical beam deflection technique.*

Optical beam deflection is typically used in studies on semiconductors and gases⁷⁶ and is not applicable to endoscopic photothermal measurements due to its size requirements and configuration.

3.1.8 Photothermal displacement

The modulated heating of a sample by an optical source produces modulated thermal expansion, which can be detected interferometrically or using a position sensor. Interferometric detection of photothermal displacement has been used to determine the absorption coefficient of the eye⁹¹. In order to achieve sufficient displacement in the sample, high laser pulse energies need to be applied. The requirement for large temperatures in the sample, the complex experimental set-up as well as its inherent susceptibility to displacement caused by environmental vibrations, photothermal

displacement can be regarded as unsuitable for non-destructive endoscopic measurements on tissue.

3.1.9 Modulated optical reflectance

Changes in the temperature of a material also produce a change in its reflectance caused by variations in the refractive index. The change in reflectance, R , is related to temperature, T , as follows:

$$\frac{\Delta R}{R_0} = \frac{1}{R_0} \frac{dR}{dT} \Delta T \quad (3.1)$$

where $R_0^{-1} dR/dT$ is the coefficient of thermal reflectance of the material, which ranges from 10^{-4} to 10^{-6} for most solids. Practical problems include the need for very accurate alignment of the probe and pump beams and loss of reflected power due to rough or uneven surfaces, which does not allow modulated optical reflectance to be applied to endoscopic measurements on tissue. A more detailed discussion of modulated optical reflectance can be found in Almond *et al*⁷⁶.

3.2 Photothermal spectroscopy on tissue

A large number of workers have applied photothermal radiometry and spectroscopy to measurements on tissue in order to investigate a variety of different problems. The interest of those studies was the use of photothermal radiometry as a technique to monitor the deposition of optical energy in tissue during clinical laser treatments. The dynamics of localised absorption of the therapeutic light by subsurface chromophores, such as haemoglobin or melanin, determine a successful outcome of the treatment. Photothermal radiometry has been applied in the planning of treatments by assessing the physical dimensions of chromophores⁹² and in the mapping of heat deposition in port-wine-stain lesions⁹³. Photothermal spectroscopy has also been applied to the investigation of skin hydration⁹⁴, the structural breakdown of sunscreens on skin⁹⁵ and to the measurement of the

thickness of the epidermis⁹⁶. Using emission spectroscopy, the group found that the presence of chemicals on the skin can be detected and their relative concentration gauged, and that chemically induced changes of skin properties can be monitored.

Since the optical fibre sensor is being developed for the *in vivo* measurement of tissue optical properties, the focus of this short review will be on the determination of optical coefficients of tissue using photothermal techniques. Long and Deutsch⁹⁷ performed measurements on *in vitro* human artery to obtain absorption coefficients. The study showed that the technique is sensitive to changes in the optical properties of tissue. The assessment of the accuracy of the method to determine absolute values of absorption coefficients was less valuable, however, since the experimentally determined values were compared to values taken from other publications. A rigorous assessment of the potential of photothermal radiometry for the determination of tissue optical properties was conducted by Prahl *et al*⁹⁸. Pulsed photothermal radiometry was used to determine optical coefficients of turbid gels from their response to a short laser pulse. Absorption and scattering coefficients were obtained with an accuracy of $\pm 10 - 15 \%$. The same technique has also been used for work described in this thesis, which is discussed in more detail in chapter 4. Vitkin *et al*⁹⁹ have used photothermal radiometry to investigate photon propagation in materials with layers of different optical coefficients. The temporal infrared response of layered samples was compared to one-dimensional analytical expressions of the time-dependent radiometric signal, which were obtained from expressions of the depth-dependent fluence distribution. This method could theoretically be applied to determine the optical properties of layered materials such as tissues.

Radiometric techniques were employed in most of the studies discussed in this section. The experimental set-up typically requires infrared optics, infrared detectors and a suitable source of optical excitation, such as lasers. The physical size of the experimental hardware prevents the use of these techniques for measurements inside the human body and most studies have therefore been restricted to regions of the human body which are easily accessible. An exception is the use of infrared transmitting fibres, which have been pioneered by Abraham Katzir.

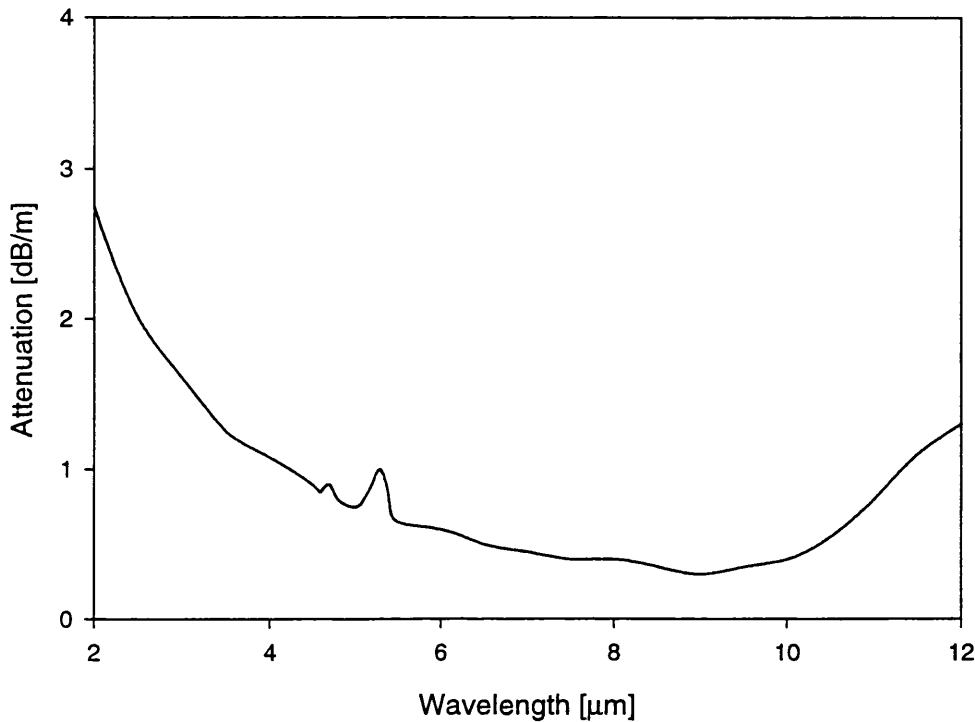


Figure 3.4 Attenuation spectrum of a typical silver halide optical fibre (data taken from Oxford Electronics Ltd., Oxford, U.K.).

Infrared-transmitting fibres have been successfully used for radiometric thermometry¹⁰⁰ and in monitoring tissue temperatures during tissue welding¹⁰¹. Infrared fibres, which are based on silver halide and have a typical transmission range of 2-12 μm , could be used for radiometric measurements during endoscopy. The losses of infrared light in the fibre due to absorption, however, are substantial. The coupling of infrared light into the fibre may also be poor, which would also reduce the sensitivity. Figure 3.4 shows a typical transmission spectrum of a commercially available infrared optical fibre. The manufacturer specified the attenuation of the fibre to be 0.5 – 1.5 dB m^{-1} at 10.6 μm . Given a detection bandwidth of infrared detectors ranging from 5 to 12 μm , the emission captured by a 2 m length fibre with an average attenuation of 0.5 dB m^{-1} would be attenuated by 8 %.

The optical fibre sensor may greatly reduce the practical problems of making photothermal measurements interstitially and during endoscopy. Since the sensing element

is a thin polymer film bonded to the end of an optical fibre, endoscopic and interstitial use is feasible. The main advantage of the optical fibre sensor over fibre-optic radiometric techniques is the potential of simultaneous photoacoustic and photothermal measurements, which may yield more diagnostic information.

3.2.1 Choice of excitation wavelength

The use of the optical fibre sensor for photothermal spectroscopy on tissue *in vivo* needs careful consideration as to which excitation wavelength is employed. In theory, a whole range of different wavelengths could be used to obtain the photothermal spectral response of tissue. Since the optical fibre sensor is being developed for the determination of optical coefficients of cancers, it may be advantageous to use a wavelength which is least affected by physiological changes in tissue, such as blood content, blood oxygenation, perfusion rate, hydration and so forth. For optimal photothermal detection, an excitation wavelength at which tissue has generally large absorption coefficients would be of benefit to produce strong signals. An excitation wavelength between 600 and 700 nm could exploit the absorption features of haemoglobin. As shown in section 1.2.2, however, the optical properties of *in vivo* tissue in the near-infrared wavelength region are strongly affected by variations in the concentration of chromophores such as haemoglobin. Variations in haemoglobin concentration with depth would produce problems in the interpretation of photoacoustic and photothermal signals since the spatial distribution of heat could not be accurately described. This would in turn lead to problems in the determination of accurate optical coefficients.

Operating the optical fibre sensor at wavelengths of high absorption would also impair its potential to probe sub-surface tissue with simultaneous detection of photoacoustic and photothermal responses. High penetration depths are required to generate acoustic transients below the tissue surface. The fundamental Nd:YAG emission at 1064 nm has a typical penetration depth of $1400 \mu\text{m}^{102}$ and would be a suitable excitation wavelength. Other suitable laser sources include diode lasers in the near-infrared which produce penetration depths around $1300 \mu\text{m}$ and the Ho:YAG laser ($\lambda = 2.1 \mu\text{m}$) in the

infrared with a typical penetration depth of 300 to 400 μm . Lasers such as the Er:YAG ($\lambda = 2.94 \mu\text{m}$), which emits light that is highly absorbed by water, would be very unsuitable since the light pulse may not pass through a polymer film of 12 μm thickness and would also penetrate the tissue to a depth of only about 4 μm .

In conclusion of this section, it can be stated that the optical fibre sensor may represent a significant contribution to photothermal techniques for the determination of tissue optical properties. Its significance to tissue diagnostics may be greatly improved by developing its ability to simultaneously detect photoacoustic and photothermal signals.

3.3 Photoacoustic spectroscopy

Although the photoacoustic potential of the optical fibre sensor is not investigated in this thesis, a brief summary of photoacoustic spectroscopy will be given for completeness.

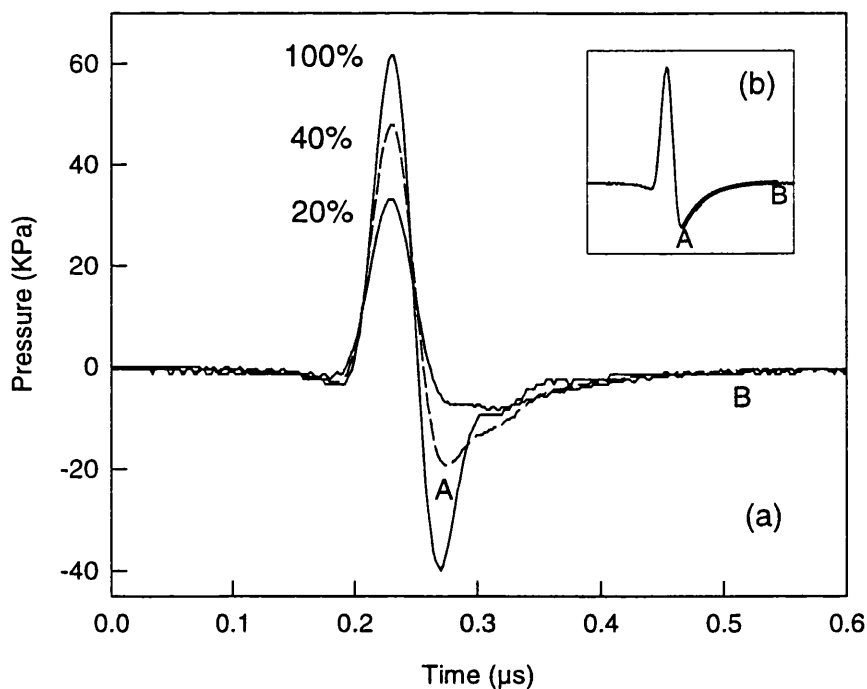


Figure 3.5 Typical photoacoustic signals generated in ink at various concentrations (a). Graph (b) illustrates how the absorption coefficient can be determined from the shape of the photoacoustic signal by fitting an exponential function between A and B.

Photoacoustic spectroscopy is based on measurements of thermoelastic waves, which are generated by the absorption of nanosecond laser pulses in a target material. Stress and thermal relaxation during the nanosecond laser pulse may be assumed to be negligible. The time-resolved detection can provide information on the optical, acoustic, and spatial properties of the medium. Both the amplitude and the time course of the stress wave can be analysed in order to obtain information about the sample under study. A thermoelastic wave, generated in an absorber, will propagate away from the irradiated volume. Provided a number of conditions for the source geometry, the boundary conditions and the detector location are met and provided there are no interfering reflections, its shape will be that of a bipolar wave with a leading compressive wave and a trailing tensile wave, as shown in Figure 3.5. The slope of the trailing wave (between A and B in Figure 3.5) is governed by the effective attenuation coefficient of an absorber. The absorption coefficient can therefore be determined from the temporal shape of the photoacoustic signal. The effective attenuation coefficients of turbid media can be determined in a similar fashion, as has been applied for measurements on tissue¹⁰³ and for characterising arterial tissue¹⁰⁴. Inhomogeneous and layered media can also be investigated using photoacoustic spectroscopy. The temporal photoacoustic response of layered materials, for example, reflects the distribution of the excitation light in the sample, revealing subsurface absorbing structures¹⁰⁵. Differences in the acoustic properties can also be detected by observing subsurface reflections of the thermoelastic waves. Photoacoustic tomography has recently become a subject of interest. A laser-induced stress transient is detected by a number of detectors. From the output of the detectors, images of the distribution of optical coefficients have been produced, showing regions of high absorption and scattering¹⁰⁶.

The optical fibre sensor has been developed as a photoacoustic sensor for the detection of differences in the properties of arterial tissue¹⁰⁷. Its photoacoustic performance has been well characterised^{108,109}, and its pressure sensing capabilities have been applied to measure pressures during lithotripsy¹¹⁰. The ability to simultaneously detect photoacoustic and photothermal signals is perhaps the most interesting aspect of the optical fibre sensor. Photothermal measurements will probe the surface of the tissue, while photoacoustic signals have the potential to reveal subsurface properties. A comparison of the diagnostic power of the photoacoustic and photothermal techniques is presented later on in this thesis.

3.4 Summary

In this chapter, the origins of optical absorption and scattering in tissue and models of light transport in tissue and their accuracy in describing the propagation of electromagnetic radiation have been discussed. Techniques for the measurement of optical properties have been reviewed by analysing their application to *in vivo* measurements inside the human body. Low coherence reflectometry, detection of coherent backscatter, spatially resolved reflectance spectroscopy and time-resolved and frequency-domain spectroscopy have been used for *in vivo* characterisation of tissue. A number of these techniques has been applied with varying success to measure tissue optical properties *in vivo* inside the human body. Spatially resolved reflectance spectroscopy has been shown to measure optical properties of turbid media with the highest accuracy. Endoscopic measurements of optical properties using this technique have shown large variations in the obtained coefficients. This is perhaps not surprising since the accuracy of spatially resolved measurements depends on the optimal spacing between the source and detector fibres. For tissue measurements in the near-infrared wavelength range, the optimal separation was of the order of 5 mm. The illuminated tissue volume is therefore relatively large and spatial variations in the optical properties may have contributed to the variations in the determined coefficients. The optical fibre sensor would obtain information on the optical properties from a relatively small volume from photothermal measurements. Deeper lying regions could be analysed using photoacoustic measurements. By making simultaneous photothermal and photoacoustic measurements, information could be obtained which would provide a unique way of detecting subsurface absorbing regions. The photothermal signal would provide optical coefficients from a very shallow depth (approximately 100 μm). The measured photoacoustic signal may be very different from a theoretical photoacoustic plot calculated using the photothermally obtained optical coefficients. This may provide a method of detecting subsurface optical properties, which would not be accessible through other optical techniques. The optical fibre sensor could also be applied to measurements deep inside the body during endoscopy, while the small physical size of the sensor may also allow interstitial measurements.

The review of the optical properties of cancers and normal tissue has shown a significant difference in the scattering coefficient between the two types of tissue. The larger scattering coefficient of carcinoma results in a reduced optical penetration depth, which would result in a faster decay of the photothermal signal. The thermal conductivity of most types of carcinoma, as discussed in section 2.5, have been shown to be greater than that of the normal surrounding tissue, which would also result in a faster decay of the photothermal signal. The combination of the differences on the optical and thermal properties may therefore produce marked differences in the time course of photothermal signals detected in normal and tumour tissue, which could be used to diagnose cancer.

As a background to the development of the optical fibre sensor for photothermal measurements, the thermal properties of tissue and theoretical models of heat transport have been reviewed. The finite element method has been chosen as a tool for the interpretation of photothermal signals detected using the optical fibre sensor due to its flexibility in handling complex geometries.

A review of photothermal techniques has also been given. Photothermal radiometry, as perhaps the most established technique, has been used for work described in this thesis and is compared against the performance of the optical fibre sensor. Pyroelectric detectors can be seen as an alternative to the optical fibre sensor due to their ability to detect stress (in which case they act as a piezoelectric transducer) as well as temperature over a broad bandwidth. This makes pyroelectric transducers suitable for simultaneous photoacoustic and photothermal measurements. There are, however, problems in the endoscopic use of such detectors at the tip of an optical fibre. The pyroelectric transducer requires electrodes on each side of the sensing material, which may obstruct the transmission of the excitation laser pulse. The transducer at the tip of a fibre would also need to be connected by wiring, which affects the frequency response of the system by essentially producing a low-pass filter. These problems would need to be resolved if pyroelectric transducers could be used at the tip of an optical fibre.

A brief overview of photoacoustic methods has also been given. The optical fibre sensor can be used for the simultaneous detection of photoacoustic and photothermal signals. The potential of simultaneous measurements with the sensor will be discussed in this thesis.

In the following chapters, the optical fibre sensor and its use for the determination of optical coefficients from photothermal responses of tissue will be presented. The output of the optical fibre sensor as a Fabry-Perot interferometer is described in chapter 5. The numerical model of the sensor will be introduced in chapter 6, while the experimental results and their analysis using the numerical model and model-based parameter estimation are presented in chapter 7. In chapter 8, the optical fibre sensor is compared to other photothermal detectors and a comparison of the sensor with pulsed photothermal radiometry addresses the sensitivity of the two methods to the optical coefficients of tissue. Pulsed photothermal radiometry, as a method of probing tissue optical properties, is perhaps most closely related to the proposed use of the optical fibre sensor and hence provides a technique against which the performance of the sensor can be compared. Pulsed photothermal radiometry was used to determine the optical coefficients of turbid gels. The theoretical and experimental aspects of this method, which were developed by Scott Prahl, are presented in the next chapter.

4 DETERMINATION OF OPTICAL COEFFICIENTS USING PULSED PHOTOTHERMAL RADIOMETRY

In the preceding chapter, various photothermal techniques for the non-destructive evaluation of materials have been reviewed with the aim of establishing which techniques are applicable for tissue diagnostics. The main objective of the work presented in this thesis is the development of the optical fibre sensor for the photothermal determination of the optical coefficients of tissue. Pulsed photothermal radiometry will be discussed in this chapter as a closely related photothermal technique with which optical properties of targets, including tissue can be extracted from the detected signal. The theoretical concepts, practical requirements and methods are explained and measurements on purely absorbing as well as turbid gels and their analysis are presented.

4.1 Introduction

Pulsed photothermal radiometry (PPTR) relies on the detection of black-body infrared radiation emitted from the surface of a target in which the temperature distribution has been disturbed by, for example, the application of a laser pulse. A temperature rise of only a few degrees above ambient levels is typically needed for radiometric detection, which for most materials allows measurements to be made without damaging or changing the sample under study. By analysing the heating and cooling of the target, information on the optical or thermal properties can be obtained. Pulsed photothermal radiometry has also been used for depth analysis and non-destructive evaluation of subsurface thermal properties^{111,112} and for measurements of changes in the thickness and thermal coefficient of a particular layer in laminated materials¹¹³. The depth distribution of optical coefficients has been the subject of a number of investigations in the biomedical field that involved the use of PPTR. The aims of those studies were, for example, to predict laser-induced subsurface temperature distributions¹¹⁴, to correlate the photothermal signal with the subsurface distribution of optical

parameters¹¹⁵ and to determine the depth of chromophores in the human skin¹¹⁶. The results showed that PPTR can be used to obtain information on the spatial distribution of optical and thermal coefficients, provided certain limitations of this technique^{117,118} are taken into account. PPTR has also been applied as a method to specify the initial heat deposition by a laser pulse in complex tissue such as port-wine-stain lesions¹¹⁹. PPTR could thereby be used to determine the depth and distribution of the abnormal vessels constituting the port-wine-stains, and so help in the planning of their treatment.

In this chapter, an analytic theory¹²⁰ for determining the absorption and scattering coefficients of aqueous gels from the temporal shape of the photothermal signal is employed. For the analysis of the signals it was assumed that the thermal and optical properties were homogeneously distributed in the target. Water was used as base material since its thermal properties are well known and are very close to those of soft tissue¹²¹. This chapter closely follows the work of Prahl *et al* (1992).

4.2 Pulsed Photothermal Radiometry – Theory

The photothermal signal results from a sudden temperature rise in the target, which is due to the absorption of a pulse of optical energy. The spatial distribution of temperature in the target is determined by its optical and thermal properties, its structure, as well as by the illumination geometry. In this section, an analytic theory for the interpretation of photothermal signals will be described. The absorbed laser energy distribution is used as a heat source, and an analytic expression for the heat conduction is obtained. For this, a number of simplifying assumptions are made. The target is assumed to have uniform optical and thermal characteristics. All deposited optical energy is converted to heat. In practice, there are also photomechanical and photochemical processes to which energy may get lost. These processes would need to be taken account of in the energy balance, should they prove significant. For the work presented in this chapter, these processes have been assumed to be negligible. The light used for the excitation of the photothermal signal is normally incident on the target and the pulse length is

short compared to the thermal relaxation time of the target. The material is considered to be semi-infinite and therefore optically and thermally isolated.

Based on these assumptions, an analytic theory can be derived based on the heat conduction equation for the one-dimensional case¹³³

$$\frac{\partial^2 T}{\partial z^2} = \frac{1}{\alpha} \frac{\partial T}{\partial t} \quad (4.1)$$

where T is the temperature, α is the thermal diffusivity, t is time and z is the spatial co-ordinate which is zero at the surface and increases into the material. The thermal diffusivity is given as

$$\alpha = \frac{k}{\rho c} \quad (4.2)$$

where k is the thermal conductivity, c is the specific heat and ρ is the density. Under the assumption of negligible radial heat diffusion, Green's functions and the method of images can be employed to describe the temperature in the material after the application of a pulse of optical energy¹²².

$$T(z,t) = \frac{1}{\sqrt{4\pi\alpha t}} \int_0^\infty T(z',0) \left[\exp\left(-\frac{(z-z')^2}{4\alpha t}\right) + \exp\left(-\frac{(z+z')^2}{4\alpha t}\right) \right] dz' \quad (4.3)$$

$T(z', 0)$ describes the initial temperature distribution in the sample, which depends on the optical and thermal properties of the material as well as the incident fluence, and z' is the integration variable that covers the spatial extent of the distributed heat source. The total amount of infrared radiation M_e of all wavelengths emitted by a black body is related to its temperature T according to Stefan-Boltzmann law (equation (4.4)), where σ is Stefan-Boltzmann constant and T_0 is the unperturbed temperature in the material.

$$M_e = \sigma(T^4 - T_0^4) \quad (4.4)$$

The signal measured using PPTR can be obtained by integrating the Stefan-Boltzmann law over all depths and by weighting with the infrared absorption coefficient of the material,

$$S(t) = \eta a_D \varepsilon \sigma \mu_{IR} \int_0^\infty [T(z,t)^4 - T_0^4] \exp(-\mu_{IR} z) dz \quad (4.5)$$

where η is the detector efficiency, a_D is the detector area, ε is the emissivity of the sample and μ_{IR} is the average infrared absorption coefficient of the material over the wavelength range

detected. The infrared absorption coefficient determines the depth from which contributions to the measured signal are detected. A small value of μ_{IR} results in large detection depth but also reduced signal amplitude. In the limit of $\mu_{\text{IR}} = 0$ the PPTR signal disappears completely since neither absorption nor emission of infrared light is possible. For a typical value of $\mu_{\text{IR}} = 120 \text{ mm}^{-1}$ in the 7-12 μm detection range, the μ_{IR}^{-1} detection depth is 8.3 μm .

For small temperature rises, the bracketed quantity in $S(t)$ can be expanded using the binomial theorem and terms of quadratic order or lower can be neglected. Equation (4.5) can be rewritten as

$$S(t) = 4\eta a_{\text{D}} \varepsilon \sigma T_0^3 \mu_{\text{IR}} \int_0^{\infty} [T(z,t) - T_0] \exp(-\mu_{\text{IR}} z) dz \quad (4.6)$$

4.2.1 Non-scattering homogeneous absorber

The light distribution in a non-scattering homogeneous absorber is described by the Lambert-Bouguer law. Under normal incidence,

$$E(z) = E_{\text{inc}} \exp(-\mu_a z) \quad (4.7)$$

where the energy fluence in the material, $E(z)$, decays exponentially with depth, starting from the incident light fluence at the surface E_{inc} . The absorption coefficient μ_a , at the incident wavelength determines the rate of the decay with increasing depth. Assuming that all the light is converted to heat, then the initial temperature in the material is

$$T(z,0) = \frac{E_{\text{inc}} \mu_a}{\rho c} \exp(-\mu_a z) \quad (4.8)$$

where ρ is the density and c is the specific heat of the material. Substituting the initial temperature distribution into equation (4.3), and using the resulting temperature field to solve equation (4.6) gives

$$S(t) = \frac{4\eta a_{\text{D}} \varepsilon \sigma T_0^3 E_{\text{inc}}}{\rho c} \frac{\mu_{\text{IR}} \mu_a}{\mu_{\text{IR}}^2 - \mu_a^2} [\mu_{\text{IR}} f(\mu_a^2 \alpha t) - \mu_a f(\mu_{\text{IR}}^2 \alpha t)] \quad (4.9)$$

where $f(x) = \exp(x) \operatorname{erfc}(x^{1/2})$, and $\operatorname{erfc}(x)$ is the complimentary error function¹²² of x . The signal calculated with equation (4.9) decays monotonically with time. The rate of decay depends on the optical and thermal parameters that are present in the material. The infrared absorption coefficient determines the amount of infrared emission from within the sample and is therefore important for the calculation of the surface temperature.

4.2.2 Homogenous scattering and absorbing media

The diffusion approximation of the radiative transport equation is used to describe the initial temperature distribution in a turbid medium. Although the diffusion approximation takes account of important aspects of light propagation in tissue, such as absorption, anisotropic scattering and mismatched boundaries, it has been shown to be inaccurate in the estimation of fluence rates in turbid media close to the source where the incident light has not become diffuse¹²³. A distance of several mean free paths is typically required for the light to lose directionality. It is therefore slightly surprising that Prahl *et al* have applied the diffusion approximation to describe the fluence distribution in the target since PPTR only detects infrared emissions from the first few microns at the surface of the sample. The diffusion approximation, however, has the major advantage of being amenable to analytic manipulation, which enables the derivation of an analytic expression for photothermal signals generated in turbid media. Prahl argues that while the diffusion approximation is accepted as accurate when scattering dominates absorption, it is also accurate when absorption dominates scattering since the diffusion solution reduces to the Lambert-Bouguer law. Prahl assumed the diffusion approximation to hold for values of the scattering coefficient that are comparable to the absorption coefficient. Its appropriateness was tested experimentally by the author of this thesis and the results are discussed in the following sections.

The work presented in this chapter aimed to establish the accuracy with which optical coefficients can be determined using PPTR and to compare its performance to the optical fibre sensor. The accuracy of the diffusion approximation in describing fluence distributions in PPTR was also of interest. The relative simplicity of applying an analytical theory, in comparison to the computational effort involved with numerical models such as

the Monte Carlo method, would be advantageous for the analysis of photothermal signals detected using the optical fibre sensor. The appropriateness of the diffusion approximation for the interpretation of radiometric measurements and measurements made using the optical fibre sensor is discussed at the end of this chapter.

The solution for a one-dimensional, uniform, collimated beam incident on a semi-infinite slab with mismatched boundaries is given as¹²⁴

$$E(z) = A \exp(-\mu_{\text{eff}} z) + B \exp(-\mu_{\text{tr}} z) \quad (4.10)$$

with

$$A = \frac{E_{\text{inc}} (9 + 6k) \mu_s' D}{(1 + k \sqrt{4\mu_a D})(1 - 9\mu_a D)} \quad B = \frac{-2E_{\text{inc}}}{(1 - 9\mu_a D)}$$

where $\mu_s' = \mu_s (1 - g)$ is the reduced scattering coefficient, g the average cosine of the scattering angle, $\mu_{\text{tr}} = \mu_a + \mu_s'$ the transport coefficient, $k = (1 + r_d)/(1 - r_d)$ is a constant which depends on the internal diffuse reflection coefficient r_d of the target, $D = (3\mu_{\text{tr}})^{-1}$ is the optical diffusion constant, and $\mu_{\text{eff}} = (3\mu_{\text{tr}}\mu_a)^{1/2}$ is the effective attenuation coefficient.

The photothermal signal for an initial temperature distribution as given in equation (4.10) is

$$S(t) = C \frac{\mu_a}{\rho c} [A f(\mu_{\text{eff}}^2 \alpha t) + B f(\mu_{\text{tr}}^2 \alpha t)] \quad \mu_{\text{IR}} \rightarrow \infty \quad (4.11)$$

where $C = 4 \eta \sigma \varepsilon a_D T_0^3$ and the infrared absorption coefficient is assumed to be much larger than the transport and effective attenuation coefficient. When this assumption is invalid the photothermal signal is given by

$$S(t) = C \frac{\mu_a \mu_{\text{IR}}}{\rho c} \left(\frac{A}{\mu_{\text{IR}}^2 - \mu_{\text{eff}}^2} [\mu_{\text{IR}} f(\mu_{\text{eff}}^2 \alpha t) + \mu_{\text{eff}} f(\mu_{\text{IR}}^2 \alpha t)] + \frac{B}{\mu_{\text{IR}}^2 - \mu_{\text{tr}}^2} [\mu_{\text{IR}} f(\mu_{\text{tr}}^2 \alpha t) + \mu_{\text{tr}} f(\mu_{\text{IR}}^2 \alpha t)] \right) \quad (4.12)$$

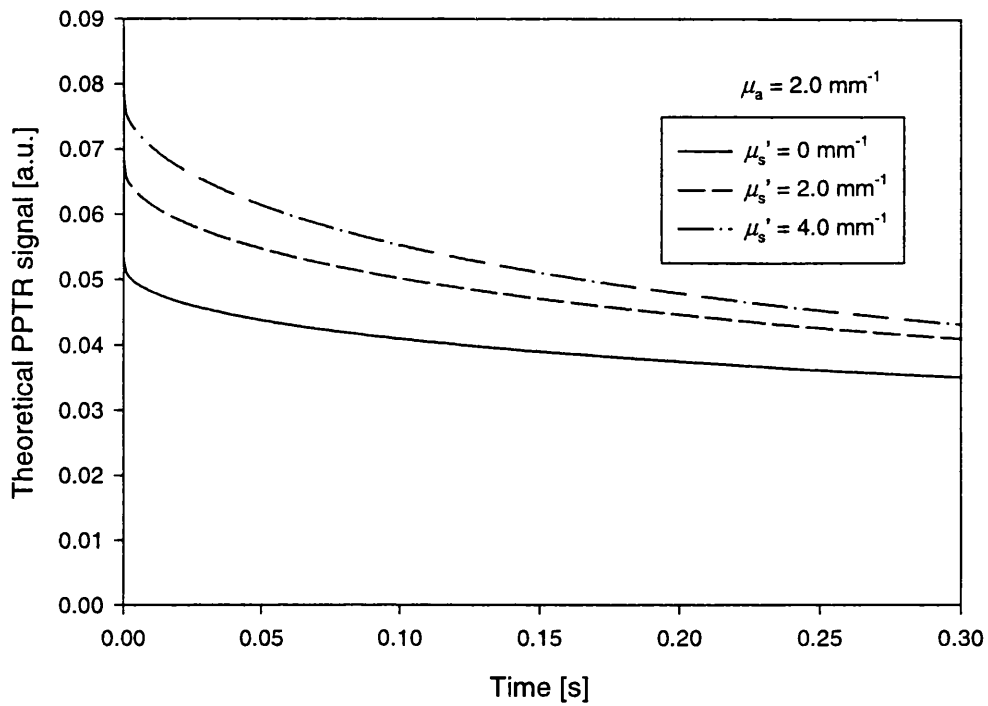


Figure 4.1 Theoretical PPTR responses showing the effect of scattering on the decay of the signal.

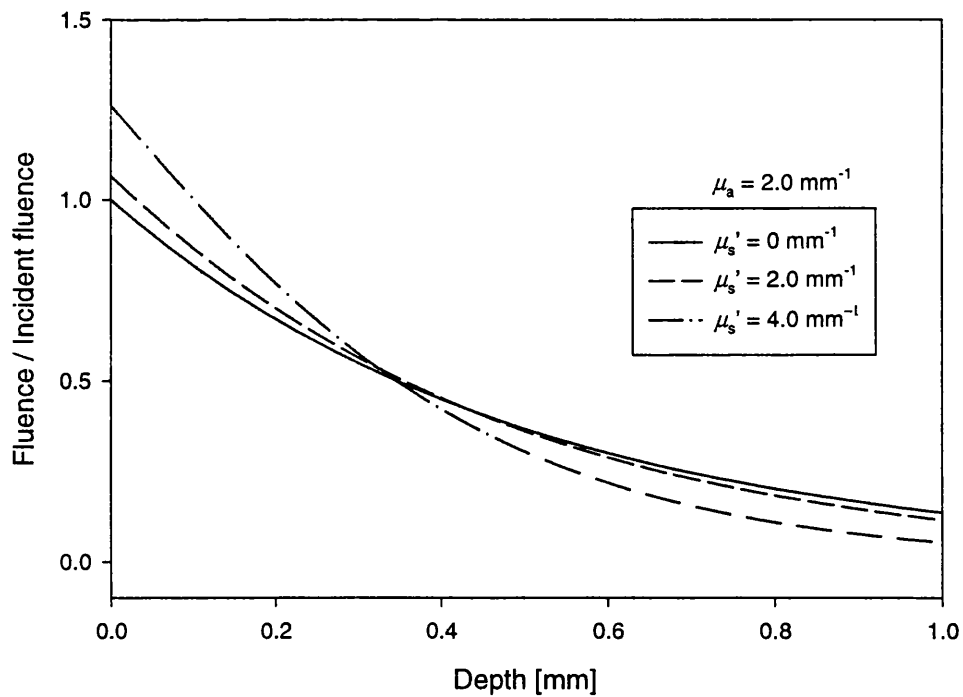


Figure 4.2 Theoretical fluence profiles for different reduced scattering coefficients obtained using equation (4.10).

Theoretical signal profiles are shown in Figure 4.1 to demonstrate the effect of scattering on the PPTR signal. The corresponding fluence profiles are shown in Figure 4.2. The signals and fluence profiles were calculated for a fixed absorption coefficient ($\mu_a = 2.0 \text{ mm}^{-1}$) and scattering coefficients ranging from 0 to 4.0 mm^{-1} . As the scattering increases, the fluence near the surface as well as the initial temperature increases.

4.3 Pulsed Photothermal Radiometry - Measurement and analysis

4.3.1 Set-up and methods

Homogeneously absorbing gels were made by mixing aqueous solutions of gelatine with different concentrations of a near-infrared molecular absorber (Zeneca, S109564). The absorption coefficients of non-scattering gels were determined by measuring the transmittance through a glass cuvette at 1064 nm, the wavelength used for the excitation of the photothermal signal. The absorption coefficients in the gels ranged from 2.0 mm^{-1} to 6.0 mm^{-1} . The values of μ_a were deliberately chosen to be higher than those found in tissue at 1064 nm. High absorption coefficients provided strong infrared emissions and consequently a good signal to noise ratio.

Turbid gels were made by mixing absorbing gels with different amounts of polystyrene microspheres. The absorption coefficient of the turbid gels was held constant at 2.7 mm^{-1} . The reduced scattering coefficients ranged from 1.1 mm^{-1} to 4.3 mm^{-1} at 1064 nm and were calculated using Mie Theory¹²⁵, incorporating information on the refractive index and the size distribution of the particles. The refractive index of the gel was taken to be equal to that of water ($n = 1.33$). The liquid gels were poured into Petri dishes to solidify. The optical coefficients of the turbid gels are not typical for those found in tissue at 1064 nm. The absorption coefficient in particular is higher than its average tissue equivalent. The turbid gels were not intended to represent tissue. They were instead used to establish whether the diffusion approximation is adequate in describing photothermal signals detected on targets where the scattering coefficient is similar to the absorption coefficient. Since diffusion theory

requires (a) $\mu_a \ll \mu_s (1 - g)$ and (b) the light to be totally diffuse, combinations of optical coefficients such as those chosen for the turbid gels provide a test of the validity of the diffusion approximation for the interpretation of photothermal measurements for the case of $\mu_a \sim \mu_s'$.

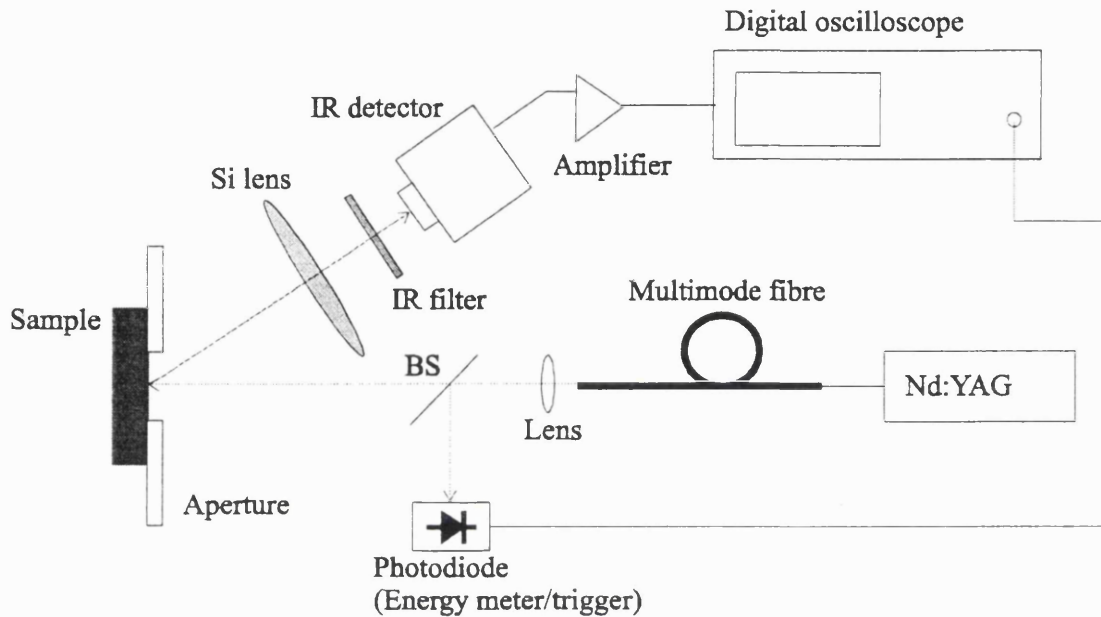


Figure 4.3 Experimental set-up for measurements using pulsed photothermal radiometry.

Figure 4.3 shows the experimental set-up. The gel samples were placed behind a metal aperture of 20 mm diameter. A pulsed fixed-Q Nd:YAG laser (InnoLas, Rugby, U.K.) emitted 200 μs pulses at 1064 nm. The pulse length was short compared to the time scale of photothermal detection and instantaneous heating of the samples was assumed. The output of the laser was coupled into a 1 mm multimode fibre, which by the use of mode scrambling, homogenised the beam. The light exiting the fibre was collimated and imaged onto the sample at normal incidence using a 5x microscope objective. This produced an illuminated area of approximately 6 mm in diameter with a nearly uniform irradiance profile ($\pm 10\%$). The fluence incident on the sample was 700 mJ/cm^2 . The infrared radiation emitted from the sample after the arrival of a laser pulse was detected using a photoconductive liquid nitrogen cooled HgCdTe detector (Fermionics, Simi Valley, California, U.S.A.) positioned at an angle of 15°

from the normal, which had a bandwidth of 10 kHz. The active area of the detector was 1 mm² and was positioned at the focal plane of a silicon lens. The lens was used in a 1:1 conjugate ratio to provide a 1 mm² area of detection in the centre of the area of photothermal excitation. A band pass filter (7 - 11 μm) limited the detected infrared bandwidth to a region in the water absorption spectrum that has a near constant μ_R . The output of the detector was monitored after amplification using a digital oscilloscope. For the measurement of the pulse energy, a fraction of the incident light was imaged onto a photodiode using a cover slip as a beam splitter. The photothermal response of the gels to a single pulse was measured.

4.3.2 Performance of the photoconductive infrared detector

In this section, the performance of the photoconductive infrared detector in terms of linearity, sensitivity, noise and response time is assessed. The results of this evaluation will be compared to the performance of the optical fibre sensor in chapter 8.

4.3.2.1 Linearity

The average linearity L_R as a figure-of-merit can be expressed as percent deviation from a straight line¹²⁶ using

$$L_R [\%] = \frac{100}{n} \sum_{i=0}^n \frac{|X_i - sT_i - b|}{X_i} \quad (4.13)$$

where X_i is the output of the detector, T_i is the temperature in the sample and n is the number of data points. $X_i = sT_i + b$ is the linear regression through the data.

To measure the linearity of the radiometric detector, a black body was made from a block of graphite, as shown in Figure 4.4. Graphite has an emissivity of approximately 0.90 – 0.93 and a reasonably high thermal conductivity (75 – 195 W m⁻¹ K⁻¹)¹²⁷ and can therefore be used as a material for an ‘ideal black-body’. The bottom of a hole (∅ 1 cm, depth 2 cm) drilled into the graphite rod was placed in the focus of an off-axis ellipsoidal reflector. The radiometric detector was placed in the other focus.

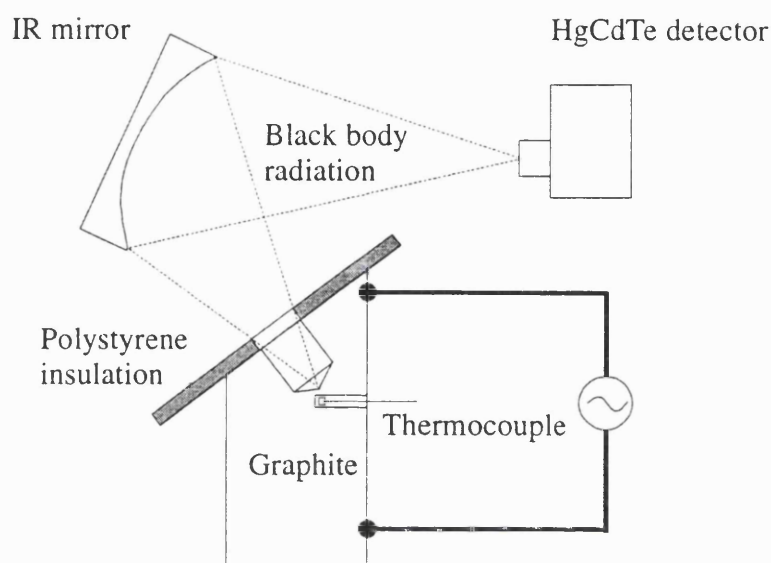


Figure 4.4 *Experimental set-up for measuring the linearity of the radiometric detector using a black-body.*

An insulating cover of polystyrene sheets was attached to the remaining surfaces to prevent infrared emission from areas other than the opening of the drilled hole. A thermocouple was inserted into a second hole, which ended close to the emitting volume to measure the core temperature of the graphite. The accuracy of the thermocouple set-up (RS 219-4315, Digitron) was ± 0.1 °C. The temperature of the graphite rod was controlled by varying the electrical current flowing through the material. The linearity of the radiometric detector was calculated to be $L_R = 1.0\%$ over a temperature range of 25 K. Although the radiometric detector has shown a linear relationship with the blackbody temperature, it has to be borne in mind that the amount of emitted infrared radiation is not linear with temperature. Figure 4.5 shows the output of the radiometric detector over a temperature range of 25 to 50 °C together with the radiant excitation of a perfect blackbody. The excitation displays non-linear behaviour, which can be explained with the shift of the maximum excitation towards shorter infrared wavelengths according to Wien's displacement law. For a detection range of 6.9 to 11.5 μm , shorter wavelengths therefore

contribute more to the photothermal signal with increasing temperature than longer wavelengths.

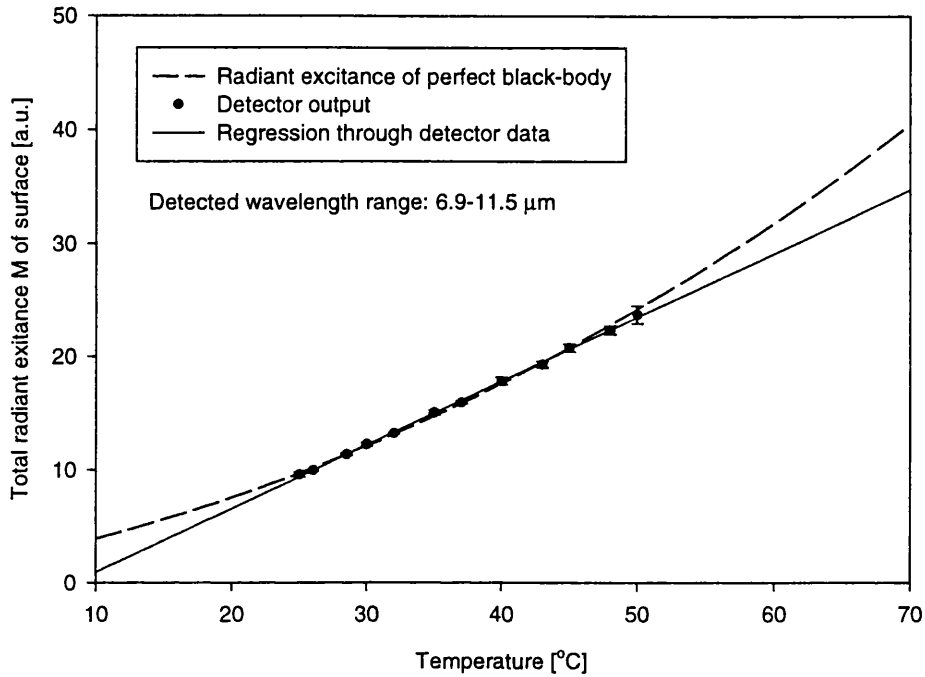


Figure 4.5 Output of the HgCdTe detector with increasing temperature together with the linear regression in comparison to the radiant exitance of a blackbody.

The non-linearity produced by the shift in the excitation peak is 3.5%/10K expressed as the deviation from a straight line. For temperature increases of 10-15K, the non-linearity of the detected emission is small and can therefore be approximated by the linear regression shown in Figure 4.5.

4.3.2.2 Sensitivity

The dc thermal sensitivity was obtained from the linearity measurements. The sensitivity of the radiometric detector configured with a wideband (100 MHz) amplifier was measured 136 mV °C⁻¹.

The sensitivity of a detector expressed in terms of mV K^{-1} is not very useful since the sensitivity depends on a variety of factors, such as the experimental set-up. It is therefore more useful to estimate the thermal noise floor from the sensitivity and the system noise characteristics.

4.3.2.3 Noise

The thermal noise floor of the radiometric detector was estimated from the dc sensitivity and the unaveraged random noise of 5 mV as approximately 40 mK. This figure compares favourably with values stated in published literature^{128,129}. The thermal noise floor could be improved by using a bandwidth-limited amplifier, suitable low pass filters and signal averaging. The amplifier of the current PPTR set-up was designed for applications up to 100 MHz. For photothermal radiometry a bandwidth of less than 1 MHz would be sufficient to capture the rise times of a few μs , while the amplification of higher frequencies increases the noise on the signal. It has been shown that bandwidth limitation and the optimisation of radiometric detector-amplifier combinations can produce a thermal noise floor of less than 1 mK¹³⁰.

4.3.2.4 Response time

The transient response of a temperature transducer to a sudden rise in temperature can be described with an exponential approximation¹³¹ given in equation (4.14)

$$T(t) = T_f + (T_0 - T_f) \exp(-t / \tau) \quad (4.14)$$

where T_0 and T_f are the initial and final temperature, respectively. The time constant of the transducer is given as τ . It describes the time it takes the output of the transducer to reach 63.2 % of the final value after an instantaneous temperature rise.

The response time of the radiometric detector was determined from the rise time of a photothermal signal. The response time of the PPTR detector and electronic circuits was

measured to be 240 μs , which is roughly the length of the laser pulse. The response time measurement was therefore limited by the pulse length of the laser. The HgCdTe detector, as a photonic detector, has a much shorter response time of approximately 0.5 μs , which can be estimated from the bandwidth of 2 MHz (manufacturer's data).

4.3.2.5 Specificity

Specificity is a measure of the relative sensitivity of a detector to the desired physical quantity compared to other influences, such as vibration, humidity etc. A possible source of interference is usually electronic noise from other devices, which can be removed through shielding. The stability of the optical fibre sensor is predominately affected by vibrations. Shaking of the optical fibre produces significant fluctuations in the detected intensity, which may be due to bending losses in the fibre. For the measurements presented in this thesis, it was possible to limit the effects of vibrations by fastening the fibre to the optical table.

4.3.3 Non-scattering absorbers

To determine the absorption coefficient from the temporal shape of the photothermal signal, two different approaches are suggested by Prahl. The first method relies upon normalisation of the signal to the peak height. Normalising the signal creates an expression independent of the incident fluence and calibration factors. The only unknown parameter is the absorption coefficient, which can be calculated for any time t , provided the constants for the infrared absorption coefficient and the thermal diffusivity of water are known.

The normalisation method, however, relies on accurate measurements of the early part of the signal. Any noise or signal variation at early times would introduce an error in the estimation of the peak amplitude. To avoid this, a method based on a non-linear two-parameter fitting algorithm is employed. The two-parameter fit is also used to obtain the system calibration constant, which can then be used in the analysis of signals detected in

scattering gels. Equation (4.9) is modified to illustrate that the photothermal signal depends on a scaling multiplier K and the absorption coefficient μ_a . The values for the thermal diffusivity $\alpha = 0.144 \text{ mm}^2 \text{ s}^{-1}$ and infrared absorption coefficient $\mu_{\text{IR}} = 120 \text{ mm}^{-1}$ are held constant.

$$S(t) = K \frac{\mu_{\text{IR}} \mu_a}{\mu_{\text{IR}}^2 - \mu_a^2} [\mu_{\text{IR}} f(\mu_a^2 \alpha t) - \mu_a f(\mu_{\text{IR}}^2 \alpha t)] \quad (4.15)$$

The scaling multiplier $K = 4\eta \sigma \epsilon a_D T_0^3 E_{\text{inc}} / \rho c$ represents the system calibration constant $4\eta \sigma \epsilon a_D T_0^3$ which is scaled by the initial temperature rise $E_{\text{inc}} \mu_a / \rho c$. The absorption coefficient is determined by varying both K and μ_a until the theoretical signal converges with the detected photothermal signal. A computer program was used for the non-linear two parameter fit according to the Levenberg-Marquardt method using available routines¹³². The program calculated the residual for a parameter pair (K, μ_a) between the theoretical signal $S(t)$ and the measured signal. A residual is defined as the sum of the squares of the differences between the calculated and the measured signal. The minimum of the residual represents the best fit to the data and determines a pair (K, μ_a) . The absorption coefficient is therefore uniquely determined since K only reflects the amplitude of the signal. A time interval of the photothermal signal from 5 - 160 ms was used for the fit. Later times were discarded since they are dominated by thermal diffusivity and contain relatively little optical information¹³³. The initial temperature gradient, which is determined by the optical properties of the target, changes at later times into a relatively flat temperature profile, which diffuses deeper into the material. The decay of the photothermal signal is then characterised by thermal coefficients. The convergence criterion for an acceptable fit was a change in residuals of less than 0.0002.

Figure 4.6 shows the typical photothermal response of a non-scattering absorbing gel together with the best fit to the measurement. The absorption coefficient of the gel was 5.4 mm^{-1} . The absorption coefficient obtained by fitting equation (4.15) to the signal was 5.8 mm^{-1} . Similar results were obtained for a range of different absorption coefficients. The 'true' μ_a and the fitted values and their standard deviations were obtained from four repeated measurements on different parts of the gels and are listed in Table 4.1.

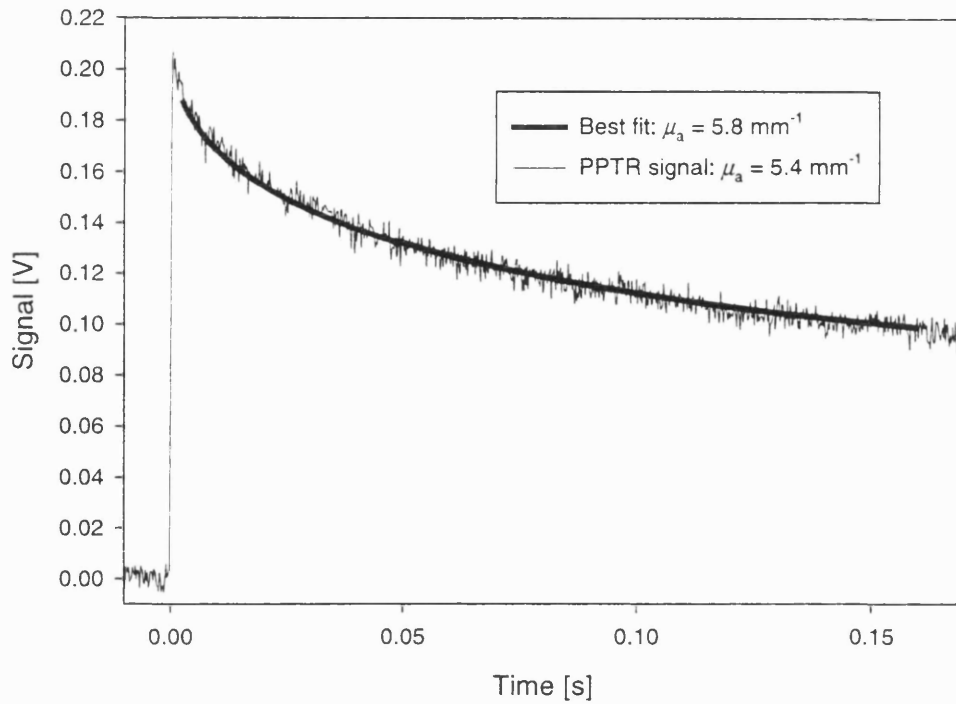


Figure 4.6 Typical PPTR signal detected on a purely absorbing gel together with the best fit to the data.

<i>Known μ_a [mm^{-1}]</i>	<i>μ_a [mm^{-1}] Two parameter fit</i>
5.42	5.40 ± 0.45
4.39	4.36 ± 0.18
3.33	3.45 ± 0.16
2.70	2.90 ± 0.51
2.15	2.10 ± 0.42
1.31	1.37 ± 0.27

Table 4.1 Comparison of the ‘true’ absorption coefficient to μ_a (\pm SD) determined from photothermal measurements. The standard deviations were calculated using the fitted absorption coefficients obtained from four measurements.

The error in the determined values of μ_a is of the order $\pm 10\%$ for gels with high absorption. Standard deviations in the determined values of $\pm 20\%$ have been produced by gels of low

absorption coefficient. The large error could be explained by the increased penetration depth of the excitation light, which produced a relatively flat temperature profile with increasing depth and therefore a less pronounced change in the shape of the photothermal signal. This, together with a reduced signal to noise ratio, results in a wider range of absorption coefficients that produce an adequate fit. This will be discussed further in section 4.4.

A value for K , scaled to the incident fluence, was obtained from the measurements on non-scattering absorbers. K represents a system calibration constant, which will be used in the analysis of signals measured on turbid gels. The variation in K/E_{inc} for the values listed in Table 4.1 was $\pm 5\%$.

4.3.4 Absorbing and scattering medium

From equation (4.12), it can be seen that the theoretical PPTR signal depends on K , μ_R , α , μ_s' and μ_a . Since it is assumed that α and μ_R are constant, the number of variables is reduced to three. A three parameter fitting routine could be employed to fit equation (4.12) to a signal from a turbid gel. It has been shown¹²⁰, however, that such treatment does not yield a unique triplet (K , μ_s' , μ_a). Figure 4.7 below depicts two theoretical PPTR signals, which were obtained by using different optical properties while leaving the amplitude of the signals unrestrained. The temporal shape of the signal alone is therefore not sufficient to determine all three parameters. To reduce the number of variables, the system calibration constant, which was obtained from measurements on homogeneous absorbers, was assumed to be a fixed parameter. This reduced the variables in the fitting program to the absorption and reduced scattering coefficient, which allowed the optical properties to be determined from the photothermal signal. Figure 4.8 below shows the photothermal response of a turbid gel and the result of the best fit to the experimental data. The optical coefficients and their standard deviation were obtained from four repeated measurements on different parts of the gels are shown in Table 4.2. The 'known' absorption coefficients of the gels were determined from measurements of their transmittance before the scatterers were added. The 'known' reduced scattering coefficient was calculated using Mie theory.

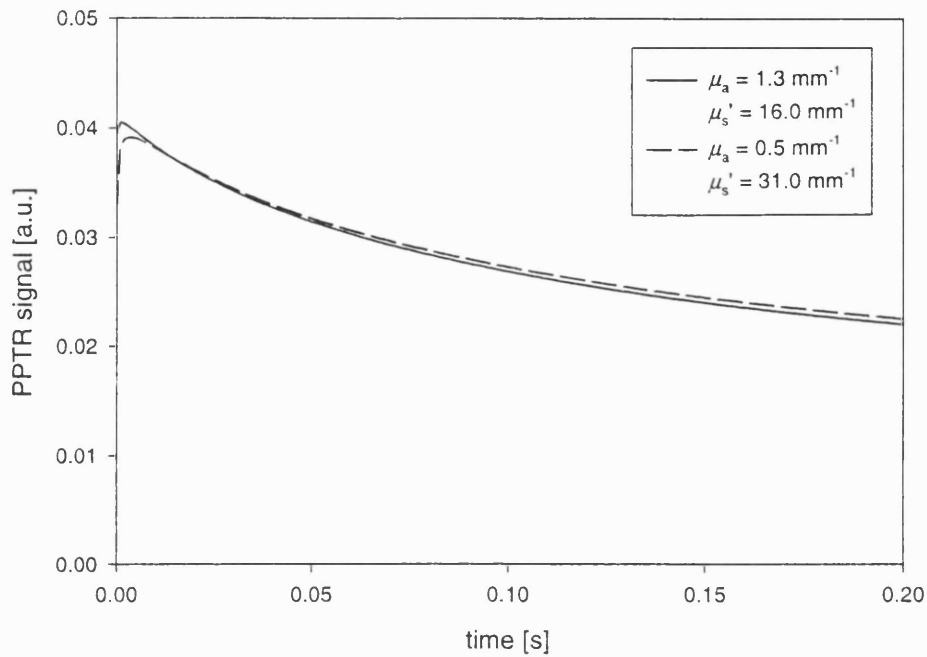


Figure 4.7 Theoretical radiometric photothermal signals calculated using two different sets of μ_a , μ_s' , and K .

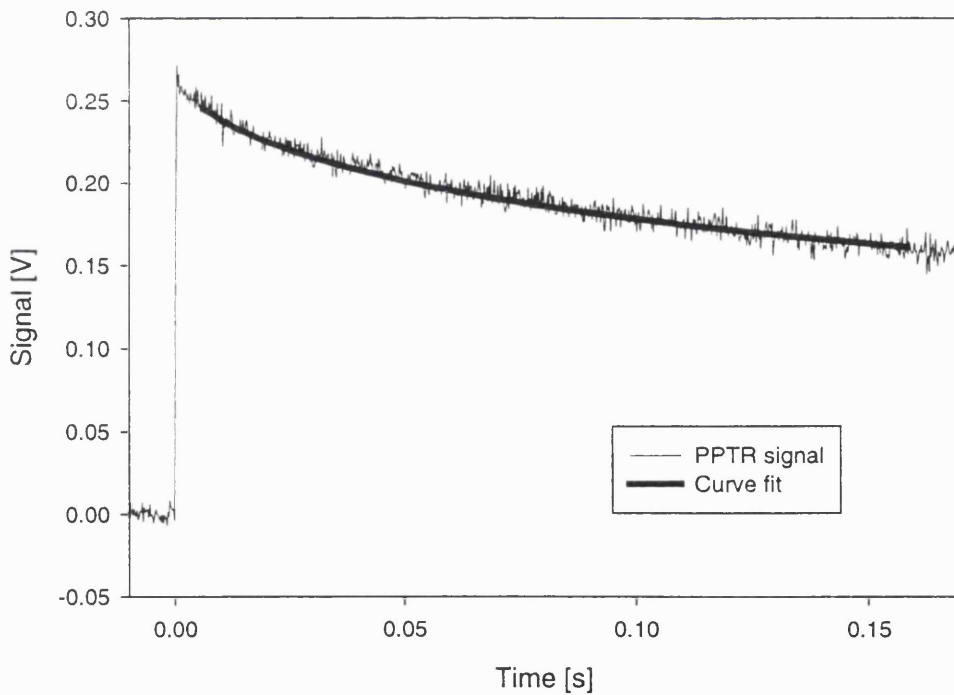


Figure 4.8 PPTR response of a turbid gel together with the best fit. The optical coefficients of the gel were $\mu_a = 2.70 \text{ mm}^{-1}$ and $\mu_s' = 2.80 \text{ mm}^{-1}$. The optical coefficients obtained from the non-linear curve fit were $\mu_a = 2.84 \text{ mm}^{-1}$ and $\mu_s' = 2.54 \text{ mm}^{-1}$.

<i>Known μ_a [mm⁻¹]</i>	<i>Derived μ_a [mm⁻¹]</i>	<i>Known μ_s' [mm⁻¹]</i>	<i>Derived μ_s' [mm⁻¹]</i>
2.70	2.79 ± 0.08	1.06	0.97 ± 0.16
2.70	2.84 ± 0.12	2.80	2.89 ± 0.22
2.70	2.71 ± 0.07	4.30	4.12 ± 0.34

Table 4.2 Comparison of the 'known' absorption and reduced scattering coefficients of the turbid gels with those determined from PPTR signals. The standard deviation was calculated from the variation in the coefficients determined from 4 individual measurements.

The error in the fitted values is of the order of $\pm 5\%$ for the absorption coefficient and $\pm 15\%$ for the reduced scattering coefficient.

A sensitivity analysis carried out by Prahl *et al* showed that the calculated signal is most sensitive to changes in μ_a . Both the absorption and the reduced scattering coefficient influence the initial distribution of the excitation light but it is absorption that governs the conversion of optical energy to heat. A 30% change in the thermal diffusivity altered the derived values of μ_a and μ_s' by 5% and 15% respectively. Prahl concluded that the PPTR signal is primarily dependent on the absorption coefficient. A more detailed assessment of the sensitivity of pulsed photothermal radiometry will be given in chapters 8 where the performance of PPTR is compared to that of the optical fibre sensor.

4.4 Confidence limits on the determined optical coefficients

The absorption and scattering coefficients of turbid gels were determined using pulsed photothermal radiometry with an error of $\pm 10\text{-}15\%$ compared to the values of μ_a and μ_s' obtained from transmittance measurements and Mie theory. The standard deviation of the signals represented the variation in the radiometric signal due to various sources of experimental error. Such sources included, for example, electrical noise from the laser and noise in the detector. Inhomogeneities in the distribution of optical properties in the aqueous gels may also have affected the photothermal signals. Slow dehydration of the gels was a source of experimental error. The loss of water increased the concentration of the absorber close to the gel surface, which led to errors in the determined absorption coefficient. The solidified gels were removed from the Petri dishes immediately before taking measurements and the photothermal response was detected on the side of the sample that had not been exposed to air. The measurements had to be completed within a short time in order to obtain accurate results. Measurements at later times showed significant systematic errors in the determined values. Leaving a gel exposed to air for approximately 10 min resulted in a systematic overestimation of μ_a of 10%.

PPTR signals can be used together with the analytic theory to calculate the confidence limits of the optical coefficients that were obtained using this method. While the mean and the standard deviation of the coefficients are an indication of the repeatability, the confidence limit is a statistical measure of the uncertainty in the determined parameter, which may provide information on the limitations in the determination of optical properties using PPTR. Four individual measurements on a non-scattering gel were averaged and the residuals were calculated for different absorption coefficients and system calibration constants. The minimum in the residuals represented the μ_a and the system response constant that produced the best fit to the experimental data. Figure 4.9 shows an example of a contour plot for measurements on a gel with a 'true' absorption coefficient of $\mu_a = 5.4 \text{ mm}^{-1}$.

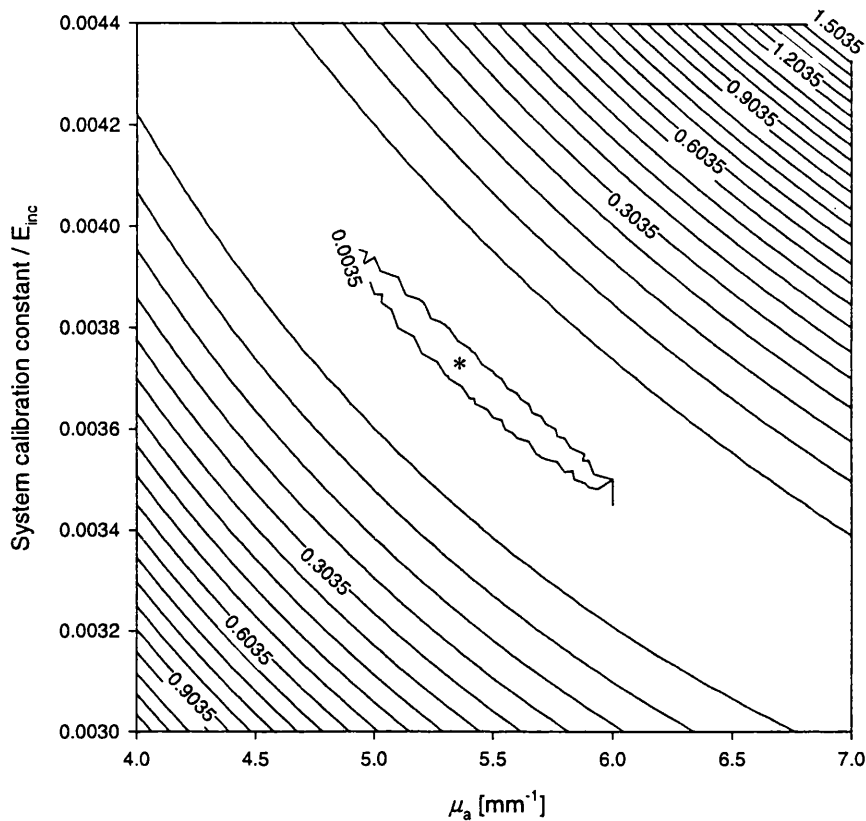


Figure 4.9 Residuals contour plot for a non-scattering, absorbing gel.

The asterisk represents the minimum in the residuals and therefore best fit to the data, $S(t)$, which corresponds to $\mu_a = 5.3 \text{ mm}^{-1}$. Assuming signal noise of $\Delta S = \pm 2.0 \text{ mV}$, the variation around the true minimum was obtained by calculating the residuals between the theoretical plot for the best fit including additional signal noise $S(t) \pm \Delta S$ and the experimental data. The range of possible absorption coefficients between the minimum residual and the residual for $S(t) \pm \Delta S$ was subsequently used as an confidence limit for the fitted values. In Figure 4.9, the residual for $S(t) \pm \Delta S$ is depicted by the innermost contour. The possible range of absorption coefficients, which would produce an equally good fit to the experimental data, is 4.8 to 6.0 mm^{-1} or $\pm 10\%$. Similar confidence limits in μ_a were calculated for all other measurements on non-scattering gels. The confidence limits for the absorption and reduced scattering coefficient of turbid gels were somewhat higher. Some

measurements produced confidence limits on the reduced scattering coefficient as high as $\pm 25\%$, while the absorption coefficient was typically estimated within $\pm 15\%$.

4.5 Discussion

The optical coefficients determined using a two-parameter fit are remarkably close to the known values of μ_a and μ_s' and have been obtained with a standard deviation of 5-15% compared to the values obtained from transmittance measurements and Mie theory. The results are in keeping with the findings by Prahl *et al*, who reported an accuracy of 10-15% in the determined coefficients. However, the confidence limits of the determined values indicate that the optical coefficients have a larger margin of uncertainty. The confidence limits of μ_a and μ_s' of $\pm 15\%$ and $\pm 25\%$ provide a measure of the certainty that the determined optical coefficients represent the true values. The values of confidence limits can be seen as the result of the noise on the signal as well as the use of a fixed system response constant. Any variation in the system response constant or errors in the measurement of the pulse energy, which was used to normalise the signals, would lead to deviations in the determined absorption and scattering coefficients. This would in turn result in a broadening of the χ^2 contour and hence an increase of the confidence limits.

The agreement of the determined optical coefficients with the measured or calculated ('known') values is still acceptable, which is perhaps a little surprising given that the analytical theory was based on the diffusion approximation. The diffusion approximation is said to be inaccurate close to sources and in media where the value of the reduced scattering coefficient is comparable to the absorption coefficient. This should, at least in theory, render it inappropriate for the radiometric measurements discussed in this chapter. An explanation for the good agreement of the analytic expression of the PPTR signal with the data may be found by considering the large absolute values of μ_a . At high absorption coefficients, the penetration depth is shallow and effects of scattering, such as an increase in subsurface fluence, may be restricted to small distances below the target boundary. Scattering may therefore only affect the shape of the signal at early times. Figure 4.10 shows fluence profiles calculated using the diffusion approximation and the MC

method. For μ_s' smaller or comparable to μ_a , the diffusion approximation shows good agreement with results obtained from a MC model (Figure 4.10(a)). At higher μ_s' , however, fluence profiles obtained using the diffusion approximation produce marked differences to the MC plots especially at low depths as shown in Figure 4.10(b).

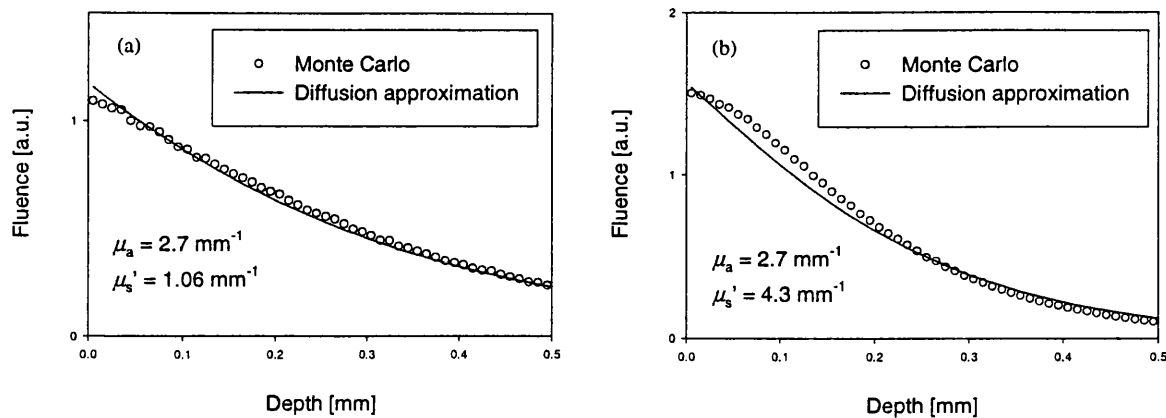


Figure 4.10 *Subsurface fluence profiles in turbid gels computed using the Monte Carlo method and the diffusion approximation. Good agreement between the diffusion approximation and the Monte Carlo method can be noted for μ_s' smaller than μ_a (a), while an increase in μ_s' produces marked differences in the fluence profiles.*

The effect of such a deviation was investigated by fitting the diffusion approximation to the MC results. The fit was accomplished by varying the optical parameters manually and yielded $\mu_a = 1.8 \text{ mm}^{-1}$ and $\mu_s' = 8.5 \text{ mm}^{-1}$. Theoretical PPTR signals were calculated for the two pairs of coefficients and are shown in Figure 4.11. The theoretical signals illustrate that the decay between 20 and 120 ms is very similar despite large differences in the optical coefficients. Only early times ($t < 20$ ms) indicate the difference in the optical properties. The time window for the analysis of PPTR signals, however, is typically between 5 and 120 ms. Earlier times are excluded to avoid interference from sources such as the laser power supply. It can therefore be concluded that the diffusion approximation is an adequate description of subsurface fluence provided the optical coefficients, in particular μ_a , possess high values and that the analysis takes amplitude information of the signals into account.

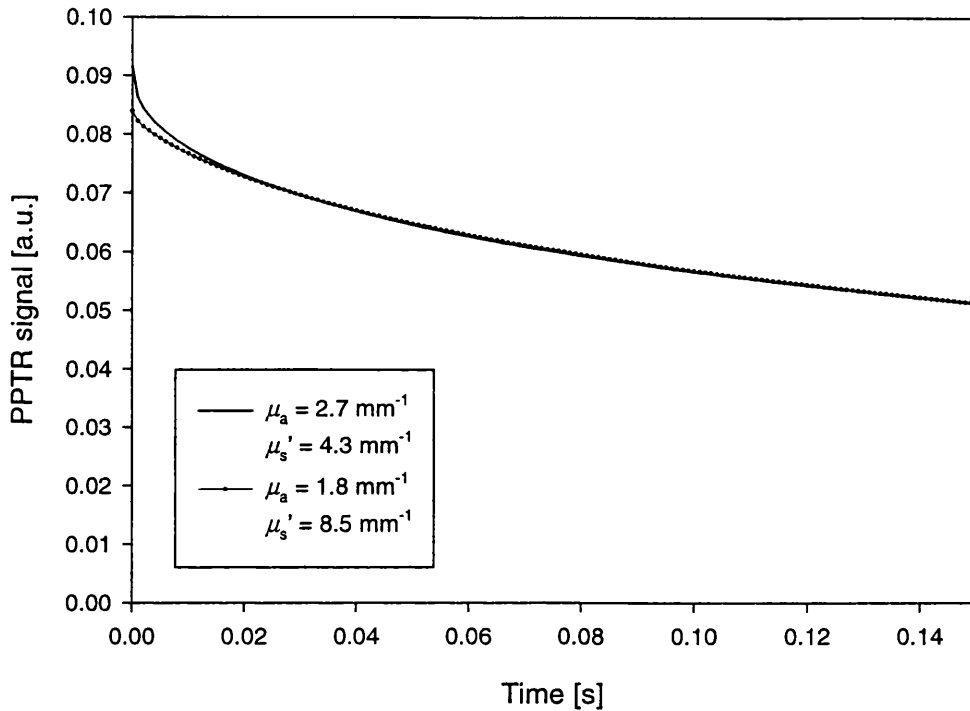


Figure 4.11 Normalised theoretical PPTR plots obtained using two sets of different optical coefficients.

The system response constant has to remain fixed in order to limit the range of scattering coefficients that can be obtained from the curve fit. Despite obvious differences in the fluence distributions, as shown in Figure 4.10, the diffusion approximation appears to model PPTR signals with adequate accuracy. This may also indicate that PPTR is not highly sensitive to detailed variations in the initial temperature profile in turbid media and that changes in the optical properties are detected due to changes in the amplitude of the signal, rather than its shape.

Larger discrepancies between experimental data and theory could be expected for low μ_a such as those found in tissue since the one-dimensional thermal geometry, where the diameter of the excitation area should be very much larger than the e^{-1} penetration depth, does not apply. These problems are also worsened by a poor signal to noise ratio due to the weak emissions from the sample.

Irrespective of the absorptivity of the tissue, the determination of optical coefficients using PPTR also has the problem of varying, and usually unknown, thermal parameters of tissue, such as specific heat. The specific heat and density affect the initial temperature rise in the target according to $T_0 = E_{\text{inc}} \mu_a c_{\text{Tissue}}^{-1} \rho_{\text{Tissue}}^{-1}$. By assuming that the amplitude (or system response constant) is fixed, the values of c_{Tissue} and ρ_{Tissue} are also regarded as constants. Any variation in the thermal properties of target tissue would therefore introduce an error into the determination of optical coefficients, which would be difficult to take account of.

4.6 Conclusions

The two-parameter fit provided a robust method of deriving the optical coefficients from measurements of the infrared response of non-scattering and turbid gels. Pulsed Photothermal Radiometry demonstrated the ability of photothermal techniques to determine the optical coefficients from the amplitude and temporal shape of the signal. Such treatment is only possible, however, if the thermal properties of the target are known and are assumed to be constant. Under these assumptions, PPTR can be used as a non-invasive, non-contact technique for probing the optical properties of turbid materials.

The validity of the diffusion approximation is dependent upon the optical properties of the material under study. Diffusion theory necessitates that scattering events are more dominant than events of absorption and that the light has become totally diffuse. For the turbid gels measured in this study, as well as tissue, this is a valid assumption for the red and near-infrared wavelength range. PPTR, however, only probes the very surface of the sample (typically 8-10 μm) where this assumption may not be valid. The results presented in this chapter as well as observations made by Prahl *et al* indicate that the diffusion approximation of the radiative transfer equation is a suitable method to describe the light transport in turbid media and is also applicable in the calculation of the initial temperature distribution. The diffusion approximation has been shown to be slightly inaccurate in the calculation of fluence distributions close to the surface of a scattering medium. The deviation from results obtained using the MC method makes the diffusion approximation

less suitable for the description of the distribution of excitation light in front of the optical fibre sensor. It will be shown later that photothermal signals detected using the sensor decay faster than those measured using PPTR due to the influence of radial heat diffusion. The time window that is used for the determination of optical coefficients will be shorter (approximately 50 ms), which will require a more accurate description of the light distribution close to the sensing film. The MC method is therefore the preferred model of light transport in turbid media and will be applied to calculate the initial temperature distribution in the turbid target and the optical fibre sensor.

The results presented in this chapter have shown that the infrared response from a turbid medium can be used to determine optical properties provided information about the amplitude of the signal is available. The system calibration constant K/E_{inc} incorporates all parameters that are present in the experimental set-up, such as emissivity, detector area, sensitivity etc. The value for K is obtained from measurements on absorbing-only gels. It has been suggested by Prahl *et al* that, if the ratio K/E_{inc} is unknown, measurements of the diffuse reflectance R_d can be made, which, together with the increase in the amplitude of the early signal, can be used as a check on the validity of the diffusion approximation. As scattering increases, the fluence near the surface and hence the temperature increases. The diffuse reflectance would provide an additional constraint for the two-parameter fit. A unique pair (μ_a, μ_s) could then be derived. This, according to Prahl, would remove the need to obtain amplitude information of the photothermal signals, such as the system calibration curve and the incident fluence, which are difficult measurements to perform accurately. It could be argued, however, that the knowledge of the incident fluence and reflectance may still not be sufficient to allow an accurate determination of optical coefficients from photothermal measurements if the specific heat capacity and density of the tissues vary significantly. The diagnosis of breast cancer, for example, would require a comparison of normal breast tissue, which is characterised by a higher fat content, and cancerous tissue, which may contain more water. In this example, the uncertainty in the amplitude of the signal will be strongly related to the uncertainty in the thermal coefficients. This would in turn have an adverse effect on the accuracy of the determined optical parameters.

The work outlined in this chapter has shown that pulsed photothermal radiometry can be used to determine the optical coefficients of samples with known thermal properties.

The optical properties of turbid gels have been estimated from their infrared response with an accuracy of $\pm 15\%$. The absorption coefficient of absorbing-only gels was determined using PPTR with an accuracy of $\pm 10\%$ for μ_a ranging from 1.3 to 5.4 mm^{-1} . Measurements at lower μ_a have been shown to be affected by the limited sensitivity of the radiometric set-up and the derived values for the absorption coefficient showed an increased error.

5 THE PHOTOACOUSTIC-PHOTOTHERMAL OPTICAL FIBRE SENSOR – THEORY

In this chapter, the principles of operation and theoretical considerations for the design of a photoacoustic-photothermal optical fibre sensor are described. The output of a low finesse Fabry-Perot interferometer will be discussed by considering the effects of different reflection coefficients and materials on the overall sensitivity. The interaction of the sensing film with acoustic and thermal transients will be discussed and factors limiting sensitivity will be examined.

5.1 Principles of operation

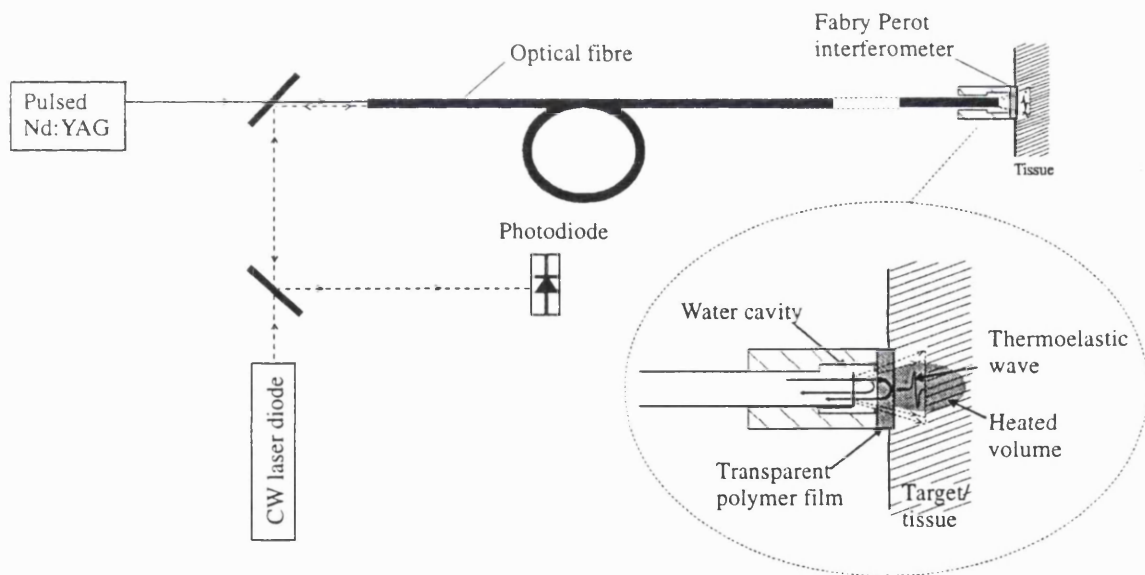


Figure 5.1 Schematic diagram of the photoacoustic-photothermal optical fibre sensor.

The experimental configuration of the photoacoustic-photothermal optical fibre sensor is shown in Figure 5.1. The sensing element is a thin (typically tens of microns) transparent

polymer film mounted at the distal end of an optical fibre. The film is in contact with the target. Low energy Q-switched pulses are launched into the fibre, transmitted through the polymer film and absorbed in the target. The rapid thermal expansion in the target generates an ultrasonic thermoelastic wave, which propagates towards the fibre as well as into the tissue. The mechanical stress associated with the acoustic wave results in the modulation of the optical thickness of the polymer film as the wave propagates towards the fibre. The acoustic wave is accompanied by heat diffusion from the target into the polymer film, which also contributes to a change in optical thickness of the film due to thermal expansion and provides the means of making photothermal measurements.

The changes in film thickness are detected by illuminating the polymer film with coherent light from a tuneable diode laser, the output of which, together with the excitation laser pulses, is also coupled into the optical fibre. The mismatch in refractive index between the polymer film and the surrounding media gives rise to Fresnel reflections from the two faces of the film. The film thereby acts as a low finesse Fabry-Perot interferometer. The reflected light travels back along the optical fibre to a photodiode for detection.

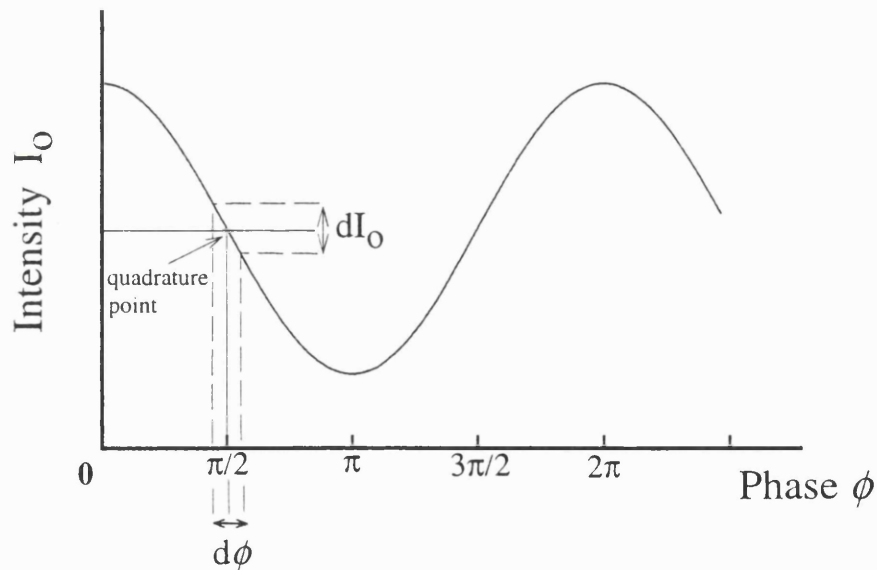


Figure 5.2 Intensity output of a low finesse Fabry-Perot interferometer as a function of phase bias ϕ . The diagram illustrates the working point of the interferometer – the phase bias has to be set to quadrature to produce the most linear relationship between phase shift and intensity.

Any acoustically or thermally induced change in the thickness or refractive index of the film results in an optical phase difference between the two reflections and hence a modulation in the optical power that is incident on the photodiode. For photoacoustic and photothermal measurements, it is necessary to operate the interferometer at a phase bias that corresponds to the so-called point of quadrature (see Figure 5.2). For small phase shifts, this results in a near linear relationship and maximum sensitivity between the change in optical thickness and the modulation of optical power. The required phase bias is obtained by changing the wavelength of the tuneable diode laser.

5.2 Low finesse Fabry-Perot interferometer output

In this section, the output of the sensing polymer film acting as a low finesse Fabry-Perot interferometer will be discussed. The assessment of the optical fibre sensor given in this chapter is an extension of an analysis by Paul Beard¹⁴⁴. The interferometric phase sensitivity is one of the key parameters in this evaluation since it provides a measure of the intensity modulation produced by the acoustically or thermally generated phase modulation. In addition to the phase modulation term, there is also a dc component, which affects the sensor performance and has to be taken into account for the optimisation of the sensor. How the factors that influence phase sensitivity and dc level interrelate, will be examined with the objective of achieving maximum intensity modulation for a given measurand-induced phase modulation.

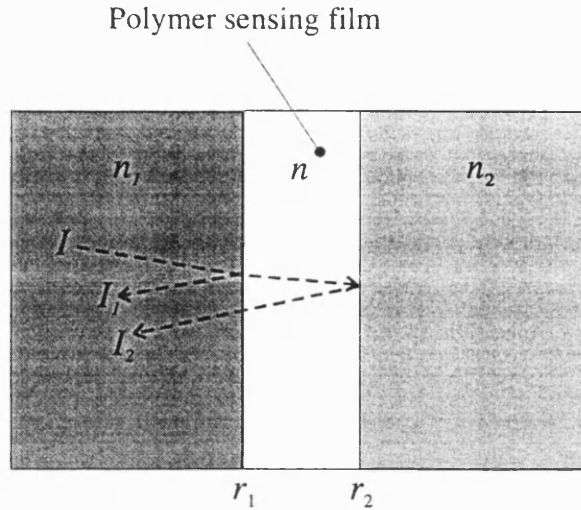


Figure 5.3 Polymer sensing film acting as a low finesse interferometer.

Consider a sensing film of refractive index n illuminated by coherent light of intensity I at normal incidence (Figure 5.3). The film is in contact with two media of different refractive index n_1 and n_2 . The mismatch in refractive index results in Fresnel reflections of intensity I_1 and I_2 from the two interfaces of the sensing film. The intensity reflection coefficients are r_1 and r_2 . The reflection coefficients considered in this example are relatively small (<0.05) and multiple reflections in the film can therefore be neglected. The reflections from the faces of the polymer film form the two beams of a low finesse Fabry-Perot interferometer. The resultant intensity I_0 can be derived from the coherent superposition of the reflected intensities I_1 and I_2 where Φ is the total phase difference between the two beams:

$$I_0 = I_1 + I_2 + 2\sqrt{I_1 I_2} \cos \Phi \quad (5.1)$$

The phase difference is caused by the optical path length difference between the two reflections. The derivation of the equation is based upon the treatment by Hecht and Zajac¹³⁴.

5.2.1 Phase sensitivity and dc level

For the case of acoustically or thermally induced changes in the optical thickness of the film, and hence optical path length differences of the interferometer, the total phase difference Φ contains two terms – the phase bias term ϕ that defines the working point of the interferometer and the acoustically and thermally induced signal term $d\phi$ (see also Figure 5.2):

$$\Phi = \phi + d\phi \quad (5.2)$$

Inserting equation (5.2) into equation (5.1) and expanding gives

$$I_0 = I_1 + I_2 + 2\sqrt{I_1 I_2} (\cos \phi \cos d\phi - \sin \phi \sin d\phi) \quad (5.3)$$

To achieve optimum sensitivity it is necessary to set the phase bias term ϕ at quadrature where $\phi=(2m+1)\pi/2$ (for integer m) by, for example, tuning the wavelength of the laser. At the first point of quadrature $\pi/2$, equation (5.3) can be simplified to

$$I_0 = I_1 + I_2 - 2\sqrt{I_1 I_2} \sin d\phi \quad (5.4)$$

Assuming only small changes in $d\phi$, it can be shown from equation (5.4) that the output of the interferometer consists of the simplified time varying component dI_0 and the dc component I_{dc} :

$$dI_0 = -2\sqrt{I_1 I_2} d\phi \quad (5.5)$$

$$I_{dc} = I_1 + I_2 \quad (5.6)$$

There is a linear relationship between the measurand-induced phase modulation $d\phi$ and the corresponding intensity modulation dI_0 . The phase modulation $d\phi$ has to be smaller than 0.35 rad in order to ensure a linearity of better than 2.0% as shown in Figure 5.4. The dependence of the reflected intensity on phase shift has been calculated using the time varying component dI_0 from equation (5.4).

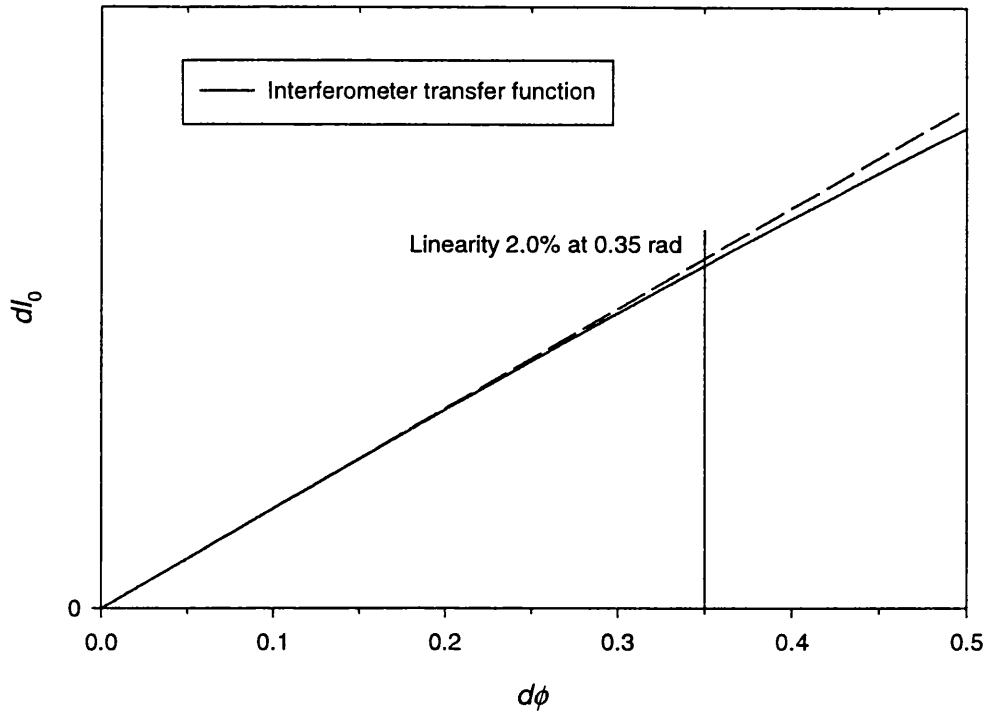


Figure 5.4 Maximum permissible phase shift of the Fabry-Perot interferometer while maintaining linearity.

I_1 and I_2 can be written in terms of the Fresnel reflection coefficients, r_1 and r_2 , which are defined by the refractive index mismatches at the boundaries of the sensing film.

$$I_1 = I r_1 \quad (5.7)$$

$$I_2 = I(1 - r_1)^2 r_2 \quad (5.8)$$

where

$$r_1 = \left(\frac{n - n_1}{n + n_1} \right)^2 \quad (5.9)$$

$$r_2 = \left(\frac{n - n_2}{n + n_2} \right)^2 \quad (5.10)$$

The phase sensitivity of the interferometer, defined as intensity modulation per unit phase shift $dI_0/d\phi$, and the dc level I_{dc} can now be written as

$$\frac{dI_0}{d\phi} = 2I(1 - r_1)\sqrt{r_1 r_2} \quad (5.11)$$

and

$$I_{dc} = I(r_1 + (1 - r_1)^2 r_2) \quad (5.12)$$

Maximum phase sensitivity can be obtained by deliberate selection of I , r_1 and r_2 . These parameters also affect the dc component, which is an undesirable part of the interferometer output. If the dc level is too high it will saturate the photodiode, limiting the maximum phase sensitivity that can be achieved by increasing I . It also produces a large photocurrent with accompanying shot noise that can adversely affect the noise characteristics of the sensor system.

5.2.2 Effect of reflection coefficients on signal intensity modulation

Since the sensing film of the optical fibre sensor has to allow the transmission of excitation pulses, only low values of reflection coefficients (typically less than 0.1) are considered. The analysis is therefore limited to the case of a low finesse Fabry-Perot interferometer.

The first option in the optimisation could be to choose reflection coefficients with the sole aim of obtaining maximum phase sensitivity. Figure 5.5 below shows the effect of different combinations of reflection coefficient on the phase sensitivity using equation (5.11) for an incident intensity of $I = 1$ mW.

To achieve the highest phase sensitivity, it would be feasible to have an air-backed film. Such an arrangement would increase the phase sensitivity, which can be seen in Figure 5.5. An air-backed film in contact with water would result in $r_1 = 0.06$ and $dI_0/d\phi = 0.018$. By contrast, a film surrounded by water with $r_1 = 0.0016$ would produce a significantly lower phase sensitivity of $dI_0/d\phi = 0.003$.

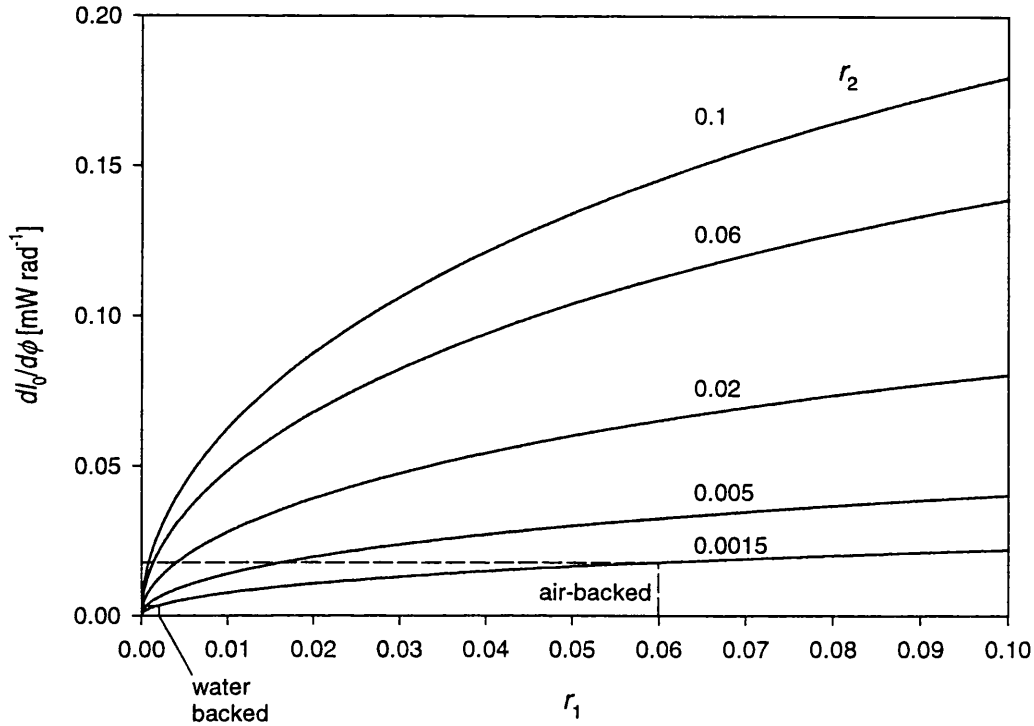


Figure 5.5 Normalised phase sensitivity $dI_0/d\phi$ for different reflection coefficients r_1 and r_2 ($I = 1 \text{ mW}$).

If the primary constraint in the optimisation is limited laser power, then the maximisation of the phase sensitivity would give the best possible sensitivity.

However, if sufficient laser power is at hand and the primary limitation is the saturation threshold of the photodiode, the optimisation should aim for the highest phase sensitivity and lowest dc level. If it was possible to freely choose values for r_1 and r_2 while sufficient laser power was available, a combination of the highest phase sensitivity together with the lowest dc level could be achieved. This can be illustrated by defining a figure of merit M , which is the ratio of the normalised phase sensitivity to the dc level.

$$M = \frac{dI_0/d\phi}{I_{dc}} \quad (5.13)$$

Substituting equations (5.11) and (5.12)

$$M = \frac{2(1-r_1)\sqrt{r_1 r_2}}{r_1 + (1-r_1)^2 r_2} \quad (5.14)$$

If the reflections I_1 and I_2 are substituted back into equation (5.13), then M can be recognised as the fringe visibility, where I_{\max} and I_{\min} are the maximum and minimum intensities of the interferometer output.

$$M = \frac{2\sqrt{I_1 I_2}}{I_1 + I_2} = \frac{I_{\max} - I_{\min}}{I_{\max} + I_{\min}} \quad (5.15)$$

Therefore, the highest possible phase sensitivity could be achieved by selecting r_1 and r_2 such that $M = 1$ and increasing the incident laser intensity just below the saturation threshold of the photodiode. This relationship is shown in Figure 5.6 below where the maximum of each curve ($M=1$) represents the maximum phase sensitivity together with the lowest dc level. Using the example of the air-backed and water-backed configurations of the sensing film, it can be seen from Figure 5.6, that maximum phase sensitivity is not necessarily the best criterion for the optimisation.

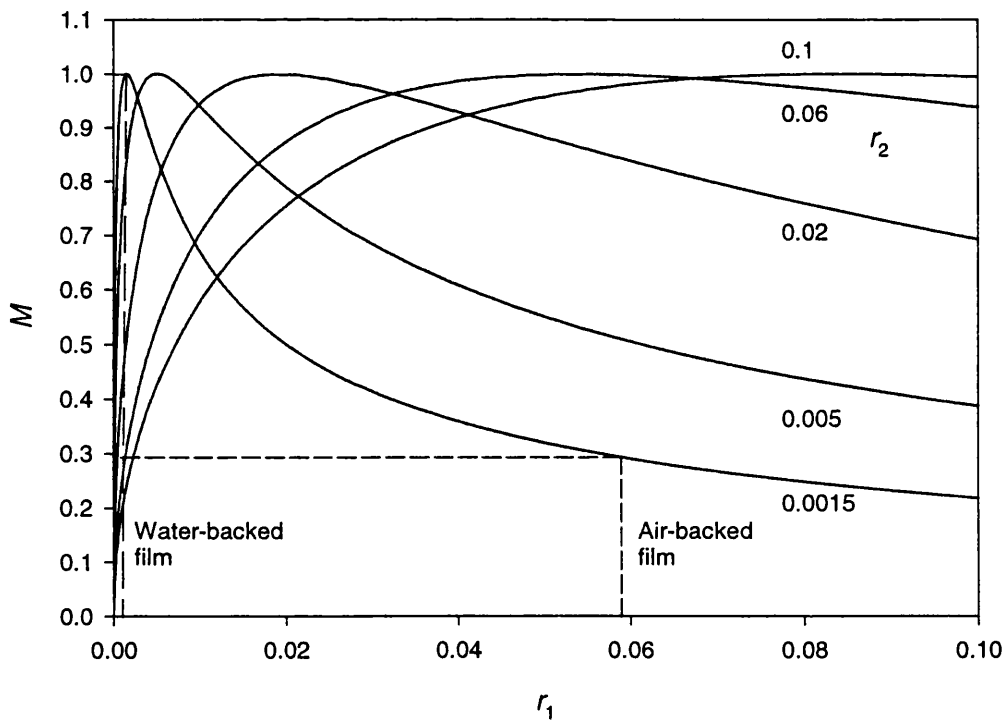


Figure 5.6 Fringe visibility M for different reflection coefficients r_1 and r_2 .

An air-backed film results in a fringe visibility of $M = 0.29$ ($r_1 = 0.058$, $r_2 = 0.0016$) while a film that is surrounded by the same medium, such as water, produces a theoretical fringe visibility of $M = 1$. The reduced figure of merit M for an air-backed film is due to different reflection coefficients, r_1 and r_2 . Both approaches are justified but the trade-offs connected with each of them should be considered. If, for example, only limited laser power is available and the photodiode has a high saturation threshold, the reflection coefficients could be chosen such that maximum phase sensitivity is obtained without considering the dc level. But if sufficient laser power is at hand, a high fringe visibility is advantageous since the laser power can be increased just below the saturation threshold of the photodiode, which would give maximum possible phase sensitivity.

For the application in the optical fibre sensor, the polymer film has to be transparent to allow the transmission of the excitation laser pulses. The reflection coefficients at the boundaries of the film will therefore be relatively small (<0.05). Since laser power of several tens of mW are available from diode lasers, the reflected intensities will be of the order of hundreds of μW . Given that the saturation threshold of a typical photodiode, such as a Hamamatsu S6468, is of the order of $30 \mu\text{W}$, it is likely that the saturation threshold will be the limiting factor in the optimisation. Optimisation of the reflection coefficients should therefore aim at high fringe visibility, which is produced by equal reflection coefficients at the faces of the film. It has been shown that optimum acoustic sensitivity of the sensing film is achieved by backing it with water¹³⁵. This configuration not only allowed the intended use of the optical fibre sensor for simultaneous photoacoustic and photothermal measurements, but also produced equal reflection coefficients, which produces maximum fringe visibility.

Another possible configuration of the optical fibre sensor is the glass-backed polymer film. In this case the sensing film is bonded to the end of an optical fibre. Maximum phase sensitivity could be achieved by coating the free interface of the film with a reflective coating, which is transparent to the excitation pulses, to achieve the desired reflection coefficient.

5.2.3 Phase sensitivity of different materials for the sensing film

In the previous section, it has been demonstrated that the reflection coefficients of the polymer sensing film should be optimised to achieve maximum fringe visibility. The refractive index of tissue has been reported to be around 1.4. Measurements on tissue using the optical fibre sensor would possibly require a contact medium to produce thermal continuity, where water is an ideal choice. A refractive index close to that of water ($n = 1.33$) could therefore be assumed on one side of the polymer film. Water could then be brought in contact with the illuminated side of the film to achieve a fringe visibility of $M = 1$. The curve shown in Figure 5.7 below, which shows the effect of different sensing film materials on phase sensitivity, has been calculated for those conditions.

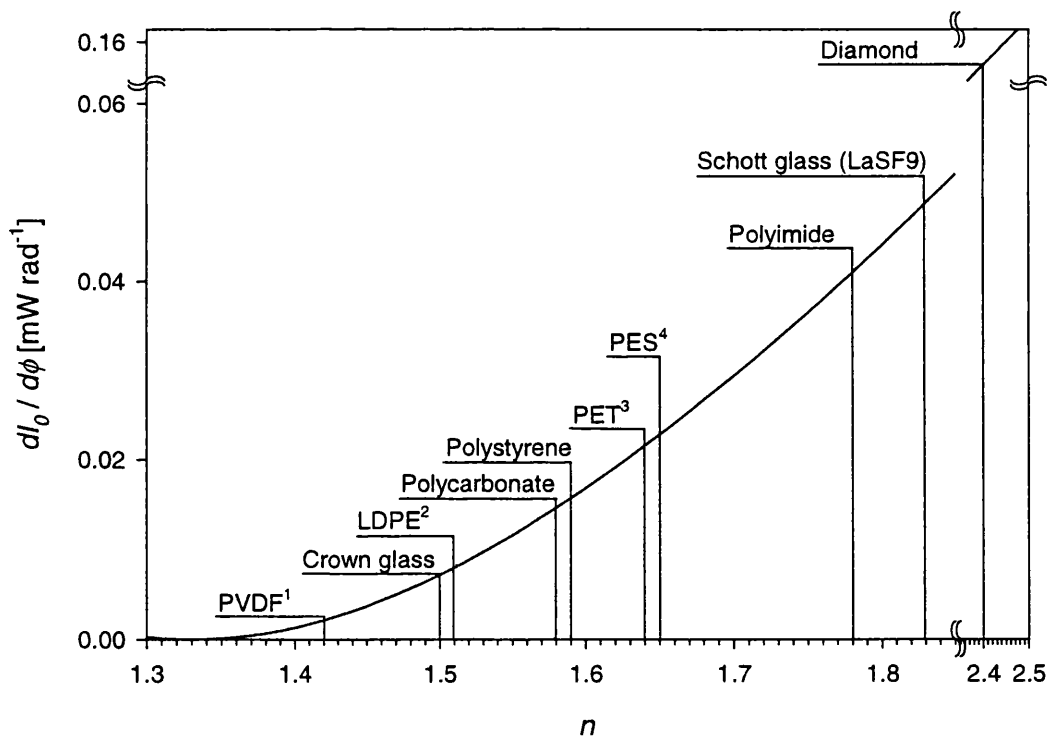


Figure 5.7 Phase sensitivities of different film materials in contact with water (¹Polyvinylidene flouride, ²low density polyethylene, ³polyethylene terephthalate, ⁴polyethersulfone).

In Figure 5.7, the dependence of phase sensitivity upon the refractive index of the film material is plotted using equation (5.11) for an incident intensity $I = 1\text{mW}$. Figure 5.7 shows considerable variations in the calculated phase sensitivity for the different materials even though the differences in refractive index are small. The reflection coefficient is related to the square of the refractive index mismatch between the film and water. If the reflection coefficients are equal then the phase sensitivity is also a quadratic function (equation (5.11)) of the Fresnel reflection coefficients, which explains the large deviations in phase sensitivity for relatively small differences in refractive index.

Given that the phase sensitivities were calculated for a fringe visibility of unity, it would in principle be possible to achieve the same phase sensitivity for each material by increasing the emitted power of the laser. If the available laser power is limited, a material with a large refractive index mismatch, such as PET, polyimide or diamond, would be preferable. With such materials, maximum phase sensitivity per unit incident intensity could be achieved.

5.2.4 Illumination of the sensing film using an optical fibre

So far, the performance of a Fabry-Perot interferometer has been discussed for the case of light which is normally incident on the sensing film. In the experimental configuration of the optical fibre sensor, the interferometer is illuminated by divergent light from an optical fibre. The effects of divergent light on the phase sensitivity will be examined in this section.

In the case of a collimated beam, all the light incident on or reflected from the film is travelling on the same optical path. Each point across the reflected optical field, which is due to the interference of the two reflections from the film boundaries, is associated with the same phase bias. The modulated signal intensity from each point across the reflected beam arriving at the photodiode is therefore in phase. This is not the situation if the interferometer is illuminated by a divergent beam. A variety of different path lengths and hence phase biases exist, depending on the incident angle of the rays. This can lead to partial or even total cancellation of the signal.

Pérennès *et al* have investigated the performance of a Fabry-Perot interferometer which was illuminated by light from a multimode optical fibre¹³⁶. The following section reproduces some of the results of their study for reference. Expressions for the effect of beam divergence, fibre tilt angle and wedge angles of the film were derived. The intensity distribution of the light exiting the distal end of the fibre was regarded as uniform, which is also termed “top hat” profile. The maximum divergence angle depends on the numerical aperture (N.A.) of the fibre, which, in air, is given as $\theta_f = \arcsin(\text{N.A.})$. Light exits the fibre at angles between 0.0 and θ_{d1} as shown in Figure 5.8.

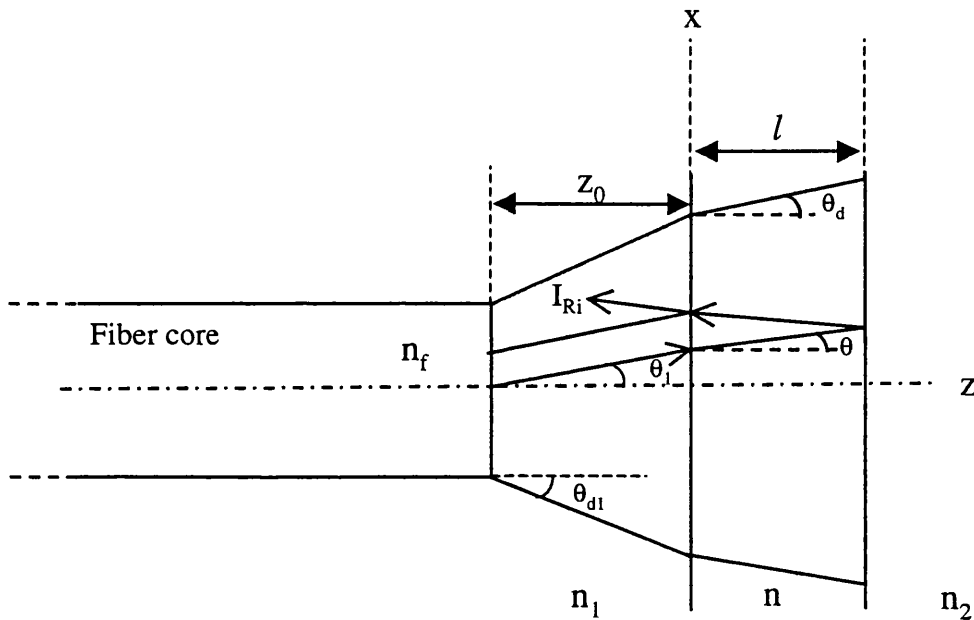


Figure 5.8 Diagram of a Fabry-Perot interferometer illuminated by the divergent beam from an optical fibre.

Angle θ_{d1} and θ_d represent the most diverging rays in the medium between fibre and the interferometer and inside the interferometer, respectively. The angles θ_{d1} and θ_d are related by Snell's law

$$n_1 \sin \theta_{d1} = n \sin \theta_d \quad (5.16)$$

where n_1 is the refractive index of the medium in front of the interferometer and n is the refractive index of the medium in the Fabry-Perot interferometer.

The expression for the optical path length difference depending on the angle of refraction is given as:

$$\Delta = 2nl \cos \theta \quad (5.17)$$

The derivation of equation (5.17) is given in Appendix B. Equation (5.17) demonstrates that the optical path length difference, or effective optical thickness, decreases with increasing angle of incidence.

The phase difference $\phi = 2\pi \Delta \lambda^{-1}$ corresponding to the optical path length difference in equation (5.17) is therefore

$$\phi(\theta) = \frac{4\pi nl}{\lambda} \cos \theta \quad (5.18)$$

where λ is the wavelength of the incident light. An increasing angle of incidence reduces the phase difference.

Returning to the findings by Pérennès *et al*, the reflected intensity I_{Ri} for a single diverging wavefront travelling at an angle θ is given by

$$I_{Ri} = \frac{I_0}{\Delta\phi} \left(r_1 + (1-r_1)^2 r_2 + 2\sqrt{r_1 r_2} (1-r_1) \cos \phi(\theta) \right) \quad (5.19)$$

where I_0 is the total intensity incident on the interferometer, r_1 and r_2 are the reflection coefficients on each side of the sensing film, and $\Delta\phi$ is the total phase dispersion or the difference in the phase differences for $\theta = 0$ and $\theta = \theta_d$. $\Delta\phi$ is a measure of the range of different optical path lengths taken by wavefronts at different angles θ in the interferometer. Rays at an angle $\theta = 0.0$ have the greatest phase difference, while those propagating at the divergence angle of the optical fibre θ_d produce the smallest phase difference. The effect of divergent light is therefore to create dispersion in the phase difference, which can be expressed as

$$\Delta\phi = \phi_{\max} - \phi_{\min} = \frac{4\pi nl}{\lambda} (1 - \cos \theta_d) = \phi_0 (1 - \cos \theta_d) \quad (5.20)$$

where ϕ_0 is the phase difference at normal incidence. Due to the uniform intensity distribution of the light emitted by the optical fibre, a uniform distribution of phase difference D can be defined within an interval:

$$\begin{cases} D(\phi) = 1 \text{ for } \phi_0 - \Delta\phi < \phi < \phi_0 \\ D(\phi) = 0 \text{ elsewhere} \end{cases} \quad (5.21)$$

An expression for the total amount of reflected light I_R is obtained by integrating equation (5.19) over the range of phase dispersion caused by the divergence of the optical fibre:

$$I_R = \int_{\Delta\phi} D(\phi) I_{Ri}(\phi) d\phi = I_0 \left(r_1 + (1-r_1)^2 r_2 + \frac{2\sqrt{r_1 r_2} (1-r_1)}{\Delta\phi} \int_{\phi_0 - \Delta\phi}^{\phi_0} \cos\phi d\phi \right) \quad (5.22)$$

Evaluation of equation (5.22) yields

$$I_R = I_0 \left(r_1 + (1-r_1)^2 r_2 + 2\sqrt{r_1 r_2} (1-r_1) \frac{\sin(\Delta\phi/2)}{\Delta\phi/2} \cos\left(\phi_0 - \frac{\Delta\phi}{2}\right) \right) \quad (5.23)$$

where I_0 is the total light intensity incident on the interferometer. The maximum and minimum of the reflected intensity occur when $\phi_0 - \Delta\phi/2 = 2k\pi$ and $\phi_0 - \Delta\phi/2 = (2k+1)\pi$, respectively, where k is an integer. The analytical solution for the dispersion-dependent fringe visibility is given as

$$\gamma = \frac{2\sqrt{r_1 r_2} (1-r_1) |\sin(\Delta\phi/2)|}{r_1 + (1-r_1)^2 r_2 \Delta\phi/2} = \gamma_0 \frac{|\sin(\Delta\phi/2)|}{\Delta\phi/2} \quad (5.24)$$

where γ_0 is the fringe visibility for a collimated beam. Equation (5.24) describes the visibility of fringes reflected from the interferometer before entering the optical fibre. The expression is valid for small cavity thicknesses and small internal beam divergence to allow for near complete overlap of the two reflections. This is a reasonable assumption for cavities of less than a few hundred microns in thickness illuminated by low numerical aperture fibres (N.A. ≤ 0.2). It is also assumed that the distance between fibre and interferometer is small and that the fibre diameter is sufficiently large to keep degradation in fringe visibility due to aperturing by the fibre small. The above assumptions are adequate since multimode fibres have relatively large core diameters, and the interferometer cavity is typically mounted close to or onto the fibre. Equation (5.24) can now be used to calculate

the fringe visibility for different divergence angles and cavity thicknesses. Figure 5.9 shows the relationship between the internal divergence angle and fringe visibility. The Fabry-Perot interferometer was assumed to be a polymer film with a refractive index of $n = 1.64$ in contact with water ($n_1 = 1.33$) on both sides. The beam divergence for an optical fibre of N.A. = 0.1 (in air) was calculated to be 4.3° in water, which produced an internal maximum beam divergence of 3.5° in the film. Figure 5.9 shows that for a beam divergence of 3.5° a cavity thickness of more than $20 \mu\text{m}$ would be required before fringe visibility is significantly degraded. Polymer films of $12 \mu\text{m}$ thickness have been used in the optical fibre sensor for photothermal measurements. Although the selection of such a thin film was based on thermal considerations, which will be explained in section 7.1.4, the small cavity thickness also produces a very low degradation of fringe visibility. Expression (5.24) has been validated experimentally by Pérennès *et al.*

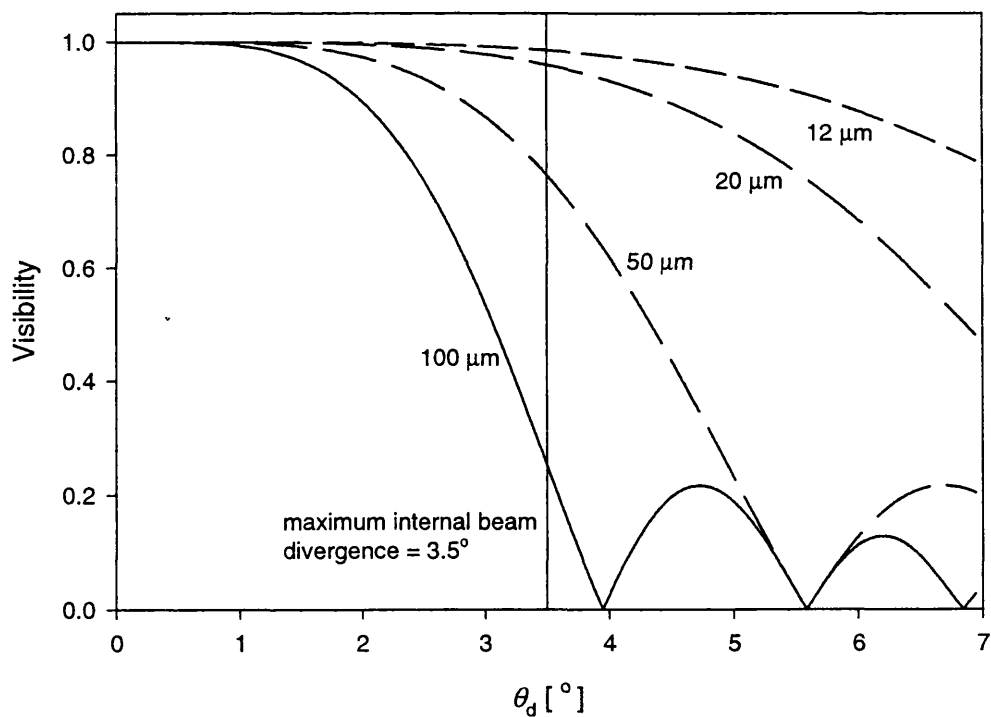


Figure 5.9 Effect of beam divergence on fringe visibility of a low finesse Fabry-Perot interferometer for different cavity thicknesses ($z_0 = 0$, $n_1 = n_2 = 1.44$, $n = 1.64$).

The analysis in the following two sections describes departures from the ideal Fabry-Perot interferometer. The discussion of the effect of a tilt angle and a wedged interferometer are again a reproduction of the findings by Pérennès *et al.*

5.2.4.1 Effect of a tilt angle between fibre and interferometer

A tilt angle between the fibre end-face and the interferometer results in a break-up of axial symmetry and a different distribution of angles in the Fabry-Perot. Figure 5.10 illustrates the problem.

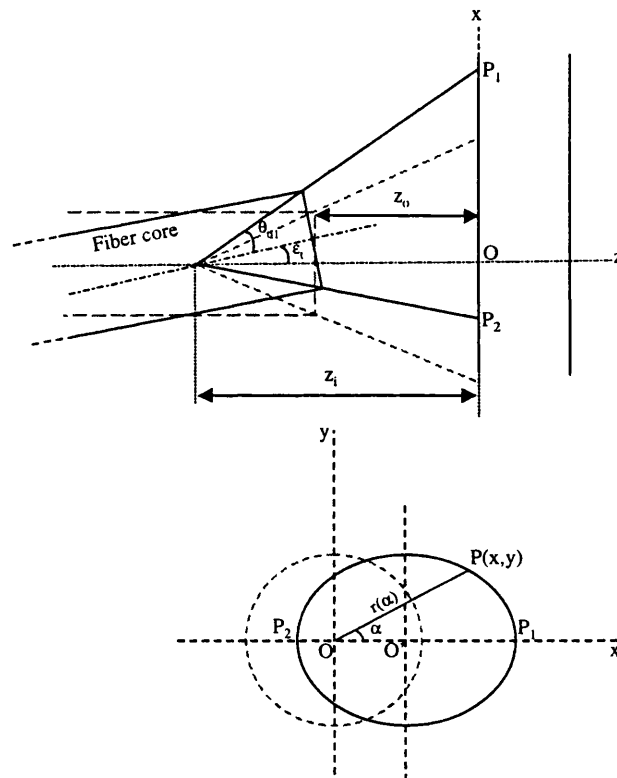


Figure 5.10 Illumination of the Fabry-Perot interferometer by an optical fibre positioned at an angle. The ellipse centred at O' represents the area of the interferometer exposed to the incident light.

The expression for the reflected intensity when the optical fibre is positioned at an angle is given as:

$$I_R = I_0 \left(r_1 + (1-r_1)^2 r_2 + 2\sqrt{r_1 r_2} (1-r_1) \frac{1}{\pi} \int_0^\pi \frac{\sin(\Delta\phi(\alpha)/2)}{\Delta\phi(\alpha)/2} \cos\left(\phi_0 - \frac{\Delta\phi(\alpha)}{2}\right) d\alpha \right) \quad (5.25)$$

The derivation of equation (5.25) can be found elsewhere¹³⁶. Equation (5.25) was evaluated numerically and the fringe visibility calculated for different phase dispersions obtained by changing the cavity thickness. Figure 5.11 shows the visibility over average phase dispersion for small values of the ratio of tilt angle and beam divergence, such as those encountered in the optical fibre sensor. The results illustrate that for low phase dispersion, i.e. small cavity thickness and beam divergence, the effect of tilt on fringe visibility is small.

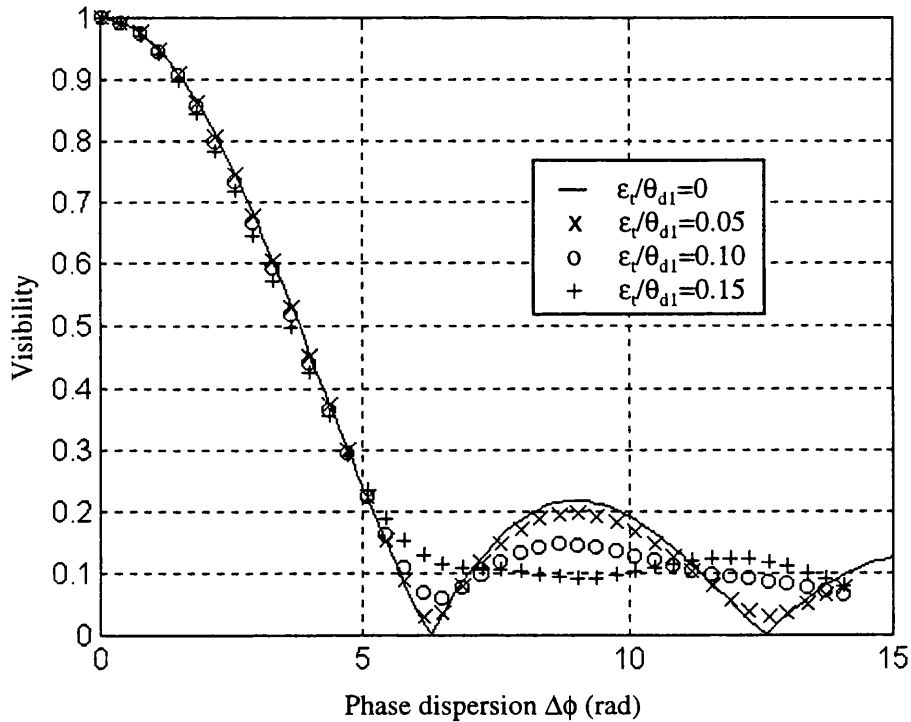


Figure 5.11 Effect of phase dispersion on fringe visibility for different ratios of tilt angle and beam divergence.

5.2.4.2 Effect of a wedge

The effect of non-parallel faces of the interferometer has also been investigated by Pérennès *et al.* A wedge angle in the interferometer introduces a varying thickness across the illuminated area. Figure 5.12 shows the illumination geometry for a wedged cavity.

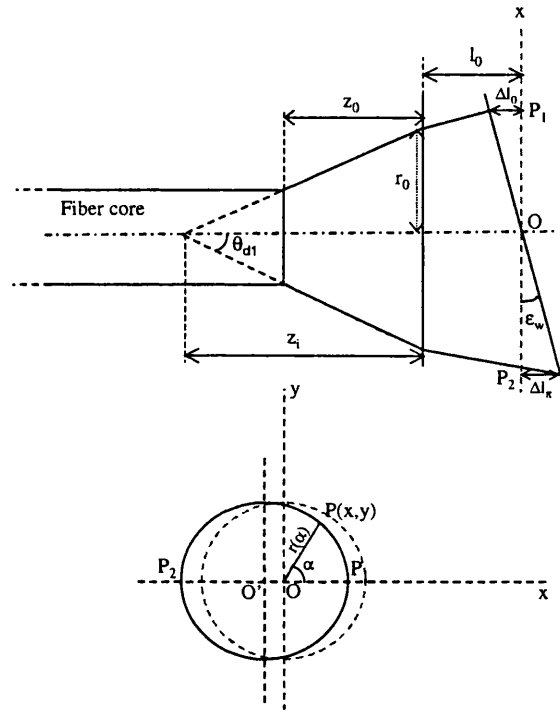


Figure 5.12 Illumination of a wedged interferometer cavity by an optical fibre.

The wedge angle was assumed to be small enough to allow for overlap and interference of the reflections to occur. The axial symmetry, similar to the effect of a tilt angle, is broken. The cavity now produces a varying thickness for the different incident angles of the divergent beam. It varies along each radial direction α between l_0 and $l_0 - \Delta l(\alpha)$ where $\Delta l(\alpha)$ is given as

$$\Delta l(\alpha) = r + \tan \epsilon_w \cos \alpha \quad (5.26)$$

The total reflected intensity is obtained by integrating the reflected intensity over angle α between 0 and π . The results show that a wedge has a significant effect on the fringe

visibility. This effect is increased the further the fibre is distanced from the interferometer. In the case of the optical fibre sensor, only very small distances, or even no separation, between fibre and interferometer are of interest and such problems can be neglected. The reduction in fringe visibility is perhaps not surprising as thickness variations of the same order of magnitude as the wavelength of the light will produce significant variation in the phase difference. Thickness variations of a few tens of nm will therefore be significant. The effect of different wedge angles on visibility is illustrated in Figure 5.13 below.

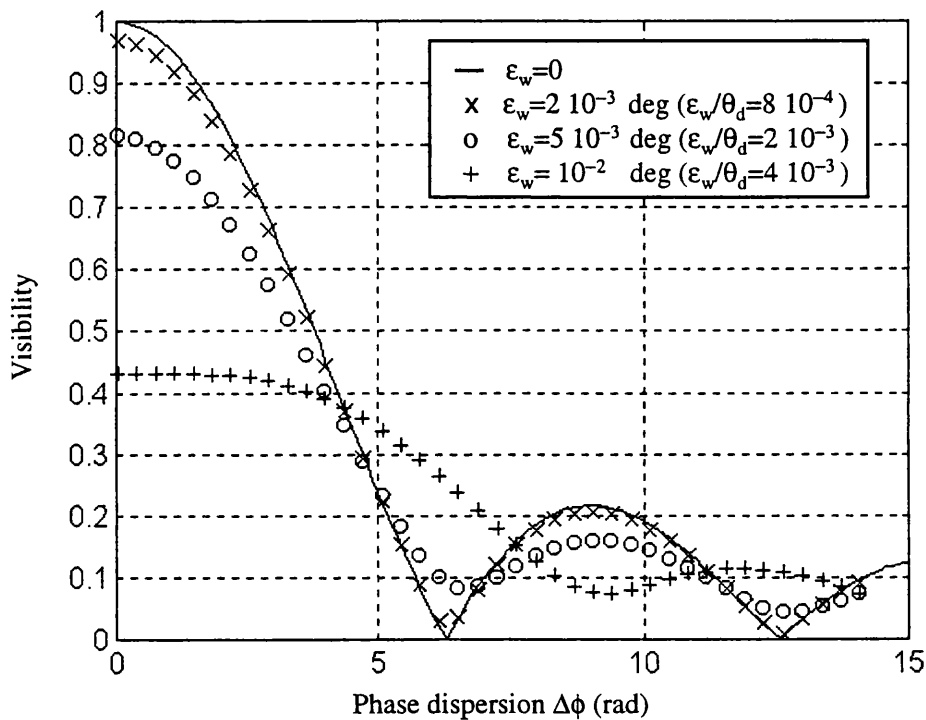


Figure 5.13 Effect of different wedge angles on fringe visibility.

Unlike the fibre tilt, a wedge in the interferometer cavity significantly affects fringe visibility for small values of phase dispersion. The comparison of Figure 5.13 and Figure 5.9 shows that wedge angles two orders of magnitude smaller than tilt angles begin to reduce visibility significantly for identical experimental conditions. From similar calculations, Pérennès *et al* estimated that variations in cavity thickness should not exceed 60 nm across the illuminated area in order to maintain maximum visibility.

5.3 Interaction of thermal and acoustic transients with the sensor

In this section, the interaction of thermal and acoustic transients with the sensing film will be discussed. A measurand-induced phase shift between the two Fresnel reflections is caused when an acoustic wave is incident on the film or heat diffuses through the film. The static phase shift, for normal incidence, is described with equation (5.27)

$$\phi = \frac{4\pi n l}{\lambda} \quad (5.27)$$

where n is the refractive index of the film material, l is the film thickness and λ is the wavelength of the incident light. The strain caused by the acoustic wave or the thermally induced thickness change produces a path length difference dl and a change in refractive index dn , so that equation (5.27) can be rewritten as

$$d\phi = \frac{4\pi}{\lambda} (n dL + L dn) \quad (5.28)$$

From equation (5.28) it can be seen that the detected photoacoustic and photothermal signals are related to changes in film thickness as well as changes in refractive index. The contribution of the two parameters to the signal will be discussed in the following sections. The expressions for the change in thickness are derived for the one-dimensional case, in which a plane pressure wave or a plane of heat propagates through the film.

5.3.1 Acoustically induced phase modulation

Although the detection of acoustic responses is not the topic of this thesis, expressions for acoustically induced phase modulation will be stated here for completeness. The phase modulation, $d\phi_L$, due to an acoustically induced change in the thickness of the polymer sensing film can be described with equation (5.29)

$$d\phi_L = \frac{4\pi n}{\lambda} dL_p \quad (5.29)$$

where dL_p denotes the acoustically induced thickness change. The change in thickness dL_p due to an incident acoustic field $P(z,t)$ is obtained by integrating the pressure field over the thickness of the sensing film. For an acoustically induced thickness change dL_p this yields

$$dL_p = - \int_0^L \frac{P(z,t)}{E} dz \quad (5.30)$$

where L is the thickness of the sensing film, t is time, z is the spatial co-ordinate and E is the Young's modulus of the polymer.

Some materials that are optically isotropic under normal conditions can become birefringent when put under mechanical stress due to, for example, a pressure wave, which would contribute to the phase modulation. An expression for the phase modulation $d\phi_N$ due to the acoustically induced change in refractive index dn_p ¹³⁷ alone can also be obtained from equation (5.27).

$$d\phi_N = \frac{4\pi L}{\lambda} dn_p \quad (5.31)$$

with

$$dn_p = \frac{n^3 p \sigma}{2} \frac{dL}{L} = \frac{n^3 p \sigma}{2L} \int_0^L \frac{P(z,t)}{E} dz \quad (5.32)$$

where n denotes the refractive index, p is the photoelastic constant of the material and σ is Poisson's ratio. The expression for the total acoustically induced phase shift is therefore

$$d\phi_p = \frac{4\pi n}{\lambda} \frac{1}{E} \left(1 + \frac{n^2 p \sigma}{2} \right) \int_0^L P(z,t) dz \quad (5.33)$$

5.3.2 Thermally induced phase modulation

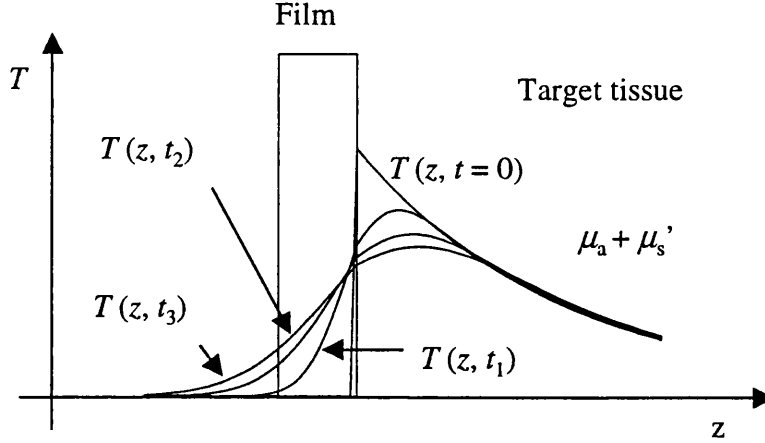


Figure 5.14 Temperature profile in the target and the sensing film along the central axis of the optical fibre sensor at different steps in time.

In analogy to the acoustic interactions, the thermally induced thickness modulation dL_T can also be obtained as the integral of the time-varying temperature distribution $T(z,t)$ across the film for each step in time as

$$dL_T = \beta_1 \int_0^L T(z,t) dz \quad (5.34)$$

where β_1 is the thermal expansion coefficient of the film material. Figure 5.14 illustrates the propagation of heat from the heated region in the target at $t = 0$ across the sensing film at times $t > 0$. Temperature transients also affect the refractive index. The temperature dependence can be described in analogy to equation (5.34) as

$$dn_T = \frac{n \gamma}{L} \int_0^L T(z,t) dz \quad (5.35)$$

where dn_T is the change in refractive index due to a transient temperature field across the sensing film and γ is a temperature coefficient of the refractive index of the material, also termed thermo-optic coefficient. Information on the temperature dependence of the

refractive index of polymers is usually not in the literature and the effect of temperature could theoretically be significant. However, for the proposed photothermal application of the optical fibre sensor it is not relevant whether the phase modulation is predominantly caused by a change in film thickness or a change in refractive index in the film. The net thermally induced phase modulation is given as:

$$d\phi_T = \frac{4\pi n}{\lambda} (\beta_1 + \gamma) \int_0^L dT(z, t) dz \quad (5.36)$$

Both the thermally induced change in film thickness and refractive index are taken account of in the temperature integral. The refractive index, β_1 , γ appear in front of the integral and therefore only have an effect on the amplitude of the signal while the temporal shape of the photothermal signal is determined for each point in time by the integration of the temperature distribution across the film.

5.4 Thermal Sensitivity

The thermal sensitivity is given by the change in optical phase, $\delta\phi_T$, to the mean temperature change in the film, δT :

$$\frac{\delta\phi_T}{\delta T} = \frac{4\pi n L}{\lambda} (\beta_1 + \gamma) \quad (5.37)$$

This expression corresponds to the dc thermal sensitivity, when the temperature distribution is uniform across the film. In Table 5.1, a number of different polymers, their thermal expansion coefficients, thermo-optic coefficients and thermal sensitivities are listed.

<i>Material</i>	<i>n</i>	β_t $\times 10^{-5} \text{ } ^\circ\text{C}^{-1}$	γ $\times 10^{-5} \text{ } ^\circ\text{C}^{-1}$	$d\phi_T/dT$ ($l=50 \text{ } \mu\text{m}$) $\text{rad } ^\circ\text{C}^{-1}$
¹ PMMA	1.49	7.3	-9.6	-0.027
Polystyrene	1.59	3.2	-5.4	-0.028
Polycarbonate	1.58	5.2-6.2	-8.6 to -10.3	-0.042 to -0.051
² PET	1.64	1.9-6.5	-3.6 to -12.3	-0.022 to -0.076
³ LDPE	1.51	15	-20.8	-0.070
⁴ PVDF	1.42	11	-11.9	-0.010
⁵ PES	1.65	5.5	-10.7	-0.067
Polyimide	1.78	2.0	-5.1	-0.043
Glass (crown)	1.50	0.9	-1.2	-0.004
Glass (Schott, LaSF9)	1.83	0.86	-2.4	-0.022
Diamond	2.40	0.1	-0.67	-0.011

Table 5.1 Temperature sensitivities of different materials for $\lambda=800 \text{ nm}$, $l=50 \text{ } \mu\text{m}$ (¹Polymethylmethacrylate, ²polyethylene terephthalate, ³low density polyethylene, ⁴polyvinylidene flouride, ⁵polyethersulfone).

The thermo-optic coefficients were obtained using¹³⁸

$$\gamma = \frac{dn}{dT} = -\frac{K}{6n}(n^2 + 1)(n^2 - 1) \quad (5.38)$$

where K is the volumetric thermal expansion coefficient, which can be approximated¹³⁹ from the linear expansion coefficient using $K = 3 \cdot \beta_t$. The data shown in Table 5.1 illustrates that the thermo-optic effect is dominant compared to the change in the physical thickness of the film. The thermo-optic coefficients also have negative signs, which

indicates that the phase shift due to thermal expansion is counteracted by the thermo-optic coefficient. There are notable differences in the thermal sensitivities of the materials, which could be exploited if a very sensitive photothermal detector was required. Diamond, for example, could be an interesting material despite the low thermal expansivity. Its high refractive index of $n = 2.4$ would result in high phase sensitivity which would be further complemented by the high quality of the reflecting surfaces, enabling a fringe visibility close to unity to be achieved. Polymers tend to have less flat surfaces, reducing the fringe visibility. Polymer films, however, are of interest in the development of a photoacoustic detector where a low Young's modulus is advantageous. Diamond has a high Young's modulus, which would make it unsuitable as a material for the sensing film. Since the proposed concept of the optical fibre sensor seeks to exploit the prospect of simultaneous photoacoustic and photothermal measurements for tissue diagnosis, polymers are the most suitable materials for the sensing film. The choice of polymers, however, is further limited by the availability of sufficiently thin films with good uniformity of thickness and clarity.

The phase sensitivity and the thermal sensitivity can be combined to obtain an expression for the change in intensity due to a unit change in temperature. Multiplying phase sensitivity and thermal sensitivity yields the overall system sensitivity as:

$$\frac{dI_0}{dT} = \frac{8\pi n L I (1-r_1) \sqrt{r_1 r_2}}{\lambda} (\beta_1 + \gamma) \quad (5.39)$$

Equation (5.39) is only valid for a set-up of low phase dispersion, which can be achieved with a 12 μm film and a low divergence fibre (N.A. < 0.1).

Since the reflections from the interfaces of the sensing film are caused by the refractive index mismatch between the film and surrounding medium, it is necessary to take variations in n in the adjacent medium into account. Assuming the surrounding medium to be water, the temperature dependent change in refractive index¹⁴⁰ at a typical laser diode wavelength of 800 nm is described by its thermo-optic coefficient of $-8.0 \cdot 10^{-5} \text{ K}^{-1}$. The difference in the thermo-optic coefficients of a PET film and water are therefore of similar magnitude. The resultant changes in the reflection coefficients give rise to a temperature coefficient of the overall system sensitivity (equation (5.39)) of approximately 0.03% K^{-1} . The temperature coefficient of the refractive index of water can therefore be neglected.

5.5 Noise analysis

In this section, the effects of noise generated by the different components of the experimental set-up of the sensor are discussed. The noise analysis includes two main types of noise: noise due to environmental factors and noise caused by the components of the set-up. Environmental noise includes disturbances such as temperature fluctuations, shocks and vibrations, while noise associated with the set-up stems from the photodiode, the amplifying electronics, and the laser. Environmental noise typically affects the signal at low frequencies and can therefore be neglected in photoacoustic applications, where bandwidths of up to 100 Mhz are required. Photothermal measurements, however, are taken at frequencies of less than 1 MHz and low frequency disturbances due to vibrations of, for example, the optical fibre, can affect the performance of the sensor. While these disturbances may pose a problem for *in vivo* measurements, they do not affect measurements taken in a controlled laboratory environment and are therefore neglected. Should the sensor be applied to *in vivo* measurements, however, these low frequency perturbations will need to be addressed. The sensor system is limited by the noise performance of its individual components: the photodiode, the operational amplifier and the diode laser. The aim of this section is to identify the main sources of noise and to estimate a value of the noise floor produced by the laser diode and the photodiode-amplifier configuration that were used for the measurements presented in the following chapters.

5.5.1 Photodiode noise

Noise produced by a photodiode includes four types: shot noise due to the photocurrent, shot noise due to the dark current, thermal noise caused by the shunt resistance, and $1/f$ noise. The photodiode is assumed to be reverse biased.

- (i.) The r.m.s. shot noise current per unit bandwidth, i_{sp} , due to the photocurrent I_{ph} is given as

$$i_{sp} = \sqrt{2eI_{ph}} \quad (5.40)$$

where e is the electronic charge ($e = 1.6 \cdot 10^{-19}$ C).

- (ii.) The shot noise current per unit bandwidth, i_{sd} , due to the dark current, I_d , is

$$i_{sd} = \sqrt{2eI_d} \quad (5.41)$$

- (iii.) The r.m.s. thermal noise current, or Johnson noise current, per unit bandwidth, i_{Rsh} , due to the shunt resistance, R_{sh} , is

$$i_{Rsh} = \sqrt{\frac{4kT}{R_{sh}}} \quad (5.42)$$

where k is the Boltzmann constant and T is the absolute temperature.

- (iv.) $1/f$ noise, $i_{1/f}$, becomes more dominant at frequencies of less than 100 Hz and is governed by the following characteristics¹⁴¹:

$$i_{1/f} = i_{nf} \sqrt[4]{1 + (f_f / f)^2} \quad (5.43)$$

where i_{nf} is the noise floor current due to all noise sources, f_f is the corner frequency beyond which the $1/f$ noise becomes insignificant and the overall noise is dominated by the noise floor level due to the Johnson noise and the photocurrent and dark current shot noise.

The total r.m.s. noise current per unit bandwidth is defined as follows:

$$i_{np} = \sqrt{i_{sp}^2 + i_{sd}^2 + i_{Rsh}^2} \sqrt[4]{1 + (f_f / f)^2} \quad (5.44)$$

The noise contributions by the different noise sources will be estimated for a typical high speed photodiode such as the Hamamatsu¹⁴² S1223, which can be used for simultaneous photoacoustic and photothermal measurements. For this model, the shunt resistance is $R_{sh}=1 \text{ G}\Omega$, the dark current, for a reverse bias voltage of 20 V, is $I_d=10 \text{ nA}$ and the photosensitivity S is 0.52 A/W at 780 nm. The photocurrent consists of the contributions from the dc level intensity, I_{dc} , and the signal intensity modulation, dI_0 . As discussed in section 5.2, $I_{dc} \gg dI_0$ and the contributions of the signal intensity modulation to the noise can be neglected. For an intensity of $I_{dc}=100 \text{ }\mu\text{W}$ incident on the photodiode, a photocurrent of $I_{ph} = 52 \text{ }\mu\text{A}$ is generated. Using the values $k = 1.33 \cdot 10^{-23} \text{ J K}^{-1}$, $T = 298 \text{ K}$, $e = 1.6 \cdot 10^{-19} \text{ C}$, the individual noise contributions, neglecting $1/f$ noise, are quantified:

$$i_{sp} = 4.1 \cdot 10^{-12} \text{ A Hz}^{-1/2}$$

$$i_{sd} = 5.64 \cdot 10^{-14} \text{ A Hz}^{-1/2}$$

$$i_{Rsh} = 3.98 \cdot 10^{-15} \text{ A Hz}^{-1/2}$$

From the estimated noise currents it can be seen that the shot noise due to the photocurrent is dominating the noise characteristics. If the incident intensity were to be decreased, shot noise due to the dark current would become more significant. Over the photoacoustic bandwidth of typically 25 MHz, the dark current would dominate the noise when the incident intensity falls below 0.54 nW. This is very much smaller than typical dc level intensities, which are of the order of several tens of microwatts. For both photoacoustic and photothermal applications it can be concluded that the noise of the photodiode is dominated by shot noise due to the photocurrent.

5.5.2 Amplifier noise

Photodiode detection systems typically require some form of amplification to convert the small photocurrent to a measurable voltage. To obtain the overall noise characteristics of the system, a noise equivalent model¹⁴³ of the photodiode/op-amp circuit is used. Figure 5.15 shows the system noise model.

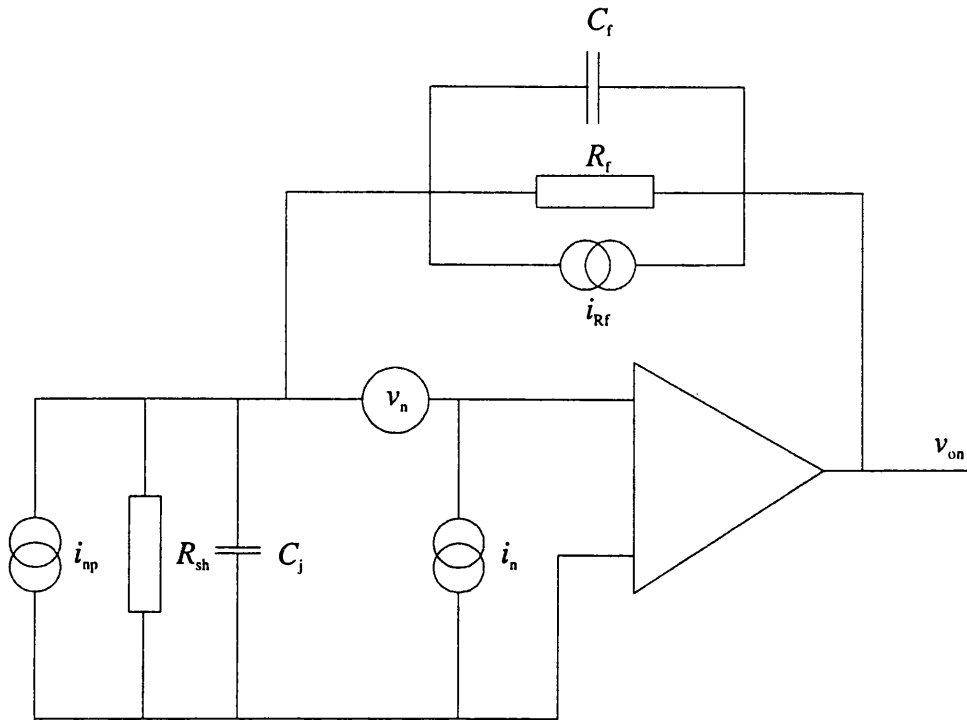


Figure 5.15 Noise model of a photodiode – current amplifier combination

In such a system, the total noise and the signal-to-noise ratio (SNR) depend on the noise generated by both the photodiode and the amplifier. The noise sources produced by the system can be assigned to three categories:

- i. Photodiode noise - shot noise, Johnson noise, $1/f$ noise
- ii. Current noise in the amplifier - input bias current noise, i_n , Johnson noise current, i_{Rf} , from the feedback resistor, Z_f , and $1/f$ noise
- iii. Voltage noise in the amplifier, v_n , which also includes $1/f$ noise.

The current noise sources associated with the amplifier are listed below. The contribution of $1/f$ noise is included for each type of noise in the form of the factor $(1 + (f_t/f)^2)^{1/4}$:

- i. The photodiode noise current produces a voltage across the feedback resistor Z_f comprising the feedback resistor R_f and the feedback capacitance C_f in parallel. The noise voltage, v_{op} , at the output is:

$$v_{op} = i_{np} Z_f \quad (5.45)$$

where

$$Z_f = \frac{R_f}{1 + j\omega R_f C_f} \quad (5.46)$$

- ii. The input bias noise current, i_{ib} , produces a voltage v_{oi} at the output which is given as:

$$v_{oi} = i_{ib} Z_f \sqrt[4]{1 + (f_f / f)^2} \quad (5.47)$$

The thermal noise current is given as

$$i_{Rf} = \sqrt{\frac{4kT}{R_f}} \quad (5.48)$$

where R_f is the feedback resistance. The corresponding noise voltage at the output, v_{of} , is therefore

$$v_{of} = i_{Rf} Z_f \sqrt[4]{1 + (f_f / f)^2} \quad (5.49)$$

- iii. The noise voltage in the amplifier, v_n , appears at the output as voltage v_{ov} . Assuming an ideal op-amp, where no current flows through the input terminal, v_{ov} is obtained from

$$\frac{v_{ov} - v_n}{Z_f} = \frac{v_n}{Z_p} \quad (5.50)$$

$$v_{ov} = v_n \left(1 + \frac{Z_f}{Z_p} \right) \sqrt[4]{1 + (f_f / f)^2} \quad (5.51)$$

where Z_p is the impedance of the photodiode, consisting of the shunt resistor R_{sh} and capacitance C_f in parallel.

The total r.m.s. noise voltage, including $1/f$ noise, is obtained from the square root of the sum of the squares of the individual contributions:

$$v_{on} = \sqrt{v_{op}^2 + v_{oi}^2 + v_{of}^2 + v_{ov}^2} \quad (5.52)$$

The contributions of the different sources of noise are illustrated in Figure 5.16 and are calculated using the following values:

$$\begin{array}{ll}
 i_{np} = 4.1 \cdot 10^{-12} \text{ A Hz}^{-1/2} & R_f = 30 \text{ k}\Omega \\
 i_n = 10 \cdot 10^{-15} \text{ A Hz}^{-1/2} & C_f = 0.3 \text{ pF} \\
 v_n = 20 \cdot 10^{-9} \text{ V Hz}^{-1/2} & C_j = 7 \text{ pF} \\
 R_{sh} = 1 \text{ G}\Omega & f_t = 100 \text{ Hz}
 \end{array}$$

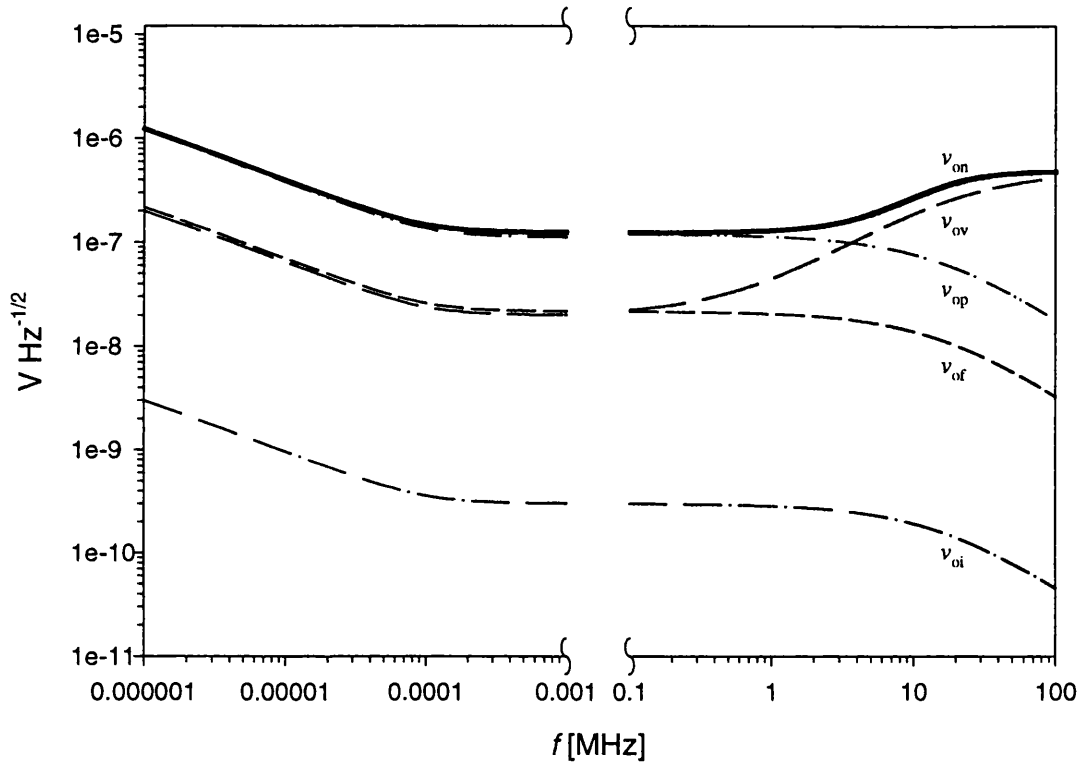


Figure 5.16 Contributions of the individual noise sources to the system noise voltage v_{on} appearing at the amplifier output (v_{op} – photodiode noise, v_{ov} – amplifier input noise voltage, v_{of} – Johnson noise current, v_{oi} – amplifier input noise current).

Figure 5.16 shows that the total noise of the photodiode-amplifier circuit for frequencies below 1 MHz is dominated by the photodiode noise, which as section 5.5.1 showed is largely due to photocurrent shot noise, and $1/f$ noise. For high frequency bands, the amplifier input noise voltage gradually dominates over than the photocurrent shot noise.

The set-up of the optical fibre sensor could perhaps be optimised by using two photodiodes for simultaneous photothermal and photoacoustic detection. The photodiode optimised for photoacoustic measurements would require a large bandwidth and could be

ac coupled thereby eliminating $1/f$ noise. Low frequency photothermal measurements would allow the photodiode-amplifier combination to be bandwidth limited to frequencies of less than 10 kHz, which would remove high frequency noise contributions. Further optimisation of the photothermal detection scheme could be achieved by using photodiodes with a larger detection area in order to obtain a higher saturation threshold and hence higher phase sensitivity, as discussed in section 5.2.1. It has to be borne in mind, however, that an increase in photodiode detection area also increases the photodiode capacitance C_f , which would produce a larger amplifier input noise voltage, v_{ov} , at high frequencies.

Integrating equation (5.52) over a 25 MHz bandwidth results in a total noise voltage at the amplifier output

$$v_{on} = 1.44 \text{ mV}$$

while a 10 kHz bandwidth used for photothermal measurements results in a total noise voltage of

$$v_{on} = 42 \text{ } \mu\text{V}.$$

The sensitivity of the photodiode-amplifier circuit, S_c , is obtained by multiplying the responsivity of the photodiode, S_R , by the impedance Z_f of the feedback resistance, which, for $\omega C_f R_f \ll 1$, $Z_f = R_f$ is given as:

$$S_c = S_R R_f \quad \text{V/W} \quad (5.53)$$

The sensitivity of the photodiode-amplifier combination is $S_c = 15.6 \text{ mV}/\mu\text{W}$, which yields an intensity noise i_{on} , or noise-equivalent power, for photoacoustic bandwidths of

$$i_{on} = 1.44 \cdot 10^{-6} / 15.6 = 0.092 \text{ } \mu\text{W},$$

while the smaller bandwidth for photothermal applications produces an intensity noise

$$i_{on} = 0.042 \cdot 10^{-6} / 15.6 = 0.0026 \text{ } \mu\text{W}.$$

These values represent the smallest detectable intensities over 25 MHz and 10 kHz respectively, using a typical photodiode-amplifier combination.

5.5.3 Laser noise

The laser, which is used to illuminate the interferometer, also contributes to the overall noise of the system. A laser causes intensity noise due to small fluctuations in the output power and phase noise, due to the finite linewidth and frequency instabilities of the emitted wavelength. The laser-related sources of noise will be discussed for a bandwidth of 25 MHz and 10 kHz for the tunable cw diode laser (Environmental Optical Sensors Inc., Boulder, USA, Model ECU-2010A) that was used for the work presented in this thesis.

5.5.3.1 Intensity noise

Intensity noise is typically of low frequency and is dominated by $1/f$ noise. The amplitude stability is quoted by the manufacturer to be $\pm 0.01\%$ maximum. For a dc level intensity of $100 \mu\text{W}$, the intensity noise is therefore $i_{\text{in}} = 0.01 \mu\text{W}$.

5.5.3.2 Phase noise

Frequency instabilities and the finite linewidth of the laser emission produce phase fluctuations, which are converted to intensity noise with a magnitude proportional to the phase sensitivity $dI_0/d\phi$ in the Fabry–Perot interferometer. The phase noise $d\phi_{\text{n}}$ due to a variation in frequency or linewidth $d\nu_{\text{n}}$ is given as

$$d\phi_{\text{n}} = \frac{4\pi n l d\nu_{\text{n}}}{c_0} \quad (5.54)$$

where c_0 is the speed of light. The intensity noise i_{n} due to the phase noise is obtained by multiplying the phase noise $d\phi_{\text{n}}$ by the phase sensitivity:

$$i_{\text{n}} = \frac{dI_0}{d\phi} d\phi_{\text{n}} \quad (5.55)$$

Using typical values of a PET film ($n = 1.65$, $l = 12 \mu\text{m}$, $c_0 = 3 \cdot 10^5 \text{ km s}^{-1}$, $I = 1 \text{ mW}$) and a linewidth of $<4 \text{ MHz}$ over a 5 second interval, the phase noise is

$$d\phi_{\text{fl}} = 3.32 \cdot 10^{-6} \text{ rad}$$

and using $dI_{\text{O}}/d\phi = 21.6 \mu\text{W/rad}$ yields a corresponding intensity noise of

$$i_{\text{fl}} = 7.16 \cdot 10^{-5} \mu\text{W}.$$

The phase noise is very low and can be neglected, especially given the small interferometer path lengths (tens of microns).

The total laser noise i_{ln} is made up of the contributions from the intensity noise i_{in} and the phase noise i_{fl} and is obtained from:

$$i_{\text{ln}} = \sqrt{i_{\text{in}}^2 + i_{\text{fl}}^2} \quad (5.56)$$

The dominant part of the laser noise is therefore the intensity noise i_{in} . The value for the laser noise for the values considered above is

$$i_{\text{ln}} = 0.01 \mu\text{W}.$$

5.5.4 Overall system noise

The overall system noise i_{sn} is obtained by adding the photodiode-amplifier noise, expressed as intensity i_{on} , as discussed in section 5.5.2, and the laser noise i_{ln} :

$$i_{\text{sn}} = \sqrt{i_{\text{on}}^2 + i_{\text{ln}}^2} \quad (5.57)$$

The smallest detectable intensity for a bandwidth of 25 MHz has been estimated as $i_{\text{on}} = 0.092 \mu\text{W}$. i_{on} and $i_{\text{ln}} = 0.01 \mu\text{W}$ therefore produce an overall system noise of

$$i_{\text{sn}} = 0.093 \mu\text{W},$$

which represents the lowest detectable signal intensity over a 25 MHz bandwidth. A much smaller detection limit of $i_{\text{on}} = 0.0026 \mu\text{W}$ was calculated for a 10 kHz bandwidth, which yields

$$i_{\text{sn}} = 0.01 \mu\text{W}$$

as the detection limit. Since the lowest detectable intensity for a 10 kHz bandwidth used in photothermal measurements is dominated by laser intensity noise, there is no gain in

optimising the detector characteristics. Photoacoustic detection may benefit from detector optimisation since the laser intensity noise may be much smaller over the very short photoacoustic detection times.

5.6 Thermal detection limit

PET has been the favoured material for the sensing film of the optical fibre sensor since its high refractive index ($n = 1.65$) provided high phase sensitivity while the surface quality, especially of very thin films, was adequate and did not unduly degrade the phase sensitivity. A 50 μm film with a phase sensitivity of $21.6 \mu\text{W rad}^{-1}$ (section 5.2.3) and a thermal sensitivity of $0.076 \text{ rad } ^\circ\text{C}^{-1}$ (section 5.4) yields an overall system sensitivity of $1.64 \mu\text{W}/^\circ\text{C}$. The smallest intensity that can be detected using a typical photodiode (over a 25 MHz bandwidth) was estimated as $0.096 \mu\text{W}$ (section 5.5.4). The smallest detectable temperature change that could be resolved by a Fabry-Perot interferometer consisting of a 50 μm film is therefore 58 mK. For photothermal measurements with a 10 kHz bandwidth, a minimum detectable intensity of $0.01 \mu\text{W}$ was calculated. The thermal noise floor for such a bandwidth and a 50 μm film is 6.1 mK. A 12 μm film, which was used in the sensor to monitor fast thermal transients, has a theoretical thermal sensitivity of $0.018 \text{ rad}/^\circ\text{C}$ and would produce a thermal noise floor of 26 mK over a bandwidth of 10 kHz. A list of the thermal detection limits produced by film made of different materials is shown in Table 5.2 below.

<i>Material</i>	<i>Thermal detection limit [mK]</i>
¹ PMMA	57.3
Polystyrene	22.9
Polycarbonate	13.4 – 16.0
² PET	6.1 – 20.9
³ LDPE	17.9
⁴ PVDF	464.6
⁵ PES	6.5
Polyimide	5.8
Glass (crown)	368.9
Glass (Schott, LaSF9)	9.5
Diamond	6.2

Table 5.2 *Thermal detection limits of various materials calculated for a film thickness of 50 μm and a bandwidth of 10 kHz. (¹Polymethylmethacrylate, ²polyethylene terephthalate, ³low density polyethylene, ⁴polyvinylidene flouride, ⁵polyethersulfone)*

5.7 Discussion

To optimise the optical fibre sensor, the phase sensitivity, the fringe visibility and the thermal sensitivity need to be weighed up against each other in order to find the most suitable compromise. The use of thin polymer films with low reflection coefficients as the sensing element restricted the analysis to low-finesse interferometry.

It was found that the fringe visibility, rather than phase sensitivity, can be used to optimise the sensitivity of the sensor (section 5.2.2). To achieve high fringe visibility, it is necessary that the Fresnel reflection coefficients at the interfaces of the polymer film are

equal. This is achieved by bringing the film in contact with the same medium on both sides, which results in a fringe visibility of $M = 1$. This can be accomplished by backing the film with water, since liquid or gel tissue phantoms and tissue, which are in contact with the front surface, have refractive indices close to that of water. The analysis of the illumination of the Fabry-Perot interferometer using an optical fibre showed that phase dispersion due to beam divergence, fibre tilt and a wedge-shaped cavity can significantly reduce the fringe visibility. It is therefore advantageous to use films with a thickness of less than 20 μm , an optical fibre of small divergence angle and films with small thickness variation to reduce phase dispersion.

For the selection of appropriate materials for the sensing film, the requirements for photoacoustic and photothermal measurements have to be met. The material should have a low Young's modulus and an acoustic impedance close to that of water¹⁴⁴ to obtain high acoustic sensitivity. The optimisation of phase sensitivity and acoustic sensitivity can be considered separately but poses a possible conflict. Section 5.2.4 illustrated the effects of illumination of the sensing film using a multimode optical fibre. The accompanying signal cancelling effect, which reduces fringe visibility, is worsened with increasing angle of incidence and film thickness. This poses a limit to the film thickness, even though high acoustic sensitivity could possibly be achieved with thicker films. For photoacoustic applications, for example, a thick film would produce high acoustic sensitivity but would also increase the signal cancelling and would therefore reduce the overall sensitivity. The optimal photoacoustic optical fibre sensor is a compromise between the two requirements.

Photothermal measurements would benefit from a material which has a thermal conductivity close to or higher than that of water. Low thermal diffusivity would prevent fast heat diffusion into the film and the sensor could therefore not capture high frequencies. It is the high frequency components of the photothermal signal that contain information about the optical coefficients of the target¹⁴⁵. High thermal sensitivity could be obtained by selecting a material with a high thermal expansion coefficient and a high thermal coefficient of the refractive index.

The selection of a suitable material is made difficult by a number of material properties that are not listed in the literature. Young's modulus of PET, for example, may be different in the high frequency bandwidth of photoacoustic detection compared to low

frequencies¹⁴⁶. At low frequencies, the polymer chains are more susceptible to creep. At high frequencies, the configuration of the polymer chains remains more stable, which results in a different value for Young's modulus. The refractive index of PET has also been shown to possess a temperature coefficient, which is larger than the linear thermal expansion coefficient. For the calculation of the photothermal signal, however, it is of less importance which parameter contributes more to the phase modulation since the temporal shape of the signal is determined through the integration of the time-dependent temperature distribution in the sensing film, as shown in equation (5.36).

PET offers an acceptable compromise as a film material when water is used as the surrounding medium. High phase sensitivity, due to its high Fresnel reflection coefficients, is combined with adequate thermal and acoustic sensitivity¹⁴⁴. The acoustic impedance is also reasonably well matched to that of water. PET is therefore a suitable compromise as sensing film material for simultaneous photoacoustic and photothermal measurements.

So far, the discussion has only addressed polymer films as sensing elements. The sensor could also be made of stacks of dielectric films, which can be deposited directly onto the end of an optical fibre. Dielectric films are an alternative to the low-finesse interferometers made of polymer films and could be designed to produce a cavity of high finesse. Such sensors have already been developed for pressure and temperature measurements^{147,148}. The phase sensitivity could be increased to the extent that the reduced thermal and acoustic sensitivity, due to the lower thermal expansion coefficient and high Young's modulus of some of the dielectric materials, is compensated for. Another option is the deposition of dielectric films onto polymer films, in which case the advantageous acoustic properties of the polymer could be combined with the creation of a high finesse interferometer cavity. This could perhaps be achieved by depositing a stack of polymer layers of different refractive index. The main problems with polymer deposition may be the limited ability of the technique to produce adequate surface qualities and the control of the layer thickness, which, for the case of a single coating for high reflectance, needs to be half the wavelength of the incident light. The high-finesse approach is only useful, however, if the dielectric layers are deposited onto a single mode fibre where the emitted light is of low divergence in the near field. The photoacoustic-photothermal sensor discussed in this thesis is configured using a multimode optical fibre, which is characterised by high divergence in

the near field compared to a single mode fibre. Multimode fibres produce significant beam divergence and consequently phase dispersion in the interferometer, which will limit the finesse that could be achieved by stacks of dielectric films. The reduced finesse would affect the phase sensitivity to an extent where it would no longer make up for the loss in thermal and acoustic sensitivity. It is nevertheless possible to make an optical fibre sensor using a single mode fibre. Such a sensor would have disadvantages for the photothermal determination of bulk optical properties of tissue due to its small active area. The optical properties of tissue are typically considered to refer to dimensions much larger than individual cells. Multimode fibres are more suitable since the microscopic optical properties contribute to the photothermal signal and are therefore averaged over the fibre area. The reduced finesse together with the small acoustic and thermal sensitivity of a dielectric cavity on a multimode fibre make polymer films the preferred interferometer material.

The noise analysis of a typical photodiode-current amplifier combination showed that the photocurrent shot noise provides the most significant contribution to the photodiode noise. It was found that the laser intensity noise outweighs the noise contribution of the detector when a film of 12 μm thickness was used for photothermal measurements in a 10 kHz bandwidth. The thermal noise floor of a 12 μm PET film is of the order of 26 mK.

6 A NUMERICAL MODEL OF THE OPTICAL FIBRE SENSOR

In the techniques discussed in the preceding chapters, the analysis of heat transport was usually simplified to one spatial dimension in order to obtain an analytic expression for the detected photothermal signal. In the discussion of pulsed photothermal radiometry in chapter 4, it was assumed that a plane of heat is generated at the surface of a semi-infinite target and that the subsequent analysis could be simplified to one spatial dimension. This allows solutions of the heat diffusion equation to be obtained more easily. A one-dimensional thermal geometry situation was produced experimentally by ensuring that the diameter of the excited area was large compared to the optical penetration depth and thermal diffusion length. Detecting the photothermal signal emitted from a small area in the centre of the excited region made the assumption of one-dimensional heat conduction valid.

The analysis of measurements made using the optical fibre sensor is different from most implementations of techniques such as pulsed photothermal radiometry in that the ratio between the areas of photothermal excitation and detection is almost unity. Radial heat diffusion at the edges of the heated volume has a significant effect on the sensor signal and needs to be taken into account. To obtain an analytic expression for the heat transport in the optical fibre sensor and the target, it would be necessary to find a solution to the heat conduction equation in three spatial dimensions. The solution would have to be obtained with respect to boundary conditions and an initial temperature distribution in the target for finite beam sizes etc. Such solutions are usually very difficult and sometimes impossible to derive. The restrictions and simplifications, such as infinite or semi-infinite dimensions and optical and physical homogeneity, also make them less suitable for the analysis of 'real life' tissue measurements. Mixed boundary conditions or complex geometries add further problems, which cannot be addressed satisfactorily using analytical methods.

Numerical methods, such as finite differences and finite elements (FE), offer very flexible ways of simulating heat conduction in three spatial dimensions and are therefore suitable for the calculation of transient temperature distributions in the tissue and the sensor. The basic idea of these methods is the substitution of the derivatives in the heat diffusion equation by differences. This converts the partial differential equation into sets of

algebraic equations, which can be solved for a variety of boundary and initial conditions. The temperature can be calculated for each point in a discrete grid. The solution, however, is always an approximation of the exact solution but convergence can be maximised by using a fine mesh.

The calculation of photothermal signals of the optical fibre sensor requires two models: (1) a model of the light transport in the target and (2) a model of the transient heat conduction in the target and the optical fibre sensor. The Lambert-Bouguer law and a Monte Carlo model have been applied to model the light transport in non-scattering and turbid media respectively, while a two-dimensional finite element model (FEM) is used for the calculation of transient heat conduction. The theoretical photothermal signal is obtained from the output of the FEM. The numerical model discussed in this chapter is applied solely to ‘forward’ calculations in which the optical and thermal properties define the temporal characteristics of the photothermal signal. For convenience, the numerical model of light and heat transport will be referred to as FEM in this thesis, implying that the model of light transport is included.

The determination of optical coefficients from experimental data using a theoretical model requires statistical techniques such as model-based parameter estimation. Model-based parameters estimation (MBPE), which is discussed in section 6.2, is a statistical procedure of obtaining parameters by fitting the predictions of the numerical model to the experimental observations.

6.1 A Finite Element model of the optical fibre sensor

The application of the optical fibre sensor produces a localised heat source in the target tissue. The photothermal signal detected by the sensor is the result of axially diffusing heat in the centre of the heated volume and radially diffusing heat at the edges, since the ratio of the areas of optical excitation and detection of the sensor are almost unity. The sensor therefore works differently to pulsed photothermal radiometry, which generally employs a much larger ratio of the area of excitation to the area of detection and therefore allows the detection of axial heat diffusion. The method of finite elements takes account of radial heat

loss by allowing the calculation of three-dimensional heat conduction in the optical fibre sensor and the tissue.

Since the experimental configuration of the optical fibre sensor is axially symmetric, the FEM could be simplified to a two-dimensional geometry, which represents a cross-section of the sensor as shown in Figure 6.1.

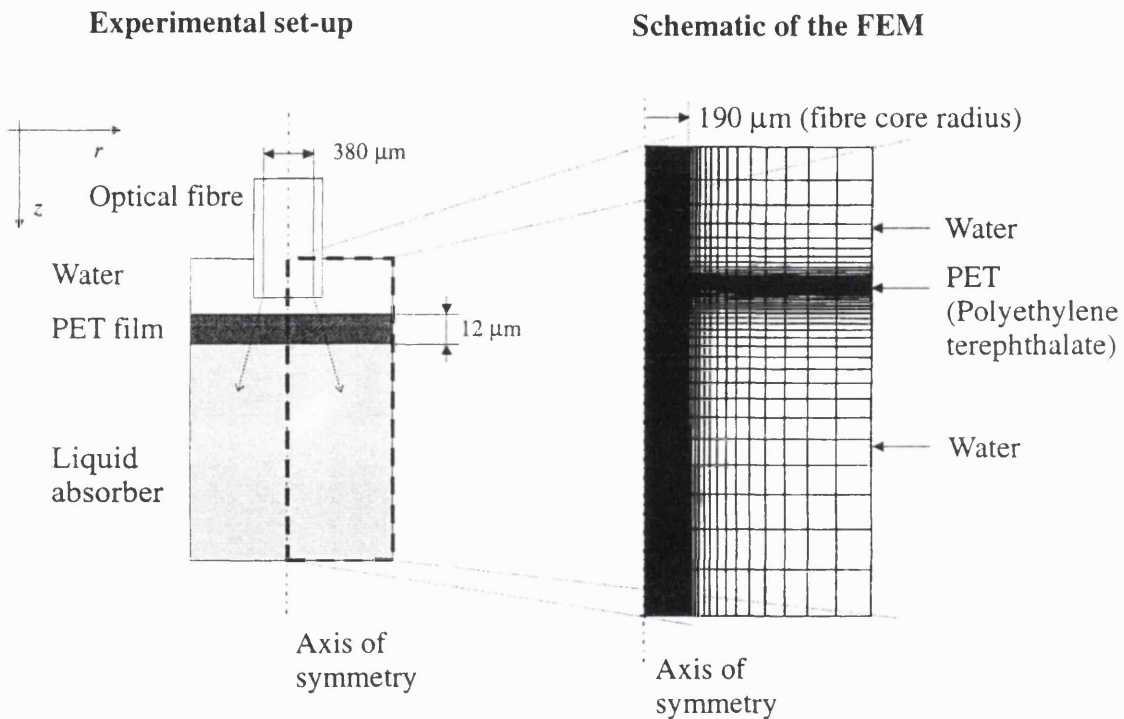


Figure 6.1 Diagram showing the interpretation of the experimental geometry of the optical fibre sensor in the 2D finite element model.

The dimensions of the FE geometry were chosen such that the region used for the calculation of the photothermal signal was distant from the mesh boundaries. This ensured that the boundary conditions did not have an influence on the solution at the centre. The mesh represented a surface of 6 mm length and 2 mm width. Adiabatic boundary conditions were chosen for the free edges of the mesh. The material properties were distributed across the mesh according to the dimensions of the optical fibre sensor. The film was considered to be in perfect thermal contact with the media adjacent to the two interfaces, which is a

valid assumption in liquid targets. The thermal coefficients of the absorber and the backing material were set to those of water. The thermal properties of polyethylene terephthalate (PET) were assigned to the elements representing the film layer. The thermal and optical properties of the materials were assumed to be isotropic and unaffected by temperature changes.

The distribution and density of the nodes were determined from convergence tests. A FEM represents an approximation of some exact analytical description and the convergence of the model to the exact solution is dependent upon the node density. The FEM of the optical fibre sensor was tested by calculating photothermal signals for absorption coefficients in the target that were two times greater than the maximum effective attenuation coefficient used during measurements. The extreme absorption coefficient produced large temperature gradients across the film and the node density could then be increased until the computed signals did not show significant changes. The nodes were distributed uniformly across the film area over which the photothermal signal was calculated. A distance between the nodes of $\Delta z = 0.2 \mu\text{m}$ across the film thickness ($12 \mu\text{m}$) and $\Delta r = 5 \mu\text{m}$ across the fibre radius ($200 \mu\text{m}$) was found to model the temperature distributions with sufficient accuracy and acceptable computation time. The model contained a total of 35000 nodes. In order to combine short computation times with adequate convergence of the solution, the node density was varied across the mesh. The node density in regions far from the polymer film was determined by a one-way bias, which distributed the nodes densely close to the sensing film and sparsely in areas distant from the film. To take account of radial heat diffusion, elements were used that created an axially symmetric mesh. This simplified a potentially very complex 3D problem to a two-dimensional problem, which also greatly reduced computation time.

6.1.1 The finite element model for the interpretation of measurements on non-scattering liquid absorbers

The initial temperature distribution in a non-scattering absorber was calculated using the Lambert-Bouguer law. The initial nodal temperatures were computed according to the coordinates of each individual node. A schematic of the illumination geometry of the optical fibre sensor is given in Figure 6.2.

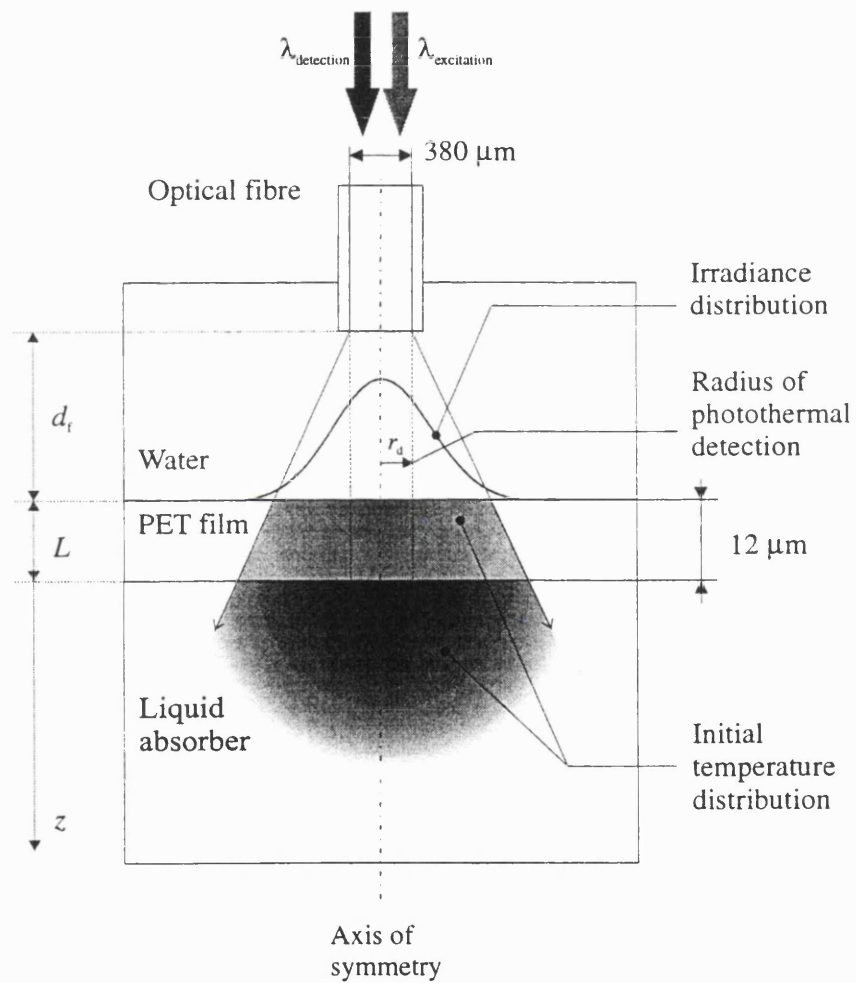


Figure 6.2 *Illumination geometry of the optical fibre sensor.*

The polymer film and the adjacent absorbing target are illuminated by the divergent light exiting a low numerical aperture optical fibre (N.A. = 0.12). Verdaasdonk *et al* have found that the irradiance distribution produced by a multimode optical fibre changes from a uniform irradiance across the radius at the tip of the fibre (top-hat profile) to a Gaussian distribution with increasing distance from a plain cleaved fibre tip¹⁴⁹. According to Verdaasdonk *et al*, a Gaussian distribution can be assumed at a distance of about eight times the fibre radius. In the optical fibre sensor, the fibre tip is positioned at a distance of 0.2 - 0.5 mm from the film and the fibre has a radius of 190 μm for which a combination of a Gaussian and top-hat irradiance distribution could apply. The irradiance distribution of a 400 μm optical fibre was measured using a CCD camera.

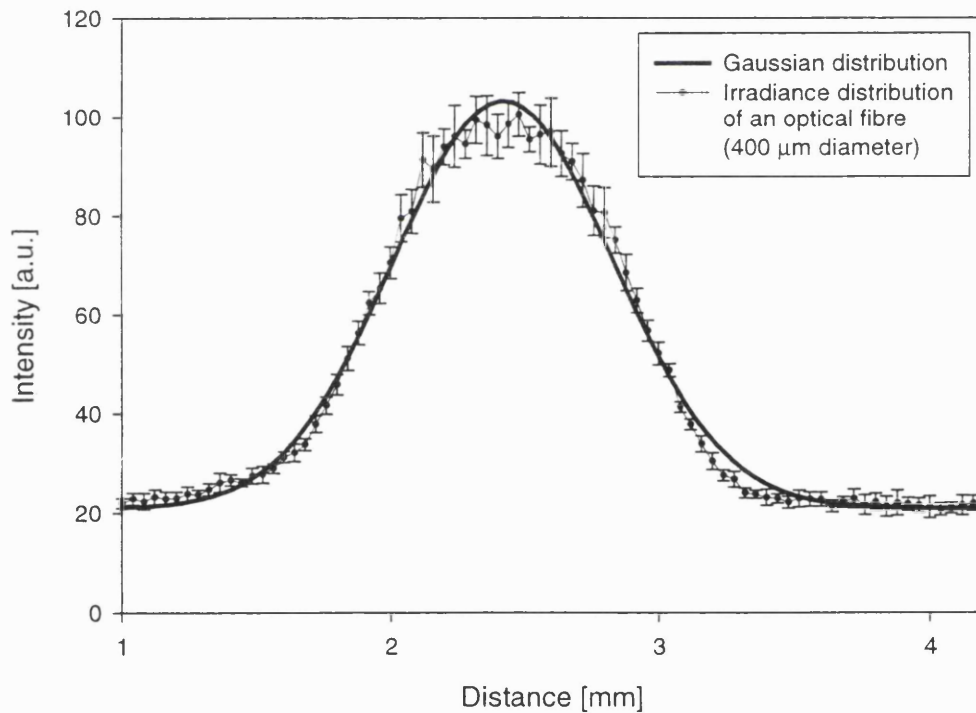


Figure 6.3 Intensity distribution of light exiting a 400 μm multimode fibre at a distance of 10 mm from the fibre tip. The error bars represent the standard deviation of eight measurements.

The distance between the tip of the optical fibre and the CCD could not be reduced to less than 10 mm due to a glass window, which could not be removed from the camera. A closer separation would have been advantageous for a more accurate measurement of the irradiance distribution of the fibre. The measurements (Figure 6.3) confirmed that a Gaussian irradiance distribution exists in the far field of the optical fibre. Since the sensing film and the target were typically positioned at smaller distances to the fibre than eight times its radius, both a Gaussian and modified Gaussian were used to compute photothermal signals. A Gaussian beam profile was used in the FEM to describe the energy distribution of the incident light for the excitation and detection wavelength as given in equation (6.1)

$$E(r) = E_0 \exp(-2r^2 / w^2) \quad (6.1)$$

where r is the distance from the axis, E_0 is the fluence at $r = 0$, w is the e^{-2} radius of the Gaussian profile. The difference between the signals was insignificant and a pure Gaussian, which is also amenable to the analytic manipulations that are described in the next paragraph, was used for all following investigations.

The delivered pulse energy E_p is the volume under the Gaussian and is obtained through integration (equation (6.2)).

$$E_p = 2\pi E_0 \int_0^w \exp(-2r^2 / w^2) r \, dr \quad (6.2)$$

The peak fluence E_0 can be obtained from equation (6.2) by solving the integral for $r = 0$. The solution is shown in equation (6.3):

$$E_0 = \frac{2 E_p}{\pi w^2 (1 - e^{-2})} \quad (6.3)$$

The peak fluence E_0 at depth z is also affected by the divergence of the beam, which is incorporated by multiplying the pulse energy by the ratio of the area of the optical fibre ($A_{\text{fib}} = \pi w^2$) at $r = 0$ and the area of illumination A at depth z . The dependence of area A on depth z can be obtained for the case of illumination by the divergent beam from a fibre using

$$A(z) = \pi (r_f + z \tan(\alpha))^2 \quad (6.4)$$

where r_f denotes the fibre core radius and α half the divergence angle of the beam, which can be calculated from the numerical aperture of the fibre $\alpha = \sin^{-1}(\text{N.A.})$. The peak fluence at depth z is therefore:

$$E_0 = \frac{2 E_p}{(1 - e^{-2}) A(z)} \quad (6.5)$$

Substituting equation (6.5) into equation (6.1), yields an expression for the divergent irradiance distribution of the light exiting the fibre depending on radius and depth:

$$E(z, r) = \frac{2 E_p}{(1 - e^{-2}) A(z)} \exp(-2r^2 / w^2). \quad (6.6)$$

Measurements using the sensor in distilled water have shown that a portion of the incident excitation pulse energy is deposited in the film, causing an immediate phase modulation. The photothermal signal is therefore a superposition of the phase modulation generated in the sensing film and additional contributions from thermal transients from the adjacent media. The transmitted light intensity and hence initial temperature rise in the film and the target is reduced by Fresnel reflections due to refractive index mismatches at the film interfaces. For the polymer film, the incident optical energy as given in equation (6.6) is reduced by the reflections from the first interface and the transmitted energy is calculated using

$$E(z, r)(1 - r_1) \quad d_f \leq z < d_f + L \quad (6.7)$$

where r_1 is the reflection coefficient of the first optical boundary. Neglecting multiple reflections in the transparent polymer film, the pulse energy transmitted to the absorber is given by

$$E(z, r)(1 - r_1 - (1 - r_1) r_2) \quad z \geq d_f + L \quad (6.8)$$

where r_2 is the reflection coefficient at the interface of film and absorber.

The excitation laser pulse coming from the optical fibre first undergoes a small attenuation in the water at the back of the sensing film. The initial temperature rise in the water T_w between the fibre tip and the polymer film is the result of absorption of the incident light and the light reflected from the surface of the sensing film. The temperature distribution due to the light coming from the optical fibre is given by equation (6.9)

$$T(z, r) = \frac{E(z, r) \mu_{a(w)}}{\rho_w c_w} \exp(-\mu_{a(w)} z) \quad 0 \leq z < d_f \quad (6.9)$$

where ρ_w is the density, c_w is the specific heat capacity, $\mu_{a(w)}$ is the absorption coefficient of water and d_f is the distance between fibre and film. The temperature due to the absorption of the light reflected at the first interface of the film is denoted as T_{r1} and is calculated using equation (6.10)

$$T_{r1}(z, r) = \frac{E(z, r) \mu_{a(w)} r_1}{\rho_w c_w} \exp(-\mu_{a(w)} d_f - \mu_{a(w)} (d_f - z)) \quad (6.10)$$

$$0 \leq z < d_f$$

For a PET film in contact with water, a fraction of 1.1% of the incident light is reflected at each interface. Subsequent multiple reflections are therefore quickly reduced in intensity and can be neglected. The contributions of the Fresnel reflections to the temperature in the sensing film are very small for highly transparent materials such as PET and could perhaps be neglected. The reflections would have a significant effect, however, if a more absorbing sensing material was used. The temperature in the water at the back of the film T_w is the sum of equations (6.9) and (6.10):

$$T_w(z, r) = T(z, r) + T_{r1}(z, r) \quad 0 \leq z < d_f \quad (6.11)$$

The temperature distribution in the sensing film T_f dependent on depth z and radius r is calculated as

$$T_f(z, r) = \frac{E(z, r) \mu_{a(P)}}{\rho_1 c_1} \exp(-\mu_{a(w)} d_f - \mu_{a(P)} (z - d_f)) + T_{r2}(z, r) \quad (6.12)$$

$$d_f \leq z < d_f + L$$

where $\mu_{a(P)}$ is the absorption coefficient, ρ_1 is the density and c_1 is the specific heat capacity of the polymer film. T_{r2} is the temperature increase due to light reflected at the second optical boundary which can be calculated in a similar manner as illustrated in equation (6.10). The initial temperature distribution in a non-scattering absorber T_a adjacent to the sensing film illuminated by a divergent beam is given by

$$T_a(z, r) = \frac{E(z, r) \mu_a}{\rho_2 c_2} \exp(-\mu_{a(w)} d_f - \mu_{a(P)} L - \mu_a (z - d_f - L)) \quad (6.13)$$

$$z \geq d_f + L$$

where ρ_2 is the density and c_2 is the specific heat capacity of the absorber. Equations (6.11), (6.12) and (6.13) were used to assign initial temperatures to individual nodes according to their position in the mesh. The subsequent computation of transient heat conduction was performed using a finite element software package called Abaqus. The photothermal signal was calculated by integrating the calculated temperatures across the film thickness and the fibre core radius for each time increment. The temperatures were weighted by the Gaussian intensity distribution of the sensing light across the film and the area of illumination as given in equation (6.14)

$$S(t) = K\pi \int_{d_f}^{d_f+L} \int_0^{r_f} \left((r + \Delta r)^2 - r^2 \right) \exp(-2r^2 / w^2) T_n(z, r, t) dz dr \quad (6.14)$$

$$d_f \leq z \leq d_f + L \quad r \leq r_f$$

where $S(t)$ is the photothermal signal, K is the system response constant, which includes the thermal expansion coefficient, pulse energy, sensor sensitivity and other amplitude-related parameters, r is the radius, Δr is the radial distance between the nodes, r_f is the fibre core radius and T_n is the nodal temperature. Figure 6.4 shows theoretical thermal signals calculated for different μ_a using the FEM of the optical fibre sensor configured with a 12 μm PET film in contact with a water-based absorber. The effect of radial heat diffusion manifests itself in a generally faster decay of the signal compared to one-dimensional heat conduction as observed in pulsed photothermal radiometry.

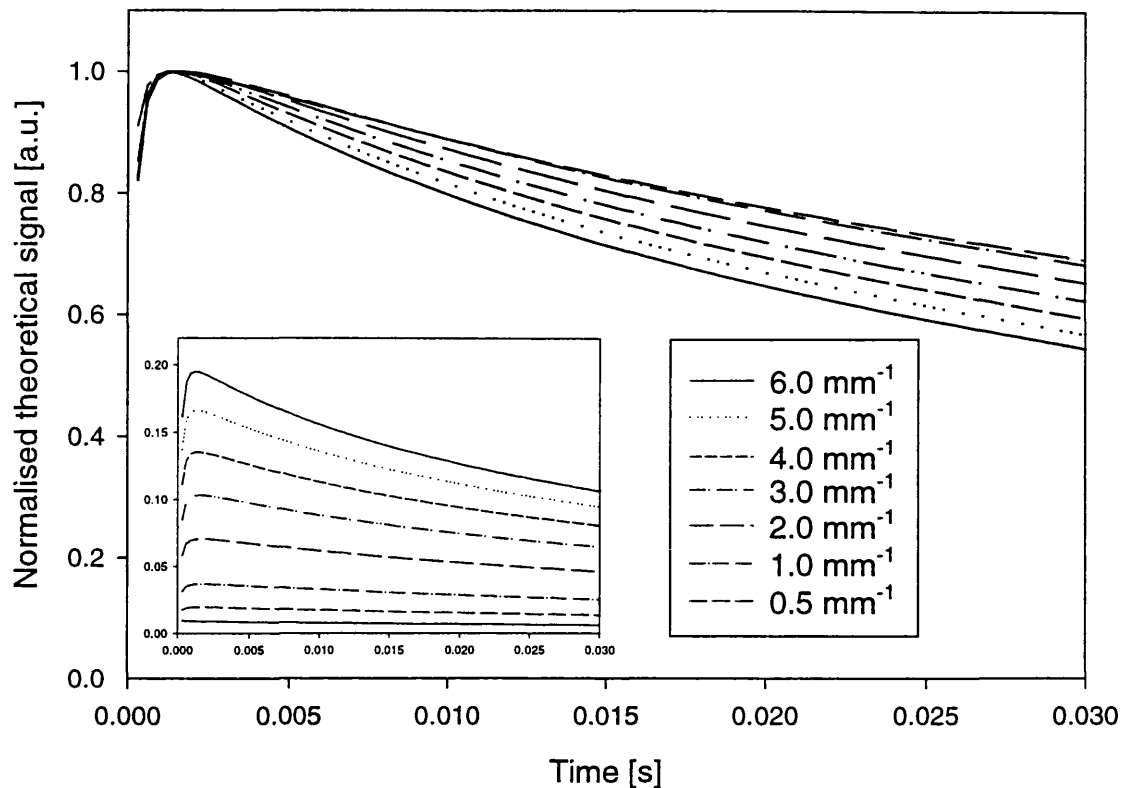


Figure 6.4 Theoretical photothermal signals calculated for different μ_a and a film thickness of $12 \mu\text{m}$ using the finite element model of the optical fibre sensor. The inset shows the rise in amplitude of the photothermal signal with increasing absorption coefficient.

The photothermal response is characterised by an initial increase of the signal and a subsequent decrease, which is produced by an initial temperature in the target that is larger than the temperature in the polymer film as illustrated in Figure 6.5. Heat conduction from the target into the polymer film produces an initial increase in the photothermal signal, as shown in Figure 6.4. The rate of the increase is dependent upon the absorption coefficient. An increase in the absorption in the target produces a faster initial increase of the signal. The shape of the decay, however, does not vary greatly between signals that were calculated using different absorption coefficients (Figure 6.4). Later times are characterised by gradual cooling of smooth temperature distributions that are devoid of large gradients. This suggests that later times ($t > 20 \text{ ms}$) of the photothermal signal do not provide as much information on the initial conditions and hence optical coefficients as times shorter than 20 ms.

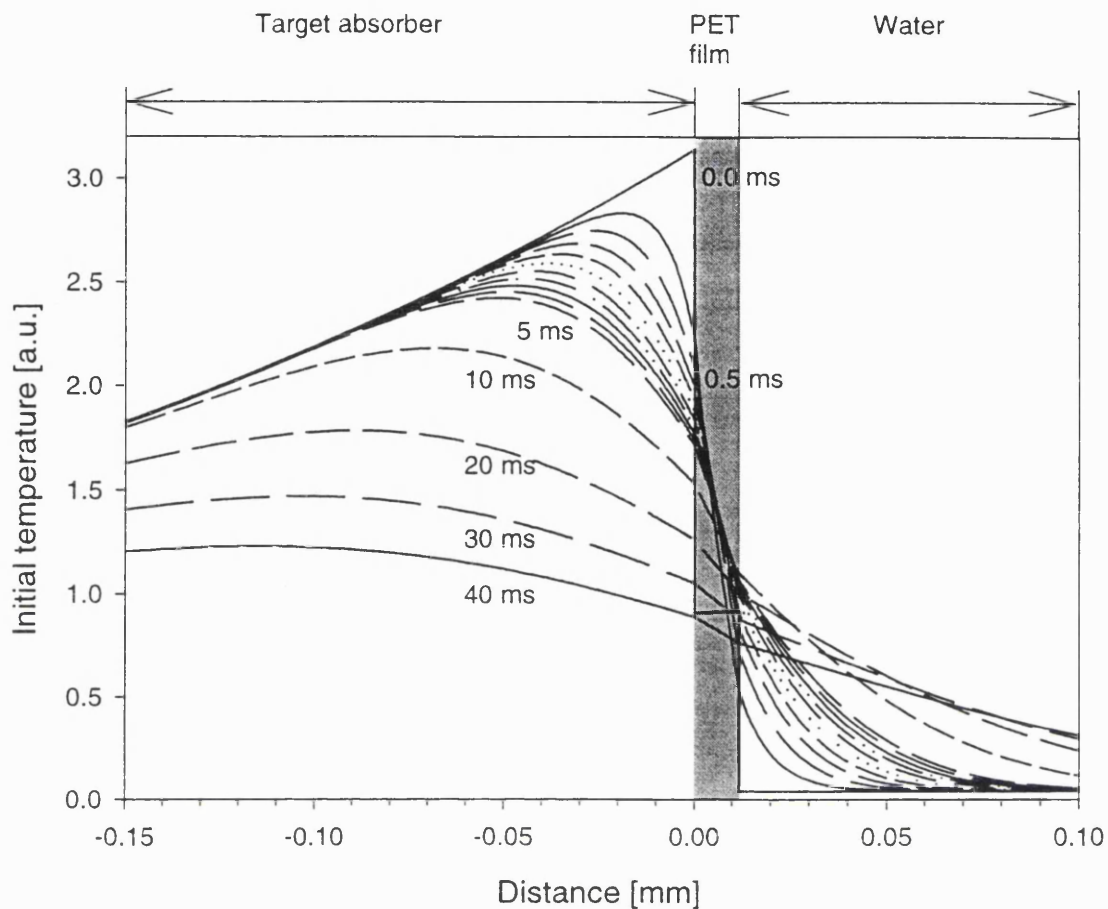


Figure 6.5 Computed temperature profiles across the target absorber and water-backed polymer sensing film at different times. The absorption coefficient of the target was 3.0 mm^{-1} and the absorption coefficient of the polymer film was 0.25 mm^{-1} . The excitation light is assumed to be incident from the right hand side.

On the basis of these results, the determination of optical coefficients from photothermal signals of the optical fibre sensor could be limited to times shorter than 20 ms. This, however, would also result in the limitation of photothermal investigations to shallow depths. The depth to which a target can be probed photothermally is equal to the thermal diffusion length μ_D , which can be obtained from equation (6.15) below

$$\mu_D = \sqrt{2\alpha t} \quad (6.15)$$

where α is the thermal diffusivity and t is the duration of the measurement. For a measurement of 20 ms duration, the thermal diffusion length in a water-based medium is

approximately 82 μm . Optical coefficients could therefore only be obtained from depths smaller than 82 μm . Analysing measurements using an extended time window of 0 to 40 ms would result in a thermal diffusion length of 116 μm . The extended time window would allow the analysis of early parts of the signal. This would give an insight into the properties of very superficial layers of the target, while the analysis of later times of the photothermal signal could yield information on optical coefficients of deeper layers.

6.1.2 Hybrid Monte Carlo/Finite Element model for measurements on turbid media

The principal aim of the development of the optical fibre sensor is its use for determining absorption and scattering coefficients of tissue. The calculation of the light distribution and hence initial temperature distribution in tissue therefore requires the modelling of light transport in turbid media. Various methods could be employed, ranging from accurate numerical models to less accurate analytical approximations. The Monte Carlo (MC) method (see also section 1.3.1.1) was chosen to compute the distribution of deposited photon energy in a scattering medium. MC models represent the most accurate description of light transport in turbid media especially at shallow penetration depths where analytical models, such as the diffusion approximation of radiative transport show inaccuracies¹⁵⁰. A MC model is a stochastic method which simulates the paths taken by photons in the tissue where they undergo scattering and absorption events according to probabilities given by the scattering and absorption coefficients. The degree of scattering anisotropy is described by assigning a value between 0 and 1 to g , which represents the mean cosine of the scattering angle.

An existing MC model¹⁵¹ was adapted to simulate the diverging beam from an optical fibre. The original program was altered in order for it to vary the launch angle of the photons randomly between normal incidence and the divergence angle of the fibre. The model simulated the propagation of photon packets for an axially symmetric geometry in which the target could have various layers of different optical properties. The scattering anisotropy could also be varied by assigning different values to g . The strong forward

scattering found in tissue in the near-infrared wavelength range could be incorporated by setting the mean cosine of the scattering angle to $g = 0.9$ ^{152,153}.

The MC program also took account of effects of specular reflections on the light distributions by allowing for a refractive index mismatch at the interface between the water and the polymer film. In the MC model, the polymer film was considered to be a non-scattering, weakly absorbing layer on the target. This configuration ensured that multiple reflections in the film were taken into account. The absorbed energy density obtained from the MC model was listed in a two-dimensional array for depth z and radius r . A convolution program¹⁵⁴ re-calculated the energy density distribution according to the dimensions of a Gaussian beam of finite diameter and a given pulse energy. The temperature distribution was determined from the energy density as shown in equation (6.16)

$$T_0(z, r) = \frac{Q(z, r)}{\rho c} \quad (6.16)$$

where T_0 is the initial temperature rise, $Q(z, r)$ is the energy density distribution and ρc is the specific heat per unit volume of the tissue. The temperature distribution in the turbid medium was then incorporated into the FEM. The initial temperature increase in the sensing film and the water which backed the film was calculated using equations (6.11), (6.12) and (6.13), which were described in section 6.1.1. The total initial temperature rise in film and water was obtained by adding the temperature rise due to the incident light from the optical fibre and the contributions of diffuse light that is back-scattered from turbid media. The intensity of the back-scatter was calculated from the diffuse reflectance of the target, which is one of the results of the MC simulations, weighted by the reflection coefficient r_1 . The initial temperature distribution was incorporated into the FEM and transient heat conduction calculation and subsequent computation of the photothermal response was carried out in analogy to that of the absorbing-only case.

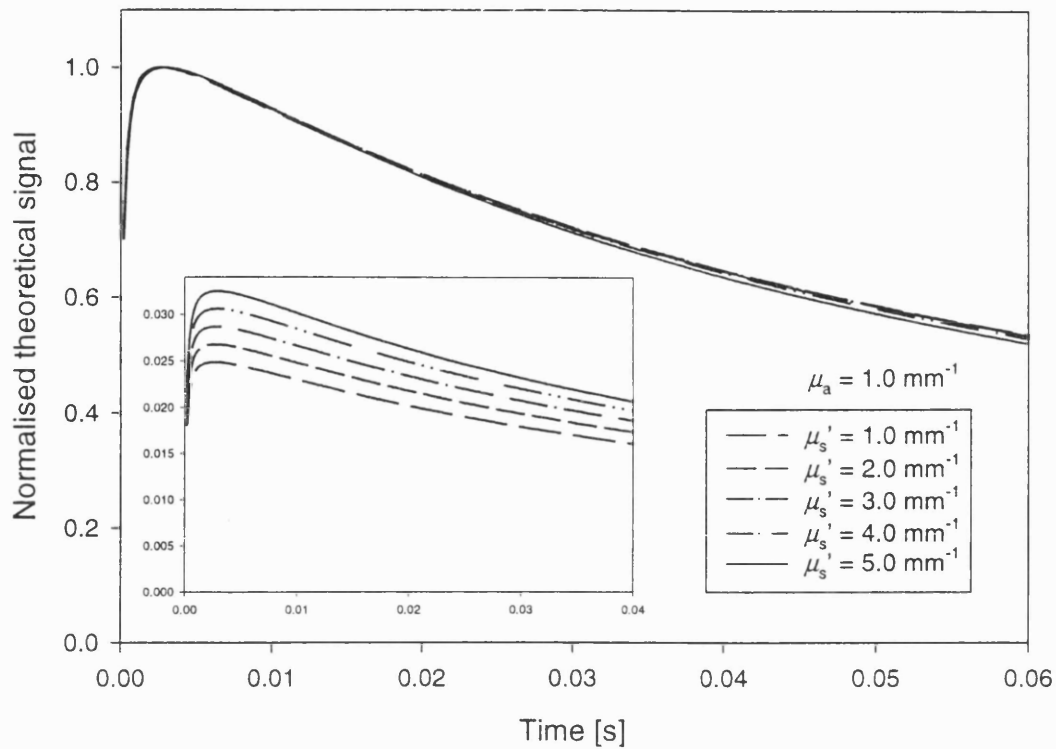


Figure 6.6 Theoretical plots of photothermal responses calculated for different reduced scattering coefficients using the finite element model. The absorption coefficient was held constant.

Figure 6.6 shows theoretical plots calculated using the hybrid Monte Carlo/finite element model for different combinations of optical coefficients. An increase in amplitude and a slightly faster decay are due to the decreased penetration depth of the light, which is produced by an increase in the scattering coefficient. The small effect of μ_s' on the shape of the signal suggests that the determination of the reduced scattering coefficient from photothermal signals will be reliant on the amplitude rather than the temporal characteristics of the signals. The numerical model of the sensor will be applied to the determination of optical coefficients from photothermal signals in conjunction with model-based parameter estimation, which is discussed in the following section.

6.2 Model-based parameter estimation

The application of the optical fibre sensor to determine optical coefficients of tissue has the inherent problem that the coefficients are obtained from the very indirect measurement of thermally induced thickness changes of the sensing film. During a photothermal measurement a number of processes occur, in which one physical quantity is converted to another, i.e. optical energy to heat, heat to thermal expansion etc. These processes contribute to a situation in which the quantity one is interested in becomes remote from the quantity that is measured, which in turn contributes to a larger uncertainty in the determined quantity. Model-based parameter estimation can be used to obtain information from indirect measurements and provides statistical tools for the extraction of information from data using mathematical models. Parameter estimation can incorporate the uncertainties in all properties that are involved in the measurement and estimate the parameter of interest together with an estimate of the uncertainty of the parameter. The estimated uncertainty is based on the uncertainty of all other parameters that may have played a role in the measurement. Model-based parameter estimation (MBPE) is a method for estimating constants that appear in models and for aiding of modelling of phenomena. The aim of MBPE can be described as the determination of a set of parameters that are most likely to have produced a particular measurement.

MBPE is an extension of other parameter estimation techniques, usually referred to as curve-fitting or χ^2 minimisation, which can be used to obtain coefficients from experimental data. A χ^2 minimisation technique was, for example, applied to the determination of the optical coefficients from the radiometric photothermal signal as discussed in chapter 4. χ^2 minimisation was used to obtain parameters as well as their confidence limits but it is also characterised by the use of constants for model parameters which may vary from one measurement to another. The ‘constants’ may therefore have an uncertainty, which would influence the estimated parameter and its confidence limit. MBPE is a more rigorous approach in which all parameters that could have an effect on the experimental observation are included in the parameter estimation. Moreover, the parameters enter the estimation procedure with an initial uncertainty that will affect the final uncertainty of the parameters one is interested in.

MBPE can also be described as a study of inverse problems. In the inverse problem, such as in the case of the photothermal sensor, not all constants of a model are known. Instead, the values of the constants, also called parameters, are estimated from indirect measurements using MBPE. MBPE utilises minimisation or optimisation techniques where model parameters are being varied in order to achieve minimal discrepancy between the experiment and the model predictions. The minimisation of the difference between experiment and model prediction produces a set of parameters with a maximum likelihood of representing the unknown 'true' constants. In the following section, the concept of MBPE and the maximum a posteriori estimation in particular are discussed. The discussion of the theoretical concepts is taken from a publication by Beck¹⁵⁵.

6.2.1 Model in matrix terms

It is assumed that the model represents a smoothly varying function of the parameters and that the model can be linearised around a set of parameters β . The linear output of the model is the dependent variable η and can be calculated using

$$\eta = X \beta \quad (6.17)$$

where X is the design matrix, which contains the derivatives with respect to the parameters. η is a vector of dimensions $[n \times 1]$, where n is the number of observations, X is a $[n \times p]$ matrix and β is a $[p \times 1]$ vector, where p is the number of parameters.

6.2.2 Linear maximum a posteriori estimation (MAP)

Maximum a posteriori estimation is a variation of general model-based parameter estimation. MAP uses prior information regarding the parameters as well as information regarding the measurement errors. Incorporation of prior knowledge reduces the initial uncertainties in the parameters to a greater extent than estimation methods that ignore prior information. This information is based on the belief of the investigator and typically includes mean values and variances. The knowledge of these parameters is probabilistic, i.e. the parameters are viewed to have probability distributions.

6.2.2.1 Assumptions

In MAP a number of simplifying assumptions are made:

1. Additive errors in the measurements

The error in the measurement is dependent upon the individual sources of error and can be combined to one value.

2. *Zero mean measurement errors*

The measurement errors have no systematic bias.

3. *Uncorrelated variances*

The measurement errors of a photothermal signal at a particular point in time do not depend on errors at any other point in time.

4. *Errors have normal distribution*

The error distribution is Gaussian. This assumption may not be true, for example if the measurement is affected by sporadic electrical noise spikes.

5. *Errorless independent variables*

The errors in the values of time are negligible.

6. *Parameters are constants but are unknown. There is subjective prior information on the parameters.*

6.2.2.2 *Estimation involving subjective information*

Maximum a posteriori parameter estimation is used to obtain a set of parameters that maximises the probability density function of Y given β , $f(Y | \beta)$, where Y represents the $[n \times 1]$ vector of measured observations. $f(Y | \beta)$, which is given in equation (6.18), associates a probability density to each experimental value for Y given a fixed parameter vector β :

$$f(Y | \beta) = (2\pi)^{-n/2} |\psi|^{-1/2} \exp \left[-\frac{1}{2} (Y - \eta)^T \psi^{-1} (Y - \eta) \right] \quad (6.18)$$

where ψ is the $[n \times n]$ covariance matrix of the measurement errors.

In the maximum likelihood method, which can be seen as a less rigorous technique compared to MAP estimation, the probability density function is redefined as a likelihood function and directly used to obtain parameter estimates. The likelihood function has the

same form as $f(Y | \beta)$ but the measurement values Y are considered constant, while the parameters β are variable. Through maximisation of the likelihood function illustrated in Figure 6.7, a set of parameters can be obtained which represent the closest match to the experimental observation and are therefore the most likely parameters to have led to measurement Y .

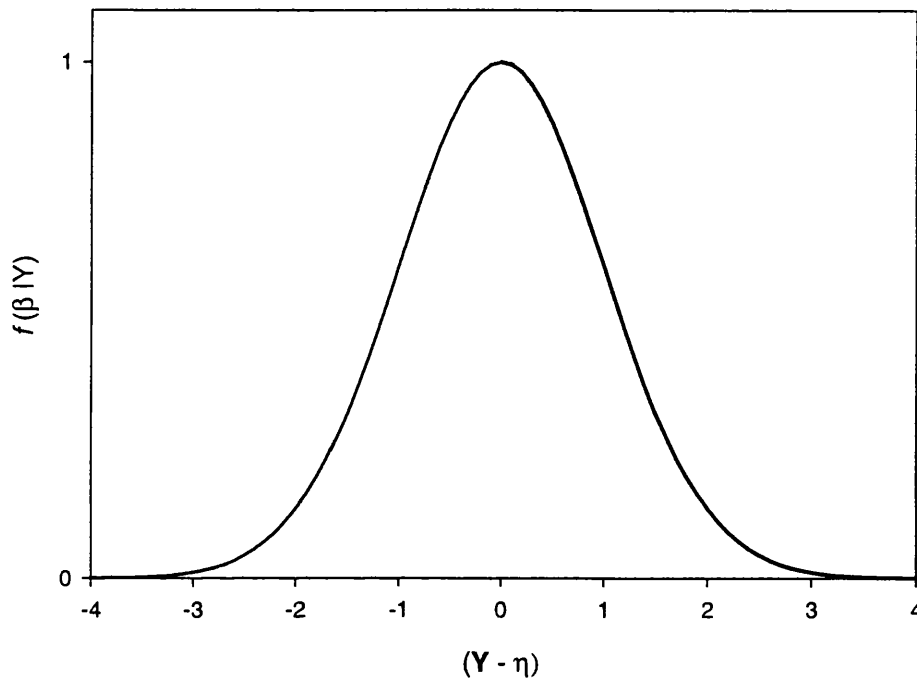


Figure 6.7 Qualitative graph of the probability density function $f(Y | \beta)$ which has a maximum where the difference between the experimental observations and model predictions is equal to zero. Through maximisation of $f(Y | \beta)$, values for β can be obtained, which might have led to measurement Y .

In MAP estimation, a form of Bayes's theorem is applied. Bayesian inference allows the inference of information when some additional knowledge about the case of investigation is available. The probability density function $f(Y | \beta)$ is related to $f(\beta | Y)$, the probability of β given Y , and the random parameter probability density $f(\beta)$ by

$$f(\beta | Y) = \frac{f(Y | \beta) f(\beta)}{f(Y)} \quad (6.19)$$

$f(\beta)$ expresses the knowledge or belief regarding the parameters and is given by

$$f(\beta) = (2\pi)^{-p/2} |V_\beta|^{-1/2} \exp\left[-\frac{1}{2}(\beta - \mu_\beta)^T V_\beta^{-1} (\beta - \mu_\beta)\right] \quad (6.20)$$

where V_β is the $[p \times p]$ covariance matrix of the parameters, and μ_β is the $[p \times 1]$ prior parameter vector based on subjective information. This information is assumed to originate from investigations, from literature or other sources. The prior information about the parameters is therefore considered independent from the new information that is contained in the measurements Y . The probability distribution of $f(Y)$ does not need to be given explicitly since it is not dependent upon β . To illustrate the concept of MAP estimation, equation (6.19) is rewritten as

$$f(\beta | Y) = K \exp\left[-\frac{1}{2}\left(\frac{(Y - \eta)^2}{\psi} + \frac{(\beta - \mu_\beta)^2}{V_\beta}\right)\right] \quad (6.21)$$

Maximisation of equation (6.21) is affected by the degree of prior knowledge that is incorporated in the form of the covariance matrix V_β . When the uncertainty in the parameters is small, the covariance matrix will also be small and the bracketed quantity is dominated by the second term. This produces estimated parameters that are very close to the initial values. The second term therefore attracts the estimated parameters in order to accommodate the prior knowledge. If the parameter is not known to a small degree of accuracy, the initial uncertainty will be large and the term that represents the prior knowledge will be small. The subsequent estimation will then be equivalent to a standard least-squares fit.

Equation (6.19) can be maximised by applying the natural logarithm:

$$\ln [f(\beta | Y)] = -\frac{1}{2} \left((n + p) \ln 2\pi + \ln |\psi| + \ln |V_\beta| + S_{\text{MAP}} \right) \quad (6.22)$$

with

$$S_{\text{MAP}} \equiv (Y - \eta)^T \psi^{-1} (Y - \eta) + (\beta - \mu_\beta)^T V_\beta^{-1} (\beta - \mu_\beta) \quad (6.23)$$

The maximum of equation (6.22) occurs at the same parameter values as $f(\beta | Y)$. Since the parameters of interest only occur in S_{MAP} , equation (6.22) can be maximised by minimising equation (6.23). Solving equation (6.23), which is described in more detail in Beck¹⁵⁵, yields an expression for the estimated parameter vector b_{MAP} :

$$b_{\text{MAP}} = \mu_{\beta} + P_{\text{MAP}} X^T \psi^{-1} (Y - X \mu_{\beta}) \quad (6.24)$$

with

$$P_{\text{MAP}} = (X^T \psi^{-1} X + V_{\beta}^{-1})^{-1} \quad (6.25)$$

The variance of the estimated parameters is not only affected by the errors in the measurement but also by the uncertainty of the prior parameters. The variance of the difference of the estimated and initial parameters is therefore of interest, which is given without derivation:

$$\text{COV}(b_{\text{MAP}} - \beta) = P_{\text{MAP}} = (X^T \psi^{-1} X + V_{\beta}^{-1})^{-1} \quad (6.26)$$

The estimated parameter covariance is an important value, since it represents the degree by which the knowledge of the parameters has increased through using MBPE. For example, if the uncertainty for an estimated parameter is large and has not been reduced significantly compared to the initial uncertainty, any other parameter value within the interval would have produced a similar agreement with the measurement. The final value of the parameter is therefore of small importance and the insignificant reduction of the initial uncertainty suggests that the knowledge in the parameter has not been increased.

6.2.3 Implementation of the minimisation algorithm

MAP estimation relies upon the linearisation of the FEM around a set of initial parameters and the subsequent evaluation of the matrix equations, as described in the previous section. While this treatment may be sufficient for linear systems or systems with only a slightly varying gradient, it poses problems for highly non-linear cases. Here, the slope obtained through linearisation of the model is not even correct at the start of each step, as illustrated in Figure 6.8.

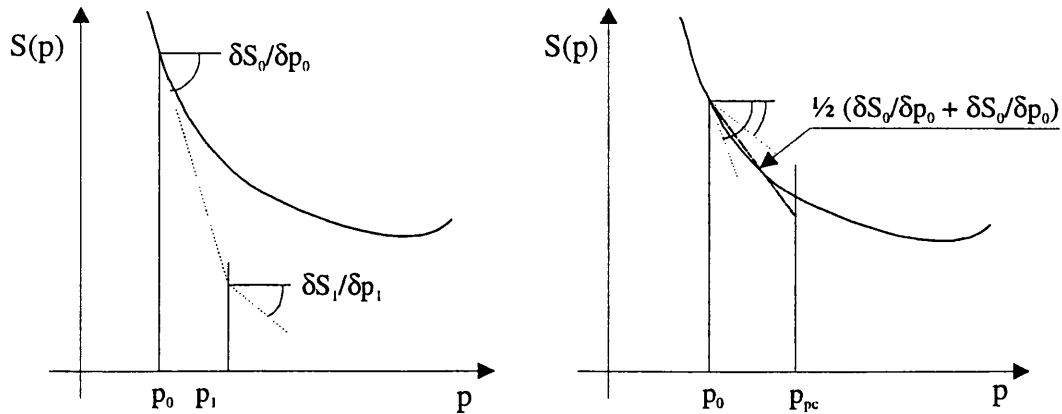


Figure 6.8 Implementation of the predictor-corrector method in which an average parameter derivative obtained from two subsequent estimations is used to predict the final parameter.

To avoid large errors in the estimated parameters, the so-called predictor-corrector method has been applied to this problem. In this method, an average gradient for each step is calculated by computing the design matrix for a set of initial parameter values. MAP estimation is applied to estimate a set of new parameters, for which the design matrix is again computed. The final set of parameters is estimated using MAP based on the initial parameters by calculating the average gradient of the two design matrices. This way the errors associated with the linearisation of a non-linear model are minimised. Convergence of the measurement and the model and hence the likelihood of the parameters can be improved by repeating the predictor-corrector estimation a number of times.

The estimation procedure was extensively tested using model data to ensure numerical accuracy. MAP estimation was able to estimate individual parameters, the initial value of which had been altered by up to 30%, with errors typically less than 1% in a single step. All other parameters had been frozen using very small initial uncertainties. The algorithm was further tested with a 20% increase in two of the twelve parameters. The error in the estimated values after a single step was again low at $< 0.1\%$ compared to the true values. Significant errors occurred in the case of a 20% increase in all parameters. MAP estimation was unable to predict the true values to less than 5%. This is perhaps not

surprising, since the parameter values represented a situation in which none of the model parameters were known accurately and had starting values far away from the convergence minimum.

In order to assess the accuracy of the estimated uncertainties of the parameters, two initial parameters were assigned large initial variances and the new parameters and their uncertainties were computed. In a second run, one of the two parameters was assigned a smaller uncertainty. The result showed a reduction in the final uncertainty in the other parameter. This test demonstrated that the increase in the knowledge of any particular parameter is dependent upon the uncertainties of the remaining model parameters.

Some of the model parameters that were included in MBPE were found to have an insignificant effect on the theoretical signal. In order to reduce computation time and to focus the analysis on parameters that have a significant effect on the photothermal signal, the gradients contained in the design matrix were normalised by typical uncertainties in the parameters, which were based on prior information taken from published work. The normalised gradients, or parameter sensitivities, showed that parameters such as the thermal coefficients of the polymer film did not affect the shape of the photothermal signal significantly. All parameters that produced similarly small gradients were excluded from the estimation. The model parameters that were eventually included in the estimation procedure were the optical and thermal coefficients of the target, the signal amplitude, and the absorption coefficient and the thickness of the polymer sensing film.

6.3 Sensitivity of the photothermal signal to changes in the model parameters

The gradients contained in the design matrix also allowed an assessment of the sensitivity of the photothermal signal to variations in the thermal and optical coefficients of tissue. This analysis is particularly useful for the envisaged application of the optical fibre sensor to *in vivo* tissue measurements. Since the diagnosis of malignant tumours is intended to be based on the detection of differences in the optical coefficients of tissue, it would be advantageous if the photothermal signal was more sensitive to the absorption and scattering

coefficients than to the thermal properties of tissue. Thermal coefficients of tissue measured *in vitro*¹⁵⁶ and *in vivo*¹⁵⁷ have been shown to have a large variance ($\pm 30\%$ compared to coefficients of water) and may therefore affect the shape of the photothermal signal more strongly than typical differences in the optical properties of normal and cancerous tissue. The normalised parameter sensitivity, S_p , was calculated by multiplying the gradients contained in the design matrix, $\delta S/\delta p$, with the typical uncertainty in the parameter, u :

$$S_p = \frac{\delta S}{\delta p} u \quad (6.27)$$

The uncertainties in the model parameters were taken from published data on the optical and thermal properties of tissue. The uncertainty in the thermal conductivity, specific heat and density are based on the range of values presented in section 2.5. The uncertainty in the absorption and reduced scattering coefficient at was based on *in vitro* measurements made by the author on tumours and normal surrounding tissue of the human kidney, liver and breast (see also section 1.5). The largest difference in the absorption and reduced scattering coefficient between normal and diseased tissue at 700 nm was used as a measure of the uncertainty on μ_a and μ_s' . The model parameters and their uncertainties are listed in Table 6.1:

<i>Parameter</i>	<i>Uncertainty</i>
μ_a [mm^{-1}] – absorption coefficient of target	± 0.2
μ_s' [mm^{-1}] – reduced scattering coefficient of target	± 0.5
μ_{a_PET} [mm^{-1}] – absorption coeff. of polymer film	$\pm 20\%$
K – calibration constant	$\pm 20\%$
k_{Tissue} [$\text{W mm}^{-1} \text{K}^{-1}$] – thermal conductivity of tissue	$\pm 0.3 \cdot 10^{-3}$ (Valvano et al ¹⁵⁶)
c_{Tissue} [$\text{J g}^{-1} \text{K}^{-1}$] – specific heat capacity of tissue	± 0.67 ($\pm 16\%$ of c_{Water})
ρ_{Tissue} [g mm^{-3}] – density of tissue	$\pm 0.05 \cdot 10^{-3}$ ($\pm 5\%$ of ρ_{Water})
L_{film} [mm] – thickness of polymer sensing film	$\pm 2.0 \cdot 10^{-4}$ (ICI data sheet)

Table 6.1 Standard deviations applied to the calculation of the parameter sensitivities.

Since the design matrix contains the first derivatives of the photothermal signal for a number of increments in time, the normalised gradients can be used to assess at which times the photothermal signal is most sensitive to a particular parameter. The absorption coefficient of the polymer film was small compared to the absorption in the target. The thermal coefficients of the target were assumed to be equivalent to those of water. Figure 6.9 below shows the sensitivity of the calculated signal to changes in model parameters.

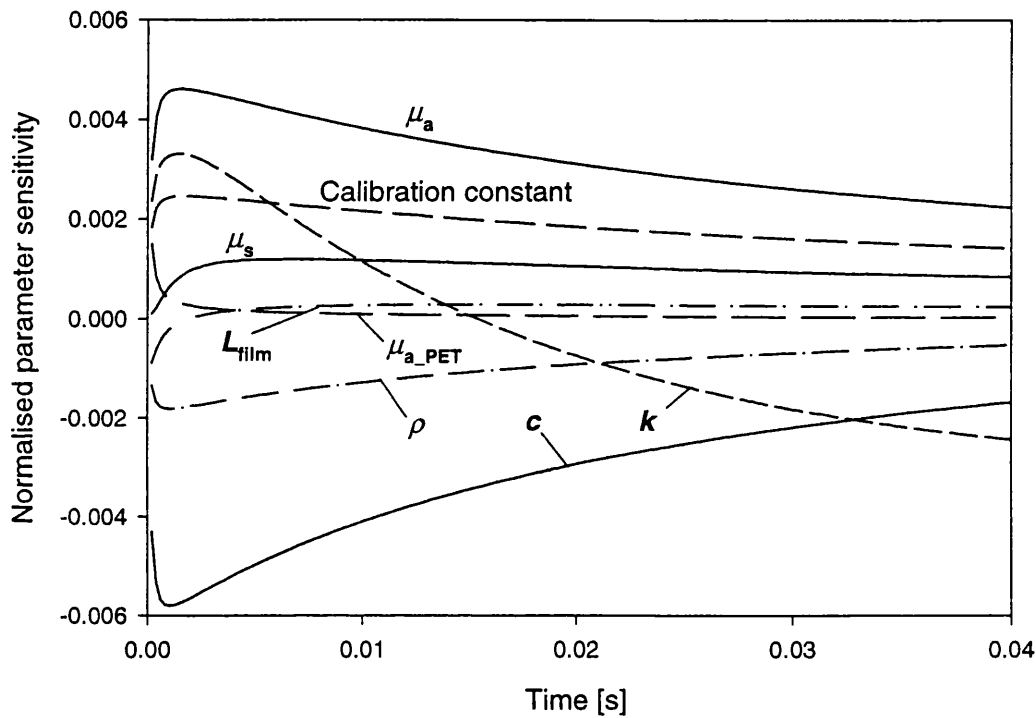


Figure 6.9 Sensitivities of all parameters included in MBPE calculated using typical uncertainties for measurements made on tissue.

The results shown in Figure 6.9 indicate that the absorption coefficient has a lesser effect on the photothermal signal than specific heat. The thermal conductivity, due to its large uncertainty also produces a significant effect on the photothermal signal, while parameters such as the absorption coefficient of the polymer film and its thickness produce low sensitivities. In fact, the sensitivity of the photothermal signal to the absorption coefficient of the polymer film is so small that the parameter could be neglected. The absorption by the

film does may important, however, when weakly absorbing targets such as tissue are investigated.

It should be borne in mind, that the normalised sensitivity of a parameter is proportional to its uncertainty as shown in equation (6.27). If the uncertainty in the thermal conductivity, density and specific heat of a particular type of tissue is small, then the sensitivity of the photothermal signal to k , ρ and c will be reduced, thereby improving the sensitivity to the optical coefficients. Since the effect of the optical parameters on the photothermal signal can not be increased easily, it is the uncertainty in the thermal tissue parameters that will determine the sensitivity of the optical fibre sensor to the optical coefficients. The uncertainty in the *in vivo* thermal coefficients of biological tissue therefore poses a significant problem for the determination of optical coefficients because the thermal properties are not only produced by the individual properties of the tissue constituents but also by physiological factors such as perfusion. Moreover, the calculated parameter sensitivities suggest that, in a worst-case scenario, a difference in the absorption coefficient from one type of tissue to another could be offset by a difference in the specific heat, for example. The uncertainty in parameters such as the pulse energy, the absorption coefficient of the film and film thickness can be reduced by making additional measurements and monitoring of the experimental set-up, which in turn will increase the normalised sensitivity of the optical parameters. Figure 6.9 also illustrates that the photothermal signal is most sensitive to changes in the optical and thermal parameters at early times. This indicates that the steep temperature gradients, which are produced by the distribution of the excitation light, are removed after approximately 20 ms. Times longer than 20 ms may therefore not contain much information on the optical coefficients.

6.4 Chapter summary

The numerical model of the optical fibre sensor allows the computation of theoretical photothermal signals for non-scattering absorbers and turbid media. Two models of light transport have been employed to calculate the initial temperature distribution – the Lambert-Bouguer law for pure absorbers and a stochastic Monte Carlo model for scattering

media. The initial temperature distribution is incorporated into a finite element model of transient heat conduction from which the theoretical photothermal signal is obtained.

Model-based parameter estimation is employed for the determination of the optical coefficients from experimental data. Parameter estimation incorporates prior knowledge of the parameters and the standard deviation of the experimental data to estimate a number of parameters, which include the optical and thermal coefficients of tissue. The reduction of the initial uncertainties of the parameters is the key criterion of the procedure, since it quantifies the increase in our knowledge of the parameters.

The analysis of the normalised parameter sensitivity has shown that the photothermal signal detected using the optical fibre sensor is as sensitive to changes in the thermal coefficients of tissue as it is to optical coefficients, if the uncertainties associated with *in vivo* measurements on tissue are large.

7 THE PHOTOTHERMAL OPTICAL FIBRE SENSOR – EXPERIMENTAL

In this chapter the optical fibre sensor is characterised in terms of its linearity, sensitivity and response time and is compared to a radiometric photothermal detector. The optical fibre sensor was used for photothermal measurements on non-scattering and turbid gelatine tissue phantoms. The absorption and reduced scattering coefficients were determined from the photothermal signals using model-based parameter estimation. Good agreement between the ‘known’ optical coefficients and the estimated values also served as a validation of the numerical model of the optical fibre sensor. The limitations of the technique due to the uncertainty in the thermal parameters are also assessed.

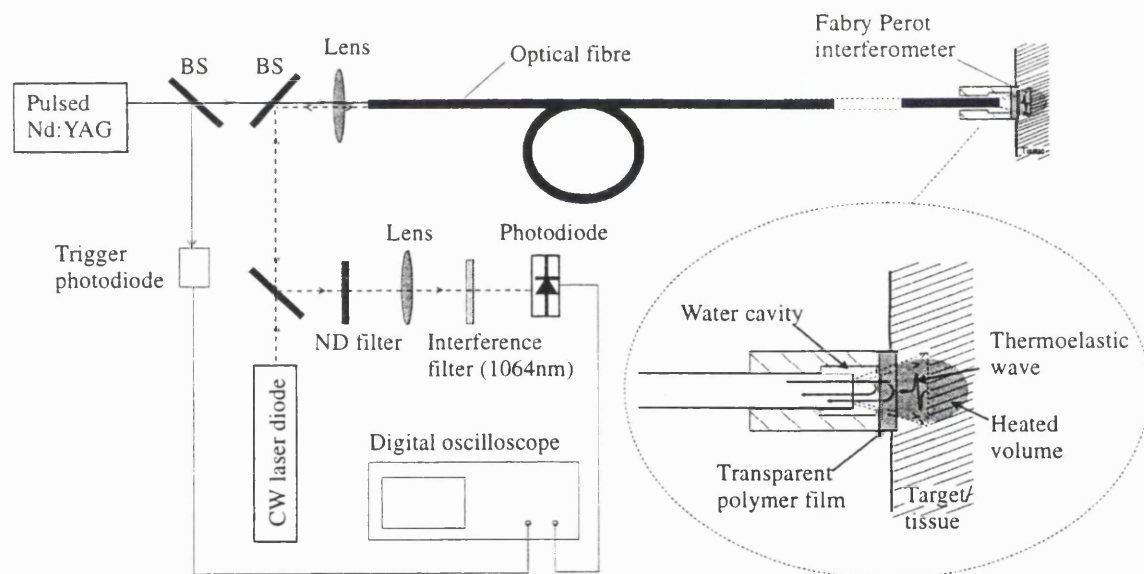


Figure 7.1 *Experimental set-up of the optical fibre sensor.*

Figure 7.1 shows the experimental set-up of the optical fibre sensor. A 12 μm PET film was mounted at a distance of approximately 0.2 – 0.3 mm in front of the distal end of a 10 m length of 400 μm multimode optical fibre of low numerical aperture (N.A. = 0.12). The

distal end of the optical fibre was plain-cleaved to ensure a smooth irradiance profile. A fixed-Q Nd:YAG laser (InnoLas Ltd., UK) was used to provide excitation pulses ($200 \mu\text{s}$, $\sim 0.04 \text{ J mm}^{-2}$) at 1064 nm. The outputs of the Nd:YAG laser and a continuous wave external cavity diode laser (774 - 794 nm, 11 mW) were launched into the optical fibre. The diode laser light illuminated the sensing film. The reflections from the faces of the film travelled back along the optical fibre and were incident on a 0.5 mm^2 15 MHz photodiode (Hamamatsu S6468). Interference filters were placed immediately in front of the photodiode to remove the 1064 nm excitation wavelength. A photodiode with a large active area would have been more suitable for photothermal measurements since it could provide higher sensitivity. It was found, however, that such photodiodes can be affected by the laboratory lighting and the measurements would have had to be carried out in the dark. It may have been possible to use large area photodiodes together with a bandpass optical filter. This was not necessary since the small area photodiode provided adequate sensitivity for photothermal measurements, while remaining unaffected by light sources other than the diode laser. The small active area provided a large bandwidth, which would have been sufficient for simultaneous photothermal and photoacoustic measurements. The fastest rise times of photothermal signals, however, are typically of the order of 0.15 ms and a bandwidth of 10 kHz was adequate. The limited bandwidth also improved the noise characteristics of the system by eliminating the high frequency components, which do not carry signal information. In the set-up used for the measurements, the cut-off frequency was limited to 10 kHz with an active low-pass filter. A 200 MHz digital oscilloscope (Tektronix TDS 360) was used to record the photothermal signals.

7.1 Performance of the optical fibre sensor

In this section, the characteristics of the optical fibre sensor as a temperature transducer are assessed.

7.1.1 Linearity

After setting the phase bias of the optical fibre sensor to quadrature, the head of the optical fibre sensor was immersed in a large volume of warm water, which was allowed to cool from a 25 K temperature increase to ambient levels. The large volume ensured that the temperature in the 12 μm sensing film decreased slowly and that no temperature gradients were produced in the film. The temperature in the water was measured with a thermocouple placed close to the sensing film. The linearity of the output of the optical fibre sensor was calculated using equation (4.13) was $L_R = 0.6 \%$.

7.1.2 Sensitivity

The dc thermal sensitivity was obtained from the measurement of the sensor linearity. The optical fibre sensor with a photodiode/amplifier configuration produces a dc thermal sensitivity of 10.0 mV $^{\circ}\text{C}^{-1}$.

Similar to the sensitivity assessment of the radiometric detector, the detection sensitivity, or thermal noise floor, is estimated from the sensitivity and noise characteristics.

7.1.3 Noise

The unaveraged noise on the signal detected using the optical fibre sensor (12 μm) was of the order of 2.5 mV, while 500 μV was achieved after taking 32 averages of the sensor

output. This corresponds to a thermal noise floor of 250 mK without averaging and 50 mK with signal averaging. The overall sensitivity could be improved by using thicker films or film materials with higher refractive index, which would produce greater phase shifts per unit temperature. Beard *et al* achieved a thermal noise floor of 6.3 mK¹⁰⁹ (32 signal averages) by optimising the fringe visibility of a 50 µm PET film. The sensitivity of the optical fibre sensor also depends on the quality of components such as the diode laser. A laser producing an output with low inherent intensity noise would also reduce the thermal noise floor as shown in section 5.5.4.

7.1.4 Response time

The response time of the radiometric detector was determined from the rise time of a photothermal signal to 63.2 % of the final value after an instantaneous temperature rise as described in section 4.3.2.4. The response time of the PPTR detector and electronic circuits was measured to be 240 µs, which is roughly the length of the laser pulse. The response time measurement was therefore limited by the pulse length of the laser. The HgCdTe detector, as a photonic detector, has a much shorter response time of approximately 0.5 µs, which can be estimated from the bandwidth of 2 MHz (manufacturer's data).

The response time of the optical fibre sensor was measured using the set-up shown in Figure 7.2. A jet of warm water (typically 2-3 °C above ambient) was directed at the sensing area of the optical fibre sensor. Water was continuously flowing onto a barrier that was attached to a solenoid. A thermocouple placed in the tube was used to ensure a stable water temperature. Activating the solenoid withdrew the barrier and the stream of water was incident on the polymer film positioned just above the optical fibre. This resulted in a step change in temperature in the medium adjacent to the film. The water also produced a sudden change in refractive index at the film surface as it moved past the tip of the optical fibre. After the step change in the signal due to the refractive index change, an increase in the signal due to thermal diffusion was detected. It was this part of the sensor response that was used for the measurement of the thermal response time.

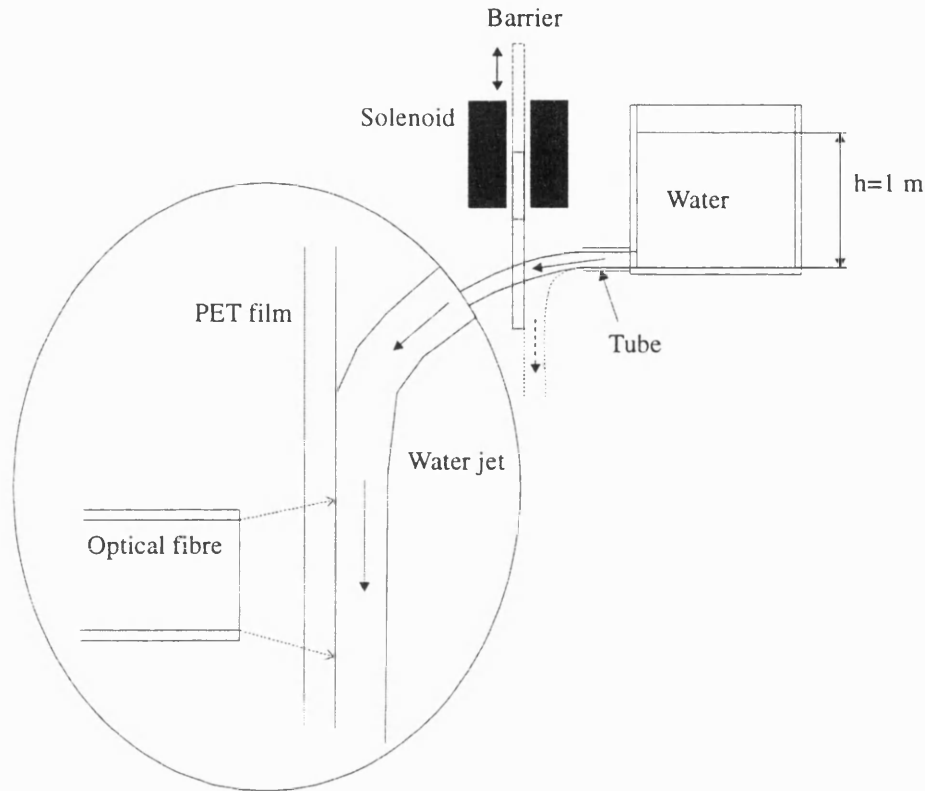


Figure 7.2 *Experimental set-up for measuring the thermal response time of the optical fibre sensor.*

This method has, however, experimental aspects, which could lead to large errors in the measured response time. Potential errors are introduced by the cooling of the water as it travels through the air and as it flows past the film. The heat transfer from the water into the sensing film may also be hindered by a boundary layer where the water molecules closest to the film may be moving very slowly compared to molecules further away from the film. Consider the situation shown in Figure 7.2 where the jet of water hits the polymer film approximately 1.0 mm above the optical fibre. By the time the water has passed the fibre, it will have travelled a distance of 1.4 mm while having been continuously in contact with the film. The velocity of the water as it reaches the film is calculated using Torricelli's theorem, which may be expressed as

$$v_0 = \sqrt{2hg} \quad (7.1)$$

where v_0 is the velocity of the water as it exits the tube, h is the height of the column of water and g is the gravity. The rise time of the sensor output due to a change in the reflection coefficient is equivalent to the time it took the water to pass across the fibre core diameter. For a height h of 1 m, the velocity of the water v_0 is 4420 mm s^{-1} . It takes the water therefore $90 \text{ }\mu\text{s}$ to travel a distance of 0.4 mm. This agrees approximately with measurements of the rise time of the sensor output ($170 \text{ }\mu\text{s}$) that was produced by the change in the reflection coefficient. Due to the high velocity of the water, it can be assumed that the water in front of the optical fibre was always immediately replaced by new water. Although a thin boundary layer certainly existed, it can be assumed that its thickness was very small and that it did not have a significant effect on the measurement of the thermal response time. The response time of the optical fibre sensor configured with a $50 \text{ }\mu\text{m}$ film was measured to be 9.5 ms.

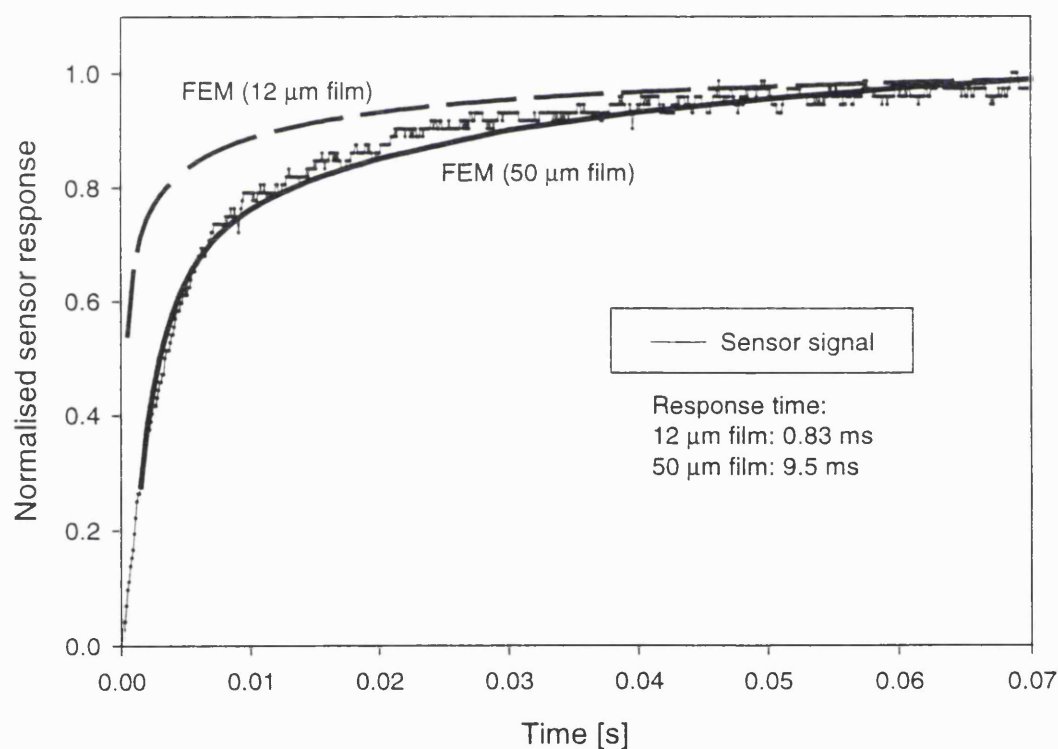


Figure 7.3 Normalised sensor response to a step change in temperature together with the theoretical response calculated using the FEM of the optical fibre sensor for a PET film of $50 \text{ }\mu\text{m}$ and $12 \text{ }\mu\text{m}$ thickness.

The measured thermal response time is compared to the thermal response calculated using a one-dimensional finite element model. A model with a fixed temperature at the film boundary and adiabatic boundary conditions elsewhere was used to calculate the signal of the optical fibre sensor for a step change in temperature. Figure 7.3 shows good agreement between the measurement of the thermal response time and the output of the FEM. The response time of a 50 μm film is comparable to the rise times produced by thermocouples. The response time of the optical fibre sensor is determined by how rapidly heat can diffuse into the sensing film. Higher thermal conductivity and smaller film thickness result in a faster response. An estimation of the response time of a 12 μm film with the help of a finite element model yielded 0.83 ms. The optical fibre sensor in its current configuration has to be considered a relatively slow temperature transducer, especially when compared to the response times of radiometric detectors.

7.1.5 Specificity

Specificity is a measure of the relative sensitivity of a detector to the desired physical quantity compared to other influences, such as vibration, humidity etc. For photoacoustic measurements, the optical fibre sensor needs to be stable for only a few microseconds. Photothermal applications require the detector system to be stable for up to 100 ms. Under laboratory conditions, this is not a problem. Vigorous shaking of the optical fibre, however, produced fluctuations in the dc level due to bending losses and signal cancelling effects as described in section 5.2.4. Such baseline variations would interfere with the photothermal signal to an extent that would prohibit a meaningful analysis of *in vivo* measurements. By comparison, shaking of the optical fibre had virtually no effect on the stability of the sensor when used for photoacoustic measurements. This source of interference would have to be eliminated before clinical measurements of the photothermal response could be carried out.

The sensor is also affected by changes in the ambient temperature, which shift the operating point away from the point of quadrature, which may result in the operation of the sensor outside of the linear region of the interferometer. For the use of the the sensor for *in vivo* measurements, this could be taken account of by setting the operating point at a

temperature of 37 °C, which should be sufficient to maintain the linear response. Moreover, temperature fluctuations of a few degrees Kelvin would not produce a phase shift large enough to move the operating point of a sensor configured with a 12 μm film into the non-linear region of the interferometer transfer function. A 12 μm sensing film should therefore be suitable for *in vivo* measurements.

7.2 Detection of photothermal signals in tissue phantoms

In this section, the materials and methods used for making water-based tissue phantoms and the experimental procedure of detecting photothermal signals are described.

Initial measurements in non-scattering liquids indicated experimental errors due to adsorption of dye molecules to the surface of the sensing film. The effect of adsorption on the time course of the photothermal signal is examined and options for overcoming adsorption are discussed.

7.2.1 Materials and methods

Absorbing and scattering tissue phantoms were made by dissolving a near-infrared absorber (Zeneca, S109564) in distilled water. The absorption coefficients of the solutions were determined from measurements of their transmittance at 1064 nm before scatterers were added. The standard deviation of the determined values was less than $\pm 1.5\%$. Scattering of light in the tissue phantoms was introduced by mixing polystyrene microspheres into the absorbing solution. The value of the reduced scattering coefficient depended upon the volume fraction of the spheres in the liquid and their size distribution. The scattering coefficient and the scattering anisotropy, g , were calculated using Mie theory¹⁵⁸. The absorber/microsphere suspension was placed into an ultrasonic bath for 30 min to reduce lumping of the scattering particles. Finally, a small, fixed percentage of gelatine was mixed into the turbid liquid, which was then heated to approximately 40 °C. The effect of the

added gelatine on the absorption coefficient of the solution at 1064 nm was measured and was found to be insignificant. The gel tissue phantoms were placed in a refrigerator to set.

7.2.1.1 Dye adsorption to the sensing film

During measurements of the photothermal response of liquid absorbers it was found that dye molecules adsorbed to the surface of the polymer film. Adsorption is the result of electrostatic and van der Waals' forces between the polymer film and the dye molecules¹⁵⁹. Van der Waals' forces, which are weak attracting forces, are due to momentary dipoles caused by fluctuations in the electronic configuration of molecules¹⁶⁰. As a molecule propagates through a medium due to Brownian motion, it may hit the surface of a solid, which causes it to be held in contact with the materials by van der Waals' forces. The infrared dye that was used in the tissue phantoms has an aromatic ring structure and electron system that is known to participate in the attracting forces, which contribute to surface binding.

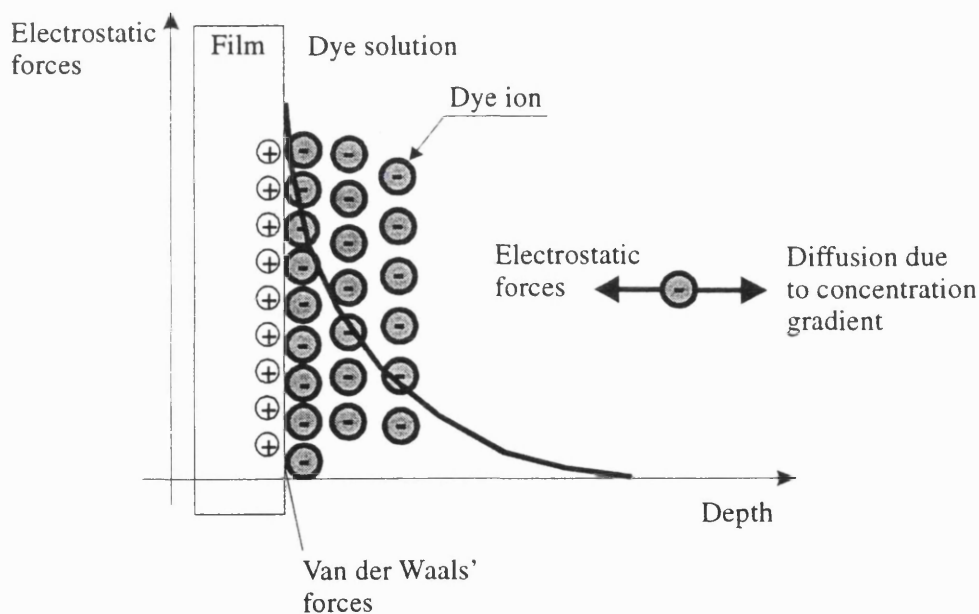


Figure 7.4 Adsorption of dye molecules onto the surface of the polymer film due to electrostatic and van der Waals' forces.

The thickness of a dye molecule layer due to van der Waals' forces is of the order of 2-3 nm. Electrostatic forces, which attract the negative ions of the dissociated dye, may perhaps play an even greater part in the build-up of a highly concentrated dye layer on the sensing film and may result in even thicker layers of elevated dye concentration.

The adsorption of dye molecules to the surface of the polymer sensing film created a thin region of increased absorption next to the film as illustrated in Figure 7.11 due to higher dye concentration than that of the remaining solution. The absorption of the excitation laser pulse in the thin layer produced a much higher initial temperature compared to the deeper regions of the dye solution. The high temperatures close to the film produced a significant increase in the signal peaks and a sharper temporal decay of the photothermal signals. This error presented an obstacle in the determination of absorption coefficients from the experimental data using the numerical model of the sensor. Even though adsorption could have been taken account of in the finite element model, it would have resulted in a more complicated situation since most of the adsorption-specific parameters, such as layer thickness and concentration gradient, would be difficult to determine with any accuracy.

Diffusion of dye molecules into the polymer film was also considered as a possible explanation of the observed anomalies. Diffusion, however, could be ruled out since the dye molecules have a large molecular weight and would therefore not be able to penetrate the polymer. To confirm that the observed effect is adsorption rather than diffusion, the photothermal response of an uncontaminated PET film in distilled water was recorded. The sensor head was then removed from the water and was submerged in a dye solution for less than 2 seconds. The sensor was then washed and its response in distilled water was measured. The signal traces are shown in Figure 7.5. The photothermal response after the exposure to the dye clearly shows the effect of adsorption, which produces a high initial temperature followed by a sharp temperature decline. This experiment also indicated that the contamination of the sensing film is the result of adsorption since diffusion of dye molecules would not have been possible given the very low permeability of PET even to small molecules such as those of water¹⁶¹. The effects of diffusion into the polymer film due to concentration gradients should also have been reversible. This was tested by exposing a contaminated film to distilled water for 24 hours, which did not remove the

contamination of the film. This finding further supported the theory that dye molecules are adsorbed to the surface of the polymer film.

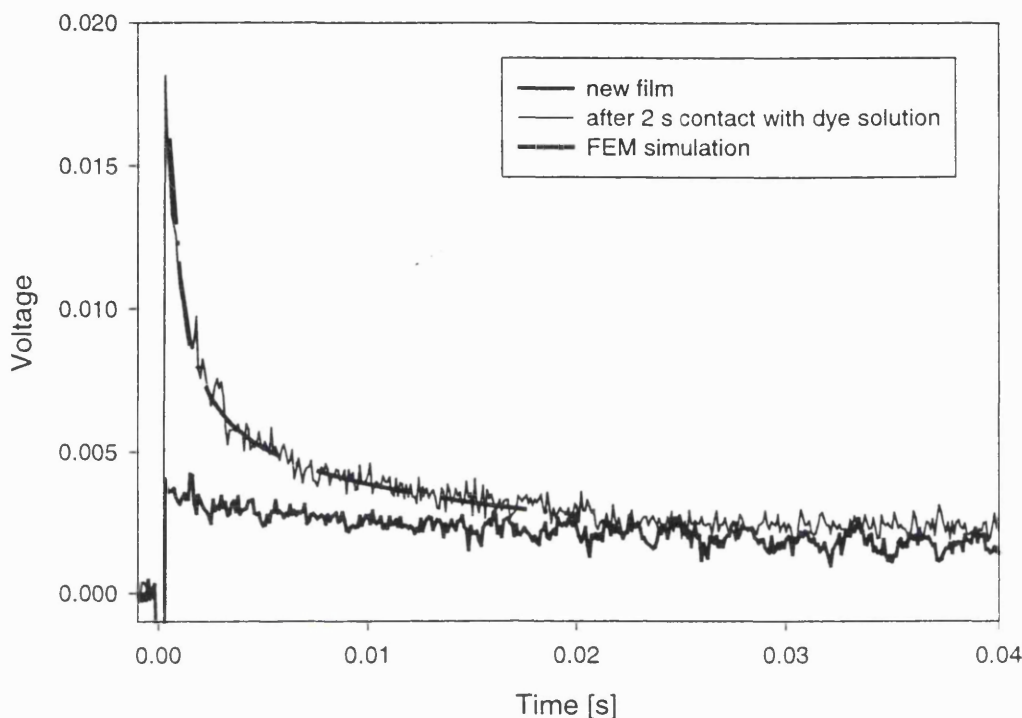


Figure 7.5 *Photothermal signal detected in distilled water before and after exposure of the sensing film to an absorbing dye. The FEM of the sensor was used to simulate the effect of a 200 nm dye layer on the surface of the PET film.*

These findings were confirmed by incorporating the effect of a dye adsorption layer into the numerical model. The concentration of the dye in the adsorbed layer was assumed to decrease exponentially with increasing depth with a e^{-1} depth of 200 nm. The magnitude of adsorption was varied manually to achieve a good fit of the model to the measurement.

The concentration of molecules in the adsorbed layer also appeared to be dependent upon the concentration of the dye. Measurements in solutions of higher absorption coefficients, hence dye concentration, produced a more pronounced peak compared to signals detected in solutions of low dye concentration. The absorption parameter used in the FEM had to be increased significantly to match the model with the data. A possible

explanation is the influence of diffusion due to the concentration gradient across the adsorbed layer. Dye molecules are held close to the surface by electrostatic forces but are also 'pulled' away from the film by diffusion due to the lower dye concentration of the solution. In highly concentrated dye solutions, the effect of diffusion is less pronounced, which allows more dye molecules to cling to the film. This therefore raises the absorption of the adsorbed layer, which produces a larger initial peak of the photothermal signal.

Various options have been tested in order to overcome the adsorption problem. Different film materials, such as glass, polyimide and polyethylene, have been used as film material, but without success. India ink, a suspension of carbon particles has been tested as an alternative absorber but also produced adsorption, which further strengthens the assumption that electrostatic forces are dominating adsorption. The range of available dyes was very limited by the fundamental emission wavelength of the Nd:YAG laser. Other dyes that may have been suitable required non-aqueous solvents, which would quickly evaporate and may have affected the PET film. Another idea was to put a hydrophobic coating on the film in order to repel the dye molecules. Siloxane, a waterproofing agent used for treating textiles as well as silicone lubricant were applied to the film but this also proved unsuccessful. For the purpose of making photothermal measurements on non-scattering absorbers that could be used to validate the numerical model of the sensor, it may have been feasible to employ a different target material such as coloured Perspex. The sensing film could have been glued to the surface of the Perspex target. Although this was an option with which adsorption could be avoided, it was not very useful. Photothermal measurements in non-scattering absorbers were required for a wide range of absorption coefficients in order to validate the FEM of the optical fibre sensor. The use of Perspex would have limited the range of μ_a . By making non-scattering samples with a high gelatine concentration, the effect of the adsorbed dye on the photothermal signal detected in distilled water was noticeably reduced but not removed. This experiment suggested, however, that adsorption could be prevented if the dye molecules were immobilised.

One solution to the adsorption problem appeared almost accidentally when measurements were made on turbid tissue phantoms. Between measurements on turbid gels, the sensor was placed in distilled water and a signal was recorded in order to monitor the stability of the set-up. It was noted that signals detected in distilled water were devoid

of the characteristic initial peak, as shown in Figure 7.5. The turbid gels contained polystyrene microspheres. It appears that the dye molecules bonded to the scattering particles became immobilised and did not affect the PET film of the sensor when it was brought in contact with the gel. Tissue phantoms of very low reduced scattering coefficient ($\mu_s' = 0.2 \text{ mm}^{-1}$) were made to achieve the nearest equivalent to non-scattering targets. These weakly scattering gels were still different, however, in terms of their light transport properties and thermal geometry to non-scattering gels. The tissue phantom could no longer be regarded as devoid of scatterers and the initial temperature distribution after the absorption of a laser pulse could not be assumed to be a continuous exponential function of depth. The initial temperature was instead determined by the highly absorbing dye coating on the microspheres, which produced a dense distribution of hotter and cooler regions. The time it takes for the temperature peaks to cool to a flat temperature profile can be estimated from the volume density of the microspheres. The lowest volume fraction of scattering particles, which effectively immobilised the dye molecules was 0.5%. If one imagines the tissue phantom to be a cube where the scattering material was pressed into one corner, the length of the cube made up of the scatterers would cover 17% of the length of the tissue phantom. Given an average microsphere diameter of 8 μm and even distribution, the distance between the scattering particles can be estimated as 39 μm . Since the microspheres can be assumed to be hotter than the surrounding water-dominated gel, the gap between the spheres will be heated from both ends. The time it takes for the temperature profile to flatten to a smooth function is therefore equal to the time it takes for the heat to diffuse over half the distance between the particles of the thermal diffusion length $\mu_D = 19.5 \mu\text{m}$. It therefore takes 1.3 ms for the temperature profile to flatten ($t = 0.5 \mu_D^2 D^{-1}$, $D = 0.144 \text{ mm}^2 \text{ s}^{-1}$). This is a fast enough time given that a typical analysis of photothermal measurements considers a time window between 0.25 to 40 ms. It was therefore acceptable that all tissue phantoms were made using a small quantity of polystyrene microspheres, which eliminated any contamination of the sensor by the dye. The presence of dye coated scatterers does introduce an error, which would need to be taken into account if the time window of the analysis was made smaller.

The adsorption of dye to the surface of the polymer film also points to possible complications for the *in vivo* use of the optical fibre sensor. Protein adsorption is a well-

known phenomenon, which can, for example, lead to complications in the acceptance of implants in patients. Protein adsorption to the optical fibre sensor may produce similar effects on the photothermal signal as the dye adsorption and would need to be addressed. Dye or protein adsorption can also affect other photothermal techniques, which may make contact with the target, such as fibre-optic radiometry.

7.2.2 Measurements on tissue phantoms

The gelatine tissue phantoms were allowed to reach room temperature after being removed from the refrigerator. The gels were cut into cubes of approximately 6 mm in width using a scalpel. This produced flat surfaces, which gave very good thermal contact between the sensor and the tissue phantom. The gels were placed against the sensing film and single laser pulses were launched into the optical fibre to generate a photothermal response from the sample. The pulses were applied every 4-5 seconds in order to prevent a shift in the baseline due to heating, which may have distorted the photothermal signal. The measurements were recorded on a digital oscilloscope and the signals were averaged over 32 acquisitions. Two measurements were made on each of a total of five different samples, which were taken from a range of different depths of the tissue phantom. The measurements on the individual samples were later compared to check for possible sedimentation of the polystyrene microspheres. The sensor was also placed in distilled water between measurements on tissue phantoms and a signal was then recorded. The signals were compared to monitor the stability of the set-up and to ensure that the sensor remained uncontaminated. The amplitude of the excitation laser pulses was monitored by diverting a fraction of the pulse to the trigger photodiode using a beam splitter. The amplitude of the laser pulses was used to normalise the photothermal signals.

The absorption coefficient of an uncontaminated PET film was estimated from the photothermal response detected in distilled water using model based parameter estimation, which produced $\mu_{a_PET} = 0.04 \text{ mm}^{-1}$. This is not in agreement with the absorption coefficients calculated from transmission spectra provided by the manufacturer, which typically ranged from $0.4 - 0.7 \text{ mm}^{-1}$ at 1064 nm. The difference can be explained with the

lack of information regarding the experimental procedure that was employed by the manufacturer to measure transmission, since it remains unclear whether the effects of specular reflections were included in the stated transmission.

7.3 Determination of optical parameters using model-based parameter estimation

The signals detected in a tissue phantom were normalised by the incident pulse energy and the standard deviation (10 measurements per tissue phantom) was calculated. The signal was reduced to 200 data points between 0.2 ms and 40 ms in increments of 0.2 ms.

The optical coefficients were determined using model-based parameter estimation. Since all tissue phantoms contained scattering particles, it should have been necessary to implement the Monte Carlo model to calculate the initial temperature distribution. A comparison of theoretical signals computed for the smallest reduced scattering coefficient ($\mu_s' = 0.2 \text{ mm}^{-1}$) using the MC model and Lambert's law showed no significant difference. The light distribution in tissue phantoms with the lowest scattering coefficient was therefore sufficiently well described using the simpler Lambert-Bouguer law and the phantoms could be regarded as pure absorbers. The measurements on the quasi non-scattering gelatine samples were used to validate the model for a wide range of μ_a . The use of the Lambert-Bouguer law reduced the computation time as well as the number of unknown optical parameters. For all tissue phantoms with higher scattering coefficients than $\mu_s' = 0.2 \text{ mm}^{-1}$, the Monte Carlo model was employed.

7.3.1 Measurements on pure absorbers

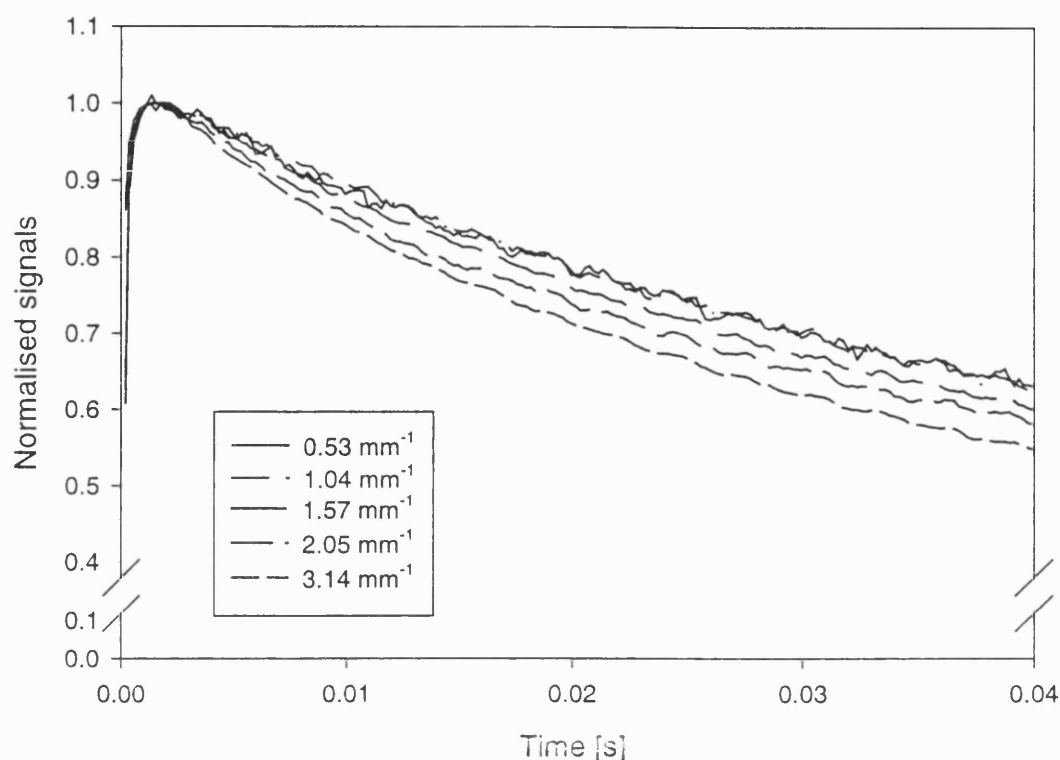


Figure 7.6 Normalised photothermal signals detected using the optical fibre sensor in quasi non-scattering gels with absorption coefficients ranging from 0.53 to 3.14 mm^{-1} .

The determination of the absorption coefficient, μ_a , from the quasi non-scattering samples was carried out in two ways. The first approach was to use all available information on the sample under study in order to reduce the uncertainty in those parameters that were not of primary interest, such as the target's thermal conductivity, specific heat and density. In the second approach, the thermal coefficients were assigned typical uncertainties found in tissue. Given that the gelatine tissue phantoms were dominated by water, it was assumed that the thermal coefficients of the gel were close to those of water and that there was only a small degree of uncertainty ($\pm 1.0\%$) in their value.

7.3.1.1 Normalised signals

The absorption coefficients were determined solely from the temporal shape of the experimental data using MBPE. This was achieved by normalising the theoretical signal calculated by the numerical model to the peak amplitude of the photothermal signals, which allowed the determination of μ_a independent of amplitude information. The measurements were normalised to the maximum of each signal. The determination of μ_a using the normalisation of the theoretical and experimental signals resulted in a method in which the absorption coefficient was obtained from the shape of the signal without the need to incorporate amplitude-related parameters. This is similar to the theoretical technique employed in PPTR⁹⁸. The absorption coefficients were obtained from photothermal signals detected in gelatine samples with ‘known’ absorption coefficients ranging from $\mu_a = 0.53 \text{ mm}^{-1}$ to $\mu_a = 3.14 \text{ mm}^{-1}$ and the results are shown in Table 7.1. Figure 7.7 shows the normalised theoretical signal calculated from the estimated parameters to the experimental data.

<i>‘Known’</i> μ_a [mm^{-1}]	<i>Initial</i> $\mu_a \pm \text{uncertainty}$ [mm^{-1}]	<i>Estimated</i> $\mu_a \pm \text{uncertainty}$ [mm^{-1}]
0.53	1.00 ± 0.70	0.52 ± 0.05
1.04	1.00 ± 1.00	0.56 ± 0.07
1.57	2.00 ± 1.00	1.30 ± 0.07
2.05	1.30 ± 1.00	2.86 ± 0.07
3.14	2.60 ± 1.00	3.61 ± 0.15

Table 7.1 Absorption coefficients estimated from normalised signals using small uncertainties in the thermal coefficients.

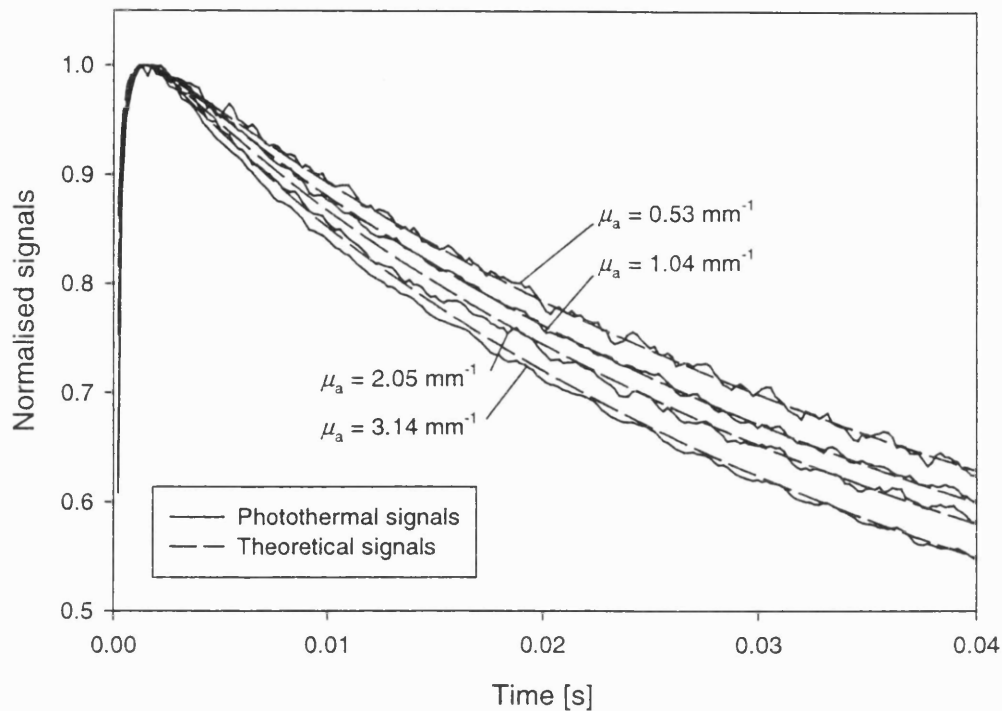


Figure 7.7 Normalised photothermal signals together with the theoretical signals calculated using the estimated absorption coefficients shown in Table 7.1.

The estimated absorption coefficients in Table 7.1 show large discrepancies compared to the ‘known’ μ_a . The deviation of the estimated μ_a from the true value ranged between 2 – 46%. This indicates that the absorption coefficient cannot be determined accurately from the shape of the photothermal signal alone. The reason for the large discrepancies in μ_a may also be explained with the effective removal of any uncertainties in the amplitude when the signals were normalised. The peak amplitude of the photothermal signals may be affected by the concentration of the dye-coated polystyrene microspheres immediately in front of the sensor. An uneven distribution of the scatterers would result in errors in the measured peak and hence the determined absorption coefficient.

7.3.1.2 Two-parameter fit

In order to improve the agreement between the numerical model and the detected photothermal signals, two parameters, the calibration constant and μ_a , were allowed to vary during the parameter estimation. The two-parameter fit was not only aimed at improving the agreement between the model and the experimental data but also at determining the calibration constant that was later used in the determination of μ_a and μ_s . The initial uncertainty in the calibration constant was assumed to be $\pm 20\%$. The pulse energy, which was monitored during the measurements, was used to normalise the experimental signals. In order to reduce the experimental error and hence improve the degree of prior information further, the peak amplitudes of the photothermal signals were also normalised and the calibration constant was adjusted accordingly.

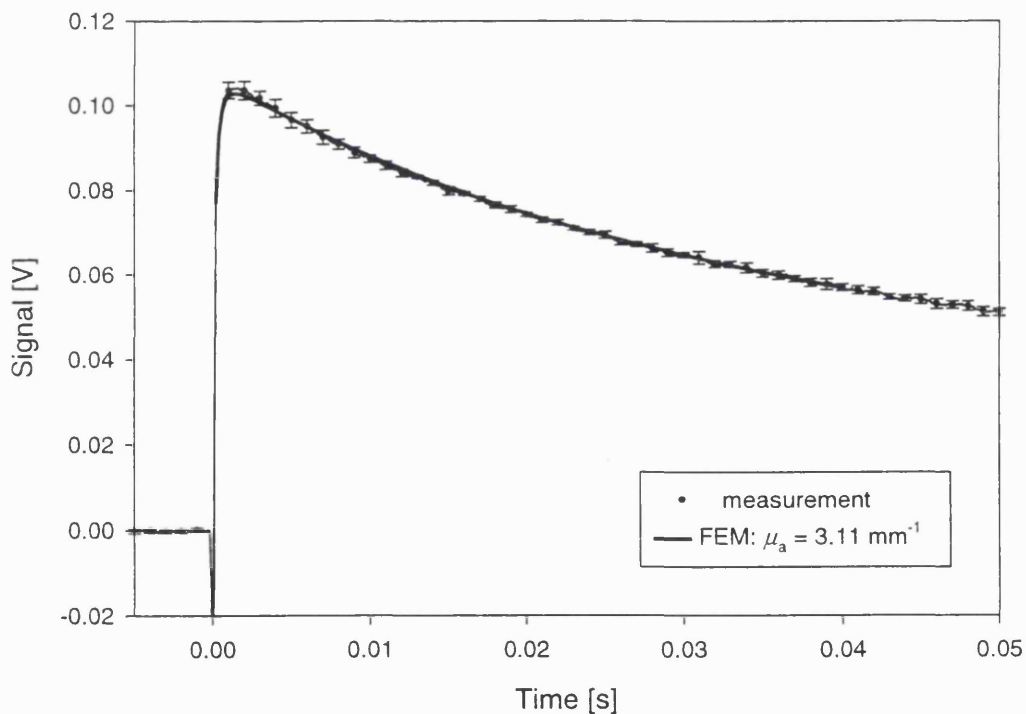


Figure 7.8 Comparison of the theoretical signal calculated from the estimated set of parameters from Table 7.2 and the experimental data for a 'true' $\mu_a = 3.14 \text{ mm}^{-1}$. The parameters were obtained using small initial uncertainties in the thermal parameters. The error bars represent the standard deviation of 10 measurements.

This yielded very small experimental errors. The sum of the squares of the difference between the experimental data and the model, χ^2 , was the goodness-of-fit measure. The final set of parameters was the one that produced the smallest value of χ^2 . The results of a two-parameter estimation for a gel with $\mu_a = 3.14 \text{ mm}^{-1}$ and low initial uncertainties are shown in Figure 7.8 and in Table 7.2 below.

<i>Parameter</i>	<i>Initial value \pm uncertainty</i>	<i>Estimated value \pm uncertainty</i>
μ_a [mm^{-1}]	2.60 ± 1.00	3.11 ± 0.03
μ_{a_PET} [mm^{-1}]	0.04 ± 0.002	0.037 ± 0.002
Calibration constant	0.1 ± 0.020	0.1 ± 0.001
k [$\text{W mm}^{-1} \text{K}^{-1}$]	$0.56 \cdot 10^{-3} \pm 5.6 \cdot 10^{-6}$	$0.553 \cdot 10^{-3} \pm 4.0 \cdot 10^{-6}$
c [$\text{J g}^{-1} \text{K}^{-1}$]	4.18 ± 0.04	4.16 ± 0.037
ρ [g mm^{-1}]	$1.0 \cdot 10^{-3} \pm 20.0 \cdot 10^{-6}$	$0.98 \cdot 10^{-3} \pm 14.0 \cdot 10^{-6}$
L_{film} [mm]	$0.012 \pm 0.2 \cdot 10^{-3}$	$0.0118 \pm 0.031 \cdot 10^{-3}$

Table 7.2 *Initial and estimated parameters and uncertainties obtained from a photothermal measurement on a tissue phantom with a ‘true’ $\mu_a = 3.14 \text{ mm}^{-1}$. The initial uncertainties in the thermal coefficients were small, which produced an estimated μ_a close to the true value.*

The estimated μ_a for small initial uncertainties in the thermal coefficients of the target, were close to the true values, as shown in Table 7.2. The uncertainty in μ_a was also greatly reduced. The reduction in the uncertainty of μ_a suggests that our knowledge in the parameter and hence our confidence in the estimated μ_a has increased significantly. The final uncertainties in the parameters can also be visualised by plotting the error in the theoretical signal caused by the uncertainties, which is shown in Figure 7.9 below.

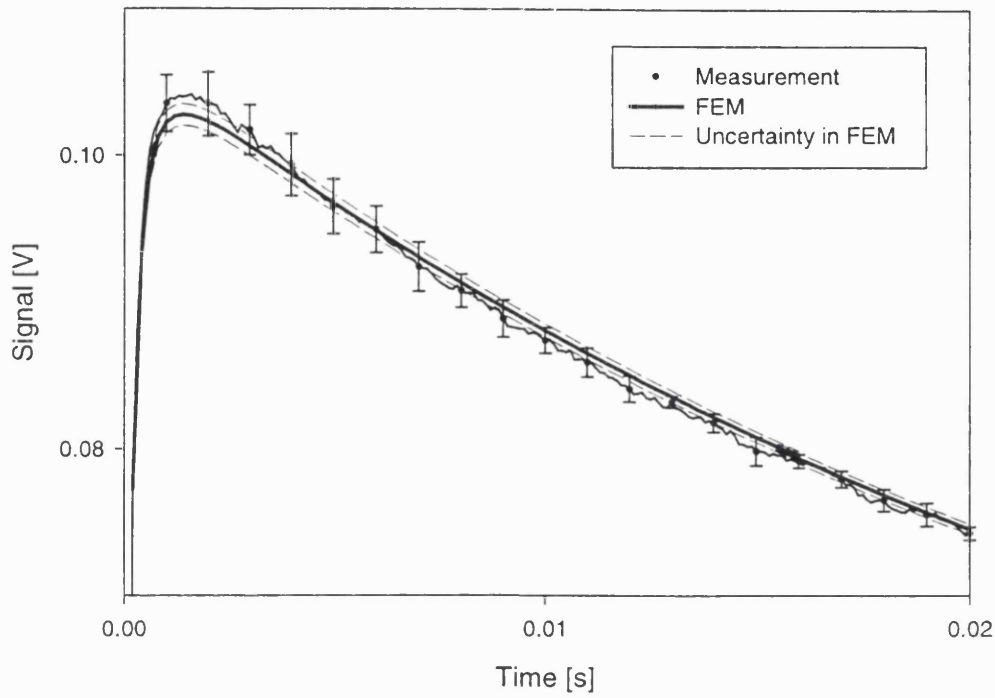


Figure 7.9 Enlarged section of the signal shown in Figure 7.8 illustrating the error in the FEM due to the estimated uncertainties in the model parameters. Note that the uncertainty of the FEM falls within the standard deviation of the measurement.

<i>'Known' μ_a</i> <i>[mm⁻¹]</i>	<i>Initial $\mu_a \pm$</i> <i>uncertainty [mm⁻¹]</i>	<i>Estimated $\mu_a \pm$</i> <i>uncertainty [mm⁻¹]</i>
0.53	0.53 \pm 0.2	0.55 \pm 0.005
1.04	0.70 \pm 1.0	1.00 \pm 0.03
1.57	1.30 \pm 0.7	1.54 \pm 0.02
2.05	1.7 \pm 1.0	2.08 \pm 0.03
3.14	2.6 \pm 1.0	3.11 \pm 0.03

Table 7.3 Absorption coefficients obtained from photothermal measurements on quasi non-scattering gels using a two parameter fit and small initial uncertainties.

Figure 7.9 illustrates that the reduced estimated uncertainties in the model parameters produce an error in the output of the FEM that lies within the standard deviation of the experimental data. The absorption coefficients of the remaining gels with μ_a ranging from 0.53 mm^{-1} to 2.05 mm^{-1} were determined using small initial uncertainties in the thermal coefficients. The results are shown in Table 7.3.

It can be seen from the estimated parameters and their reduced uncertainties that the absorption coefficient can be determined from photothermal signals with good accuracy provided the uncertainties in all other model parameters, which include the calibration constant and the thermal coefficients, are small. The good agreement between the experimental data and the theoretical signals over a range of different absorption coefficients also confirmed that the numerical model accurately represents the physical system of the optical fibre sensor.

7.3.1.3 Two parameter fit with large initial uncertainties

In the second approach, the thermal coefficients were assigned typical uncertainties that could be expected for measurements on tissue. This was simulated in the second approach for one gel as an example, in which the analysis was repeated with large uncertainties in the thermal coefficients. Table 7.4 below shows the estimated parameters for the same target using large initial uncertainties as would be found during *in vivo* measurements. The results obtained using the large uncertainties (Table 7.4) that can be expected for *in vivo* measurements on tissue show great discrepancy between the estimated and the 'known' parameters. More importantly, the final uncertainties of μ_a and the thermal coefficients have not been reduced to the extent as the results shown in Table 7.2 and the agreement between the numerical model and the photothermal signal is poor as shown in Figure 7.10.

<i>Parameter</i>	<i>Initial value \pm uncertainty</i>	<i>Estimated value \pm uncertainty</i>
μ_a [mm ⁻¹]	2.60 \pm 1.00	3.12 \pm 0.27
μ_{a_PET} [mm ⁻¹]	0.040 \pm 0.002	0.037 \pm 0.002
Calibration constant	0.100 \pm 0.02	0.085 \pm 0.0049
k [W mm ⁻¹ K ⁻¹]	0.56 $10^{-3} \pm 56.0 10^{-6}$	0.33 $10^{-3} \pm 6.0 10^{-6}$
c [J g ⁻¹ K ⁻¹]	4.18 \pm 0.67	2.69 \pm 0.19
ρ [g mm ⁻¹]	1.00 $10^{-3} \pm 0.05 10^{-3}$	1.01 $10^{-3} \pm 0.04 10^{-3}$
L_{film} [mm]	0.0120 $\pm 0.2 10^{-3}$	0.0123 $\pm 0.077 10^{-3}$

Table 7.4 *Initial and estimated parameters and uncertainties obtained from a photothermal measurement ($\mu_a = 3.14 \text{ mm}^{-1}$). The initial uncertainties in the thermal coefficients were comparable to those of tissue. Note the strong deviation of all parameters from the true values and the smaller reduction in the final uncertainties.*

The results indicate that any value of the parameter within the uncertainty would have produced a similarly good agreement with the experimental data. It also confirms the results obtained from the analysis of the normalised parameter sensitivity in section 6.3, which showed that, given the high uncertainty of tissue coefficients, the photothermal signal is as sensitive to the thermal parameters as it is to the absorption coefficient.

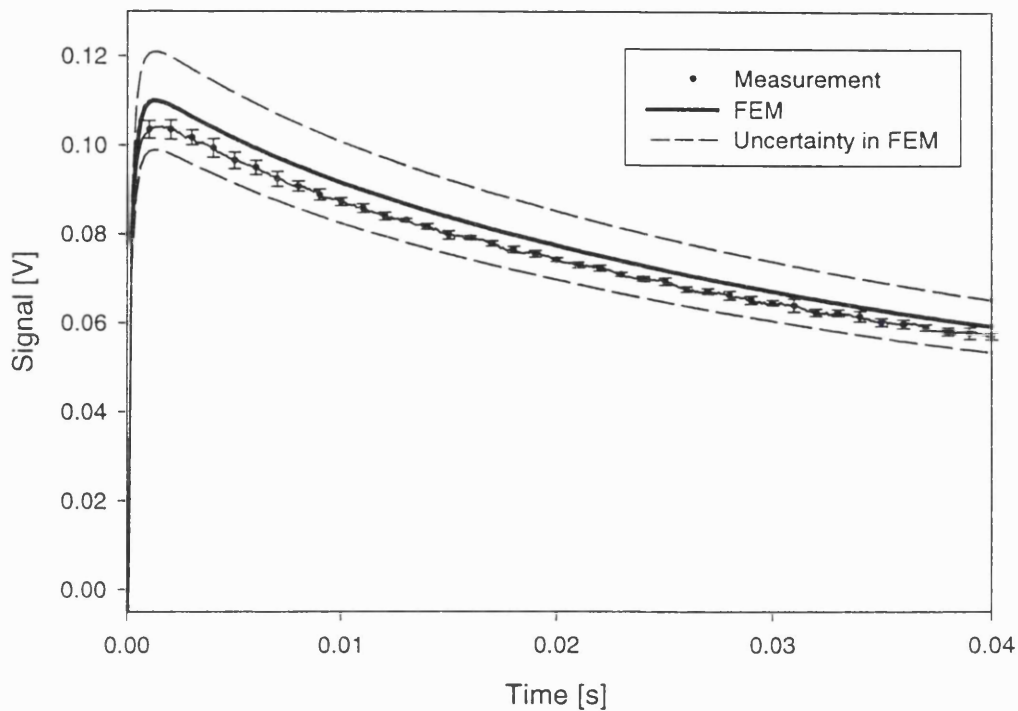


Figure 7.10 Comparison of the FEM data obtained using the set of parameters in Table 7.4 and experimental data. The parameters were obtained by assuming large initial uncertainties in the thermal parameters, which produced large final uncertainties and an unsatisfactory agreement with the data.

7.3.2 Estimation of the absorption and reduced scattering coefficient of turbid gels

The absorption and reduced scattering coefficients of three turbid gels were determined from the measured photothermal response. The absorption coefficient was the same in all three gels at $\mu_a = 2.05 \text{ mm}^{-1}$, while the reduced scattering coefficient was different (0.2, 1.22, 2.2 mm^{-1}). The values of μ_s' were chosen to represent those of tissue in order to explore the potential of the optical fibre sensor for the determination of the optical coefficients of tissue. Larger scattering coefficients also had to be avoided since the increased concentration of scatterers can lead to lumping of the spheres, in which case Mie theory does not hold. The analysis of the normalised parameter sensitivity (section 6.3) has already shown that the scattering coefficient has a much smaller effect on the amplitude and

the temporal characteristics of the signal compared to the thermal coefficients of the target. This was confirmed by the measurements made on the turbid samples as shown in Figure 7.11 below. The photothermal responses illustrate that the effect of an increase in the reduced scattering coefficient manifests itself as a small increase in the amplitude but not a significant change in the shape of the signal. The optical coefficients can nevertheless be estimated if the thermal coefficients and the calibration constant are assumed to be known and have small uncertainty.

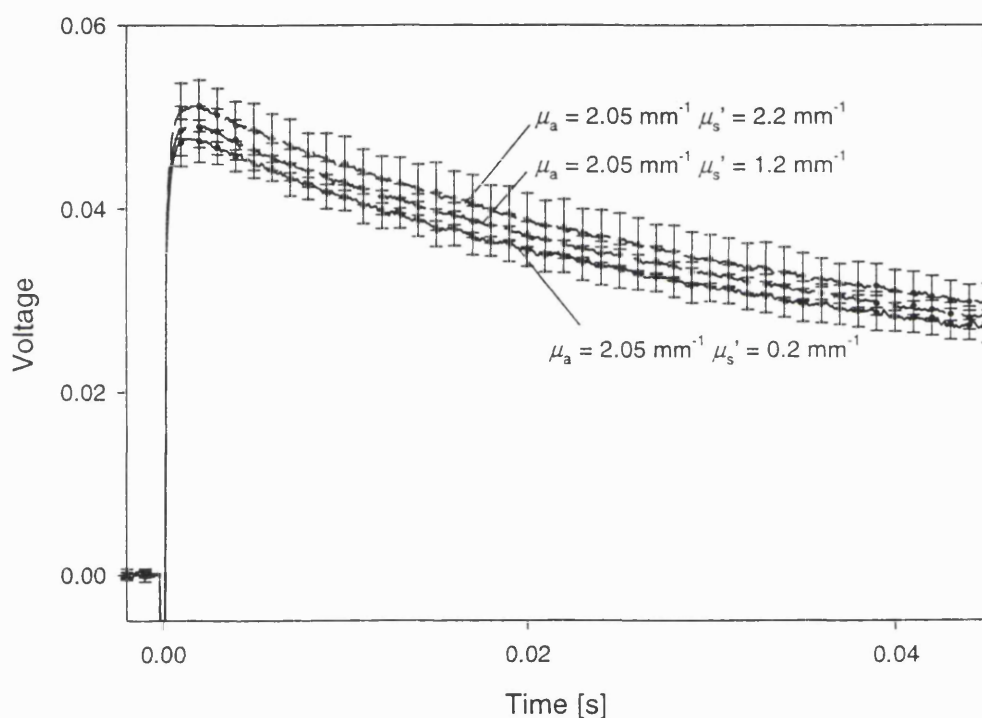


Figure 7.11 Photothermal signals detected in turbid gels. The absorption coefficient was the same in all samples, while the reduced scattering coefficient ranged from 0.2 to 2.2 mm^{-1} . The increase in the scattering coefficient does not produce a significant change in the shape of the photothermal signal.

The optical coefficients were obtained using MBPE by assigning small uncertainties to the amplitude and thermal parameters, while μ_a and μ_s' were given large uncertainties. The amplitude parameter was obtained from the measurements on the non-scattering samples.

The amplitude parameter for the subsequent measurements at higher scattering coefficients was normalised by the pulse energies but was frozen during the parameter estimation. The initial values of the thermal parameters were adjusted to take account of the volume fraction of polystyrene microspheres. A volume fraction of polystyrene of 5.5% (equivalent to $\mu_s' = 2.2 \text{ mm}^{-1}$) in water produced a thermal conductivity of $0.54 \cdot 10^{-3} \text{ W mm}^{-1} \text{ K}^{-1}$ ($k_{\text{Water}} = 0.56 \cdot 10^{-3} \text{ W mm}^{-1} \text{ K}^{-1}$) and a specific heat capacity of $4.07 \text{ J g}^{-1} \text{ K}^{-1}$ ($c_{\text{Water}} = 4.18 \text{ J g}^{-1} \text{ K}^{-1}$). The density change in the phantoms due to the polystyrene was calculated and its effect was found to be insignificant. The change in k and c did not affect the temporal characteristics of the photothermal signal, because the thermal diffusivity ($\alpha = k c^{-1} \rho^{-1}$) did not change significantly. Only the amplitude of the signal was affected by the variation in the specific heat capacity, which resulted in a slightly higher initial temperature. The initial uncertainty in the thermal parameters was set to $\pm 1.0\%$ as shown in Table 7.5, Table 7.6 and Table 7.7.

<i>Parameter</i>	<i>Initial value \pm uncertainty</i>	<i>Estimated value \pm uncertainty</i>
$\mu_a \text{ [mm}^{-1}\text{]}$	1.70 ± 1.00	2.08 ± 0.03
$\mu_{a_PET} \text{ [mm}^{-1}\text{]}$	0.040 ± 0.004	0.064 ± 0.0034
$k \text{ [W mm}^{-1} \text{ K}^{-1}\text{]}$	$0.56 \cdot 10^{-3} \pm 56.0 \cdot 10^{-6}$	$0.55 \cdot 10^{-3} \pm 40.0 \cdot 10^{-6}$
$c \text{ [J g}^{-1} \text{ K}^{-1}\text{]}$	4.18 ± 0.04	4.230 ± 0.036
$\rho \text{ [g mm}^{-1}\text{]}$	$1.0 \cdot 10^{-3} \pm 10.0 \cdot 10^{-6}$	$1.01 \cdot 10^{-3} \pm 9.0 \cdot 10^{-6}$

Table 7.5 Results obtained from experimental data using MBPE for a non-scattering gel with absorption coefficient $\mu_a = 2.05 \text{ mm}^{-1}$.

<i>Parameter</i>	<i>Initial value \pm uncertainty</i>	<i>Estimated value \pm uncertainty</i>
μ_a [mm ⁻¹]	1.70 \pm 1.00	2.08 \pm 0.03
μ_s' [mm ⁻¹]	1.0 \pm 0.5	1.44 \pm 0.14
μ_{a_PET} [mm ⁻¹]	0.050 \pm 0.004	0.0500 \pm 0.0037
k [W mm ⁻¹ K ⁻¹]	0.55 \cdot 10 ⁻³ \pm 55.0 \cdot 10 ⁻⁶	0.53 \cdot 10 ⁻³ \pm 48.0 \cdot 10 ⁻⁶
c [J g ⁻¹ K ⁻¹]	4.12 \pm 0.04	4.260 \pm 0.039
ρ [g mm ⁻¹]	1.0 \cdot 10 ⁻³ \pm 10.0 \cdot 10 ⁻⁶	1.03 \cdot 10 ⁻³ \pm 9.1 \cdot 10 ⁻⁶

Table 7.6 Results obtained from experimental data using MBPE for a turbid gel with 'known' optical coefficients $\mu_a = 2.05 \text{ mm}^{-1}$ and $\mu_s' = 1.22 \text{ mm}^{-1}$.

<i>Parameter</i>	<i>Initial value \pm uncertainty</i>	<i>Estimated value \pm uncertainty</i>
μ_a [mm ⁻¹]	1.70 \pm 1.0	1.89 \pm 0.079
μ_s' [mm ⁻¹]	1.7 \pm 0.5	2.76 \pm 0.44
μ_{a_PET} [mm ⁻¹]	0.05 \pm 0.004	0.05 \pm 0.0037
k [W mm ⁻¹ K ⁻¹]	0.54 \cdot 10 ⁻³ \pm 5.4 \cdot 10 ⁻⁶	0.53 \cdot 10 ⁻³ \pm 49.0 \cdot 10 ⁻⁶
c [J g ⁻¹ K ⁻¹]	4.07 \pm 0.04	4.13 \pm 0.038
ρ [g mm ⁻¹]	1.0 \cdot 10 ⁻³ \pm 10.0 \cdot 10 ⁻⁶	1.01 \cdot 10 ⁻³ \pm 9.7 \cdot 10 ⁻⁶

Table 7.7 Results obtained from experimental data using MBPE for a turbid gel with 'known' optical coefficients $\mu_a = 2.05 \text{ mm}^{-1}$ and $\mu_s' = 2.20 \text{ mm}^{-1}$.

The estimated values of μ_a and μ_s' contained in Table 7.6 and Table 7.7 are close to the 'known' values. The estimated uncertainties of μ_a are generally much smaller than their starting value while the final uncertainties of μ_s' have been reduced by only a small amount. This illustrates that the photothermal signal has a much lower sensitivity to μ_s' compared to

that of μ_a . The estimated parameters and their uncertainties indicate that the optical coefficients can be determined from the photothermal response of turbid gels provided the uncertainty in the other parameters is very small.

7.4 Summary

The performance of the optical fibre sensor has been found to be comparable to radiometric detectors in terms of linearity and detection sensitivity. The response time of the sensor in its current configuration makes it a relatively slow thermal transducer, which is nevertheless adequate for photothermal measurements. The performance of the sensor is discussed in more detail in the next chapter.

The results presented in this chapter have shown that μ_a and μ_s' can be determined from photothermal signals detected using the optical fibre sensor and have confirmed the validity of the numerical model. The values of the estimated absorption and reduced scattering coefficients had significance only if the initial uncertainties of the thermal coefficients and the amplitude were small. If the thermal coefficients of the tissue phantom were assumed to be unknown and entered the parameter estimation with large initial uncertainties, the estimated set of parameters produced an unsatisfactory fit to the data. Moreover, the final uncertainties were reduced to a much smaller extent compared to the calculation performed using the 'known' thermal and amplitude parameters, i.e. small initial uncertainties. Our knowledge and confidence in the optical parameters was therefore not improved by the photothermal measurement. However, the calculations involving a high degree of certainty in thermal and amplitude parameters demonstrated the potential of the optical fibre sensor to be used for the photothermal determination of μ_a .

Although the determination of the absorption and reduced scattering coefficients has, at least in principle, been demonstrated, it would be misleading to claim that the optical fibre sensor in its current configuration is suited to obtaining μ_a and μ_s' . The indication of poor sensitivity to changes in μ_s' as evidenced by the analysis shown in section 6.3 have been confirmed by the experimental data. An increase in the reduced scattering coefficient produced a relatively small increase in the signal amplitude. Nevertheless, the estimated

reduced scattering coefficient is obtained by detecting a change in the amplitude, rather than a change in the overall shape of the photothermal signal. This finding agrees with the conclusions drawn from the work on pulsed photothermal radiometry. One should bear in mind, however, that the change in amplitude could also have been brought about by variations in the specific heat and the density of the target. It is essential that the thermal parameters have high certainty if μ_s' is to be determined accurately. If the thermal coefficients enter the parameter estimation with a high degree of uncertainty, no meaningful values for μ_a and μ_s' can be obtained. Similarly, variations in the calibration constant due to changes in the detector sensitivity can also have an effect on the accuracy of the determined optical coefficients.

This chapter has highlighted a number of issues with respect to the determination of the absorption and reduced scattering coefficient that need to be addressed in order to develop the optical fibre sensor for clinical *in vivo* measurements. In the following chapter the performance of the optical fibre sensor in comparison to other photothermal detectors is addressed. The determination of optical coefficients using the sensor is analysed, limitations of the use of the technique for *in vivo* measurements are discussed and possible solutions are presented.

8 COMPARISON OF THE OPTICAL FIBRE SENSOR WITH OTHER PHOTOTHERMAL TECHNIQUES

In chapters 4 and 7, pulsed photothermal radiometry and the optical fibre sensor have been applied to the determination of optical coefficients from the laser-induced photothermal response of tissue phantoms. In this chapter, the optical fibre sensor is compared to other photothermal detection schemes, such as contact-pyroelectric detection and free-space as well as fibre-optic radiometry. The applicability of these techniques to photothermal determination of optical coefficients is discussed and compared to the optical fibre sensor with particular attention to their potential for endoscopic and interstitial implementation. Other photothermal techniques, such as optical beam deflection, modulated optical reflectance and photothermal displacement, which were discussed in chapter 3, are not included here since they are unlikely to be suitable for endoscopic measurements. Since pulsed photothermal radiometry and the optical fibre sensor have been applied to the determination of optical coefficients as part of the work presented in this thesis, the accuracy in the absorption and reduced scattering coefficient that can be obtained by the two techniques is examined.

8.1 Performance of the optical fibre sensor as a thermal detector

8.1.1 Thermal detection limit

The performance of the optical fibre sensor as a temperature transducer has been shown to be comparable to free-space radiometry using a HgCdTe detector. The thermal noise floor of the optical fibre sensor configured with a 12 μm PET film was measured as 50 mK, which was reduced to 6.5 mK when using a 50 μm film. The thermal sensitivity of the optical fibre sensor could be improved in a number of ways. The phase sensitivity could be increased by selecting polymer films with high refractive index, such as polyimide ($n =$

1.78), assuming that the sensitivity is not limited by the photodiode saturation threshold. The high refractive index would increase the reflection coefficients at the two interfaces of the sensing film. The reflection coefficients could also be optimised by depositing stacks of dielectric layers of carefully controlled thickness onto both sides of the film. The stacks of dielectric layers would need to be transparent to the excitation pulses but highly reflective to the wavelength used to interrogate the sensing film. Laser sources of low intensity noise would also significantly improve the overall sensitivity of the device as shown in section 5.5.4. Such modifications could bring the thermal sensitivity of the sensor closer to that of radiometry. If an even more sensitive thermal detector was required and the detector speed was not of high importance, an increase in the film thickness would be advantageous. Given that the thermal sensitivity of the sensor is proportional to the cavity thickness of the Fabry-Perot interferometer, it can be shown that a 100 μm film would produce a thermal noise floor of 0.5 mK, which is comparable to the 1 mK sensitivity of radiometric detectors. The overall sensitivity could also be increased using sensing film materials with a high thermal expansion coefficient.

Pyroelectric transducers may have adequate temperature sensitivity to be applied to photothermal measurements at the tip of an optical fibre. One of the main problems with this type of detector is the need to deposit electrodes on the two sides of a sensing film. The electrodes are typically made of metal, which would prevent the transmission of the excitation laser light. Possible alternatives may be the deposition of the metal electrodes in the shape of a grid, which would allow a certain fraction of the excitation laser pulse to pass through the pyroelectric detector to be absorbed by the target tissue. Other options include the deposition of transparent electrodes, which could be made from titanium nitride (TiN) or tin oxide (SnO_2). TiN layers of thickness thinner than the wavelength of visible light have been shown to have a transmittance of 74 - 47% with a sheet resistance between 1000 - 70 Ω ¹⁶². This approach would be further complicated by the likely absorption of excitation light in the electrodes, which would produce a photothermal signal in the sensor. High transparency of the electrodes would therefore be a very important parameter in the design of such detectors.

8.1.2 Rise time and bandwidth

HgCdTe radiometric detectors have a bandwidth of up to 2 MHz and are therefore much faster than the current configuration of the optical fibre sensor, which has a bandwidth of 1.2 kHz (equivalent to a rise time of 800 μ s). The bandwidth of radiometric detectors used in pulsed photothermal radiometry is often reduced in order to improve the noise characteristics. The response time of the sensor could be improved by reducing the film thickness but this would also reduce the overall sensitivity. A film of 7.5 μ m thickness, which is commercially available, would produce a thermal response time of approximately 200 μ s. If the film thickness was further reduced to 5 μ m, the sensor would have a response time of 90 μ s (11 kHz). The thermal noise floor would increase from 50 mK for a 12 μ m film to 120 mK for a 5 μ m film.

Other photothermal detectors provide similar response times and could be seen as an alternative to the interferometric approach taken with the optical fibre sensor. Pyroelectric materials act as piezoelectric detectors and have response times to stress waves as short as nanoseconds¹⁶³ and may therefore be suitable for simultaneous photoacoustic and photothermal measurements. The thermal response time of pyroelectric detectors, however, is determined by the relatively slow conduction of heat into the sensing element, which is dependent upon the thermal diffusivity and the thickness of the pyroelectric material. As was discussed in section 3.1.2, one of the disadvantages of pyroelectric detectors is their limitation to the detection of temperature changes, rather than the measurement of baseline temperatures. However, pyroelectric detectors have been shown to have a flat frequency response down to 10 Hz and have been successfully used to monitor very slow changes in temperature by employing deconvolution procedures to recover the very low frequency components of the signal¹⁶³. Polyvinylidene fluoride (PVDF) is a suitable material for the manufacture of pyroelectric transducers. It is optically transparent and could be used in the optical fibre sensor in a similar way as the Fabry-Perot interferometer provided transparent electrodes can be deposited. The disadvantage of this approach would be the need for wires to run along the fibre and the deposition of electrodes on both sides of a sensing film. Pyroelectric detectors are also characterised by a large source impedance, which may make the detection of high frequency signal components problematic when a

significant length of wiring is needed to connect the detector to an oscilloscope. The high impedance of the detector and the capacitance of the wiring would produce a low-pass filter. Impedance matching can be achieved using an amplifier with high input impedance and low output impedance. The amplifier could be a thin-film field-effect transistor (FET) positioned immediately after the pyroelectric transducer, which may add problems in terms of overall size of the sensor given its desired endoscopic application. One of the advantages of pyroelectric transducers is the likely absence of the fluctuations in the dc level observed in the Fabry-Perot optical fibre sensor when the optical fibre is shaken. The fluctuations originate from fibre bending losses and variations in the phase difference due to the changes in the path lengths travelled by the reflected rays.

8.2 Fibre-optic photothermal radiometry

The optical fibre sensor has been designed with the aim of diagnosing cancer and other tissue pathologies endoscopically. Given the experimental difficulties in using pyroelectric transducers as a photothermal detector at the tip of an optical fibre (see also section 8.1.2), fibre-optic radiometry is one of the photothermal techniques that has significant potential to be used for endoscopic photothermal measurements. Fibre-optic radiometry is very similar to PPTR but differs in the collection of the infrared emission for which optical fibres are used instead of parabolic mirrors or infrared transmitting lenses. PPTR, as discussed in chapter 4, is predominately a free-space method, which typically requires bulky equipment that would prohibit endoscopic applications. The development of infrared transmitting fibres, however, has made fibre-optic radiometric measurements possible^{164,165,166}. The losses in the IR fibres are typically between 0.2 and 0.5 dB m⁻¹ at a wavelength of 10.6 μm, which is equivalent to a maximum reduction in signal amplitude of approximately 6.0% per meter. An endoscopic radiometry system would perhaps require a fibre of 3 to 4 m length. The losses associated with the fibre would therefore be acceptable and would allow detection sensitivities very similar to those of the optical fibre sensor. Fibre-optic radiometry is likely to be less sensitive than free-space radiometry due to the losses in the fibre as well as the lower collection efficiency. Fibre-optic radiometry has been reported to

produce a thermal noise floor of 200 to 300 mK¹⁶⁶. The quoted figure is higher than that observed with free-space radiometry using parabolic mirrors, but the author attributed this to errors in the calibration procedure rather than noise from the detector and the electronic circuits. The true thermal noise floor may be smaller. The sensitivity of the optical fibre sensor is therefore slightly higher compared to fibre-optic radiometry but lower than free-space radiometry.

Infrared transmitting fibres possess a high refractive index, which results in a large numerical aperture (N.A. < 0.7) and hence acceptance angle. This is beneficial for the efficient collection of thermal emissions. Fibre-optic radiometry during endoscopy is therefore feasible but the following issues regarding the use of infrared fibres for the detection as well as excitation of photothermal signals would need to be addressed. Infrared fibres are characterised by low attenuation (< 1.5 dB m⁻¹) at wavelengths ranging from 5 µm to 14 µm and have also been shown to transmit visible wavelengths¹⁶⁷ but the attenuation of light in the visible and near-infrared spectrum is considerable. A wide range of excitation wavelength could be used but the infrared spectrum may still be the preferred choice due to the low attenuation. However, even the relatively low attenuation in the infrared wavelength region may still result in significant absorption of the excitation laser pulse and subsequent emission of infrared radiation in the fibre, which may obscure the emission that is collected from the target tissue. The maximum pulse energies that are tolerated by infrared fibres are typically much smaller than those tolerated by fused silica waveguides. The transmitted pulse energies may not be large enough to produce sufficiently strong infrared emissions for fibre-optic detection. This problem could be overcome by using a separate optical fibre to transmit the excitation laser pulses. In order to achieve the small detector size required for endoscopic measurements, the fibres would need to be parallel. Such an approach may complicate the modelling of heat conduction since the axes of photothermal excitation and detection are not coaxial. The fibre arrangement would result in only a partial overlap of the areas of excitation and detection, which may lead to the recording of signals dominated by radial heat diffusion, which contains little information on the optical coefficients compared to signals produced by predominately axially diffusing heat. To overcome this problem, the optical fibres could be positioned such that the fibre, which transmits the excitation laser pulse, is further away

from the target in order to provide a large area of excitation. If the detection fibre is positioned such that emissions from a small area at the centre of the illuminated spot are collected, one-dimensional analytical theories could be developed to interpret the signals. A similar technique has been used to investigate skin condition *in vivo*¹⁶⁸. The experimental set-up, however, may increase the size of the detector to an extent that would prohibit endoscopic or interstitial applications. Fibre-optic radiometry does nevertheless have the advantage of allowing excitation as well as emission spectroscopy¹⁶⁹. This could be achieved by varying the excitation wavelength using a tuneable laser as well as the selection of detection wavelengths using bandpass filters. The optical fibre sensor only enables excitation spectroscopy to be performed.

The optical fibre sensor has the advantage that the photothermal excitation and detection are coaxial, which allows the predominant detection of axially diffusing heat from which information about the optical properties of the target can be obtained. The axial symmetry of the sensor also allows a more straightforward theoretical modelling, i.e. two-dimensional geometry, of the light and heat transport in a scattering target. The modelling of heat conduction for an endoscopic dual fibre radiometric set-up would require a three-dimensional model, which would increase the necessary computing power. Measurements performed using dual fibre radiometry may also provide less sensitivity to the optical coefficients due to the detection of the effects of radial heat flow. It may therefore be concluded that, at the moment, the optical fibre sensor has the advantage for photothermal measurements during endoscopy and interstitial applications compared to fibre-optic radiometry provided the short-term stability can be improved. This could be achieved by using a single-mode optical fibre instead of the multimode fibre. A single-mode fibre would reduce the phase dispersion since it restricts the range of possible path lengths in the interferometer cavity. A single-mode fibre may therefore make the optical fibre sensor less susceptible to vibrations. The optical fibre sensor also has the great advantage of being suitable for simultaneous photothermal and photoacoustic measurements.

8.3 Accuracy of optical coefficients determined using photothermal techniques

Pulsed photothermal radiometry and the optical fibre sensor have been demonstrated to be applicable to the determination of the absorption and scattering coefficients of turbid media. The ability of both techniques to estimate μ_a and μ_s' close to the 'known' values, however, was strongly dependent upon accurate prior knowledge of the thermal coefficients of the target. This represents a considerable problem for determining optical coefficients from *in vivo* measurements where a very high degree of certainty in the thermal coefficients is unrealistic. *In vivo* thermal properties are dependent upon the tissue composition and have also been shown to be affected by physiological factors such as temperature-dependent perfusion. In this section, the accuracy of the absorption and reduced scattering coefficients determined using the optical fibre sensor will be discussed and a comparison to the performance of pulsed photothermal radiometry based on the results obtained from the work presented in this thesis is given.

The absorption coefficients of non-scattering gels determined from photothermal signals detected using PPTR showed differences of $\pm 5.0\%$ compared to the μ_a obtained from transmittance measurements. The variation in the absorption coefficient estimated from measurements using the optical fibre sensor was lower at $\pm 2.4\%$. The reduced scattering coefficients obtained using PPTR and the optical fibre sensor showed similar variations to the true value, which were of the order of $\pm 15\%$ for both techniques. It is important to point out that the optical coefficients could only be determined to this accuracy if the thermal coefficients were assumed to have very small initial uncertainties. The above values were calculated from the difference between the determined and the 'known' optical coefficients and should not be confused with the confidence limits or uncertainty in the estimated μ_a and μ_s' , which are discussed in the following section.

8.3.1 Confidence limits of the determined optical coefficients

A curve fit based on least squares minimisation was employed to obtain μ_a and μ_s' in PPTR, while the signals detected by the sensor were interpreted using model-based parameter estimation. Both methods rely on the minimisation of the difference between the experimental data and a theoretical model through varying the values of a number of model parameters. MBPE also incorporated prior information in the form of the initial value and uncertainty of the parameters as well as the experimental error. The methods to calculate the confidence limits or uncertainties in the estimated parameters were different in PPTR compared to the analysis of sensor signals. The least squares method of reducing the difference between the signal and the model predictions that was employed for PPTR, also produced an improvement in the knowledge of the optical parameters but without inclusion of prior information. The confidence limits of the estimated parameters were obtained from a χ^2 contour, which was calculated from the noise on the experimental data as opposed to noise in both the measurement and the parameters as it is done in MBPE. In MBPE, the improvement in the knowledge was quantified by the reduction in the final uncertainty of a parameter compared to the initial uncertainty. The estimated uncertainties of the parameters of interest were therefore not only dependent upon the error in the experimental observation but also on the uncertainties in all other parameters.

Since the methods that were employed to obtain the optical coefficients were different for PPTR and the optical fibre sensor, it is not very useful to compare the confidence limits of the determined μ_a and μ_s' that were calculated from photothermal measurements made using PPTR and the optical fibre sensor. It is likely that the uncertainty in the optical coefficients obtained using PPTR could be improved if prior information was incorporated in the parameter estimation. The potential improvements of MBPE can be illustrated with a contour plot of the residuals calculated from a photothermal signal, which was detected using the optical fibre sensor. The residuals were obtained by varying the absorption coefficient and the amplitude around the parameter pair that produced the smallest residual.

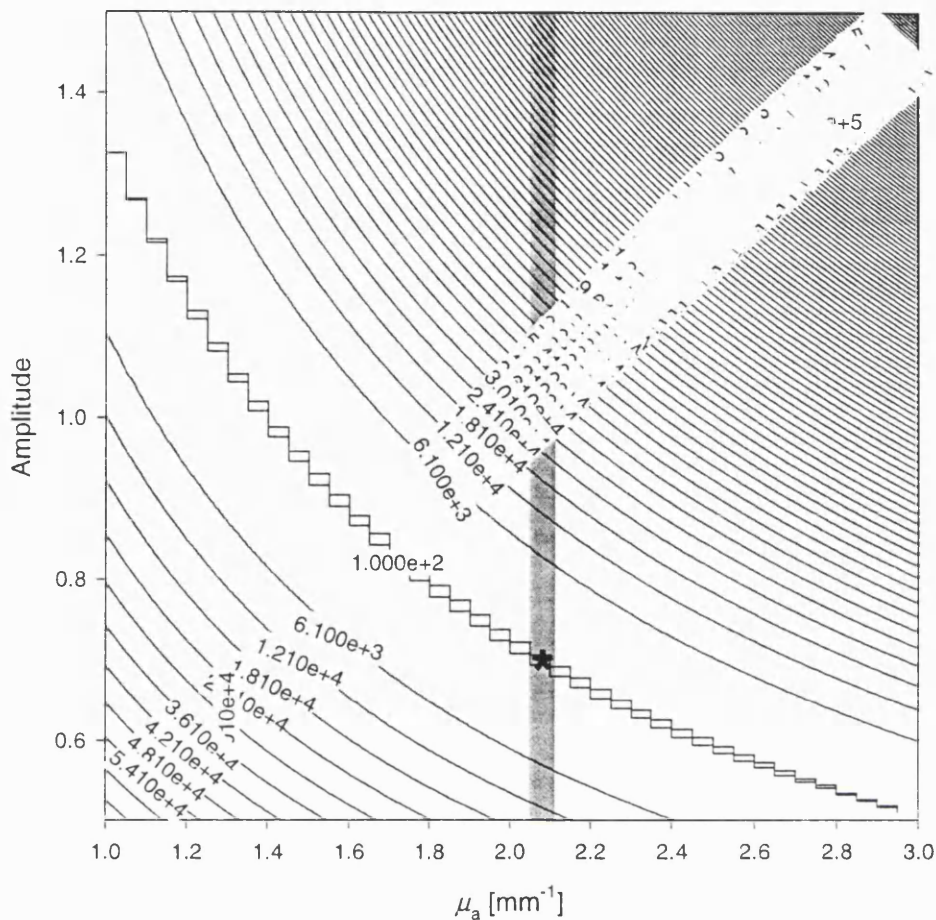


Figure 8.1 Contour plot of the residuals calculated from a photothermal signal ($\mu_a = 2.05 \text{ mm}^{-1}$) and the numerical model of the optical fibre sensor. The asterisk represents the minimum residual and the grey area the uncertainty in the estimated μ_a calculated using MBPE. The innermost contour line represents the confidence limit obtained from the noise of the signal.

Figure 8.1 shows a comparison of the confidence limit of μ_a that was obtained from the noise on the experimental data and the uncertainty in the absorption coefficient that was achieved using MBPE. MBPE produced a very much smaller margin of uncertainty than the calculated contour line since it incorporated the variances of the other parameters. The innermost contour line stretches over an enormous range of absorption coefficients and indicates that photothermal signals detected using the optical fibre sensor are not very sensitive to changes in μ_a . The small estimated uncertainty in μ_a shown in Figure 8.1

illustrates the benefits of MBPE for rigorous parameter estimation. The final uncertainty in μ_a is much smaller than the confidence obtained from the innermost contour since the range of amplitude-related parameters was effectively restrained during the estimation procedure by their initial uncertainties. The analysis of radiometrically detected signals using MBPE is therefore likely to improve the confidence in the estimated optical coefficients by including prior information on the thermal coefficients.

The estimation of the reduced scattering coefficient from photothermal signals detected using the sensor clearly demonstrated the limitations of the technique. A change in the reduced scattering coefficient by 1 mm^{-1} produced a change in the detected signal amplitude of only a few percent while showing no significant effect on the shape of the signal. This was further confirmed by the estimated uncertainties, which were only slightly reduced compared to the initial uncertainty. The small reduction in uncertainty illustrated that our knowledge in μ_s' had not been increased through the photothermal measurement and underlined the inherent low sensitivity of the technique to changes in μ_s' .

Both methods have demonstrated, however, that the optical coefficients of turbid targets can be determined photothermally with an accuracy of typically $\pm 10\%$ for μ_a and $\pm 15\%$ for μ_s' compared to the measured or calculated values of absorption and scattering. Given that the difference in the reduced scattering coefficient of cancers compared to normal tissue can be as small as 20%, the resolution in μ_s' produced by the optical fibre sensor may not be sufficient for diagnosing cancer on the basis of differences in the reduced scattering coefficient alone. The difference in the scattering of light is perhaps not the only property that could be used to differentiate cancers from normal tissue. The absorption coefficient and thermal properties of cancers *in vivo* may show characteristic differences to the healthy surroundings on which the diagnosis could be based.

8.3.2 Comparison of the parameter sensitivities

It has already been shown in section 6.3 that the normalised parameter derivatives of the theoretical signal are a convenient way of assessing the relative sensitivity of the various model parameters. In this section, the normalised parameter sensitivities are calculated for

PPTR using equation (6.27) and are compared to those obtained from the numerical model of the optical fibre sensor as described in section 6.3. Some variations on the theme of parameter sensitivities are presented and their relevance to measurements on tissue is discussed. The normalised parameter sensitivity is calculated by multiplying parameter sensitivity, which is the derivative of the theoretical signal with respect to an increment in a parameter, by the expected uncertainty in the parameter. The normalised parameter sensitivity is a measure to what extent the characteristics of a photothermal signal are affected by a particular parameter.

8.3.2.1 Pulsed photothermal radiometry

The following parameters are considered as variable during the estimation of optical coefficients using PPTR and the optical fibre sensor: the thermal conductivity, k_{Tissue} , the specific heat capacity, c_{Tissue} , the density, ρ_{Tissue} , μ_a , μ_s' and the pulse energy, E_p . PPTR has one additional unknown quantity, the infrared absorption coefficient μ_{IR} . The infrared absorption coefficient of tissue in the detected spectrum between 7 and 12 μm is generally very large ($>100 \text{ mm}^{-1}$) due to the high water content. The effect of variations by $\pm 20\%$ on the characteristics of the infrared signal is very small and μ_{IR} can therefore be neglected. The uncertainties in the parameters were the same as those used in the previous example in section 6.3. The specific heat capacity was assigned an uncertainty of $\pm 16.0\%$, while the density had an uncertainty of $\pm 5.0\%$. The thermal conductivity was assumed to be known to within $\pm 0.3 \cdot 10^{-4} \text{ W mm}^{-1} \text{ K}^{-1}$. The absorption coefficient and the reduced scattering coefficient had an uncertainty of $\pm 0.2 \text{ mm}^{-1}$ and $\pm 0.5 \text{ mm}^{-1}$ respectively. The above uncertainties were used to calculate all results presented in the following sections apart from Figure 8.4.

commented on the determination of μ_a and μ_s' using PPTR and gave an estimate of the effect of variations in the thermal coefficients. It was stated that a change in thermal diffusivity by 30% would result in an error of 5% in μ_a and 15% in μ_s' , which lead to the conclusion that the radiometric signal is primarily dependent upon the optical coefficients. This statement is correct if the variation in the thermal diffusivity ($\alpha = k c^{-1} \rho^{-1}$) is only due to a change in thermal conductivity. If, however, the change in the thermal diffusivity is due to a variation in the specific heat or the density, the discrepancy between theory and measurement would turn out to be bigger since c and ρ also affect the magnitude of the initial temperature rise. Judging from the plots shown in Figure 8.2, it may be more realistic to say that the thermal coefficients have as much influence on the amplitude and shape of a PPTR signal as the optical coefficients, whereby the absorption coefficient is more dominant than the reduced scattering coefficient. Figure 8.2 also suggests that optical coefficients of tissue can only be obtained with adequate confidence using PPTR if there is sufficient prior knowledge about the thermal coefficients to allow very small initial uncertainties to be assigned.

8.3.2.2 *The optical fibre sensor*

The parameter sensitivities of photothermal signals detected using the optical fibre sensor have already been presented in section 6.3 but are reproduced in Figure 8.3 for convenience. Figure 8.3 suggests that the photothermal signals detected in tissue *in vivo* with the optical fibre sensor are more or equally susceptible to changes in the specific heat capacity and density compared to the absorption and reduced scattering coefficient. This finding is explained by the large uncertainties in the *in vivo* thermal coefficients (see also section 2.5) that were used to calculate the normalised parameter sensitivities. Such large uncertainties would not allow the correlation of the amplitude and temporal behaviour of a photothermal signal to the optical or thermal properties since an adjustment of either of the two groups of parameters during the estimation procedure could produce a satisfactory agreement with the experimental data.

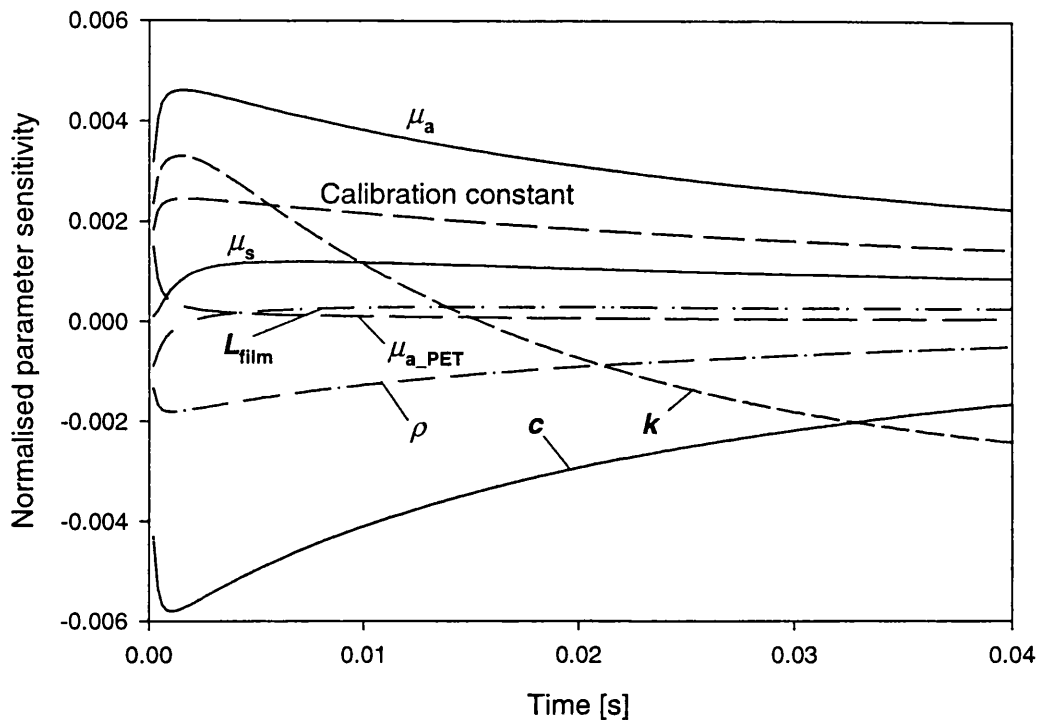


Figure 8.3 Normalised parameter sensitivities calculated using typical uncertainties in the properties of tissue *in vivo* for the case of a highly absorbing target ($\mu_a = 2.0 \text{ mm}^{-1} \pm 0.2 \text{ mm}^{-1}$).

One could therefore not conclude whether a difference in the shape and amplitude of two photothermal signals is due to a difference in the optical or the thermal coefficients of the measured tissues. The interpretation of signals detected in turbid gels showed that small uncertainties in the thermal parameters are essential in order to estimate μ_a and μ_s' at all accurately.

Determining optical coefficients of, for example, cancers may become problematic at excitation wavelengths where the difference between the optical coefficients of the tumour and the surrounding normal tissue is small. The scattering coefficient, which could be used as an indicator of tumour tissue, may deviate from the normal μ_s' by as little as 20%. Given the limited resolution in μ_s' that are obtained from measurements using the sensor, as shown in section 7.3.2, the thermal coefficients may have a more significant effect on the photothermal signal. The fundamental emission wavelength of the Nd:YAG laser at 1064 nm, which was used in the set-up of the optical fibre sensor, is used as an

example. The differences in μ_a and μ_s' of human kidney cancer and normal tissue at 1064 nm, which have been measured by the author (see section 1.5), have been used as uncertainties to calculate the parameter sensitivities as shown in Figure 8.4.

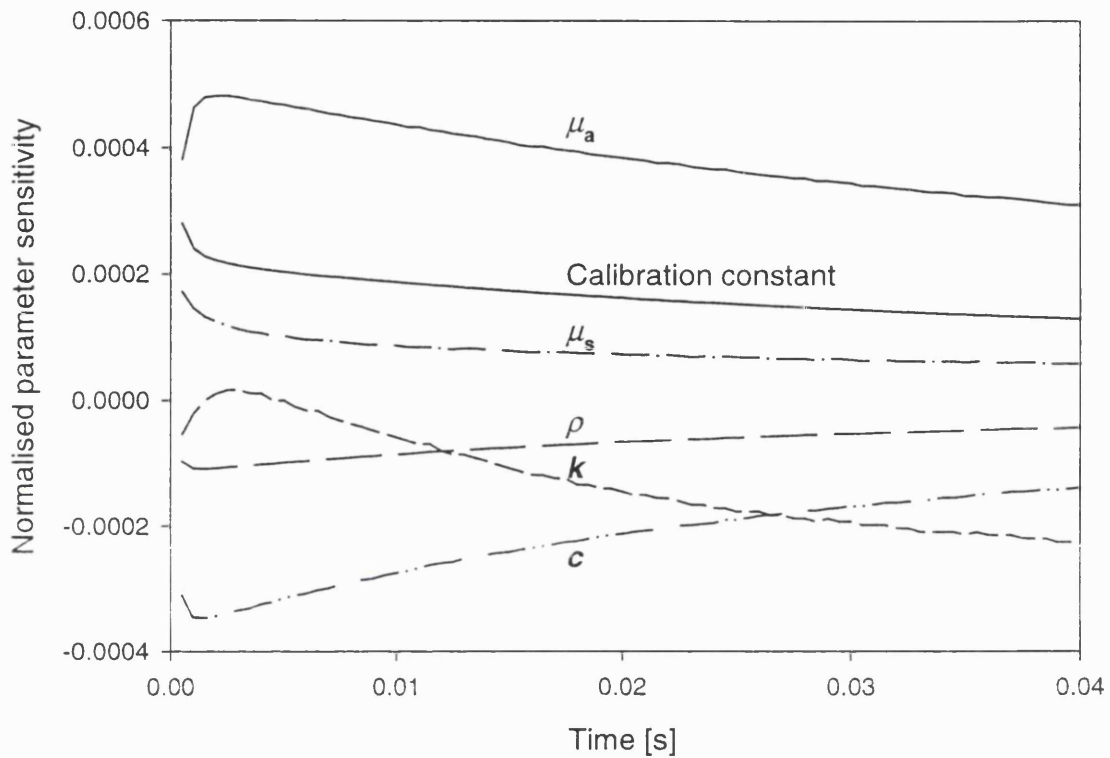


Figure 8.4 Normalised parameter sensitivities calculated using measured uncertainties in the optical coefficients of tumour and normal tissue at 1064 nm ($\mu_a = 0.03 \text{ mm}^{-1} \pm 0.02 \text{ mm}^{-1}$). Only the thermal conductivity shows a reduced sensitivity compared to a highly absorbing target (Figure 8.3).

The uncertainty in the optical parameters was based on the measurements of μ_a and μ_s' of the two types of tissue and was assumed to be $\pm 0.02 \text{ mm}^{-1}$ for μ_a , while the uncertainty for μ_s' was assumed to be $\pm 0.2 \text{ mm}^{-1}$. The uncertainty in the thermal coefficients was identical to the previous example shown in Figure 8.3. Comparing the results of Figure 8.4 to those of Figure 8.3 shows that the sensitivity of the optical coefficients relative to specific heat and density is no different to targets with higher absorption. Only the thermal conductivity

showed a significant shift to lower relative sensitivity. This can be explained by the relatively flat initial temperature profiles that are produced by low absorption in the tissue. Higher values of absorption create temperature gradients between the target tissue and the sensor as well as between shallower and deeper regions of the target tissue. For targets with high μ_a , the thermal conductivity has therefore a greater influence on the temporal characteristics of the photothermal signal. From the analysis of the normalised parameter sensitivities it can therefore be concluded that the optical fibre sensor can be applied to the determination of optical coefficients of soft tissues at weakly absorbing excitation wavelengths. The experimental results presented in chapter 7 have shown, however, that this is only possible on the basis of the detection of small changes in signal amplitude. All amplitude-related parameters therefore need to be known to high accuracy, which is a very problematic precondition for measurements of tissues *in vivo*.

The normalised parameter sensitivities are also applied to assess which photothermal technique is more sensitive to changes in the optical coefficients. This can only be achieved by normalising all theoretical photothermal signals of PPTR and the optical fibre sensor before the parameter sensitivities are calculated. The normalised signals will therefore only change in terms of their temporal characteristics, i.e. decay. Normalising the obtained parameter sensitivities with the expected uncertainty, which is the same for both PPTR and the optical fibre sensor yields the sensitivity of the shape of the photothermal signals to the optical coefficients, which is illustrated in Figure 8.5. Figure 8.5 shows that the shape of photothermal signals detected using the optical fibre sensor is less sensitive to changes in the optical coefficients compared to PPTR. The reduced scattering coefficient in particular does not show any significant effect on the decay of the signals, which is in agreement with the experimental results presented in section 7.3.2. The greater sensitivity of photothermal signals detected using PPTR may be explained with the difference in the thermal geometry compared to the optical fibre sensor. The cooling of a sample in contact with an insulator such as air will be more strongly determined by the laser-induced temperature gradients at greater depth. The heat flow in the target and optical fibre sensor is dominated by the temperature gradient between the heated target and the cooler film and to a lesser extent the laser-induced temperature gradient in the target.

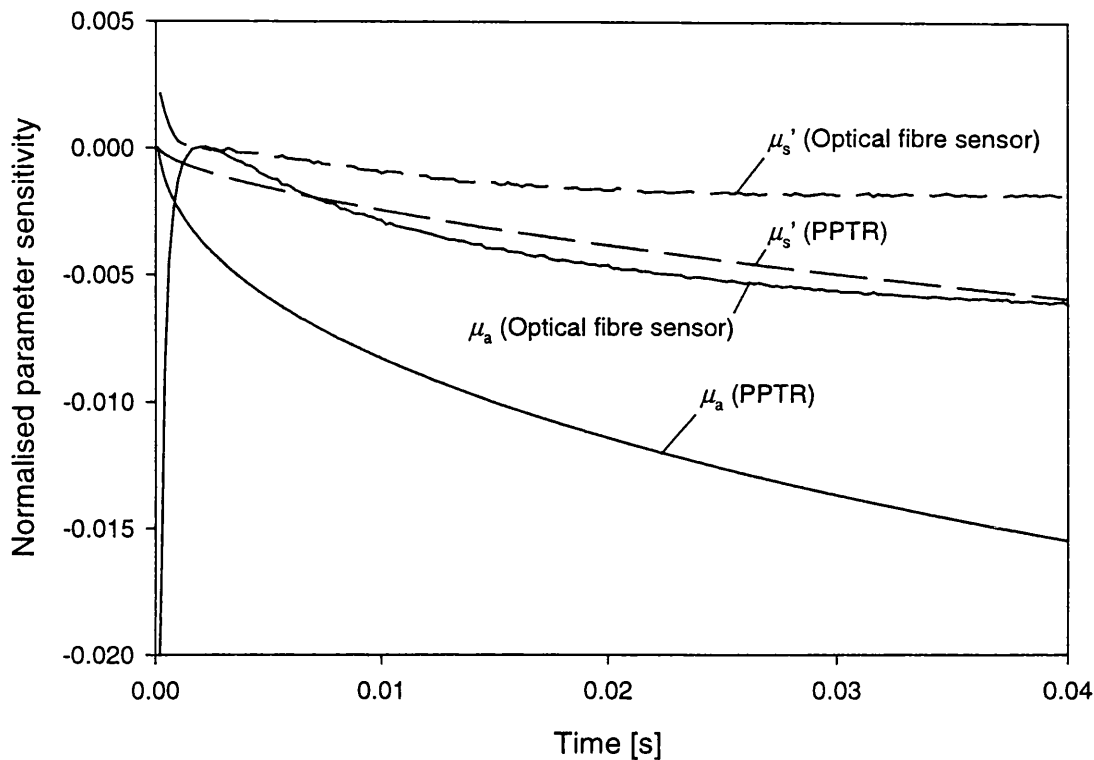


Figure 8.5 Normalised parameter sensitivities of normalised theoretical photothermal signals for PPTR and the optical fibre sensor to the optical coefficients.

Heat flow from the target into the film quickly eliminates any light-induced temperature gradients and the information content regarding μ_a and μ_s' is reduced. This perhaps also explains the high sensitivity of the photothermal signals to the optical coefficients at early times ($t < 20$ ms). The effects of radial heat flow may also reduce the sensitivity of the optical fibre sensor to the absorption and reduced scattering coefficient. Photothermal signals detected using the optical fibre sensor are therefore less sensitive to μ_a and μ_s' compared to PPTR. The higher sensitivity of PPTR to the optical coefficients may also explain why the μ_a and μ_s' determined from experimental data are close to the 'known' coefficients despite a lower signal-to-noise ratio and a parameter estimation without incorporation of prior knowledge.

The sensitivity of PPTR and the optical fibre sensor to the optical coefficients needs to be compared to their sensitivity to the thermal coefficients. If PPTR is found to be highly

sensitive to the thermal properties as well, its high sensitivity to the optical properties would be less advantageous since errors in the thermal properties would have a strong influence on the determined μ_a and μ_s' . The sensitivities of photothermal signals detected using PPTR and the sensor to the thermal coefficients were obtained in the same way as the normalised parameter sensitivity to the optical coefficients. The theoretical signals were again normalised before the normalised parameter sensitivity was calculated.

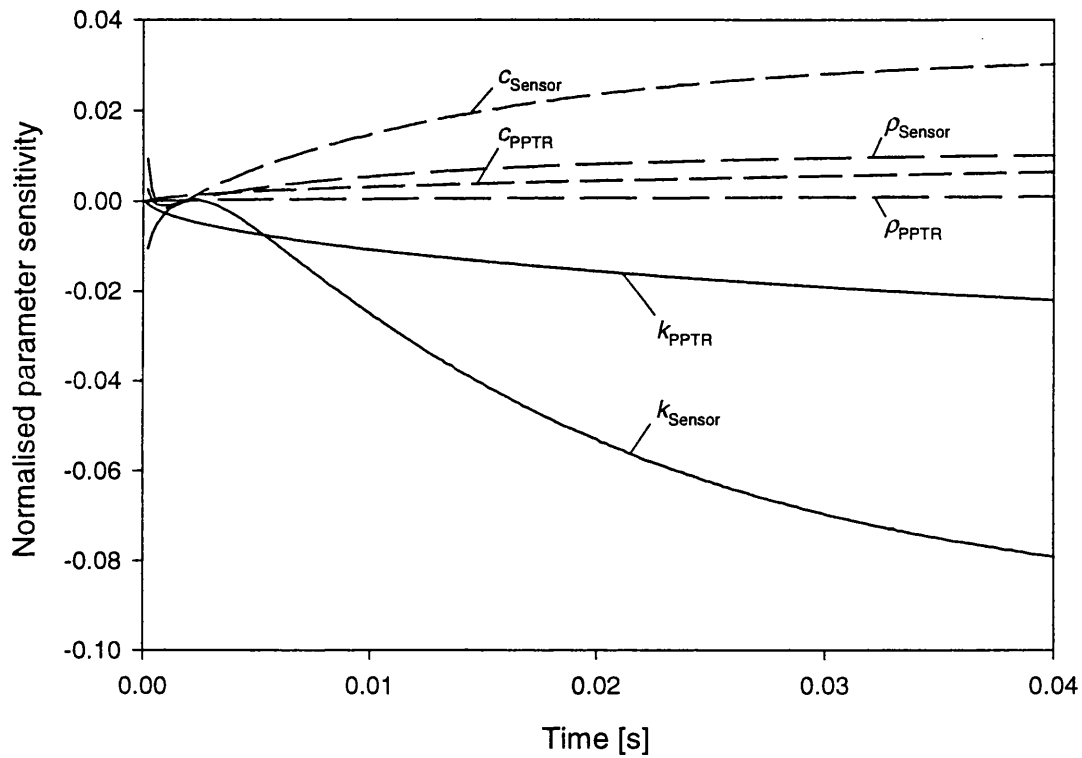


Figure 8.6 Normalised parameter sensitivities of normalised theoretical photothermal signals to the thermal coefficients.

Figure 8.6 illustrates that the optical fibre sensor is, with the exception of the density, more sensitive to the thermal parameters compared to pulsed photothermal radiometry. The results presented in Figure 8.6 were used to calculate the ratio of the sensitivity of the signals to the thermal coefficients to the sensitivity of the signals to the absorption

coefficient, which shows most clearly which technique is more sensitive to the thermal or the optical coefficients.

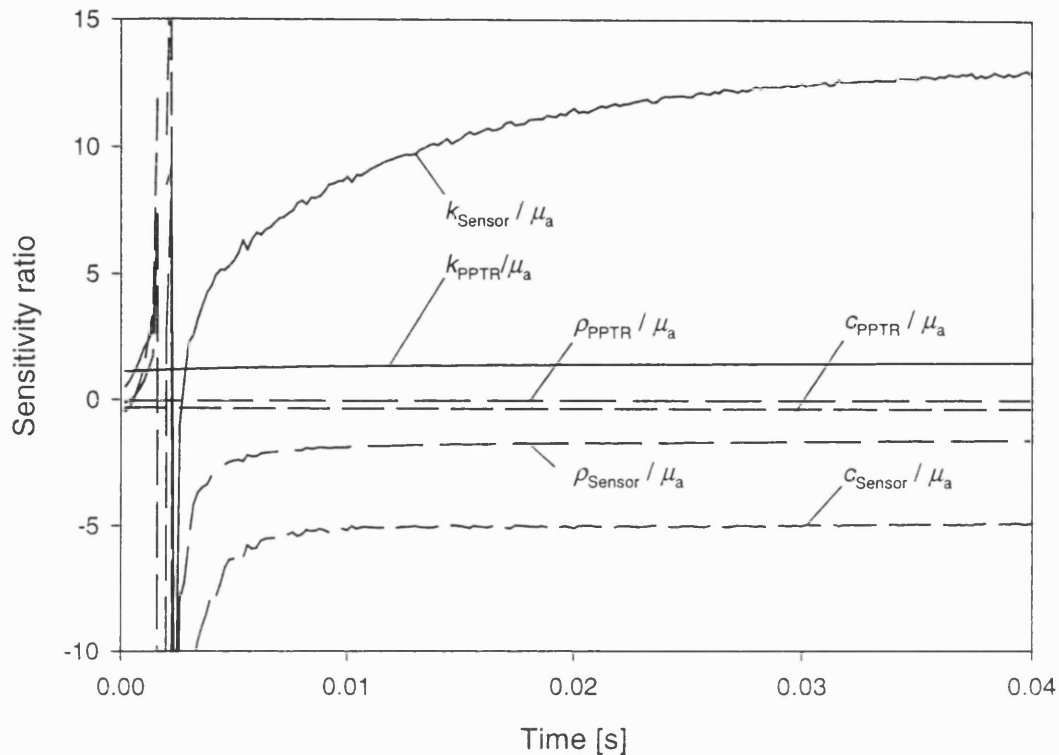


Figure 8.7 Sensitivity ratio of the thermal coefficients to the absorption coefficient of photothermal signals detected using the sensor and PPTR. The sensitivity ratio was calculated from the normalised parameter sensitivities of normalised signals.

Figure 8.7 illustrates that photothermal signals detected using the optical fibre sensor are more sensitive to the thermal coefficients compared to the optical coefficients. This may be explained by the effect of radial heat diffusion on the detected signal. Any change in the thermal properties would have a strong effect on the cooling of the laser-induced temperature rise. In PPTR, heat diffusion is considered to occur in only one spatial direction, which may limit the effects of varying thermal properties on the photothermal signal. The results also show that PPTR is less sensitive to the thermal coefficients compared to the optical fibre sensor. Since PPTR has been shown to be better suited to the determination of optical coefficients than the optical sensor, the normalised parameter

sensitivity was used to assess which configuration of the optical fibre sensor would produce the highest sensitivity to the absorption coefficient. Factors such as radial heat diffusion, thermal geometry and film thickness were investigated in order to find the optimal experimental configuration. For example, the thermal properties of the backing material of the sensing film were changed to simulate an insulating material, which was equivalent to the thermal geometry of PPTR. The ratio of the area of photothermal excitation to detection was increased to produce a one-dimensional heat conduction. The film thickness of the optical fibre sensor was also reduced to $2\ \mu\text{m}$ in order to create a thermal geometry close to that of PPTR. The normalised parameter sensitivities were calculated from normalised photothermal signals, which were calculated for various combinations of the above factors. The results are shown in Figure 8.8 below.

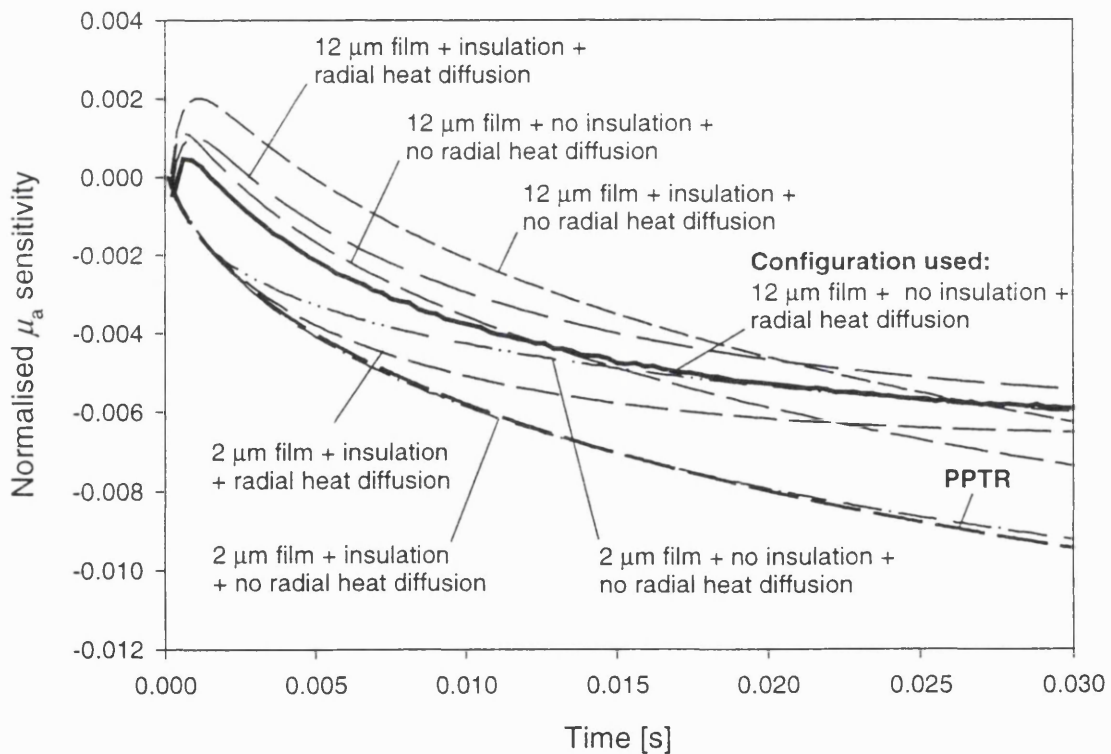


Figure 8.8 Normalised parameter sensitivities of normalised signals for various configurations of the optical fibre sensor. An optical fibre sensor detecting one-dimensional heat flow using a very thin ($2\ \mu\text{m}$) sensing film bounded by an insulator is most sensitive to the absorption coefficient and matches the sensitivity of PPTR.

It can be seen from Figure 8.8 that the current configuration of the optical fibre sensor can be improved by using a thinner film, which is backed by an insulator such as air, and a larger area of photothermal excitation compared to the area of detection. In order to maximise the sensitivity of the optical fibre sensor all three considered factors need to be adjusted. The higher sensitivity of the sensor due to a thinner film demonstrates that relatively fast changes in the temperature at the interface of the sensing film with the target tissue require a thermally thin sensing element. An insulating backing material was also found to be beneficial to the sensitivity. An insulator effectively removes the additional temperature gradient between the film and the backing material, which, for the case of a very thin sensing film, makes the monitored temperature changes more dependent upon the laser-induced temperature distribution in the target. This results in a higher sensitivity of the photothermal signal to the absorption coefficient. A large ratio of the area of excitation to the area of detection removes the effects of radial heat diffusion. The absence of radial heat flow also contributes to an increase in sensitivity to μ_a . The implementation of an insulated sensing film or reduced thickness and one-dimensional heat flow produced a sensitivity of the optical fibre sensor that matched that of PPTR.

The results presented in this section indicate that the thermal parameters have a strong effect on the photothermal signal and further suggest that photothermal techniques, such as PPTR and the optical fibre sensor, could be employed to determine the thermal rather than the optical coefficients of tissue. This could only be achieved, however, if μ_a and μ_s' are known to a high degree of certainty. Water, which is the dominating constituent of soft tissue, exhibits much stronger absorption in the infrared wavelength region compared to the visible or near-infrared spectrum. The effects of optical scattering are also much weaker. Provided other tissue chromophores, such as lipids and proteins, do not have a strong effect on the total μ_a , the optical coefficients could be regarded as equal to that of water. Using these assumptions and assuming low uncertainty in μ_a , the thermal properties of tissue may be determined from photothermal measurements made at excitation wavelengths where water has a strong absorption peak. A suitable wavelength for photothermal excitation may be in the region from 1.3 – 2.2 μm where water has absorption coefficients between of 0.7 to 6.9 mm^{-1} . Laser sources that emit in the infrared spectrum

include Er:YAG (2.94 μm), Tm:YAG (2.01 μm) and Ho:YAG (2.1 μm) lasers. The analysis of the thermal properties may provide diagnostic information.

Provided the thermal properties of tissue can be measured with good accuracy, one could use the thermal coefficients to determine μ_a and μ_s' from photothermal signals detected at visible or near-infrared excitation wavelengths. The combined information from the thermal and optical coefficients could be used to diagnose diseases such as cancer. Such dual wavelength measurements may therefore significantly improve the accuracy of the obtained optical coefficients.

8.4 Summary

The performance of the optical fibre sensor as a temperature transducer is comparable with other thermal detectors, such as radiometric and contact-pyroelectric transducers. The overall sensitivity and the response time of the optical fibre sensor could be optimised independently depending on the application. There is, however, a trade-off between the response time and the sensitivity, which typically requires that a compromise between transducer speed and sensitivity is found.

Fibre-optic photothermal radiometry is perhaps most closely related to the optical fibre sensor with which the optical properties of tissue could be determined endoscopically or interstitially. Fibre-optic radiometry has a similar sensitivity compared to the optical fibre sensor but would present problems in the delivery of the excitation pulses due to the lower damage thresholds if only one infrared transmitting fibre was used. The absorption of the excitation laser pulse by the fibre is also likely to complicate matters since it may lead to infrared emissions by the fibre itself which may obscure the emissions detected from the target. The use of a separate delivery fibre is feasible but may complicate the determination of optical coefficients due to the effect of radial heat diffusion. Fibre-optic radiometry is very likely to benefit from the higher sensitivity of radiometric signals detected using free-space radiometry to changes in the absorption and reduced scattering coefficients compared to the optical fibre sensor, as shown in section 8.3.2.2.

The comparison of the parameter sensitivities showed that pulsed photothermal radiometry and the optical fibre sensor only allow the determination of meaningful optical coefficients if the initial uncertainties in the thermal coefficients of tissue are small. This is a problem if the optical fibre sensor is used to make *in vivo* measurements, since the thermal properties of tissue are dependent upon the tissue composition and physiological conditions such as perfusion. This could perhaps be overcome by making an additional measurement using a pulsed laser with an infrared wavelength where water is the dominant tissue chromophore. The optical coefficients could be assigned small uncertainties, which would allow the determination of the thermal coefficients. The thermal coefficients could then be used to improve the accuracy of the optical coefficients at other excitation wavelengths. The normalised parameter sensitivities also showed that the shape of photothermal signals detected using the optical fibre sensor is less sensitive to the optical coefficients compared to the temporal characteristics of signals detected using PPTR. The analysis of the normalised parameter sensitivity illustrated that PPTR and the optical fibre sensor are more sensitive to thermal coefficients compared to the optical coefficients. The uncertainties in the thermal coefficients therefore need to be small for both techniques if optical coefficients are to be obtained from photothermal measurements. The optical fibre sensor has been shown to be much more sensitive to thermal coefficients compared to PPTR. This feature could be exploited for the determination of thermal parameters from photothermal signals at infrared excitation wavelengths.

The sensitivity of the optical fibre sensor to the optical coefficients could be optimised by using sensing films of less than 2 μm thickness, which are backed by an insulating backing material, and an area of photothermal excitation much larger than the area of detection. A reduction in the thickness of the film, however, will result in a reduced overall detection sensitivity. This may be overcome by using materials of high refractive index and thermal expansion coefficient for the sensing film. If a very thin film is used, the insulating backing material would need to be a solid as opposed to air, which is a very good insulator, to prevent damage and deformation to the film. One-dimensional heat flow across the sensitive region of the optical fibre sensor could be achieved by using a double clad optical fibre.

CONCLUDING REMARKS AND OUTLOOK

In this thesis, the results of the development of an optical fibre sensor for the photothermal determination of optical coefficients are presented. The aim of the work was to develop the optical fibre sensor into a device for diagnosing cancers and other tissue pathologies minimally invasively and non-destructively. The work presented in this thesis was focussed on the determination of the absorption and reduced scattering coefficients of tissue from photothermal signals detected using the sensor. Studies into the optical coefficients of tumours indicated that while there were no significant differences in the mean optical properties of tumours and normal tissue for entire groups of subjects, the absorption and reduced scattering coefficient was nevertheless significantly different for each individual subject¹⁷¹. The thermal properties of tumours could also be different from one type of tissue to another. The effect of varying thermal properties on the photothermal signal and the determined optical coefficients was addressed in this thesis.

Radiometric photothermal techniques had already been used to investigate a number of different tissues. The size and bulk of the equipment involved prohibited the use of such techniques during endoscopy and the applications were typically aimed at the characterisation of skin lesions, such as port-wine-stains, or the assessment of skin condition, such as hydration. The optical fibre sensor therefore provided an opportunity for making photothermal measurements on tissues deep inside the human body.

Pulsed photothermal radiometry was employed for the determination of optical coefficients from photothermal signals detected in turbid gels. This pilot study showed that the absorption and reduced scattering coefficients could be determined photothermally with good accuracy. The estimation of the reduced scattering coefficient from turbid gelatine samples by relying on amplitude information, however, indicated some of the fundamental problems of photothermal determination of optical coefficients, namely the insensitivity of the shape of the photothermal signal to changes in the reduced scattering coefficient within the physiological range. These problems would re-appear during the work on the optical fibre sensor. Pulsed photothermal radiometry nevertheless demonstrated the feasibility of

photothermal determination of optical coefficients with good accuracy, which was an encouraging result for the following work on the optical fibre sensor.

The description of heat conduction in the optical fibre sensor and the target required two-dimensional modelling since the optical penetration depth was similar to the diameter of the area of optical excitation. The areas of photothermal excitation and detection were also almost identical. Finite elements provided a very flexible numerical method for the computation of two- and three-dimensional heat conduction and allowed the incorporation of results from accurate, stochastic Monte Carlo models of light transport. Model-based parameter estimation was employed to determine the optical coefficients from the photothermal signals detected using the sensor. MBPE was found to be a very useful tool in analysing the dependence of the final uncertainties in the estimated optical parameters on the initial uncertainties in thermal parameters of the target. The parameter sensitivities, which are a by-product of MBPE, proved invaluable in assessing the effect of individual target properties on the photothermal signal and allowed a very useful comparison of the sensitivity of PPTR and the optical fibre sensor to the optical coefficients.

The performance of the optical fibre sensor as a technique for the determination of the absorption and reduced scattering coefficients was compared to pulsed photothermal radiometry, which represented a well-established and well characterised photothermal technique for the determination of optical coefficients. The optical fibre sensor was found to have smaller detection sensitivity and longer response times compared to radiometric detectors. The detection sensitivity and response time of the optical fibre sensor were nevertheless sufficient for photothermal measurements and the application of a numerical model allowed the determination of absorption and reduced scattering coefficients.

The optical fibre sensor has been shown to be suitable for the determination of the absorption and reduced scattering coefficients of turbid targets. However, the estimation of optical coefficients is strongly dependent upon the accurate knowledge of the thermal coefficients of the target. Large uncertainties in the thermal properties do not allow the estimation of meaningful values for μ_a and μ_s' . This poses the main problem for the use of the optical fibre sensor for *in vivo* measurements of the photothermal response of tissue where the thermal coefficients may vary greatly between different tissue types. The accuracy of optical coefficients obtained using PPTR was similarly affected by large

uncertainties in the thermal coefficients. The comparison of the normalised parameter sensitivities revealed that the temporal shape of the photothermal signals detected using PPTR is more sensitive to the optical coefficients compared to the signals detected using the optical fibre sensor in its current configuration. PPTR is for the moment a superior technique for the photothermal determination of optical coefficients. Investigations into the effects of radial heat flow, the thickness of the sensing film and the thermal properties of the backing material of the film have shown that the optical fibre sensor could be configured such that its sensitivity to optical coefficients matches that of PPTR. This would require the sensor to have an insulated sensing film of less than 3 μm thickness and to be unaffected by radial heat flow. However, the current configuration of the optical fibre sensor produced a higher sensitivity to the thermal coefficients of the target compared to PPTR. The characteristics of the photothermal signal detected by the sensor are affected by the presence of radial heat flow. The thermal properties of the target therefore have a stronger effect on the sensor signal, which results in a higher sensitivity of the optical fibre sensor to the thermal coefficients.

PPTR and the optical fibre sensor were found to be more sensitive to the absorption coefficient than the reduced scattering coefficient. This inherent insensitivity to scattering could be exploited for the monitoring of changes in the absorption coefficient. Since the variation in the reduced scattering coefficient of one type of tissue in the near-infrared wavelength range would not produce significant changes in the shape of the photothermal signal, the optical fibre sensor may be used for the determination of the absorption coefficient at different excitation wavelengths.

The issues that have been addressed in this thesis have led to ideas for future developments of the optical fibre sensor. Given the sensitivity of the optical fibre sensor to changes in the thermal properties of the target, it may be feasible to use the sensor for the measurement of thermal coefficients of tissue from its photothermal response. Such applications will only be successful, however, if the optical coefficients of the tissue are known to high accuracy. This could possibly be achieved by using pulsed optical excitation at wavelengths (e.g. 1.44 μm , 2.1 μm and 2.94 μm), where water, which is the dominant component of soft tissue, is highly absorbing. The effects of optical scattering would also be much smaller at these wavelengths compared to the visible and near-infrared region

since the magnitude of scattering decreases with increasing wavelength. If the optical coefficients of tissue can be approximated by the μ_a of water and scattering could be regarded as constant, the photothermal response detected by the optical fibre sensor could be used to determine the thermal coefficients of the tissue. The absorption and reduced scattering coefficients reported by others indicate that the optical properties are dominated by water absorption^{172,173,174}. However, the techniques that were employed to measure μ_a and μ_s in those studies were different. Feasibility studies using only one method to measure the optical properties of tissue would need to be carried out in order to establish the variance in the optical coefficients of tissue. The results would reveal whether the optical coefficients of soft tissue are in fact close or equal to water or whether they are different but could be regarded as quasi-invariant. The study would also give an indication as to whether other tissue chromophores, such as lipids and proteins, render the optical coefficients of tissue variable. Provided the optical coefficient at certain wavelengths can be considered constant, the optical fibre sensor can be used to determine the thermal coefficients of tissue. Such a technique may provide useful diagnostic information. Once the thermal coefficients have been determined at these excitation wavelengths, further photothermal measurements could be performed at excitation wavelengths in the visible and near-infrared from which the optical coefficients may be obtained using the reduced uncertainties in the thermal coefficients from the first measurement.

Since one of the main problems in the determination of optical coefficients is the necessary use of amplitude information, one could also envisage relative measurements using imaging techniques, which would avoid the calibration problems of individual point measurements. Using an array of photothermal thin-film Fabry-Perot detectors, it may be feasible to detect differences in the optical and thermal properties of tissues. The comparison of the photothermal responses would still require adequate knowledge of either the thermal or optical coefficients of the tissue in order to make the comparison of the signals detected using the array valid. The use of particular infrared excitation wavelengths may allow the detection of differences in the thermal properties of tissue as described earlier. If the thermal properties could be regarded as invariant over the imaged area, the optical properties could be mapped. A photothermal imaging device would be much bigger in size compared to the optical fibre sensor and the applications of such a device would

therefore be restricted to easily accessible organs, such as the skin. One of the targets of the device could be the detection of malignant melanoma, which is still difficult to diagnose without taking a diagnosis.

In summary, the optical fibre sensor in its current configuration is not ideally suited to the determination of optical coefficients of tissue, but the work presented in this thesis has shown that it could be developed to an extent where it would match the performance of PPTR. The optical fibre sensor in its present form is more sensitive to the thermal coefficients than the optical coefficients – an aspect that could be exploited to image tissues photothermally.

APPENDIX A: DERIVATION OF THE HEAT DIFFUSION EQUATION

The following derivation of the heat diffusion equation is published in Carslaw and Jaeger and is reproduced here for completeness. According to Carslaw and Jaeger, the theory of conduction of heat can be founded on one experiment in which a plate of some solid is given. The surfaces are parallel and are kept at different temperatures.

An imaginary cylinder inside the plate normal to the surfaces is used to derive an equation for the quantity of heat Q that flows through the plate in time t over the surface S . The temperature T_0 of the lower surface is assumed to be greater than T_1 of the upper surface. Both surfaces are at a distance d :

$$Q = \frac{k(T_0 - T_1) S t}{d}$$

where k is the thermal conductivity. The flow of heat between the two surfaces is proportional to difference of temperature of these surfaces.

Conduction of heat in an isotropic solid

An isotropic medium has structures and properties which are identical in the neighbourhood of every point inside the medium relative to all directions. Therefore, the current of heat at a point must be along the normal to the isothermal surface and in the direction of falling temperature.

Isothermal surface can be characterised as a model whereby a temperature T is the same for every point upon this surface. It can be imagined as a divider of a cooler area relative to T from a warmer area inside a solid.

The experiment described above can be used to explain the relation between the rate of change of temperature along the normal to the isothermal surface and the current of heat. In that case the isothermals are planes to the faces of the slab. The isothermals for T and $T + \delta T$

are assumed to be δx apart. The rate of flow of heat, per unit time per unit area, in direction of x increasing is

$$-k \frac{\delta T}{\delta x}$$

and in the limit of $\delta x \rightarrow 0$ we have as flux f_x

$$f_x = -k \frac{\partial T}{\partial x}.$$

This can be extended to any isothermal surface and can be taken as the fundamental hypothesis for the theory of conduction of heat by stating that the rate at which heat crosses from the inside to the outside of an isothermal surface per unit area per unit time at a point is equal to

$$-k \frac{\partial T}{\partial n}.$$

where k is the thermal conductivity, and $\partial/\partial n$ is the differentiation along the outward-drawn normal to the surface.

To find the flux at a point P across any surface, a tangent plane at P to the isothermal surface through P is taken as the XY -plane. The fluxes across the co-ordinate planes through P are

$$f_x = f_y = 0, \quad f_z = -k \frac{\partial T}{\partial z}.$$

If the normal at P to the given surface has direction cosines (λ, μ, ν) relative to these axes, the heat flux is given by

$$-k \nu \frac{\partial T}{\partial z} = -k \frac{\partial T}{\partial h}.$$

The term $\partial/\partial h$ expresses the differentiation in the direction (λ, μ, ν) , since

$$\frac{\partial T}{\partial h} = \lambda = \frac{\partial T}{\partial x} + \mu \frac{\partial T}{\partial y} + \nu \frac{\partial T}{\partial z}, \quad \frac{\partial T}{\partial x} = \frac{\partial T}{\partial y} = 0.$$

The flux of heat at any point across any surface is

$$-k \frac{\partial T}{\partial h},$$

where $\partial/\partial h$ is the differentiation in the direction of the outward normal.

The fluxes across three planes parallel to the co-ordinate surfaces are

$$f_x = -k \frac{\partial T}{\partial x}, \quad f_y = -k \frac{\partial T}{\partial y}, \quad f_z = -k \frac{\partial T}{\partial z}.$$

The differential equation of conduction of heat in an isotropic solid

The case of a solid through which heat is flowing is considered to derive a differential equation for the conduction of heat. The temperature v at a point $P(x, y, z)$ will be a continuous function of x, y, z and t . An imaginary element of volume, in this case a parallelepiped, with this point P as centre is used to describe the flow of heat across two of its faces. The edges are parallel to the co-ordinate axes and are of lengths $2dx, 2dy, 2dz$. The two planes are given as $ABCD$ and $A'B'C'D'$. The x -axis is perpendicular to these planes. The rate at which heat is flowing over the face $ABCD$ in the plane $x-dx$ is given

$$4 dy dz \left(f_x - \frac{\partial f_x}{\partial x} dx \right)$$

The rate at which heat is flowing across $A'B'C'D'$ is given by an identical expression. The expressions stand for the rates at which heat is flowing across two surfaces on either side of the point P in the direction of the x -axis. Thus the total gain of heat from these two faces is

$$- 8 dx dy dz \frac{\partial f_x}{\partial x}$$

The heat flow across the other faces can be expressed similarly as

$$- 8 dx dy dz \frac{\partial f_y}{\partial y}, \quad - 8 dx dy dz \frac{\partial f_z}{\partial z}$$

If the gaining of heat of this parallelepiped is defined as a temperature change per unit time the resulting function is

$$8 dx dy dz \rho c \frac{\partial T}{\partial t}$$

ρ and c are the density and the specific heat capacity respectively.

Both expressions stand for the rate of gain of heat of the volume element and are equal. One therefore arrives at

$$\frac{\partial T}{\partial t} + \frac{1}{\rho c} \left(\frac{\partial f_x}{\partial x} + \frac{\partial f_y}{\partial y} + \frac{\partial f_z}{\partial z} \right) = 0.$$

This equation holds at any point of any solid provided no heat is supplied at the point. The solid need not to be isotropic or homogeneous.

For the homogenous isotropic solid the heat fluxes across the three planes parallel to the co-ordinate axis are already given as f_x, f_y, f_z . The above equation becomes the heat diffusion equation

$$\frac{\partial T}{\partial t} = \alpha \left(\frac{\partial^2 T}{\partial x^2} + \frac{\partial^2 T}{\partial y^2} + \frac{\partial^2 T}{\partial z^2} \right)$$

where $\alpha = k \rho^{-1} c^{-1}$. The constant α is the *thermal diffusivity* of the material. If heat is generated in the solid so that at the point $P(x, y, z)$ heat is supplied at a rate of $A(x, y, z, t)$ the

so called heat source term is added and the above equation

$$\frac{\partial T}{\partial t} = \alpha \left(\frac{\partial^2 T}{\partial x^2} + \frac{\partial^2 T}{\partial y^2} + \frac{\partial^2 T}{\partial z^2} \right) + A(x, y, z, t)$$

APPENDIX B: SINGLE FILM INTERFERENCE

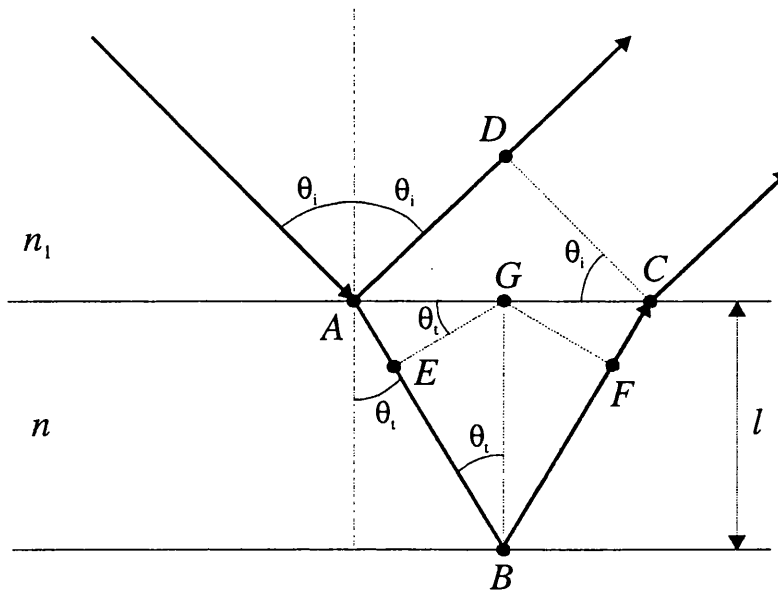


Figure 1 Single film interference of light incident at angle θ_i .

The derivation following in the following paragraph is taken from Pedrotti¹⁷⁵ to illustrate the phenomenon of interference of light produced by thin films. Consider the case shown in Figure 1 in which light strikes the film of thickness l . The incident beam of light is separated into the reflected and transmitted portions. The transmitted beam is reflected at the next interface and exits the film at the first interface at an angle identical to that of the reflected portion of the beam. The two beams travel parallel to each other and may merge at a detector where they superpose and interfere. Since the two beams travel different path lengths, a phase difference is produced, which may result in constructive or destructive interference. In the case of normal incidence, the optical path length difference, Δ , is simply the distance travelled by the light times the refractive index of the film material:

$$\Delta = 2ln \quad (2)$$

For the case of light incident at an angle, a phase difference is produced while the transmitted beam travels between the points ABC . At point C , both beams are parallel and

travel in the same medium and no further phase difference occurs. The phase difference between the two beams at points D and C is due to the difference between the optical path lengths AD and ABC . The path length difference between the beams at DC is therefore:

$$\Delta = n(AB + BC) + n_1 AD \quad (3)$$

Points E , G and F are introduced to help with the calculation by constructing the perpendiculars to AB and AC . The optical path ABC is broken apart and the optical path difference can be re-written as:

$$\Delta = [n(AE + FC) - n_0 AD] + n(EB + BF) \quad (4)$$

It can be shown, that the quantity in the square brackets vanishes. Using Snell's law (equation (5.16))

$$AE = AG \sin \theta_1 = \frac{AC}{2} \sin \theta \quad (5)$$

and

$$AD = AC \sin \theta_1 \quad (6)$$

Substituting equation (6) and (5.16) into equation (5) yields

$$2AE = AD \frac{\sin \theta}{\sin \theta_1} = AD \frac{n_1}{n} \quad (7)$$

which proves that

$$n_1 AD = 2nAE = n(AE + FC) \quad (8)$$

From equation (4) remains

$$\Delta = n(EB + BF) = 2nEB \quad (9)$$

The length EB is related to the thickness l by $EB = l \cos \theta$, which finally produces an expression for the optical path length difference depending on the angle of refraction:

$$\Delta = 2nl \cos \theta \quad (10)$$

An equivalent expression can be obtained for the angle of incidence via Snell's law. Equation (10) demonstrates that the optical path length difference, or effective optical thickness, decreases with increasing angle of incidence. This may be counterintuitive since

the beams travel a longer distance within the film at an angle. The paradox can be explained with the fact that the increase in the optical path length AD more than makes up for the increase in ABC .

PUBLICATIONS ARISING FROM THIS WORK

Laufer, J.G., Beard, P.C., Mills, T.N., "Photoacoustic-photothermal fibre sensor for the minimally invasive detection of cancers and other tissue pathologies," *Proc. SPIE*, **3596**, 217-224 (1999).

Laufer, J.G., Beard, P.C., Pérennès, F., Mills, T.N., "Progress in the development of an optical fibre sensor for the minimally invasive photothermal detection of cancer," *Proc. 10th International Conference on Photoacoustic and Photothermal Phenomena*, 606-608 (1998).

Laufer, J.G., Simpson, R., Kohl, M., Essenpreis, M., Cope, M., "Effect of temperature on the optical properties of *ex vivo* human dermis and subdermis," *Phys. Med. Biol.*, **43**, 2479-2489 (1998).

Simpson, R., Laufer, J.G., Kohl, M., Essenpreis, M., Cope, M., "Near-infrared optical properties of *ex vivo* human skin and subcutaneous tissues using reflectance and transmittance measurements," *Proc SPIE*, (1997).

In addition, aspects of this work have been presented at a number of meetings and recorded as abstracts.

REFERENCES

- ¹ Mills T.N., "Photoacoustic ultrasound for guidance at laser angioplasty", (Abst.) The Rank Prize Funds, Mini-Symposium on sensors for Medical Laser Applications (5/1988).
- ² Navarro, F., Taourel, P., Michel, J., Perney, P., Fabre, J.M., Blanc, F., Domergue, J. "Diaphragmatic and subcutaneous seeding of hepatocellular carcinoma following fine-needle aspiration biopsy," *Liver* **18(4)**, 251-4 (1998).
- ³ Sammak, B., Yousef, B., Abd El Bagi, M., Al Karawi, M., Mohamed, A., Gali, M., Al Shahed, M., "Needle track seeding following percutaneous ethanol injection for treatment of hepatocellular carcinoma," *Hepatogastroenterology* **45(22)**, 1097-9 (1998).
- ⁴ Ayar, D., Golla, B., Lee, J.Y., Nath, H., "Needle-track metastasis after transthoracic needle biopsy," *J Thorac Imaging* **13(1)**, 2-6, Review (1998).
- ⁵ Grabau, D.A., Andersen, J.A., Graversen, H.P., Dyreborg, U., "Needle biopsy of breast cancer. Appearance of tumour cells along the needle track," *Eur J Surg Oncol* **19(2)**, 192-4 (1993).
- ⁶ Henyey, L.G., Greenstein, J.L., "Diffuse radiation in the galaxy," *J Astrophys*, **86**, 70-83 (1937).
- ⁷ Mie, G., "Beiträge zur Optik trüber Medien speziell kolloidaler Metallösungen," *Annalen der Physik*, **25**, 377-445 (1908).
- ⁸ Bohren, D.F., Huffman, D.R., "*Absorption and scattering of light by small particles*," Wiley, New York (1983).
- ⁹ Elwell, C.E, "*A practical users guide to near infrared spectroscopy*," Hamamatsu Photonics KK 1995.
- ¹⁰ Duck, F.A., "*Physical properties of tissue: a comprehensive reference book*," Academic Press Inc., San Diego (1990).
- ¹¹ Kaye, G.W.C., Laby, T.H., "*Tables of physical and chemical constants*," Longman Group Ltd. (1986).
- ¹² Jaques, S.L., "Origins of tissue optical properties in the UVA, visible, and NIR regions," *OSA Trends in Optics and Photonics*, **2**, 364-371 (1996).

- ¹³ Patterson, M.S., Wilson, B.C., Wyman, D.R., "The propagation of optical radiation in tissue I. Models of radiation transport and their application," *Lasers in Med. Science*, **6**, 155-167 (1991).
- ¹⁴ Wang, L.-H., Jacques, S.L., Zheng, L.-Q., "MCML – Monte Carlo modelling of photon transport in multi-layered tissues," *Computer Methods and Programs in Biomedicine* **47**, 131-146 (1995).
- ¹⁵ Gandjbakhche, A.H., Weiss, G.H., "Random walk and diffusion-like models of photon migration in turbid media," *Progress in Optics* ed E Wolf (Amsterdam: North-Holland), 333-401 (1995).
- ¹⁶ Gandjbakhche, A.H., Weiss, G.H., Bonner, R.F., Nossal, R., "Photon pathlength distributions through optically turbid slabs," *Phys. Rev. E* **48**, 810-818 (1993).
- ¹⁷ Ishimaru, A., "Wave propagation and scattering in random media," New York, Academic Press (1978).
- ¹⁸ Star, W.M., Marijnissen, J.P.A., van Gemert, M.J.C., "Light dosimetry in optical phantoms and in tissues: I. Multiple flux and transport theory," *Phys. Med. Biol.* **33**, 437-454 (1988).
- ¹⁹ Yoon, G., Prahl, S.A., Welch, A.J., "Accuracies of the diffusion approximation and its similarity relations for laser irradiated biological media," *App. Opt.* **28**, 2250-2255 (1989).
- ²⁰ Pogue, B.W., Patterson, M.S., Jiang, H., Paulsen, K.D., "Initial assessment of a simple system for frequency domain diffuse optical tomography," *Phys. Med. Biol.* **40**, 1709-1729 (1995).
- ²¹ Arridge, S.R., Schweiger, M., Hiraoka, M., Delpy, D.T., "A finite element approach for modelling photon transport in tissue," *Med. Phys.* **20(2)**, 299-309 (1993).
- ²² Schweiger, M., Arridge, S.R., Hiraoka, M., Delpy, D.T., "The finite element method for the propagation of light in scattering media: Boundary and source conditions," *Med. Phys.* **22(11)**, 1779-1792 (1995).
- ²³ Schmitt, J.M., Knüttel, A., Bonner, R.F., "Measurement of optical properties of biological tissues by low-coherence reflectometry," *Appl. Opt.* **32**, 6032-6042 (1993).

- ²⁴ Huang, D., Wang, J., Lin, C.P., Puliafito, C.A., Fujimoto, J.G., "Micron-resolution ranging of cornea anterior chamber by optical reflectometry," *Lasers Surg. Med.* **11**, 419-425 (1991).
- ²⁵ Eddowes, M.H., Mills, T.N., Delpy, D.T., "Monte Carlo simulations of coherent backscatter for identification of the optical coefficients of biological tissues *in vivo*" *Appl. Opt.* **34**, 2261-2267 (1995).
- ²⁶ Eddowes, M.H., "Coherent backscatter and its use in measuring the optical coefficients of biological tissues," Ph.D. thesis, University College London (1995).
- ²⁷ Hebden, J.C., Arridge, S.R., Delpy, D.T., "Optical imaging in medicine: I. Experimental techniques," *Phys. Med. Biol.* **42**, 825-840 (1997).
- ²⁸ Kirkby, D.R., "A Picosecond Optoelectronic Cross Correlator using a Gain Modulated Avalanche Photodiode for Measuring the Impulse Response of Tissue." Ph.D. thesis, University College London (1999).
- ²⁹ Patterson, M.S., "Frequency-domain measurements of light propagation," in *Optical-thermal response of laser-irradiated tissue*, edited by Welch, A.J. and van Gemert, M.J.C., Plenum Press, New York and London (1995).
- ³⁰ Madsen, S.J., Anderson, E.R., Haskell, R.C., Tromberg, B.G., "Portable high-bandwidth frequency-domain photon migration instrument for tissue spectroscopy," *Opt. Lett.* **19**, 1934-1936 (1994).
- ³¹ Tromberg, B.G., Svaasand, L.O., Tsay, T., Haskell, R.C., "Properties of photon density waves in multiple-scattering media," *Appl. Opt.* **32**, 607 – 616 (1993).
- ³² Patterson, M.S., Moulton, J.D., Wilson, B.C., Berndt, K.W., Lakowicz, J.R., "Frequency-domain reflectance for the determination of the scattering and absorption properties of tissue," *Appl. Opt.* **30**, 4474-4476 (1991).
- ³³ Fishkin, J.B., Coquoz, O., Anderson, E.R., Brenner, M., Tromberg, B.J., "Frequency-domain photon migration measurements of normal and malignant tissue optical properties in a human subject," *Appl. Opt.* **36(1)**, 10-20 (1997).
- ³⁴ Kienle, A., Lilge, L., Patterson, M.S., Hibst, R., Steiner, R., Wilson, B.C., "Spatially resolved absolute diffuse reflectance measurements for noninvasive determination of the

optical scattering and absorption coefficients of biological tissue," *Appl. Opt.* **35(13)**, 2304-2314 (1996).

³⁵ Farrell, T.J., Patterson, M.S., "A diffusion theory model of spatially resolved, steady-state diffuse reflectance for the noninvasive determination of tissue optical properties *in vivo*," *Med. Phys.* **19(4)**, 879-888 (1992).

³⁶ Farrell, T.J., Wilson, B.C., Patterson, M.S., "The use of a neural network to determine tissue optical properties from spatially resolved diffuse reflectance measurements," *Phys. Med. Biol.* **37**, 2281-2286 (1992).

³⁷ Bays, R., Wagnières, Robert, D., Braichotte, D., Savary, J-F., Monnier, P., van den Bergh, H., "Clinical determination of tissue optical properties by endoscopic spatially resolved reflectometry," *Appl. Opt.* **35(10)**, 1756-1766 (1996).

³⁸ Kumar, G., Schmitt, J.M., "Optimal probe geometry for near-infrared spectroscopy of biological tissue," *Appl. Opt.* **36**, 2286-2293 (1997).

³⁹ Bevilacqua, F., Pignatelli, D., Marquet, P., Gross, J.D., Tromberg, B.J., Depeursinge, C., "In vivo local determination of tissue optical properties: applications to human brain," *Appl. Opt.* **38(22)**, 4939-4950 (1999).

⁴⁰ Simpson, C.R., Kohl, M., Essenpreis, M., Cope, M., "Near-infrared optical properties of *ex vivo* human skin and subcutaneous tissues measured using the Monte Carlo inversion technique," *Phys. Med. Biol.* **43**, 2465-2478 (1998).

⁴¹ Ripley, P.M., Laufer, J.G., Gordon, A.D., Connell, R.J., Bown, S.G., "Near-infrared optical properties of *ex vivo* human uterus determined using the Monte Carlo inversion technique," *Phys. Med. Biol.* (in press)

⁴² Laufer, J., Beard, P., Mills, T., "A photoacoustic/photothermal optical fibre sensor for the minimally invasive detection of cancers and other tissue pathologies," SPIE proc. (1999).

⁴³ Laufer, J., Simpson, R., Kohl, M., Essenpreis, M., Cope, M., "Effect of temperature on the optical properties of *ex vivo* human dermis and subdermis," *Phys. Med. Biol.* **43**, 2479-2489 (1998).

⁴⁴ Gandjbakhche, A.H., Nossal, R., Dadmarz, R., Schwartzentruber, D., Bonner, R.F., "Expected detectability of adenocarcinoma tumors within human breast in time-resolved images," *Proc. SPIE* **2387**, 111-118 (1995).

- ⁴⁵ Troy, T.L., Page, D.L., Sevic-Muraca, E.M., "Optical properties of normal and diseased breast tissues: prognosis for optical mammography," *J Biomed. Opt.* **1(3)**, 342-355 (1996).
- ⁴⁶ Welch, A.J., van Gemert, M.J.C., *Optical-thermal response of laser-irradiated tissue* Plenum Press New York (1995).
- ⁴⁷ Carslaw, H.S., Jaeger, J.C., *Conduction of heat in solids*, Oxford University Press, Oxford (1959).
- ⁴⁸ Roider, J., Birngruber, R., "Solution of the heat conduction equation," in *Optical-thermal response of laser-irradiated tissue*, edited by Welch, A.J. and van Gemert, M.J.C., Plenum Press, New York and London (1995).
- ⁴⁹ De Jesus, M.E.P., *Thermal diffusivity measurements using pulsed photothermal radiometry*, Ph.D. thesis (1994).
- ⁵⁰ Johnson, C., *Numerical solution of partial differential equations by the finite element method*, Cambridge University Press, Cambridge (1990).
- ⁵¹ Zienkiewicz, O.C., *The finite element method in engineering science*, 3rd edition, McGraw-Hill, London (1977).
- ⁵² Burnett, D.S., *Finite element analysis from concepts to applications*, Addison-Wesley publishing company, Reading, U.S.A. (1987).
- ⁵³ Valvano, J.W., "Tissue thermal properties and perfusion," in *Optical-thermal response of laser-irradiated tissue*, edited by Welch, A.J. and van Gemert, M.J.C., Plenum Press, New York and London (1995).
- ⁵⁴ Valvano, J.W., Chitsabesan, B., "Thermal conductivity and diffusivity of arterial wall and atherosclerotic plaque," *Lasers Life Sci.* **1**, 219-229 (1987).
- ⁵⁵ Valvano, J.W., Cochran, J.R., Diller, K.R., "Thermal conductivity and diffusivity of biomaterials measured with self-heated thermistors," *Int. J Thermophys.* **6(3)**, 301-311 (1985).
- ⁵⁶ Cooper, T.E., Trezek, G.J., "Correlation of thermal properties of some human tissues with water content," *Aerosp. Med.* **42**, 24-27 (1971).
- ⁵⁷ Bowman, H.F., "Heat transfer and thermal dosimetry," *J. Microwave Power* **16**, 121-133 (1981).

- ⁵⁸ Duck, F.A., *Physical properties of tissue – a comprehensive reference book* Academic Press, London (1990).
- ⁵⁹ Latyshev, V.P., Ozerova, T.M., *Kholod. Tekn.* **5**, 37 (1976); cited in Duck, 1990.
- ⁶⁰ Woodard H.Q., White, D.R., “The composition of body tissues,” *Brit. J. Radiol.* **59** 1209-1219 (1986).
- ⁶¹ Woodard H.Q., White, D.R., “The composition of body tissues,” *Brit. J. Radiol.* **59** 1209-1219 (1986).
- ⁶² Valvano, J.W., Allen, J.T., Bowman, H.F., “The simultaneous measurement of thermal conductivity, thermal diffusivity, and perfusion in small volumes of tissue,” *J Biomed. Eng.* **106**, 194-197 (1984).
- ⁶³ Jain, R.K.; Grantham, F.H.; Gullino, P.M., “Blood flow and heat transfer in Walker 256 mammary carcinoma,” *J. Natl. Cancer Inst.* **62(4)**, 927-33 (1979).
- ⁶⁴ Bowman, H.F., Cravalho, E.G., Woods, M., “Theory, measurement, and application of thermal properties of biomaterials,” *Ann. Review Biophys. Eng.* **4**, 43-80 (1975).
- ⁶⁵ Gullino, P.M., Jain, R.K., Grantham, F.H., “Temperature gradients and local perfusion in a mammary carcinoma,” *J. Nat. Cancer Inst.* **68(3)**, 519-531 (1982).
- ⁶⁶ Dudar, T.E.; Jain, R.K., “Differential response of normal and tumor microcirculation to hyperthermia,” *Cancer Res.* **44(2)**, 605-12 (1984).
- ⁶⁷ Thormählen, I., Straub, J., Grigul, U., “Refractive index of water and its dependence on wavelength, temperature, and density,” *J. Phys. Chem. Ref. Data* **14(4)**, 933-945 (1985).
- ⁶⁸ Jaywant, S.M., Wilson, B.C., Patterson, M.S., Lilge, L.D., Flotte, T.J., Woolsey, J., McCulloch, C., “Temperature-dependent changes in the optical absorption and scattering spectra of tissues: correlation with ultrastructure” *SPIE Proc.* **1882**, 218-229 (1993).
- ⁶⁹ De Jesus, M.E.P., Imhof, R.E., “Thermal diffusivity of thermally conducting films on insulating substrates,” *Appl. Phys. A* **60**, 613-617 (1995).
- ⁷⁰ Leung, W.P., Tam, A.C., “Thermal diffusivity in thin films measured by noncontact single-ended pulsed-laser-induced thermal radiometry,” *Optics Lett.* **9(3)**, 93-95 (1984).
- ⁷¹ Tam, A.C., Sullivan, B., “Remote sensing applications of pulsed photothermal radiometry,” *Appl. Phys. Lett.* **43(4)**, 333-335 (1983).

- ⁷² Leung, W.P., Tam, A.C., "Techniques of flash radiometry," *J. Appl. Phys.* **56(1)**, 153-161 (1984).
- ⁷³ Aamodt, L.C., Maclachlan Spicer, J.W., Murphy, J.C., "Analysis of characteristic thermal transit times for time-resolved infrared radiometry studies of multilayered coatings," *J. Appl. Phys.* **68(12)**, 6087-6098 (1990).
- ⁷⁴ Krapez, J.C., Cielo, P., "Optothermal evaluation of oil film thickness on water," *J. Appl. Phys.* **72(4)**, 1255-1261 (1992).
- ⁷⁵ Leung, W.P., Tam, A.C., "Thermal conduction at a contact interface measured by pulsed photothermal radiometry," *J. Appl. Phys.* **63(9)**, 4505-4509 (1988).
- ⁷⁶ Almond, D.P., Patel, P.M., "Photothermal science and techniques," Chapman & Hall, London (1996).
- ⁷⁷ Balderas-López, J.A., Mandelis, A., Garcia, J.A., "Thermal-wave resonator cavity design and measurements of the thermal diffusivity of liquids," *Rev. Sci. Instr.* **71(7)**, 2933-2937 (2000).
- ⁷⁸ Wang, C., Mandelis, A., "Measurement of thermal diffusivity of air using photopyroelectric interferometry," *Rev. Sci. Instr.* **70(5)**, 2372-2378 (1999).
- ⁷⁹ Wang, C., Mandelis, A., "Purely thermal-wave photopyroelectric interferometry," *J. Appl. Phys.* **85(12)**, 8366-8377 (1999).
- ⁸⁰ Wang, C., Mandelis, A., Garcia, J.A., "Detectivity comparison between thin-film Pd/PVDF photopyroelectric interferometric and optical reflectance hydrogen sensors," *Rev. Sci. Instr.* **70(11)**, 4370-4376 (1999).
- ⁸¹ Jenkins, T.E., *Optical sensing techniques and processing* Prentice-Hall International (UK) Ltd (1987).
- ⁸² Power, J.F., "Impulse photopyroelectric depth profiling of multilayers. Part II: Experiments with amplitude- and phase-modulated wideband spectrometry," *Appl. Spectroscopy* **45(8)**, 1252-1270 (1991).
- ⁸³ Kanstad, S.O., Nordal, P., "Experimental aspects of photothermal radiometry," *Can. J. Phys.* **64**, 1155-1164 (1986).
- ⁸⁴ Pangilinan, G.I., Ladouceur, H.D., Russell, T.P., "Temperature measurements of a thermal wave at static high pressures," *Appl. Phys. Lett.* **76(17)**, 2460-2462 (2000).

- ⁸⁵ Wright, O.B., "Laser picosecond acoustics in double-layer transparent films," *Opt. Lett.* **20(6)**, 632-634 (1995).
- ⁸⁶ Li, B., Deng, Y., Cheng, J., "Sensitive photothermal interferometric detection method for characterization of transparent plate samples," *Rev. Sci. Instrum.* **67(10)**, 3649-3657 (1996).
- ⁸⁷ Wilkens, V., Wiemann, C., Koch, Ch., Foth, H.-J., "Fibre-optic dielectric multilayer temperature sensor: in situ measurement in vitreous during Er:YAG laser irradiation," *Opt. & Las. Tech.* **31**, 593-599 (1999).
- ⁸⁸ Beard, P.C., Perennes, F., Mills, T.N., "Transduction mechanisms of the Fabry-Perot polymer film sensing concept for wideband ultrasound detection," *IEEE Transaction Ultrasonics, Ferroelectrics, and Frequency Control* **46(6)**, 1575-1582 (1999).
- ⁸⁹ Cortés, R., Khomenko, A.V., Stardumov, A.N., Arzate, N., Zenteno, L.A., "Interferometric fibre-optic temperature sensor with spiral polarisation couplers," *Optics Communications* **154**, 268-272 (1998).
- ⁹⁰ Cournoyer, A., Baulaigue, P., Lazarides, E., Blancher, H., Bertrand, L., Occelli, R., "Photothermal measurements with a Jamin interferometer," *Appl. Opt.* **36(21)** 5252-5261 (1997).
- ⁹¹ Yablon, D.A., Nishioka, N.S., Mikić, B.B., Venugopalan, V., "Measurement of tissue absorption coefficients by use of interferometric photothermal spectroscopy," *Appl. Opt.*, **38(7)**, 1259-1272 (1999).
- ⁹² Milner, T.E., Goodman, D.M., Tanenbaum, B.S., Anvari, B., Svaasand, L.O., Nelson, J.S., "Imaging laser heated subsurface chromophores in biological materials: determination of lateral physical dimensions," *Phys. Med. Biol.* **41**, 31-44 (1996).
- ⁹³ Jacques, S.L., Nelson, J.S., Wright, W.H., Milner, T.E., "Pulsed photothermal radiometry of port-wine-stain lesions," *Appl. Optics* **32(13)**, 2439-2446, (1993).
- ⁹⁴ Bindra, R.M.S., Imhof R.E., Mochan, A., Eccleston, G.M., "Opto-thermal technique for *in-vivo* stratum corneum hydration measurement," *Journal de Physique IV, Colloque C7*, supplément au Journal de Physique III, Volume 4 (1994).
- ⁹⁵ Imhof, R.E., Whitters, C.J., Birch, D.J., "Opto-thermal *in vivo* monitoring of sunscreens on skin," *Phys. Med. Biol.* **35(1)**, 95-102 (1990).

- ⁹⁶ Bindra, R.M.S., Imhof R.E., Eccleston, G.M., "In vivo opto-thermal measurement of epidermal thickness," *Journal de Physique IV*, Colloque C7, supplément au Journal de Physique III, Volume 4 (1994).
- ⁹⁷ Long, F.H., Deutsch, T.F., "Pulsed photothermal radiometry of human artery," *IEEE J. Quant. Electr.* **QE23(10)**, 1821-1825 (1987).
- ⁹⁸ Prahl, S.A., Vitkin, I.A., Bruggemann, U., Wilson, B.C., and Anderson, R.R., "Determination of optical properties of turbid media using pulsed photothermal radiometry," *Phys. Med. Biol.* **37**, 1203-1217 (1992).
- ⁹⁹ Vitkin, I.A., Wilson, B.C., Anderson, R.R., "Analysis of layered scattering materials by pulsed photothermal radiometry: application to photon propagation in tissue," *Appl. Optics* **34(16)**, 2973-2982 (1995)
- ¹⁰⁰ Belotserkovsky, E., Mesh, M., Shlifer, A., Eyal, A., Katzir, A., "IR fibreoptic radiometric thermometry for biomedical applications," *Proc SPIE* **2085**, 109-114 (1993).
- ¹⁰¹ Shenfeld, O., Eyal, O., Goldwasser, B., Katzir, A., "Temperature monitoring and control of CO₂ laser tissue welding in the urinary tract using a silver halide fibre optic radiometer," *SPIE Proc.* **1876**, 203-214 (1993).
- ¹⁰² Welch, A.C. *et al*, "Definitions and overview of tissue optics," in *Optical-thermal response of laser-irradiated tissue*, edited by Welch, A.J. and van Gemert, M.J.C., Plenum Press, New York and London (1995).
- ¹⁰³ Oraevsky, A.A., Jacques, S.L., Tittel, F.K., "Measurement of tissue optical properties by time-resolved detection of laser-induced transient stress," *Appl. Opt.* **36(1)**, 402-415 (1997).
- ¹⁰⁴ Beard, P.C., Mills, T.N., "Characterization of *post mortem* arterial tissue using time-resolved photoacoustic spectroscopy at 436, 461 and 532 nm," *Phys. Med. Biol.* **42**, 177-198 (1997).
- ¹⁰⁵ Karabutov, A.A., Podymova, N.B., Letokhov, V.S., "Time-resolved laser optoacoustic tomography of inhomogeneous media," *Appl. Phys. B* **63**, 545-563 (1996).
- ¹⁰⁶ Oraevsky, A.A., Karabutov, A.A., Esenaliev, R.O., "Laser optoacoustic imaging of breast: detection of cancer angiogenesis," *Proc. SPIE* 1999 (in press).
- ¹⁰⁷ Beard, P.C., Mills, T.N., "Evaluation of an optical fibre probe for *in vivo* measurement of the photoacoustic response of tissues," *Proc. SPIE* **2388**, 446-457 (1995).

- ¹⁰⁸ Beard, P.C., Mills, T.N., "Extrinsic optical-fibre ultrasound sensor using a thin polymer film as a low-finesse Fabry-Perot interferometer," *Appl. Opt.* **35(4)**, 663-675 (1996).
- ¹⁰⁹ Beard, P.C., Pérennès, F., Draguioti, E., Mills, T.N., "Optical fibre photoacoustic-photothermal probe," *Optics Letters* **23(15)**, 1235-1237 (1998).
- ¹¹⁰ Coleman AJ, Draguioti E, Tiptaf R., Shotri N., Saunders JE, "Acoustic performance and clinical use of a fibreoptic hydrophone," *Ultrasound in Medicine and Biology* **24(1)**, 143-151 (1998).
- ¹¹¹ Imhof, R.E., Birch, D.J., Thornley, F.R., Gilchrist, J.R., Strivens, T.A., "Optothermal transient emission radiometry," *J. Phys. E: Sci. Instrum.* **17**, 521-525 (1984)
- ¹¹² Tam, A.C., "Pulsed photothermal radiometry for noncontact spectroscopy, material testing and inspection measurements," *Infrared Phys.* **25**, 305-313 (1985).
- ¹¹³ Cielo, P., "Pulsed photothermal evaluation of layered materials," *J. Appl. Phys.* **56**, 230-234 (1984).
- ¹¹⁴ Vitkin, I.A., Wilson, B.C., Anderson, R.R., Prahl, S.A., "Pulsed photothermal radiometry in optically transparent media containing discrete optical absorbers," *Phys. Med. Biol.* **39**, 1721-1744 (1994).
- ¹¹⁵ Vitkin, I.A., Wilson, B.C., Anderson, R.R., "Analysis of layered scattering materials by pulsed photothermal radiometry: application to photon propagation in tissue," *Appl. Optics* **34(16)**, 2973-2982 (1995)
- ¹¹⁶ Milner, T.E., Smithies, D.J., Goodman, D.M., Lau, A. Nelson, J.S., "Depth determination of chromophores in human skin by pulsed photothermal radiometry," *Appl. Optics* **35(19)**, 3379-3385 (1996).
- ¹¹⁷ Sathyam, U.S., Prahl, S.A., "Limitations in measurement of subsurface temperatures using pulsed photothermal radiometry," *J. Biomed. Opt.* **2(3)** 251-261 (1997).
- ¹¹⁸ Smithies, D.J., Milner, T.E., Tanenbaum, B.S., Goodman, D.M., Nelson, J.S., "Accuracy of subsurface temperature distributions computed from pulsed photothermal radiometry," *Phys. Med. Biol.* **43**, 2453-2463 (1998).
- ¹¹⁹ Jacques, S.L., Nelson, J.S., Wright, W.H., Milner, T.E., "Pulsed photothermal radiometry of port-wine-stain lesions," *Appl. Optics* **32(13)**, 2439-2446, (1993).

- ¹²⁰ Prahl, S.A., Vitkin, I.A., Bruggemann, U., Wilson, B.C., and Anderson, R.R., "Determination of optical properties of turbid media using pulsed photothermal radiometry," *Phys. Med. Biol.* **37**, 1203-1217 (1992).
- ¹²¹ Valvano, J.W., Cochran, J.R., Diller, K.R., "Thermal conductivity and diffusivity of biomaterials measured with self-heated thermistors," *Int. J. Thermophys.* **6(3)**, 301-311 (1985).
- ¹²² Carslaw, H.S., Jaeger, J.C., "Conduction of Heat in Solids," Oxford University Press (1959)
- ¹²³ Star, W.M., "Diffusion theory of light transport," in *Optical-thermal response of laser-irradiated tissue*, edited by Welch, A.J., and van Gemert, M.J.C., Plenum Press, New York and London (1995).
- ¹²⁴ Patterson, M.S., Wilson, B.C., Graff, R., "In vivo test of the concept of photodynamic threshold dose in normal rat liver photosensitized by aluminium chlorosulphonated phthalocyanine," *Photochem. Photobiol.* **51**, 343-349 (1990).
- ¹²⁵ Bohren, C.F., Huffman, D.R., "Absorption and scattering of light by small particles," Wiley, New York (1983).
- ¹²⁶ Valvano, J.W., "Temperature measurements," *Adv. Heat Transfer* **22**, 359-436 (1992).
- ¹²⁷ *Handbook of Chemistry and Physics*, 53rd edition, published by The Chemical Rubber Company
- ¹²⁸ Anderson, R.R., Beck, H., Bruggemann, U., Farinelli, W., Jacques, S.L., Parrish, J.A., "Pulsed photothermal radiometry in turbid media: internal reflection of backscattered radiation strongly influence optical dosimetry," *Appl. Opt.* **28(12)**, 2256-2262 (1989).
- ¹²⁹ Jacques, S.L., Nelson, J.S., Wright, W.H., Milner, T.E., "Pulsed photothermal radiometry of port-wine-stain lesions," *Appl. Opt.* **32(13)**, 2439-2446 (1993).
- ¹³⁰ Berg, E.P., O'Driscoll, D., Imhof, R.E., "Fast, low noise preamplifiers for pulsed optothermal radiometry," *Proc. Photoacoustic and photothermal phenomena: 10th international conference*, 141-143 (1999)
- ¹³¹ Welch, A.J., Van Gemert, M.J.C., *Optical-thermal response of laser irradiated tissue*, Plenum Press (1995).

- ¹³² Press, W.H., Flannery, B.P., Teukolsky, S.A., Vetterling, W.T., "Numerical recipes in C," Cambridge University Press
- ¹³³ Leung, W.P., Tam, A.C., "Techniques of flash radiometry," *J. Appl. Phys.* **56**, 153-161 (1984).
- ¹³⁴ Hecht E., Zajac A., "Optics", 1st edition, (Addison-Wesley Inc.), USA, 1974.
- ¹³⁵ Beard, P.C., Mills, T.N., "Extrinsic optical-fibre ultrasound sensor using a thin polymer film as a low-finesse Fabry-Perot interferometer," *Appl. Optics* **35(4)** 663-675 (1996).
- ¹³⁶ Pérennès, F., Beard, P.C., Mills, T.N., "Analysis of a low finesse Fabry-Perot interferometer illuminated by a multimode optical fibre," *Appl. Optics* **38(34)**, 7026-7034 (1999).
- ¹³⁷ Culshaw, B., *Optical fibre sensing and signal processing*, Peregrinus Ltd. (1974).
- ¹³⁸ Butler, M.A., Buss, R.J., Galuska, A., "Properties of micrometer-thick plasma-polymerized tetrafluoroethylene films," *J. Appl. Phys.* **70(4)**, 2326-2332 (1991).
- ¹³⁹ Heinemann, H., Henning, M., Krämer, H., *Physik – Verstehen durch Üben*, VEB Fachbuchverlag Leipzig (1990).
- ¹⁴⁰ Thormählen, I., Straub, J., Grigul, U., "Refractive index of water and its dependence on wavelength, temperature, and density," *J. Phys. Chem. Ref. Data* **14(4)**, 933-945 (1985).
- ¹⁴¹ Graeme, J., *Photodiode amplifiers*, McGraw-Hill (1995).
- ¹⁴² Hamamatsu catalogue "Photodiodes", p. 28, 1995.
- ¹⁴³ Melles Griot detector guide, p.14 (1990).
- ¹⁴⁴ Beard, P.C., "Pulsed laser generation and optical fibre detection of thermoelastic waves in arterial tissues," Ph.D. thesis, University College London (1996).
- ¹⁴⁵ Leung, W.P., Tam, A.C., "Techniques of flash radiometry," *J. Appl. Phys.* **56**, 153-61 (1984).
- ¹⁴⁶ Yadav, B.R., Dongaunkar, A.G., "Temperature dependence of dynamic and static Young's modulus of polymers," *Ind. J. Pure Appl. Phys.* **20(12)**, 988-989 (1982).
- ¹⁴⁷ Wilkens, V., Wiemann, C., Koch, C., Foth, H.-J., "Fibre-optic dielectric multilayer temperature sensor: in situ measurement in vitreous during Er:YAG laser irradiation," *Optics & Laser Technology* **31**, 593-599 (1999).

- ¹⁴⁸ Wilkens, V., Koch, C., "Fibre-optic multilayer hydrophone for ultrasonic measurement," *Ultrasonics* **37**, 45-49 (1999).
- ¹⁴⁹ Verdaasdonk, R.M., Borst, C., "Ray tracing of optically modified fibre tips. 1: spherical probes," *Appl. Optics* **30(16)**, 2159-2171 (1991).
- ¹⁵⁰ Star, W.M., "Diffusion theory of light transport," in *Optical-thermal response of laser-irradiated tissue* Plenum Press, New York and London (1995).
- ¹⁵¹ Wang, L.-H., Jacques, S.L., Zheng, L.-Q., "MCML – Monte Carlo modelling of photon transport in multi-layered tissues," *Computer Methods and Programs in Biomedicine* **47**, 131-146 (1995).
- ¹⁵² Jacques, S.L., Alter, C.A., Prahl, S.A., "Angular scattering of HeNe laser light by human dermis," *Lasers Life Sci.* **14**, 309-333 (1987).
- ¹⁵³ Treweek, S.P., Barbenel, J.C., "Direct measurement of the optical properties of human breast skin," *Med. Biol. Eng. Comput.* **34**, 285-289 (1996).
- ¹⁵⁴ Wang, L.-H., Jacques, S.L., Zheng, L.-Q., "CONV – Convolution for responses to a finite diameter photon beam incident on multi-layered tissues," *Computer Methods and Programs in Biomedicine* **54**, 141-150 (1997).
- ¹⁵⁵ Beck, J.V., Arnold, K.J., *Parameter estimation in engineering and science*, John Wiley and Sons, New York (1977).
- ¹⁵⁶ Valvano, J.W., et al, "Thermal conductivity and diffusivity of biomaterials measured with self-heated thermistors," *Int. J. Thermophys.* **6**, 301-311 (1985).
- ¹⁵⁷ Anderson, J.T., Valvano, J.W., "An interlobular artery and vein based model for self-heated thermistor measurements of perfusion in the canine kidney cortex," in Roemer, R.B., McGrath, J.J. and Bowman, H.F. (editors), *Bioheat Transfer – Applications in Hyperthermia, Emerging Horizons in Instrumentation and Modelling*, HTD Vol. 126, BED. Vol 12, ASME Winter Annual Meeting, 1989, pp. 29-35.
- ¹⁵⁸ Kohl, M., Essenpreis, M., Cope, M., "The influence of glucose concentration upon the transport of light in tissue-simulating phantoms," *Phys. Med. Biol.* **40**, 1267-1287 (1995).
- ¹⁵⁹ Garbassi, F., Morra, M., Occhiello, E., *Polymer surfaces: from physics to technology*, John Wiley & Sons (1998).

- ¹⁶⁰ *Chambers Science and Technology dictionary*, ed. Walker, P.M.B., W & R Chambers Ltd and Cambridge University Press (1988).
- ¹⁶¹ *Technical information – Mylar polyester film*, DuPont
- ¹⁶² Matsutani, T., Matsue, H., Kumazaki, K., Kubo, U., Nakayama, T., “TiN film for transparent conductors formed by pulsed laser deposition in reactive gas,” *Rev. Las. Eng.* **26(7)**, 563-565 (1998).
- ¹⁶³ Power, J.F., “Impulse photopyroelectric depth profiling of multilayers. Part II: Experiments with amplitude- and phase-modulated wideband spectrometry,” *Appl. Spectroscopy* **45(8)**, 1252-1270 (1991).
- ¹⁶⁴ Eyal, O., Scharf, V., Katzir, A., “Temperature measurements using pulsed photothermal radiometry and silver halide infrared optical fibres,” *Appl. Phys. Lett.* **70(12)**, 1509-1511 (1997).
- ¹⁶⁵ Belotserkovsky, E., Mesh, M., Shlifer, A., Eyal, O., Katzir, A., “IR fibreoptic radiometric thermometry for biomedical applications,” *SPIE Proc.* **2085**, 109-114 (1993).
- ¹⁶⁶ Eyal, O., Zur, A., Shenfeld, O., Mordechai, G., Katzir, A., “Infrared radiometry using silver halide fibers and a cooled photonic detector,” *Opt. Engineering* **33(2)**, 502-508 (1994).
- ¹⁶⁷ Katzir, A., personal communication.
- ¹⁶⁸ Pascut, F., Xiao, P., O’Driscoll, D.G., Katzir, A., Gannot, I., Croitoru, N., Notingher, I., Imhof, R.E., “Fibre-optic opto-thermal hand held probe for *in vivo* measurement on human skin,” *SPIE Proc.* (2000).
- ¹⁶⁹ Imhof, R.E., Zhang, B., Birch, D.J.S., “Photothermal radiometry for NDE,” *Progress in Photothermal & Photoacoustic Science & Technology* **2(7)**, 185-236, PTR Prentice Hall, Edgewood Cliffs, New Jersey (1994).
- ¹⁷⁰ Prahl, S.A., Vitkin, I.A., Bruggemann, U., Wilson, B.C., Anderson, R.R., “Determination of optical properties of turbid media using pulsed photothermal radiometry,” *Phys. Med. Biol.* **37(6)**, 1203-1217 (1992).
- ¹⁷¹ Gandjbakhche, A.H., Nossal, R., Dadmarz, R., Schwartzentruber, D., Bonner, R.F., “Expected detectability of adenocarcinoma tumours within human breast in time-resolved images,” *Proc. SPIE* **2387**, 111-118 (1995).

¹⁷² Parsa, P., Jacques, S.L., Nishioka, N.S., "Optical properties of rat liver between 350 and 2200 nm." *Appl. Opt.* **28**, 2325-2330 (1989).

¹⁷³ Duck, F.A., *Physical properties of tissue – a comprehensive reference book* Academic Press Ltd, San Diego (1990).

¹⁷⁴ Blanc, D., Colles, M.J., "Transmission measurements on various tissue samples between 1064 and 2000 nm," *Lasers Med. Sci.* **5**, 71-75 (1990).

¹⁷⁵ Pedrotti, F.L., Pedrotti, L.S., *Introduction to optics* sec. edition, Prentice-Hall International, Inc. 1996.